Recherche du boson de Higgs dans le canal de désintégration en deux photons avec le détecteur ATLAS au LHC

P. Bernat

LAL 10-92
2010

UNIVERSITÉ PARIS XI
UFR SCIENTIFIQUE D'ORSAY

THÈSE

Pour l'obtention du titre de
DOCTEUR ÈS SCIENCES DE L'UNIVERSITÉ PARIS XI, ORSAY
Spécialité: Physique des Particules
présentée le 24 juin 2010
par

Pauline Bernat

Recherche du boson de Higgs dans le canal de désintégration en deux photons avec le détecteur ATLAS au LHC

Soutenue devant la Commission d'examen composée de:

M.	P.	BLOCH	Rapporteur
M.	M.	FONTANNAZ	
M.	A.	JUSTE ROZAS	Rapporteur
M.	M.	KADO	Directeur de thèse
M.	A.	NISATI	
M.	G.	WORMSER	Président du jury

Contents

Abstract

This document comprises of three parts related to different aspects in the search for the Higgs boson in the $\gamma\gamma$ channel with the ATLAS detector.

The first part presents a study of the intrinsic uniformity of the EM barrel calorimeter of ATLAS using the drift time measurement of ionization electrons. About 500 000 cosmic muon pulses have been recorded and compared to the signal shape predicted using the *First Principle Method*. The prediction of the signal shape allow to measure the drift time of ionization electrons in the Liquid Argon (LAr). The drift time uniformity in the Middle compartment of the barrel is derived per regions of size 0.1×0.1 in the (η, ϕ) plane and is estimated of $1.27 \pm 0.03\%$. Its impact on the calorimeter response uniformity is found to be of $0.29 \pm 0.01\%$. With the lead thickness variation expected to contribute by $\sim 0.18\%$, this leads to an intrinsic calorimeter uniformity in the barrel of 0.34%. The drift velocity of electrons is measured in the different layers of the barrel and amounts to $V_D(\mathrm{E} = 1\ \mathrm{kV/mm}) = 4.58 \pm 0.07\ \mathrm{mm}.\mu s^{-1}$ which is in good agreement with previous measurements of the electrons drift velocity in the LAr at the operating temperature of 88.5 K.

The second part treats the question of the estimate of the material upstream of the calorimeter using the material mapping in the inner detector. The knowledge of the material upstream of and in the calorimeter is essential for an accurate calibration of the photons and electrons energy reconstruction. The measurement of the upstream material is done relatively to a well isolated and well known material that is the beam pipe (BP) in order to be independent of the initial flux of photons. A study of the measurement of the material in the BP using photon conversions is presented. Given that a large fraction of the photons originate from π^0 mesons, the initial flux of photons arising in the conversion rate is normalized to the π^0 Dalitz decays. The BP conversion rate is expressed as a function of the ratio of the reconstructed BP conversions to that of Dalitz decays that is measured in data recorded at 7 TeV centre-of-mass energy. The BP conversion rate estimated in the data well agrees with prediction from the Monte-Carlo (MC) simulation: $P_{acc}(\text{data 7 TeV}) \longrightarrow 17.87 \pm 0.92\ (\text{stat})\ ^{+0.36}_{-0.72}\ (\text{syst})\ {}^{0}/_{00}$ and $P_{acc}(\text{MC 7 TeV}) \longrightarrow 17.99 \pm 0.01\ (\text{stat})\ {}^{0}/_{00}$ respectively.

The last part presents a study of the normalizations of the signal and background and the discriminating potential in the $H \to \gamma\gamma$ inclusive analysis at 14 TeV centre-of-mass energy. Different programs and MC simulations are used to estimate a Next-to-Leading Order normalization of the signal and irreducible background ($\gamma\gamma$) as well as associated systematic uncertainties. There respectively amount to 16% and 26%. The discriminating power of the transverse momentum of the diphoton system and the $\cos\theta^*$ is reappraised. In particular a strong correlation is observed between the $\cos\theta^*$ and the diphoton invariant mass. The semi-reducible background (γ-jet) is normalized at NLO with 26% of systematic error. A refined normalization that is applied after the photon identification is proposed. It accounts for the different rejection of jets originating from quarks or gluons and amounts to 1.9 ± 0.6.
The prospects for exclusion of the Higgs boson in the $\gamma\gamma$ channel at 10 TeV energy are presented as well as in the extrapolation at 7 TeV for an integrated luminosity of 1 fb^{-1}. In the later scenario, about five times the Standard Model is expected to be excluded at 95% of confidence level for Higgs boson mass around 120 GeV/c^2.

Résumé

Cette thèse a traité trois différents aspects ayant trait à la recherche du boson de Higgs dans le canal de désintégration en deux photons avec le détecteur ATLAS.

Le premier aspect est une étude sur l'uniformité intrinsèque du calorimètre électromagnétique (EM) d'ATLAS en utilisant la mesure du temps de dérive des électrons d'ionisation. Environs 500 000 signaux provenant de rayons cosmiques sont enregistrés et sont comparés à la forme du signal prédite en utilisant la méthode FPM (pour *First Principle Method*). L'ajustement de la forme prédite à celle mesurée permet de mesurer le temps de dérive des électrons d'ionization de l'argon liquide. L'uniformité du temps de dérive dans le compartiment Middle calculée par blocs de taille 0.1×0.1 dans le plan (η, ϕ) est estimée à $1.27 \pm 0.03\%$. L'impact de la variation du temps de dérive sur l'uniformité de la réponse du calorimètre est estimée à $0.29 \pm 0.01\%$. En tenant compte de la variation de l'épaisseur des plaques de plomb qui constituent le milieu passif et qui ont été mesurées par ailleurs, l'uniformité intrinsèque du calorimètre est estimée à 0.34%. La vitesse de dérive des électrons mesurée dans les différents compartiments du calorimètre est en moyenne $V_D(\mathrm{E} = 1\ \mathrm{kV/mm}) = 4.58 \pm 0.07\ \mathrm{mm}.\mu s^{-1}$ en bon accord avec des mesures antérieures de la vitesse de dérive des électrons dans l'argon liquide à la température de 88.5K.

Le second aspect aborde la question de l'estimation de la matière en amont du calorimètre, utilisant une cartographie du détecteur interne. Cette mesure est faite relativement au nombre de conversions dans le tube à vide (*beam pipe*) de manière à être indépendante du flux initial de photons. Une connaissance précise de la matière en amont du calorimètre est essentielle à la calibration en énergie des électrons et photons reconstruits dans le calorimètre. Puisqu'une large fraction des photons proviennent de mésons π^0, le flux initial de photons qui intervient dans le taux de conversions dans le beam pipe est normalisé aux désintégrations Dalitz du π^0. L'observable qui permet de comparer les données aux simulations Monte-Carlo (MC) est le rapport du nombre de conversions reconstruites dans le beam pipe et du nombre de Dalitz reconstruits. Ce rapport estimé avec les données de collision à une énergie de 7 TeV dans le centre de masse donne un bon accord sur la mesure du taux de conversion dans le beam pipe avec la prédiction du MC : $P_{acc}(\text{data 7 TeV}) \longrightarrow 17.87 \pm 0.92\ (\text{stat})\ ^{+0.36}_{-0.72}\ (\text{syst})\ {}^0\!/_{00}$ et $P_{acc}(\text{MC 7 TeV}) \longrightarrow 17.99 \pm 0.01\ (\text{stat})\ {}^0\!/_{00}$ respectivement.

Le dernier aspect est l'étude de la normalisation du signal et du bruit de fond ainsi que l'analyse du potentiel discriminant dans l'analyse inclusive du canal $H \to \gamma\gamma$ une nergie dans le centre de masse 14 TeV. Différentes simulations MC sont utilisées pour estimer une normalisation à l'ordre NLO du signal et du bruit de fond irréductible ($\gamma\gamma$) ainsi que les erreurs systématiques associées. Celles-ci représentent respectivement 16% and 26% de la section efficace totale. Le pouvoir discriminant de l'impulsion transverse du système diphoton et du $\cos\theta^*$ est aussi étudié. En particulier, une forte corrélation entre le $\cos\theta^*$ et la masse invariante diphoton est observée. Le bruit de fond semi-réductible (γ-jet) est normalisé à NLO avec 27% d'erreurs systématiques. Une nouvelle normalisation qui s'applique après l'identification des photons est proposée. Elle prend en compte la différente réjection des jets provenant de quark ou de gluon et est estimée à 1.9 ± 0.6.

Les perspectives d'exclusion du boson de Higgs dans le canal diphoton à 10 TeV et l'extrapolation à 7 TeV pour un luminosité intégrée de 1 fb^{-1} sont présentées. Dans le dernier scénario, environ 5 fois le Modèle Standard est exclu à 95% de niveau de confiance pour une masse du boson de Higgs autour de 120 GeV/c^2.

Introduction

The Standard Model (SM) of particle physics describes elementary particles and their interaction. In particular it interprets the fundamental electromagnetic, weak and strong forces in terms of local gauge symmetries. This description in terms of symmetries requires that particles be massless. The most acclaimed mechanism proposed to allow particles to carry a mass in a gauge invariant way is the Higgs mechanism. It introduces a scalar field that generates mass terms through a spontaneous symmetry breaking mechanism. This mechanism also predicts the existence of a fundamental scalar particle, the Higgs boson, which has not yet been discovered. Its mass is a free parameter of the theory although theoretical constraints, experimental direct searches and experimental indirect constraints from precision measurements indicate that a light SM Higgs is preferred, with a mass typically below 200 GeV/c^2.

The Large Hadron Collider has produced its first proton-proton collisions in december 2009 at a centre-of-mass energy of 900 GeV and is now producing 7 TeV collisions while increasing the luminosity. Among the high energy particle physics experiments at LHC are the two general-purpose detectors: ATLAS (A Toroidal LHC ApparatuS) and CMS (Compact Muon Solenoid). Both should be able to confirm if the Higgs mechanism is responsible for the SM symmetry breaking and hopefully give indications of physics beyond the SM.

This thesis is dedicated to the search of the SM Higgs boson in the diphoton decay channel with the ATLAS detector. The Higgs decay into two photons is among the most important channels in the low mass range, typically $100 < m_H < 150\ GeV/c^2$. Despite its small branching ratio, about 0.2%, it has a conspicuous event yield, a very clean signature with two well-isolated photons in the final state and a narrow resonance width. This channel however suffers from a very large background. Part of which is completely irreducible and part of which is due to jets faking photons. The ATLAS sensitivity to such signal critically relies on the detector ability to accurately reconstruct the invariant mass of the two photons and to discriminate photons from jets. In this thesis two essential aspects of this search are treated: the photon energy resolution and a critical study of the background discrimination based on the kinematical properties of the signal and background processes. This work is organized in three independent parts:

A.- A study of the intrinsic uniformity of the calorimeter using 2008 cosmic muon data is presented in the first part of the manuscript. The drift time uniformity is estimated in the Middle compartment of the electromagnetic (EM) calorimeter (barrel part), which contains the most important fraction of the EM shower (about 70%). Its impact on the calorimeter response uniformity and contribution to the energy resolution constant term are derived.

B.- A study of the innermost part of the inner detector material using conversions and π^0 Dalitz decays is presented in the second part. The radiation length of the BP is measured with 7 TeV data and compared to the prediction from the layout design in order to get a reference number for the normalization of upstream material. A precise estimation of the material upstream of the calorimeter is indeed essential for an accurate calibration of the photon energy recontruction.

C.- A study of the signal and background normalization and discrimination potential in this channel is presented in the third part. The signal, the reducible and irreducible backgrounds normalizations are studied, at a centre-of-mass energy of 14 TeV. Different Monte-Carlo generators and Matrix Element calculation programs are used to derive the normalizations at the Next-to-Leading Order (NLO) in perturbative QCD and estimate associated systematic uncertainties. The discriminant power of various variables and the correlation between them are studied in detail.

Finally these studies are used in the context of a study of the prospects of Higgs boson exclusion at 10 and 7 TeV centre-of-mass energy.

Chapter 1

Motivation

The Standard Model (SM) [1] of particle physics is a quantum field theory that describes the fundamental forces and matter constituents in nature. The SM comprises three of the four fundamental interactions - the electromagnetic, weak and strong interactions that are described in terms of gauge theories based on symmetry. Mass terms for gauge bosons break the gauge invariance of the theory. To allow the particles to carry a mass, the Higgs mechanism introduces a scalar doublet in the theory. The spontaneous breaking of the SM symmetry generates mass term for gauge bosons, including for a new boson introduced by the scalar doublet that is the Higgs boson. Its mass is a free parameter of the theory that is however constrained by the theory and experiments.
The general picture of the SM is presented in this section and the Higgs mechanism is introduced. (A detailed description of the SM can be found in [2]). It is followed by an overview of the theoretical and experimental constraints on the Higgs boson mass.

1.1 The Standard Model of Particle Physics

In quantum field theories the fundamental interactions are described by the principle of local gauge symmetry. The Lagrangian of a physical system described by the interaction of a certain symmetry contains the symmetry, *i.e* it is invariant under a local gauge transformation of the symmetry group.

The SM theory is a combination of local gauge symmetry groups: $SU(2)_L \times U(1)_Y \times SU(3)_c$.

- The electromagnetic and weak interactions are described into the electroweak gauge symmetry group $SU(2)_L \times U(1)_Y$ proposed by Glashow, Salam and Weinberg [3–5] in 1960s. The $U(1)_Y$ abelian, group of coupling g', is mediated by a unique boson B. The $SU(2)_L$ non abelian group, of coupling g, is mediated by three vectorial bosons, W^1, W^2 and W^3. The quantum numbers associated to these groups are respectively the hypercharge Y and the weak isospin T.

- The strong interaction is described by the non-abelian quantum chromodynamic theory (QCD) of symmetry $SU(3)_c$. The Lie group rules [6] imply 8 mediators, the gluons, that are massless.

Table 1.1 lists the properties of the bosons associated to the different interactions.

Interaction	boson	mass (GeV/c^2)	charge Q/spin J
electromagnetic	γ(photon)	0	0/1
weak	$W^{\pm}$ et Z^0	80.4 et 91.2	$\pm$1/1 et 0/1
strong	g(8 gluons)	0	0/1
gravity	graviton	0	0/2

Table 1.1: The four fundamental interactions and their associated boson(s). The gravity is not described by the SM.

The matter fields comprise three generations of left-handed and right-handed fermions (spin 1/2). The left-handed fermions are weak isospin doublets of leptons (L) and quarks (Q):

$$L_1 = \begin{pmatrix} \nu_e \\ e^- \end{pmatrix}_L, \quad L_2 = \begin{pmatrix} \nu_\mu \\ \mu^- \end{pmatrix}_L, \quad L_3 = \begin{pmatrix} \nu_\tau \\ \tau^- \end{pmatrix}_L \tag{1.1}$$

$$Q_1 = \begin{pmatrix} u \\ d \end{pmatrix}_L, \quad Q_2 = \begin{pmatrix} c \\ s \end{pmatrix}_L, \quad Q_3 = \begin{pmatrix} t \\ b \end{pmatrix}_L \tag{1.2}$$

The left-handed fermions are also triplets of $SU(3)_c$ (only quarks interact in QCD). The right-handed fermions are weak isospin singlets and do not interact weakly. There are also singlets of $SU(3)_c$.

$$e_{R1} = e_R^-, e_{R2} = \mu_R^-, \tau_{R3} = \tau_R^- \tag{1.3}$$

$$u_{R1} = u_R, u_{R2} = c_R, u_{R3} = t_R \tag{1.4}$$

$$d_{R1} = d_R, d_{R2} = s_R, d_{R3} = b_R \tag{1.5}$$

There is no right-handed neutrinos, these particles are massless in the SM.

The experiments have observed that the fermions and the weak bosons have a mass. Mass terms in the Lagrangian of the theory break the SM symmetry though. The so-called Higgs mechanism was introduced in 1964 [7–9] as a solution to the electroweak symmetry breaking. The introduction of the Higgs scalar field doublet allows the particles to carry a mass in a gauge invariant way. In the GSW model, the $SU(2)_L \times U(1)_Y$ symmetry is spontaneously broken to $U(1)_{em}$. The remaining symmetry is the gauge group of the electric charge, mediated by the photon. The electric charge is given by the relation of Gell-Mann Nishijima:

$$Q = T^3 + \frac{Y}{2} \tag{1.6}$$

where T^3 is the third component of the weak isospin.

The bottom particles from the lepton doublets are of charge -Q, while the top-doublet particles, the neutrinos, are chargeless. The top and bottom quarks have a fractional charge, 2/3 and -1/3 respectively. Except for the neutrinos, the fermions of second and third generations are unstable and decay into fermions of the first family that is almost sufficient to describe all ordinary matter. Table 1.2 summarizes the particle content of the SM and indicates their mass and electrical charge Q.

Leptons			Quarks		
particle	mass (GeV/c^2)	Q	particle	mass (GeV/c^2))	Q
e	511.10^{-6}	-1	u(up)	$(1.5-3)10^{-3}$	2/3
ν_e	$< 3.10^{-9}$	0	d(down)	$(3-7)10^{-3}$	-1/3
μ	106.10^{-3}	-1	c(charm)	1.25 ± 0.09	2/3
ν_μ	$< 2.10^{-4}$	0	s(strange)	$(95 \pm 25).10^{-3}$	-1/3
τ	1.77	-1	t(top)	$172.3^{+10.2}_{-7.6}$	2/3
ν_τ	< 0.018	0	b(bottom)	4.1-4.7	-1/3

Table 1.2: Particles content of the SM.

The GSW model predicts the existence of two neutral and two charged mediators of the interaction. Neutral bosons (B^μ and W^3) are linear combinations of the photon and the weak boson Z that "unify" the two interactions while the charged bosons (W^1 and W^2) are the weak boson $W^\pm$. This model predicts therefore the existence of neutral current for the weak interaction. Neutral currents were observed for the first time in 1973 with the Gargamelle experiment at CERN. The W and Z boson were then directly observed for the first time at CERNs proton-antiproton collider experiments. In 1983, the UA1 and UA2 experiences with the SppS at CERN have observed that the weak bosons were massive and heavy ([10] and [11]), $M_Z \approx 91\ GeV/c^2$ and $M_W \approx 80\ GeV/c^2$. These discoveries had proven that the symmetry of the electroweak interaction has to be broken at a certain scale, of the order of these masses. The Higgs mechanism has been introduced as a solution to the spontaneous breaking of the EW symmetry.

1.2 The Higgs Mechanism

1.2.1 The Spontaneous Breaking of EW Symmetry

The Higgs mechanism consists in introducing a new boson in the theory, a doublet of Higgs complex scalar field:

$$\phi = \begin{pmatrix} \phi_+ \\ \phi_0 \end{pmatrix} = \frac{1}{\sqrt{2}} \begin{pmatrix} \phi_1 + i\phi_2 \\ \phi_3 + i\phi_4 \end{pmatrix} \tag{1.7}$$

where ϕ_0 and ϕ_+ denote a neutral and a charged field respectively. In the Higgs sector of the SM the Lagrangian of the theory is written as:

$$\mathcal{L}_\mathcal{H} = (D_\mu \phi)^\dagger (D^\mu \phi) - V(\phi) \tag{1.8}$$

The first term on the right side of the Lagrangian represents the electroweak bosons interaction with the Higgs field. The invariance of the Lagrangian under a local gauge transformation $(SU(2)_L \times U(1)_Y)$ requires the covariante derivate [12] to have the form:

$$D_\mu = \partial_\mu - igT\sigma^a W^a_\mu - ig'\frac{Y}{2}B_\mu \tag{1.9}$$

σ^a (a=1,2,3) are the Pauli matrices, T and Y are the aforementioned weak isospsin and hypercharge associated to the $U(1)_Y$ and $SU(2)_L$ symmetry groups of independent coupling g' and g, respectively.

$V(\phi)$ is the scalar potential associated to the complex doublet ϕ, of the form:

$$V(\phi) = \mu^2(\phi^\dagger\phi) + \lambda(\phi^\dagger\phi)^2 \tag{1.10}$$

It is displayed in Figure 1.1 for the particular case ($\lambda > 0$, $\mu^2 < 0$). The ground state of the Higgs field is given by the minimum of the potential which has an infinite number of values in that scenario. The absolute value of the field at the minima of the potential is the so called *expected value* of the field, $|\phi| = v/\sqrt{2}$. As the ground state in infinitely degenerated, one state is chosen as the reference ground state for the local gauge transformation. It is commonly of the form:

$$\phi_0 = \frac{1}{\sqrt{2}}\begin{pmatrix} 0 \\ v \end{pmatrix}, (\phi_1 = \phi_2 = \phi_4 = 0, \phi_3 = v) \tag{1.11}$$

where the non null *vacuum expected value* (v.e.v) is $v = \sqrt{\frac{-\mu^2}{\lambda}} \sim 246$ GeV.

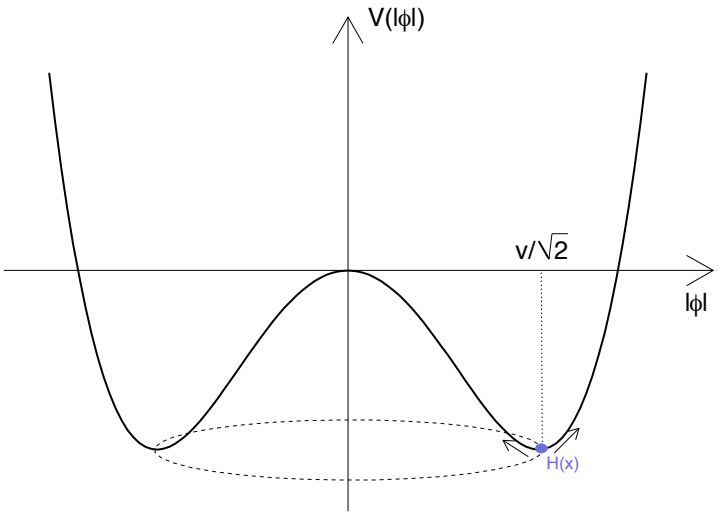

Figure 1.1: Schematic view of the Higgs potential. The dashed ellipse illustrates the infinite minima of the potential. $H(x)$ corresponds to a local transformation of the Higgs field around one chosen group state.

The local transformation of the Higgs field near the *vev* of the form:

$$\phi_0 \rightarrow \frac{1}{\sqrt{2}}\begin{pmatrix} 0 \\ v + H(x) \end{pmatrix} \tag{1.12}$$

introduces the mass terms for gauge bosons in equation 1.8.

1. The W boson mass is given by the relation $m_W = \frac{1}{2}vg$.

2. The masses for the neutral bosons are hidden in a mixture of the field B_μ and W^3_μ. These are obtained by diagonalizing the mass matrix. The orthogonal combination gives the

neutral Z boson mass $m_Z = \frac{v}{2}\sqrt{g^2+g'^2}$. One linear combination gives a massless boson, the photon. The electric charge is given by the relation:

$$e = g\sin(\theta_W) = g'\cos(\theta_W) \tag{1.13}$$

$$\cos(\theta_W) = \frac{g}{\sqrt{g^2+g'^2}} \longrightarrow \frac{m_W}{m_Z} = \cos(\theta_W) \tag{1.14}$$

θ_W is the Weinberg angle or weak mixing angle that gives the ratio of the W and Z boson masses, at the tree-level of the theory.

The Higgs boson mass is given by the relation $m_H = \sqrt{-2\mu^2} = \sqrt{2\lambda v^2}$. λ reminds a free parameter of the potential. The Higgs mass is therefore a free parameter of the theory.

In the EW sector of the SM, the complete Lagrangian of the theory is written as:

$$\mathcal{L}_{\mathcal{H}} = (D_\mu\phi)^\dagger(D^\mu\phi) - V(\phi) + \mathcal{L}_{boson} + \mathcal{L}_{fermion} + \mathcal{L}_{Yukawa} \tag{1.15}$$

$\mathcal{L}_{boson}$ denotes the kinetic energy term for the $U(1)$ and $SU(2)$ gauge fields:

$$\mathcal{L}_{boson} = -\frac{1}{4}B_{\mu\nu}B^{\mu\nu} - \frac{1}{2}tr(W_{\mu\nu}W^{\mu\nu}) \tag{1.16}$$

$B_{\mu\nu} = \partial_\mu B_\nu - \partial_\nu B_\mu$ is the anti-symmetric tensor of the gauge field B_μ and $W_{\mu\nu} = \partial_\mu W_\nu - \partial_\nu W_\mu - ig[W_\mu, W_\nu]$ the tensor of the non abelian $SU(2)$ symmetry.

$\mathcal{L}_{fermion}$ denotes the terms of interaction with gauge fields and $\mathcal{L}_{Yukawa}$ contains the mass and kinetic terms for the fermions ($\psi_i = L_i, Q_i$). Mass terms of the form $m\overline{\psi}\psi$ for fermions are not allowed in the theory as these break the local gauge invariance of the SM symmetry $SU(2)_L \times U(1)_Y$. A local transformation of the symmetry introduces mass terms made of a combination of up and down components of the doublet. The invariance of the Lagrangian under local gauge transformation is however preserved when coupling the fermions to the Higgs boson. The so-called Yukawa coupling terms are of the form:

$$\mathcal{L}_{Yukawa} = \lambda_\psi(\overline{\psi_L}\phi\psi_R + \overline{\psi_R}\phi^\dagger\psi_L)\ , \quad \psi_L = (L_i, Q_i), \psi_R = (e_i, d_i, u_i) \tag{1.17}$$

The local gauge transformation $H(x)$ introduces two terms per fermion in the Lagrangian, of the form:

$$\frac{\lambda_l}{\sqrt{2}}v(\overline{L_L}l_R + \overline{l_R}L_L) + \frac{\lambda_l}{\sqrt{2}}(\overline{L_L}l_R + \overline{l_R}L_L)H(x) \tag{1.18}$$

The mass of the fermions are then given by the Yukawa couplings: $m_l = \lambda_l v/\sqrt{2}$. Because of the form of the Higgs field near the *vev* (equation 1.12), the mass terms are only introduced for the lower member of the left-handed doublets. This is not a problem for leptons when assuming that the neutrinos are massless. However, in order to give a mass to the upper member of quark doublets, the Higgs field would need to have a non-null upper component. The trick is to couple the quarks with the conjugate of the Higgs field $\phi_c = -i\sigma_2\phi^*$. The local gauge invariance of the symmetry is then preserved and the mass terms are of the form:

$$\mathcal{L}_{Yukawa} = \lambda_u^{ij}u_i\overline{Q_j}\sigma_2\phi^* + \lambda_d^{ij}d_i\overline{Q_j}\phi + \lambda_l^{ij}\overline{L_i}l_j\phi \quad + \quad h.c \tag{1.19}$$

(i, j) denotes the fermion generation. The measured mass of the fermions, leptons and quarks, translate a variation of several order of magnitude of the Yukawa coupling:

$$\lambda_{\nu_e} \leq 6.10^{-8} \ , \quad \lambda_e \approx 3.10^{-6} \ , \quad \lambda_b \approx 3.10^{-2} \ , \quad \lambda_t \approx 1$$

The Yukawa couplings introduce the fermions mass in a gauge invariant way but do not predict them and in particular do not predict the large difference between fermion masses. The large difference in Yukawa couplings is called the *flavor hierarchy*.

1.3 Constraints on the Higgs boson mass

The Higgs mass is a free parameter of the theory, defined by its self-coupling $\lambda(Q^2)$. Although the Higgs boson has not yet been discovered, theoretical arguments put lower and upper limits on its mass based on the evolution of the running coupling $\lambda(Q^2)$. Direct experimental searches as well as precision measurements on EW parameters of the SM also constrain the Higgs boson mass.

1.3.1 Theoretical arguments

There are mainly three theoretical arguments that constrain the Higgs mass range according to a domain or scale of validity of the SM.

1. **The Unitarity:** the elastic scattering diagrams of the W boson are illustrated in the SM picture by the Feynman diagrams (a) and (b) in Figure 1.2. The corresponding cross section increases with the scattering energy when calculated in perturbative development as a function of the coupling constant. As a consequence, it violates the unitarity for energy above 1.2 TeV. The Higgs mechanism is a solution to restore it. The Higgs

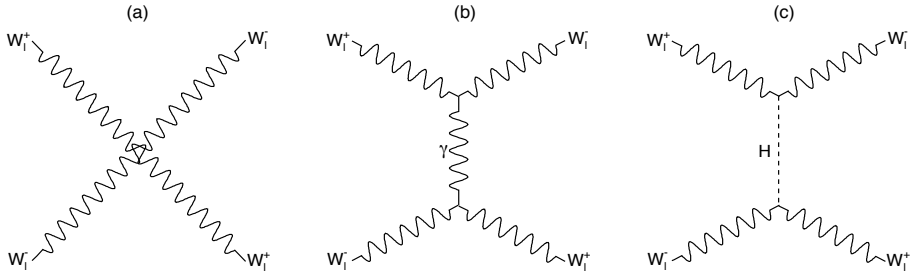

Figure 1.2: Feynman diagrams of $W^+W^- \to W^+W^-$ scattering.

coupling to the W boson introduces a third diagram, represented in Figure 1.2(c), which balances the contributions that increase with the energy for a certain Higgs boon mass. It leads to an upper limit on Higgs mass:

$$m_H^2 < \left(\frac{8\pi\sqrt{2}}{3G_F}\right) \sim 700 \ GeV/c^2, (s >> m_H^2) \tag{1.20}$$

2. **The Triviality:** the Higgs mass is given by its self-coupling:

$$m_H^2 = \frac{4\lambda(v)m_W^2}{g^2} \tag{1.21}$$

At the tree-level there is no constraint on the Higgs mass. The higher order corrections to the Higgs self-coupling lead to the definition of the running coupling constant. The energy dependence of $\lambda(Q^2)$ is given by the renormalization group evolution (RGE):

$$\frac{\partial\lambda}{\partial t} = \beta(\lambda) \ , \quad t = log\Big(\frac{Q^2}{Q_0^2}\Big) \tag{1.22}$$

where Q the renormalization scale and Q_0 an arbitrary scale, *a priori* free to reach the Planck scale. The Feynman diagrams corresponding to one-loop corrections are illustrated in Figure 1.3(b-d). The contributions from the Higgs boson, fermions and gauge bosons lead to the equation:

$$\beta(\lambda) = \frac{1}{16\pi^2}\Big[12\lambda^2 + 6\lambda g_t^2 - 3g_t^4 - \frac{3}{2}\lambda(3g^2 + g'^2) + \frac{3}{16}[2g^4 + (g^2 + g'^2)^2]\Big] \tag{1.23}$$

where $g_t = \sqrt{2}\dfrac{m_t}{v}$ denotes the Higgs coupling to the top quark.

At high Higgs masses, the contribution from the Higgs boson (proportional to λ^2) dominates. The RGE is approximatively:

$$\frac{d\lambda(Q^2)}{dt} = \frac{3}{4\pi^2}\lambda^2(Q^2) \longrightarrow \frac{1}{\lambda(Q^2)} = \frac{1}{\lambda(Q_0^2)} - \frac{3}{4\pi^2}\ln\Big(\frac{Q^2}{Q_0^2}\Big) \tag{1.24}$$

At a certain energy scale, the coupling constant becomes infinite (it is the Landau pole). A Cut-off is therefore introduced that limits the domain of validity of the SM:

$$\lambda(Q_0^2 = \Lambda_{NP}^2) \to \infty \ , \quad \frac{1}{\lambda(v^2)}\Big(= \frac{2v^2}{m_H^2}\Big) > \frac{3}{4\pi^2}\ln\Big(\frac{\Lambda_{NP}^2}{v^2}\Big) \tag{1.25}$$

$$\longrightarrow \qquad m_H^2 < \frac{8\pi^2}{3}\frac{v^2}{ln(\Lambda_{NP}^2/v^2)} \tag{1.26}$$

where $Q_0 = \Lambda_{NP}$ is the scale where new physics happen. If the SM is valid up to the Planck scale, the Higgs boson is relatively light, $m_H < 140\ GeV/c^2$, while an upper limit on the SM validity range at 10 TeV allows Higgs mass to $m_H \lesssim 500\ GeV/c^2$.

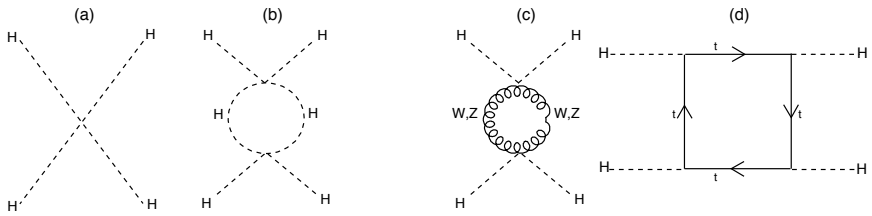

Figure 1.3: Feynman diagrams of the Higgs boson self coupling and the one-loop correction.

3. **The Vacuum stability:** at low Higgs masses, mainly top quark and weak boson loops arise, because of their strong coupling to the Higgs boson (Figure 1.3(c-d)). The RGE is approximatively of the form:

$$\beta(\lambda) = \frac{1}{16\pi^2}\Big[-3g_t^4 + \frac{3}{16}[2g^4 + (g^2 + g'^2)^2] + \theta(\lambda)\Big] \tag{1.27}$$

which leads to a new expression of the coupling constant:

$$\lambda(Q^2) = \lambda(v^2)\frac{1}{16\pi^2}\Big[-12\frac{m_t^4}{v^4} + \frac{3}{16}(2g_2^4 + ((g_2^2+g_1^2)^2)\Big] ln\frac{Q^2}{v^2} \tag{1.28}$$

The constraint of a positive coupling $\lambda(Q^2)$ implies that $m_H > 70\ GeV/c^2$ for a SM validity scale $Q \sim 1\ TeV$.

Figure 1.4 shows the sector for the Higgs boson mass as a function of the validity scale of SM. A domain of validity of the SM extended at the Planck scale involves a relatively light Higgs

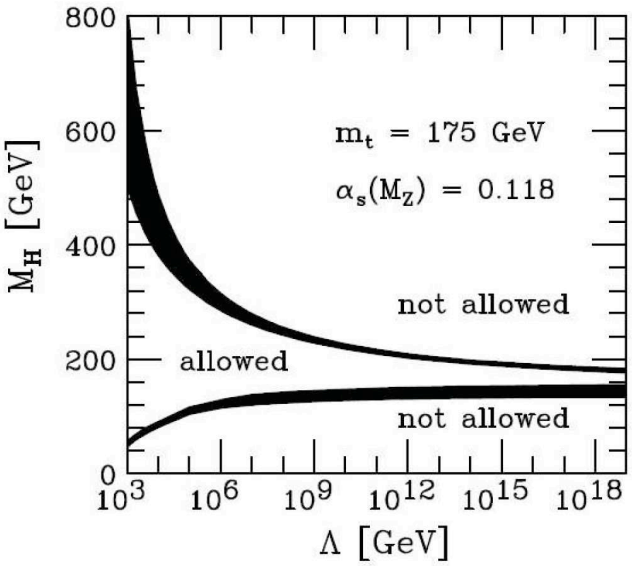

Figure 1.4: Theoretical limits on the SM Higgs boson mass as a function of the energy scale Λ.

boson, with a mass range $[120, 180]$ GeV/c^2. While for $\lambda \sim 1\ TeV$ a larger mass range is allowed, $m_H \in [70, 600]$ GeV/c^2.

1.3.2 Direct and Indirect experimental limits

1. **Direct searches**

   At LEP experiments at CERN, e^+e^- collisions with a centre-of-mass energy from 90 to 209 GeV were produced. The Higgs was mainly searched in the Higgsstrahlung production mode ($e^+e^- \rightarrow Z^* \rightarrow ZH$), in the $b\bar{b}$ decay mode. Combined results from ALEPH, DELPHI, OPAL and L3 experiments at LEP have established a lower limit on Higgs mass at 114.4 GeV/c^2 at 95% of Confidence Level (CL) [13]. A 2.8 σ excess was observed in ALEPH experiment around 115 GeV/c^2 although not confirmed by the other LEP experiments [14].

   At CDF and DØ experiments at Tevatron, $p\overline{p}$ collision are produced with an energy in the centre-of-mass $\sqrt{S} = 1.96\ TeV$. In 1995, the top quark was discovered, achieving the picture of the SM[1)], except for the Higgs boson. The Higgs boson is mainly searched

[1)] The tau neutrino was observed in 2001 in the DONUT experiment

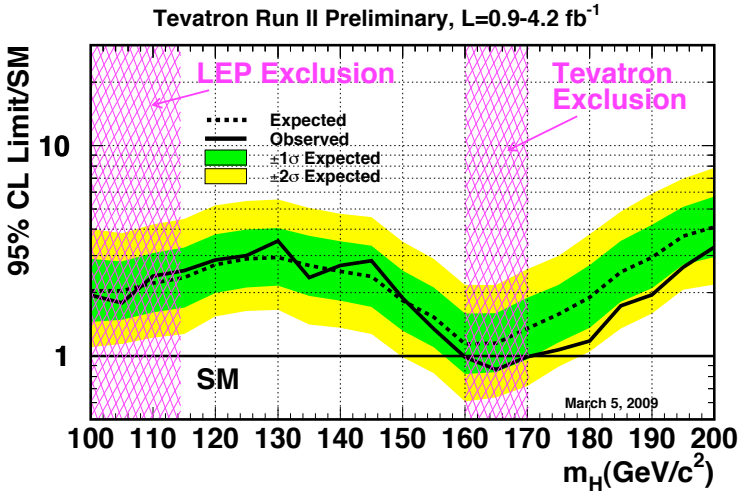

Figure 1.5: Observed and expected upper limit on the ratios to the SM cross section at 95% CL as a function of the Higgs mass.

in Tevatron experiments when produced in association with a weak boson, in the $b\bar{b}$ decay channel. DØ and CDF combined results and exclusion limits on the Higgs boson mass have been published for an integrated luminosity of 4.2 fb^{-1} [15]. As illustrated in Figure 1.5, the range of Higgs mass between 160 and 170 GeV/c^2 has been excluded at 95% CL.

2. **Indirect constraints**

The EW sector of the SM is basically described by three parameters: the two coupling constants, g and g' and the *vev*, or equivalently the W and Z masses and the electromagnetic constant coupling α_{em}. The Higgs boson arises in the radiative corrections to the SM parameters. Indirect limits on the Higgs boson mass are derived from the precision measurement of electroweak observables that have been performed at LEP, at SLAC (SLD) and Tevatron experiments.

The production of approximatively 16 millions Z at LEP has provided an estimation of the higher order corrections to the process $e^+e^- \rightarrow Z \rightarrow f\overline{f}$. The total and partial widths of the Z are accurately measured. The hadronic partial width in heavy quarks is also measured at SLD. These both also estimate the $\sin^2\theta_{eff}$ in asymmetry measurements. As the Higgs boson couplings to the W boson and the top quark are strong, corrections to their mass also depend on the Higgs mass. Figure 1.6(a) illustrates the limits on the Higgs mass as a function of the W boson and the top quark masses from the LEP, SLD and Tevatron measurements [16]. Direct measurements of the top and W masses at Tevatron and LEP are shown at 68% of CL, as well as indirect measurements from the Z production at LEP and SLD.

The Higgs boson mass is constrained by fitting the SM using the set of SM parameters $\{G_F, m_t, m_Z, \alpha_{QED}, \alpha_{em}\}$ measured in the different experiments. Figure 1.6(b) displays

the distribution of the global least-squares fit of the SM $\Delta\chi^2 = \Delta\chi^2 - \Delta\chi^2_{min}$ as a function of the Higgs mass [17] . The yellow region corresponds to the Higgs boson mass window

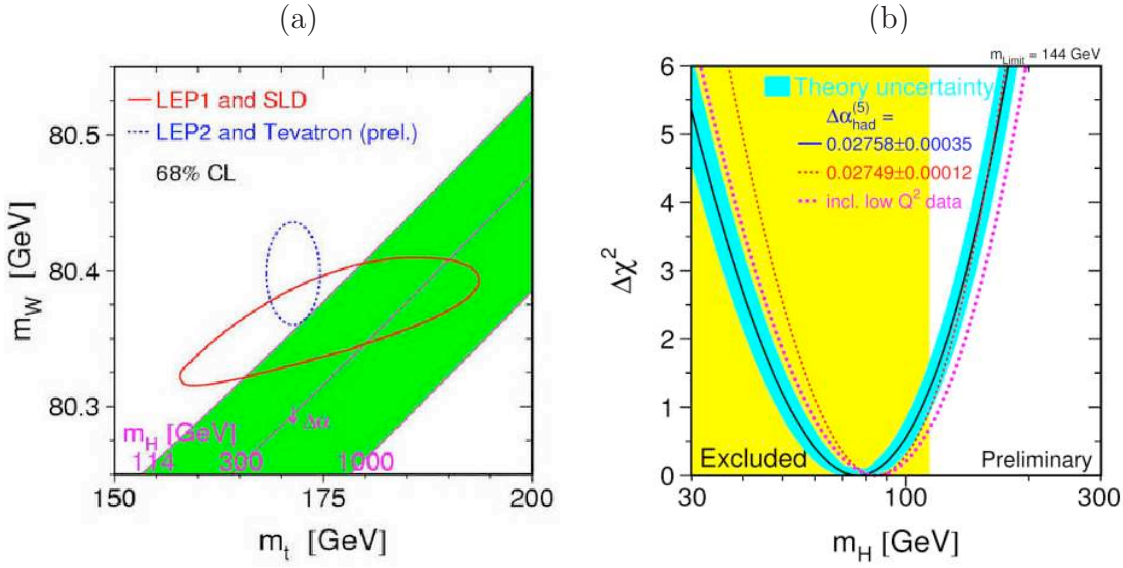

Figure 1.6: (a): Measurements of (solid lines) and indirect constrains (dashed lines) on the W mass as a function of the top mass, in LEP (run I and II), SLAC and Tevatron. (b): Global fit of the SM as a function of the Higgs mass. The direct limit established by LEP is represented by the yellow region, although not including in the fit. The theoretical errors are represented by the blue band.

excluded by the LEP experiments. The most probable value found from χ^2 minimization is $m_H = 85^{+39}_{-28} GeV/c^2$. The direct limit from LEP and exclusion from Tevatron are not considered in this fit. The Gfitter group has recently computed a fit of the SM χ^2 including these experimental inputs [18] giving more constrained result: $m_H = 120^{+15}_{-5} GeV/c^2$.

The theoretical arguments imposed to preserve the SM validity and experimental limits and constraints on the Higgs mass indicate that a light SM Higgs boson is preferred. As described in the next chapters the Higgs decay into two photons arise at low masses and will be an important mode in LHC Higgs searches.

1.4 The Limitations of the SM

The SM describes the elementary particles and their interaction in a relatively simple formalism. However, the SM cannot be the ultimate theory for various reasons:

- The fourth known fundamental interaction, *the gravitation*, is not included in the SM formalism. It is a long-distance interaction which coupling constant is about $g = Gm_p/\hbar c \approx 10^{-38}\ GeV^{-2}$ (m_p is the proton mass). This yields a scale at which the SM is no longer valid, defined by the Planck Mass $M_P = \sqrt{1/g} = 10^{19}\ GeV$. This also indicates that the SM could be an effective theory valid at the energy scale of GeV-TeV order, hiding a more elaborate model of at larger scales.

- The SM describes in a unified framework the electroweak and strong interactions based on unitarity Lie groups but it does not unify them in a common symmetry group. The running coupling constants of the three SM gauge symmetries ($\alpha_i^{-1} = g_i^2/4\pi$), which evolutions with Λ are described according to the RGE, therefore do not converge at large scales, as show in Figure 1.7 [19]. This underlies that the SM, if seen as an effective theory of an unified gauge theory, is no longer valid. Theoretical models propose the unification

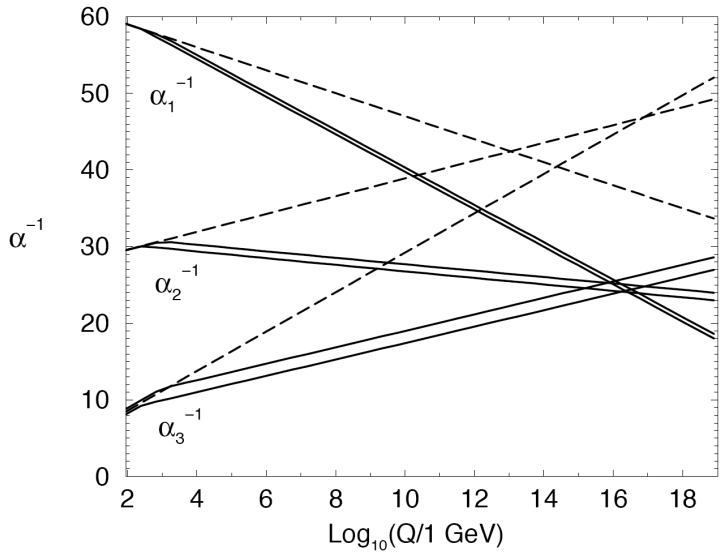

Figure 1.7: RG evolution of the inverse gauge couplings in the SM (dashed lines) and in the MSSM (solid lines).

of the SM interactions in a larger single gauge group containing the SM symmetries as subgroups [20]. Supersymmetry models or Grand Unified Theory unify the gauge symmetry groups of the SM $SU(3)_c \times SU(2)_L \times U(1)_Y$ into larger Lie group, SU(5) (or O(10)) for instance although these do not provide a natural explanation to the symmetry breaking needed for the particles mass.

- The *gauge hierarchy* or the fine-tuning problem: the radiative corrections to the Higgs boson mass in the SM correspond to loops of fermion as illustrated in Figure 1.8(a). The fermion loops induce corrections of the form:

$$\Delta^f m_H^2 = N_f \frac{\lambda_f^2}{8\pi^2}\Big[-\Lambda^2 + 6m_f^2 ln\Big(\frac{\Lambda}{m_f}\Big) - 2m_f^2\Big] + \theta(1/\Lambda^2) \tag{1.29}$$

where N_f is the number of fermions. These are divergent in quadrature with the energy scale Λ. The radiative corrections lead to a divergent correction term to the bare mass of the Higgs boson:

$$m_H^2 = m_{H,0}^2 + \delta m_H^2 = m_{H,0}^2 + C\Lambda^2$$

Λ is an arbitrary scale that can *a priori* go from any energy range to the Planck scale, while the *Unitarity* imposes that the Higgs mass be below the TeV scale. The divergence

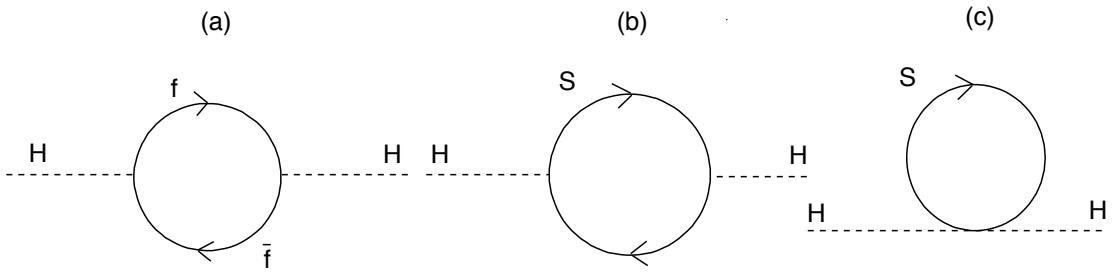

Figure 1.8: (a): Feynman diagram of the one-loop corrections to the Higgs mass due to a fermion f in the SM. (b-c): Feynman diagrams of the one-loop corrections to the Higgs mass due to a scalar boson S that arise in the SUSY models.

of the corrections with Λ squared implies that the bare mass should be tuned "by hand" to compensate these corrections. If $\Lambda = M_P = 10^{19}\ GeV$, a tuning of sixteen order of magnitude is needed[2)]. The *fine-tuning* of the Higgs bare mass indicates that the SM is no natural at the Planck scale.

- Astrophysical observations have shown that there is a large contribution from the so-called cold dark-matter in the universe that is not described in the SM. New models of particle physics are needed to describe this non-baryonic matter. As well, non null value of the cosmological constant Λ_c in the SM is not natural. The Higgs potential contribution to the cosmological constant in the SM is of the form:

$$\Lambda_c = 8\pi g_G V(H)_c = 8\pi g_G \Big(\frac{m_H v}{2\sqrt{2}}\Big)$$

g_G is the coupling constant of gravity. A SM Higgs boson mass at 100 GeV/c^2 brings a contribution of 50 order of magnitude larger than what found in experimental researches. SUSY models bring solutions for the possible unification of the fundamental interactions described in the SM and the gravitation, allowing a non null value of the cosmological constant Λ_c.

- The *flavor hierarchy* in the SM is not natural from an esthetic standpoint. There is no reason for several order of magnitude of difference between the Yukawa coupling of the Higgs to the fermions or similarly the fermion masses.

Among the extensions to the SM are the supersymmetric (SUSY) models that bring a solution to the *fine tunning* issue of the SM. The key idea of the SUSY models is to associate superpartners to the SM bosons and fermions. The addition of one bosonic degree of freedom per fermionic degree of freedom cancels the quadratic divergences. The new particles loop in the radiative correction from the fermion superpartners to the Higgs of the form:

$$\Delta^S m_H^2 = N_S \frac{\lambda_S}{16\pi^2}\Big[\Lambda^2 + 2m_S^2 ln\Big(\frac{\Lambda}{m_S}\Big)\Big] + N_S \frac{\lambda_S^2}{16\pi^2} v^2 \Big[-1 + 2m_S^2 ln\Big(\frac{\Lambda}{m_S}\Big)\Big]\theta(1/\Lambda^2) \qquad (1.30)$$

[2)] A two-order tuning is required if the SM is replaced at the 10 TeV scale, which is still relatively natural.

cancel the divergence when $N_s = 2N_f$ and $\lambda_s = \lambda_f^2$. They are replaced by terms proportional to $m_f^2 - m_{\tilde{f}}^2$, where $m_{\tilde{f}}$ is the mass of the boson associated to the SM fermion f.

Chapter 2

The Higgs Production and Decay Modes at LHC

2.1 The Higgs Production Mode at LHC

Figure 2.1 (left) displays the cross section of the SM Higgs boson production modes at LHC as a function of its mass, at a centre-of-mass energy of 14 TeV.

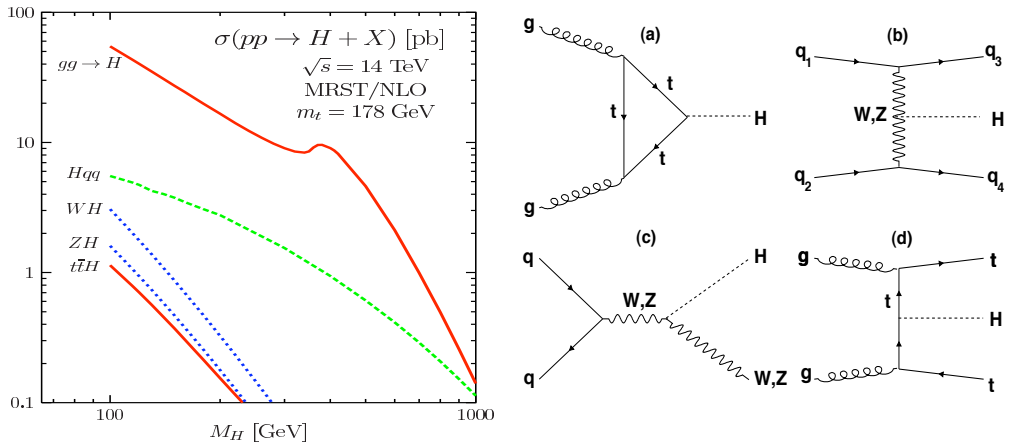

Figure 2.1: Left: Cross section of the Higgs production modes at LHC (14 TeV) as a function of its mass. Right: Feynman diagrams of Higgs boson production at LHC.

The main process of Higgs production is the gluon fusion, represented by the diagram 2.1(a). The Higgs boson couples only indirectly to gluons via a triangular loop of quarks, mainly the top. As shown in Figure 2.1 (left), this production process is dominant by several order of magnitude, in the whole range of Higgs mass that will be scanned at LHC.

The sub-leading Higgs production mode is the Vector Boson Fusion (VBF). This process, illustrated by the diagram 2.1(b) presents a particular topology. The quarks interact via a W boson, this process is therefore electro-weak and does not imply a color exchange between initial-state quarks. The two final quarks generate forward jets and are produced in opposite hemispheres in η, leading to a central rapidity gap where no QCD activity is expected but the Higgs decay products.

The Higgs is also produced in association with a W or Z boson, and also with a top quark pair, as shown in 2.1(c) and 2.1(d) respectively.

The VBF and associated production modes are different compared to the gluon fusion process since the Higgs is produced in association with something else in the final state. This allows a better discrimination between signal and background although the sensitivity is typically reduced at low luminosities.

All these production modes are considered inclusively in the study dedicated to the search of the Higgs boson through its decay into two photons.

2.2 The Higgs Boson Decay Mode in the SM

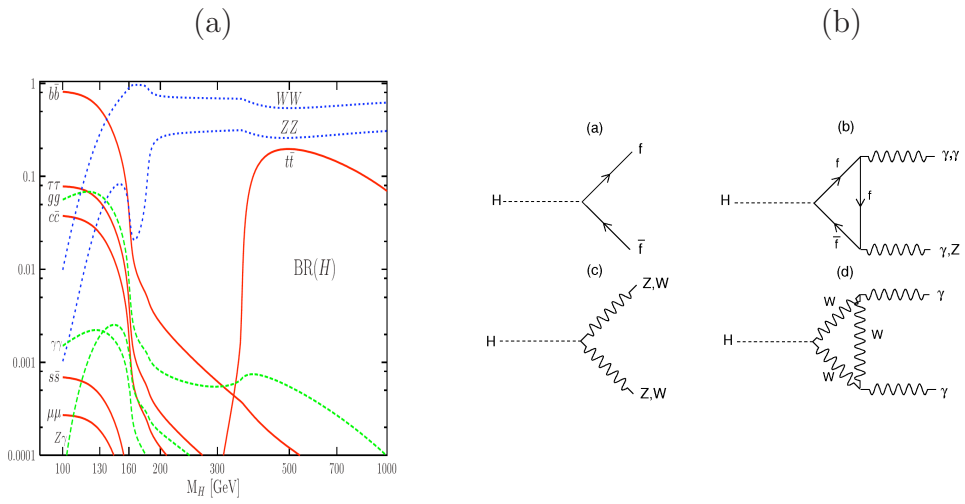

Figure 2.2: (a): Branching ratios of the SM Higgs as a function of its mass. (b): Feynman diagrams of SM Higgs decay modes.

In the SM, the Higgs mass is a free parameter of the theory. It fixes the Higgs coupling to gauge bosons and fermions. The Higgs boson branching ratios (BR) are shown as a function of its mass in Figure 2.2. The Feynman diagrams of the different Higgs decay modes are illustrated in the same Figure. Three mass regions appear:

- In the *low mass range* ($100 \leq m_H \lesssim 130\ GeV/c^2$) the Higgs mainly decays into a $b\bar{b}$ pair, $BR_{b\bar{b}} \approx 70 - 75\%$, due to the Higgs coupling to fermions proportional to their mass. The discovery potential of Higgs search in this channel at LHC is however small due to large QCD background.

  The $H \to \tau\tau$ channel has a smaller branching ratio, about 8%, and suffers from large background from the $Z \to \tau\tau$ decay process. However, when searching the Higgs in the VBF production mode, this is a promising channel at low masses.

  The $\gamma\gamma$ and $Z\gamma$ decay modes also occur in the low mass range and are rare due to the indirect Higgs coupling to the photon. The Higgs decay into two photons is made through fermions, mainly top quark, and W boson loops.

Despite its small branching ratio, the $H \to \gamma\gamma$ is a very important channel at low masses, $100 < m_H < 150$ GeV/c^2. It presents a very clean signature and have a narrow width, although large associated background.

- In the *intermediate mass range (*$130 \leq m_H \lesssim 200\ GeV/c^2$*)* the BR of the aforementioned decay modes rapidly decreases. The WW and ZZ channels open and have a large branching ratio due to their stronger coupling to the Higgs. The bump in the ZZ channel profile at $m_H \approx 2M_W \approx 160\ GeV/c^2$ arises when the two W are on-shell.

  The $ZZ \to llll, l = e, \mu$ channel is very important channel at medium to high masses ($m_H \geq 200\ GeV/c^2$). It presents a clean signature with four electrons or muons. At low mass, it is also promising although it requires an accurate reconstruction of low energy leptons momentum and direction.

- At $m_H \approx 2m_{top} \approx 350\ GeV/c^2$, the top pair decay opens and increases rapidly due its very strong coupling to the Higgs. However large QCD background and background from the WW channel lead impossible any Higgs search through this channel.

  At larger masses the $t\bar{t}$ decay BR rapidly decreases as a consequence of the different behavior of the partial widths $\Gamma_{H\to t\bar{t}}$ and $\Gamma_{H\to VV}$ (V = W,Z), that are respectively proportional to m_H and m_H^3.

Chapter 3

The Large Hadron Collider

The Large Hadron Collider (LHC) is a 27 km circumference accelerator installed in the LEP (Large Electron Positron Collider) tunnel, at CERN. It is the highest-energy accelerator ever built.

At the LHC proton beams collide with the nominal energy in the centre-of-mass $\sqrt{s} = 14\ TeV$. There are four collision points in the LHC ring where high energy particle physics experiments are installed. Among these detectors is the general-purpose ATLAS (A Toroidal LHC ApparatuS) experiment.

In this chapter, a brief description of LHC proton beams characteristics and experiments installed at LHC is presented.

3.1 The Accelerator Complex

The Large Hadron Collider (LHC) accelerator complex is installed 100 meter underground in the CERN site. It has been constructed in the LEP tunnel, with a complex system of beam acceleration already installed in the site. Two proton beams pre-accelerated to the energy of 450 GeV are injected in opposite directions in the LHC and accelerated in its 27 km of circumference to reach a nominal energy of 7 TeV per beam. A sketch of the beam accelerator complex is shown in Figure 3.1.

A source of hydrogen is used to produce the protons [21]. The proton beams are injected in the linear proton accelerator LINAC2 and accelerated to 50 MeV. The beams then reach the synchrotron PSB(Booster) which accelerates them up to 1.4 GeV. They are then injected into the two proton synchrotrons, the *Proton Synchrotron* and *Super Proton Synchrotron*, that respectively increase their energy to 25 and 450 GeV. Finally, the beams are injected in the LHC accelerator.

The magnetic systems of the LHC are made of superconducting niobium-titanium magnets. The challenge of the LHC is to have dipole delivering a high magnetic field, knowing that the circumference of the tunnel is fixed, in order to have proton beams at 7 TeV nominal energy. For a radius of 4.3 km and a coverage of the magnets on 17 km of the LHC circumference, the dipoles are expected to operate at a field strength of 8.36 Tesla(T) which is approaching the upper limit of niobium-titanium accelerator magnets, around 10 T. At Tevatron (at Fermilab), HERA (at DESY) or RICH (at BNL), the same alloy is used but the magnets are cooled at 4.2 K, limiting the delivered magnetic field at 5 T. To achieve the nominal beam energy expected

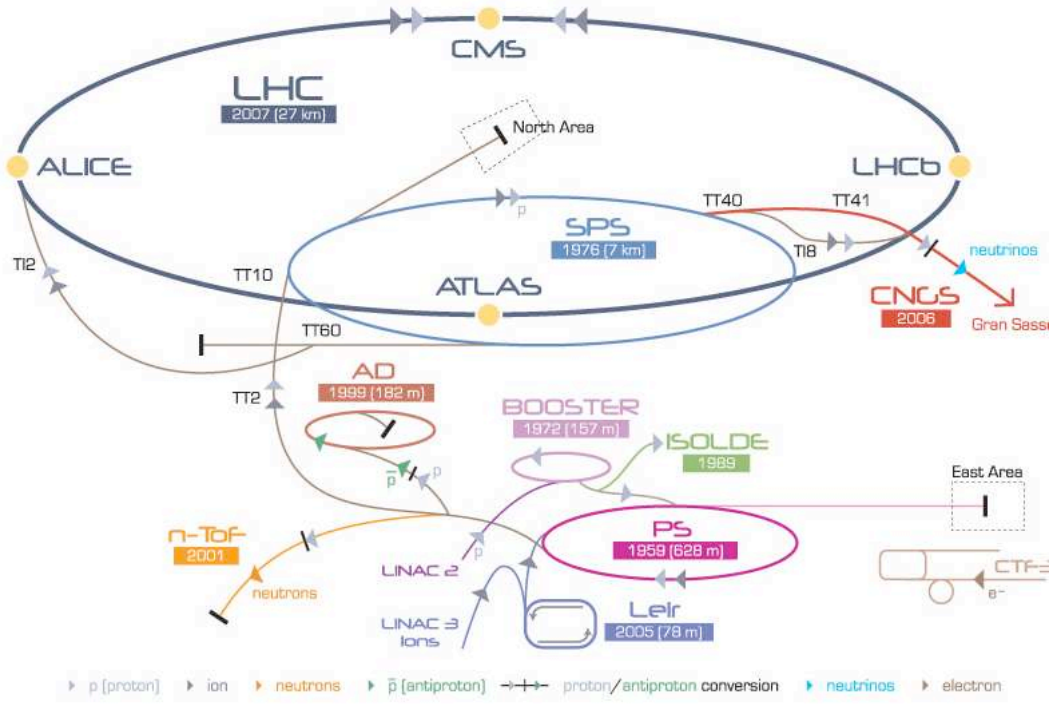

Figure 3.1: The CERN accelerator complex. Once injected in the LHC, the proton beams are accelerated to reach the 7 TeV energy and collide in four different points, where ATLAS, ALICE, CMS and LHCb experiments are installed.

(a) (b)

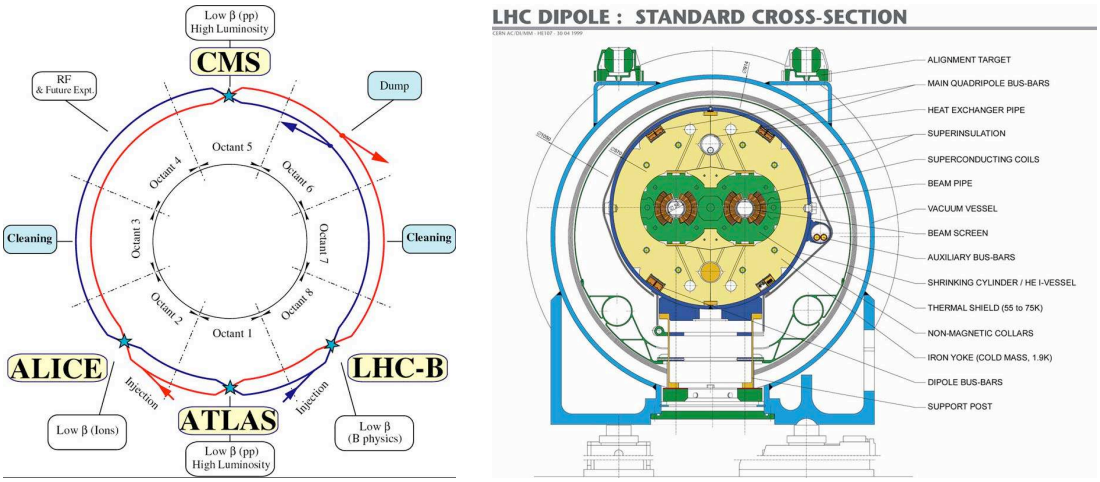

Figure 3.2: (a) Sketch of the LHC accelerator. The protons beams are shown as well as the four main particle physics experiments installed at the LHC beams collision points. (b) Design (transversal view) of the LHC dipole. The two separated vacuum pipes are represented in the cryogenic system.

at LHC, the magnets are cooled to the temperature of the superfluid Helium T = 1.9 K (at atmospheric pressure).

In the LEP experiment, beams of electrons and positrons were accelerated into opposite direction in a common pipe. In the LHC, the use of two proton beams imposes to accelerate them into two separated pipes, as shown in Figure 3.2(a-b). A complex system of dipoles is used to maintain the protons in a circular orbit. In order to save costs, the two pipes are in the same cryostat system, as illustrated in Figure 3.2(b). Commonly, the beam 1 (blue in Figure 3.2(a)) circulates in the clockwise sense while the beam 2 (red) circulates in anti-clockwise sense. The LHC is approximatively circular, actually made of eight octants separated by straight sections. The proton beams are focalized by quadrupoles and are accelerated by Radio Frequency cavities placed in one straight section. Systems of *momentum* and *betatron cleaning* are also disposed in the sections: the *momentum cleaning* collimates the beams and cleans it from protons with an momentum too far from the nominal value; the *betatron cleaning* cleans the beams from protons with an oscillation amplitude too far from the nominal orbit . The dump part represented in Figure 3.2(a) on the top-right side is used to stop and evacuate the beams.

Figure 3.2(a) shows the beams interaction points where the different physics detectors are located.

- In addition to the proton beams, phases with beams made of heavy ions (Pb and Au) are planed at LHC. A Large Ion Collider Experiment [22] (ALICE) is a detector dedicated to heavy ions collisions . It will study the quark-gluon plasma (QGP) in order to understand the matter confinement at early time of the Universe.

- The Large Hadron Collider beauty (LHCb) experiment [23] is a one-side forward detector which will perform measurements on physics phenomena involving B mesons to understand the matter-antimatter asymmetry.

- A Toroidal LHC ApparatuS (ATLAS) detector is a multi-purpose experiment [24]. Searches of the SM Higgs boson as well as measurements of the EW parameters of the SM will be done. Searches for new particles as indication on physics beyond the SM, studies on dark matter, studies on extra-dimension theories are among the large spectrum of possible physics with the ATLAS experiment.

- The Compact Muon Solenoid (CMS) is also a general-purpose experiment [25]. The two detectors vary in their magnetic system and the technology used in their sub-detectors. In CMS the tracking detector is entirely made of Silicon and the electromagnetic (EM) calorimeter is made of about 80000 lead-tungsten (PbWO4) scintillating crystals. The Tracking and calorimeter (EM and hadronic) systems are contained in a superconducting solenoid delivering a magnetic field of 4 T. In ATLAS (see section 4), only the Inner Detector is surrounded by a solenoid delivering 2 T.

- The TOTEM [26], for TOTal Elastic and diffractive cross section Measurements is located near CMS. It will study the diffractive physics and particularly elastic diffractive scattering at low momentum transfer in order to measure the absolute luminosity of the LHC and the total cross section of proton proton collision.

- The Large Hadron Collider forward (LHCf) detector is a special-purpose LHC experiment for astrophysics studies at high energy within the particles produced at large pseudo

rapidity [27] (see section 4.1 for the definition of the pseudo radipity). It consists of two small detectors located at 140 m on each side of the interaction point.

3.2 The Luminosity

The MC simulations predict the cross section σ of a particle physics process in p-p collision while the detector counts event rates ($\dot{\mathrm{N}}$). The event rate corresponds to the cross section multiplied by the *instantaneous luminosity* $\mathcal{L}$:

$$\dot{\mathrm{N}} = \mathcal{L}\sigma$$

The instantaneous luminosity is proportional to the flux of protons and is defined by the beam parameters. Table 3.1 lists the beam characteristics for two luminosity scenario at LHC. The nominal beam life time is about 22h [28] although the luminosity is reduced by a factor 2 after 10h, imposing new beam injection to LHC. The luminosity needs to be measured frequently, notably to control the quality of data. The generic term of lumi-block is used and corresponds to a short stable-beam period $\theta(min)$. The *absolute* integrated luminosity given by:

$$\mathrm{N} = \int \mathcal{L}\sigma$$

is assigned to a lumi-block while the *relative* luminosity indicates the relative difference between a lumi-block and its immediate neighbor. To properly compare data with MC simulations an accurate prediction of the process cross section and partons pdf at LHC energy and a precise measurement of the absolute luminosity are required. The measurement of the relative luminosity is also crucial to estimate the beam evolution with time.

LHC characteristics	Typical values	
	Low Luminosity	Nominal Luminosity
Circumference	27 km	
Injection energy	450 GeV	
beam energy	3.5 TeV	7 TeV
Magnetic field of a dipole	8.4 Tesla	
Low/Nominal luminosity	$10^{31}\ cm^{-2}.s^{-1}$	$10^{34}\ cm^{-2}.s^{-1}$
Luminosity-beam life-time	$\sim$ 10-22 h	
Number of bunches	156	2808
Number of protons per bunch	$\sim 10^{10}$	$\sim 10^{11}$
Time interval between two bunches	50 ns	25 ns
Space interval between two bunches	15 m	7.5 m
Bunch length	7.55 cm	
Transverse beam size at the interaction point	16.7 μm	

Table 3.1: Typical LHC characteristics.

3.2.1 Definition

The luminosity can be written as:

$$\mathcal{L} = \frac{N_p^2 k_b f_{rev} \gamma}{4\pi\beta^* \epsilon_n} F \tag{3.1}$$

It depends on the beams and collisions parameters:

- N_p is the number of protons ($10^{10} - 10^{11}$) per bunch and k_b the number of bunches per beam (2808).
- f_{rev} is the frequency of resonance (11245 Hz, corresponding to beams crossing each 25 ns).
- β^* is the amplitude function and represents the beam focalization at the collision point (0.55 m). ϵ_n is the normalized emittance (3.75 $\mu m.rad$).
- F is mainly the reduction factor, related to the angle of beam crossing (285 μrad) and the mis-centering of the beam collision. It is estimated around 0.9.

The beams have a transverse sizes $\sigma_x = \sigma_y \approx 16.7\mu m$ at the interaction point. The product of the emittance ($\epsilon = \epsilon_n/\gamma$) with the β^* function corresponds to the beams crossing surface (modulo the factor 4π): $\epsilon\beta^* = \sigma^2 = \sigma_x\sigma_y \approx 280\ \mu m^2$.

The luminosity plan at LHC was defined in Chamonix Workshop [29]. In December 2009, first collisions were seen at LHC at 900 GeV energy in the centre-of-mass. There were 5.10^{10} protons per bunch, two bunches per beam and no crossing angle between the beams. At the end of March 2010, first collisions at 7 TeV centre-of-mass energy have been recorded at LHC with the same numbers of protons per bunch and bunches per beam than at 900 GeV collisions. The number of protons per bunch will increase to 7.10^{10} and the number of bunches per beam should progressively evolve to finally correspond to a time interval between two beam crossings of 50 ns. This would correspond to an instantaneous luminosity of about $2.10^{32}\ cm^{-2}.s^{-1}$. The first phase of the LHC with 7 TeV collisions will last the time to record data for an integrated luminosity of approximatively 1 fb^{-1}. It will be followed by a long shut-down period dedicated to LHC and experiments maintenance. In the second phase collisions with an energy in the centre-of-mass between 10 and 14 TeV are expected and a nominal luminosity $\mathcal{L} = 10^{34} cm^{-2}.s^{-1}$ is expected to be reached.

3.2.2 The Luminosity Measurement

The direct measurement of the luminosity based on the beam parameters suffers from about 20% of systematic uncertainty which rapidly become a leading contribution to the total systematic error on physic results. Different systems [30] are used in ATLAS to measure the relative luminosity for different luminosity scenarios. Figure 3.3 sketches the different luminosity measurement methods and their relative precision.

- The Minimum Bias Trigger Scintillator (MBTS) system is made of two symmetric (in z) arrays of 16 scintillator plates installed on the inner face of the end-cap calorimeter cryostats, covering a pseudo-rapidity region $2.1 < \eta < 2.8$. It will be used to trigger on minimum bias events and provide a measurement of the relative luminosity.

- Studies of the EM and hadronic calorimeters are performed based on their response variation with the luminosity. In the hadronic calorimeter, the variation of the collected current in photo-multipliers (PM) used to read out the scintillating tiles gives an information on the luminosity variation. A measurement of the relative luminosity with a precision of 10-15% is expected, the main source of uncertainty coming from the PM response linearity. In the EM calorimeter the measurement of the current delivered by the HV power supply provides a estimation of the relative luminosity with a precision of few % [31, 32]. These methods need to calibrate the absolute luminosity with others detectors, introducing new experimental systematic errors.

- The Zero Degree Calorimeter (ZDC) will measure neutral particles (γ, π^0, η) in the forward direction ($|\eta| > 8.3$). It will give information on the centrality of the collisions and on the relative luminosity.

- The LUminosity monitor using Cherenkov Integrating Detector (LUCID) detector [33] is designed to measure the relative luminosity and will measure it with a precision of 2-5%. The LUCID detector consists of 168 tubes filled with C_4F_{10} gas pointing to and disposed at 17 meters from the interaction point on each side of ATLAS. It covers a range in rapidity of $5.6 < |\eta| < 5.9$. The detector is located between the wheels of the muon chambers. It is a Cherenkov detector and detects charged particles at large pseudo-rapidity. It measures the relative luminosity through the number of inelastic scatterings, proportional to the number of charged particles produced and detected near the longitudinal axis. It will scan a large dynamic range although the saturation phenomena occurs for a too high multiplicity and limits the detector operation at high luminosity. Its threshold is around a luminosity $\mathcal{L} \approx 4 - 5.10^{33}\ cm^{-2}s^{-1}$ as shown in Figure 3.3. LUCID will be used to measure the absolute luminosity in ATLAS collisions although it needs to be calibrated.

The detector used for calibration is ALFA, the detector for the Absolute Luminosity measurement For Atlas [34]. It is a scintillating fiber tracker composed of 20 plans arranged in a UV geometry, housed in Roman Pots. The Roman Pots are in garage position when inactive and come close to the beam, at 10 σ in beam transversal size unity in beams/measures position. Two stations of these Roman Pots are located at 240 m on each side of the ATLAS interaction point (IP). Each station is composed of an upper and a lower detector. The measurement of the absolute luminosity will be performed by intercepting the proton elastically scattered at the ATLAS IP. ALFA detects charged particles produced at very small angle ($10.6 < |\eta| < 13.5$), in the coulomb region that is well described by the theory. This will allow to determine the differential proton-proton elastic cross section as a function of the quadratic momentum transferred at the IP. In low luminosity schemes, $\mathcal{L} \lesssim 10^{27}\ cm^{-2}s^{-1}$ a precision of 2-3% is ensured by a dedicated magnet setting. A detailed description of the ALFA detector and performances evaluated in beam tests can be found in [35].

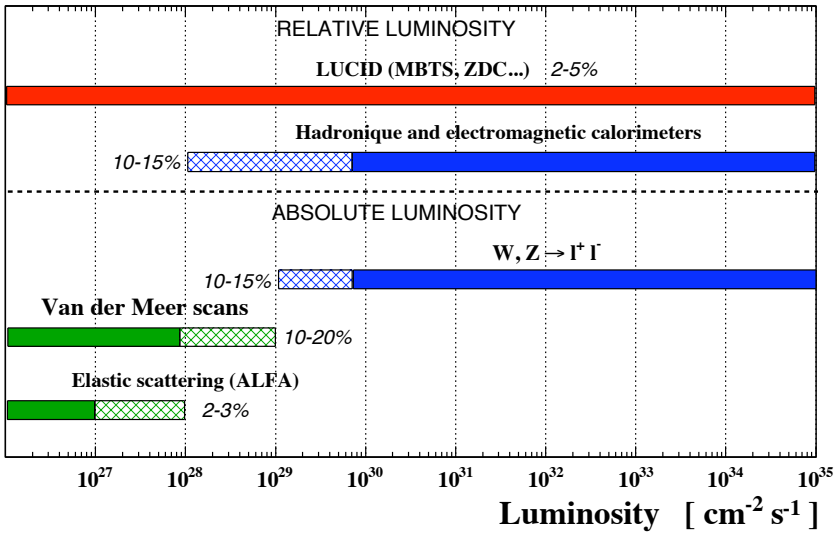

Figure 3.3: Schematic view of the different detector systems used to measure the relative and absolute luminosity. The colored regions represent their operating regime and the dashed region the domain where their measurement precision (indicated in %) decreases. The absolute luminosity is measured with ALFA at low luminosity. The Van Der Meer Scans method uses the beam parameters and beam overlap region to measure the luminosity. It suffers from large systematic errors due associated to the beams position. The relative luminosity is measured with LUCID in a large dynamic range. The measurement precision is however limited at high luminosity due to the accuracy of ALFA absolute luminosity measurement extrapolation. The W and Z production rates are also used, their cross sections are known at 10-15% accuracy. A method based on the EM and hadronic calorimeters is also proposed to measure the relative luminosity.

Chapter 4

The ATLAS detector

The ATLAS detector at LHC is 46 m long, 22 m in diameter and weighs 7000 tons. It is the largest detector installed at CERN. Figure 4.1 illustrates the ATLAS machine and its sub - detectors: the Inner Detector (ID) surrounded by a solenoid magnet, the electromagnetic (EM) and hadronic calorimeters and the muon spectrometer with its muon chambers and a large system of toroidal magnets.

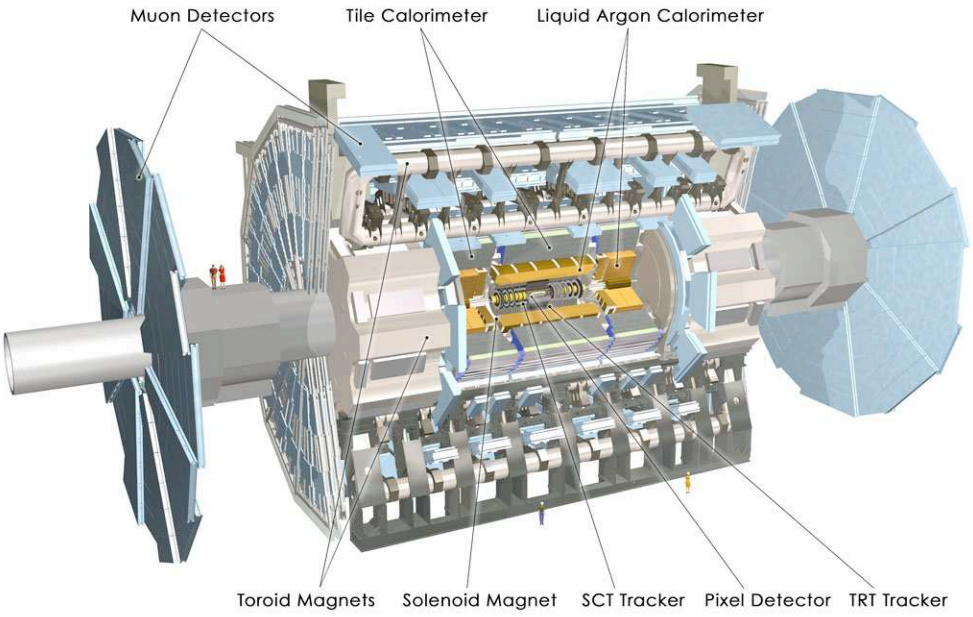

Figure 4.1: The ATLAS detectors and its sub-systems.

4.1 The ATLAS Coordinate System

The beams direction defines the (longitudinal) z axis, the (x, y) plan is transversal to the beam axis. The x axis points from the interaction point to the LHC ring center and the y axis is oriented upwards. As by construction the detector is symmetric around $z = 0$, a A side and a C side are defined, corresponding respectively to positive and negative z domain. The azimuthal

angle ϕ of a particle is the angle measured in the (x, y) plan between the particle direction and the x axis. The polar angle θ is defined from the beam axis. The pseudo-rapidity η is related to the polar angle:

$$\eta = -ln\Big(tan\Big(\frac{\theta}{2}\Big)\Big)$$

where $\eta = 0$ denotes the upward direction ($\theta = 90°$); larger η correspond to directions closer to the longitudinal axis ($\theta = 0° \leftrightarrow \eta \to \infty$). The pseudo-rapidity approximates the rapidity when assuming the particles mass negligible with respect to their momentum. The rapidity y is defined as:

$$y = -\frac{1}{2}ln\Big(\frac{E + P_z}{E - P_z}\Big)$$

E and P_z being the energy and z component of the momentum, respectively. In the approximation of a null transverse momentum for the partons involved in the interaction, the pseudo rapidity is given by:

$$E = \frac{1}{2}(x_1 + x_2)\sqrt{s}\ , \quad P_z = \frac{1}{2}(x_1 - x_2) \ \longrightarrow y = \frac{1}{2}ln\Big(\frac{x_1}{x_2}\Big)$$

x_i being the fraction of momentum of a proton carried by the parton i involved in the process. The number of particles produced per unity of η is uniform which suggests a detector geometry defined in the (η, ϕ) plane. The size of the cells are defined in a cone $\Delta R = \sqrt{\Delta\eta^2 + \Delta\phi^2}$ where $\Delta\eta(\Delta\phi)$ is the size in the $\eta(\phi)$ direction, $\Delta\eta \sim \Delta\theta/\sin\theta$ when the cells are small.

In proton-proton collisions at LHC, the partonic interaction has a longitudinal boost which is small but *a priori* unknown, due to width of the beams and the motion of partons inside the proton. Conserved variables based on the transversality of the collision are therefore preferred. The transverse momentum P_T as well as the transverse energy E_T of a particle are defined in the (x, y) plan. The transverse momentum is essentially null in the beam collision frame[1)]. The neutrinos interact weakly and escape undetected although they carry energy from the hard process. The missing transverse energy $\not{E}_T$ ($\vec{\not{E}}_T = -\vec{E}_T$) is estimated through an accurate measurement of the transverse energy deposited in the detector sub-systems.

4.2 The Inner Detector

The first detector system located in ATLAS immediately after the beam pipe is the Inner Detector (ID). It is a tracking detector which aims at efficiently reconstructing the charged particles momentum and direction, with an accurate resolution among a large dynamic range. The resolution on the measurement of the transverse momentum of charged particles is expected to be:

$$\frac{\sigma(P_T)}{P_T} = 0.05\%P_T \oplus 1\% \quad (P_T \text{ in GeV/c})$$

A good vertex resolution is also needed to accurately reconstruct the primary vertex as well as secondary vertices that arise in b-jets [36]. It is contained in a cylinder of 3.5 m height

[1)] The partons have a motion in the proton and carry in average a transverse momentum $k_T \approx 200{-}300\ MeV/c$

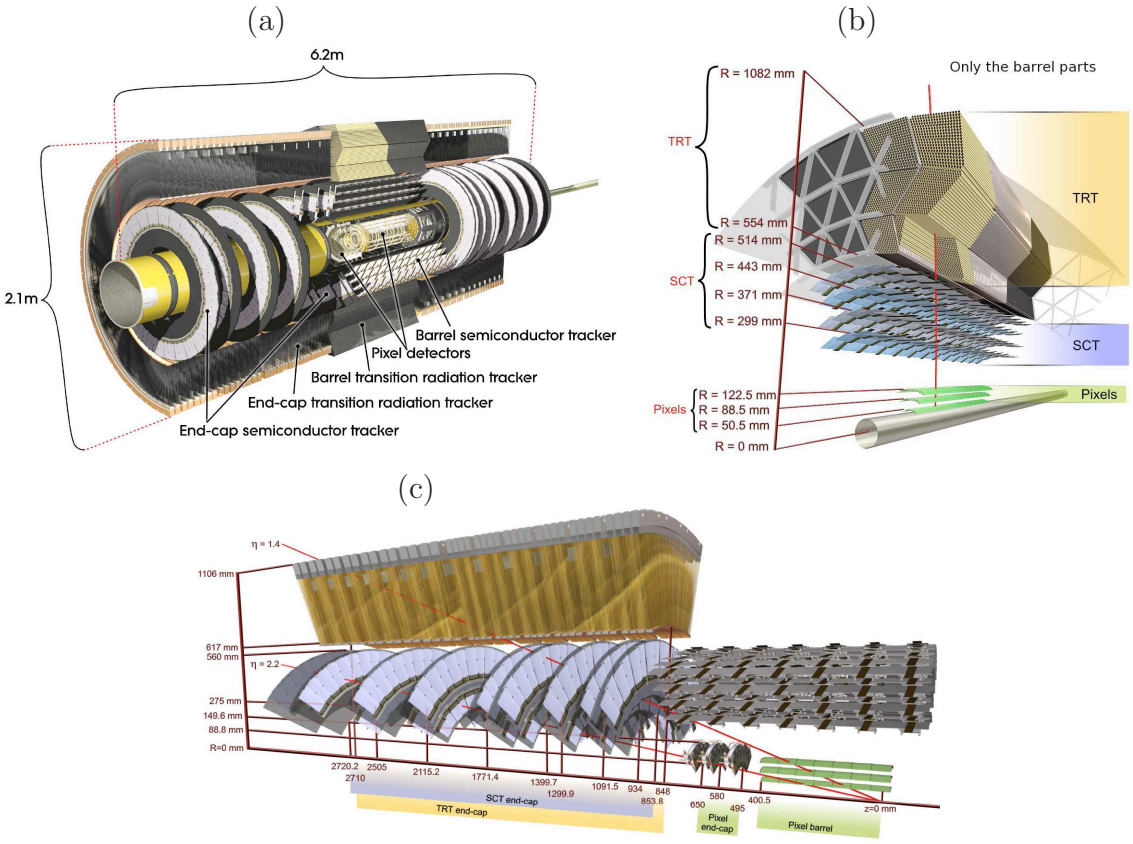

Figure 4.2: (a) Sketch of the Inner Detector of ATLAS. (b)/(c) Transversal view of the sub-detectors structure of the barrel/end-cap part of the three ID sub-detectors.

and 1.2 m radius, under a solenoid magnet delivering a field of 2 T. The ID is made of three sub-systems made with different and complementary purposes and technologies. Each detector comprises of a central (barrel) part and two end-cap parts (one on each side of the barrel), as illustrated in Figure 4.2(b-c). A sketch of the ID detectors geometry (inner, outer radius, η coverage) is shown in Figure 4.3.

4.2.1 The Pixel Detector

The Pixel Detector provides an accurate measurement of the charged particle tracks close to the interaction point. It is required to have a fast and accurate pattern recognition in a high multiplicity environment, an accurate vertexing algorithm and a good resolution on the transverse impact parameter.

The Pixel consists of three layers of detectors in the central (barrel) region of internal radius at 50.5, 88.5 and 122.5 mm respectively. The end-caps are made of three wheels installed at a z position between 49 and 65 cm from the interaction point, with a radius ranging from 90 to 150 mm. The Pixel detector is made of planar pixel sensors of 250 μm thickness layer of Silicon where a n-n type junction creates a diode that is then reverse-biased. The passage of charged particles creates electron-hole pairs that drift towards the electronic read-out system made of 16 front end chips. There are in total approximatively 80 millions of pixels in the ID corresponding to 1744 modules of 46080 readout channels. The Pixel detector covers an area

of approximatively 2 m^2. It is maintained at $-10°C$ to reduce excessive leakage current caused by radiation damage.

The geometry of the Pixel detector is such that the tracks hit at least three layers of the detector. To allow a good spatial resolution for tracks and vertices, the pixels have a very small size, $\Delta_{R-\phi} \times \Delta_z = 50 \times 400\ \mu m^2$, which corresponds to a resolution of 10 μm in the $R-\phi$ plan and 115 μm in the z direction.

The innermost layer of the Pixel detector is the so called B-layer, due to its ability to tag the b-jets. It is used for an accurate reconstruction of the secondary vertex when a B meson is produced and decays (The B mesons have a life time of about $c\tau \sim 500\mu m$. B Meson with an energy of 50 GeV could travel 50 mm before decaying, leading to a secondary vertex distinct from the primary vertex).

The B-layer will be strongly exposed to radiations, justifying its replacement after about 4-5 years of ATLAS run-periods. The IBL (Insertable B-Layer) [37] will be installed in 2015 (phase I of SuperLHC project). A range of new Pixel sensor technologies are under study to build $250 \times 50\ \mu m^2$ Pixel modules with increased radiation hardness.

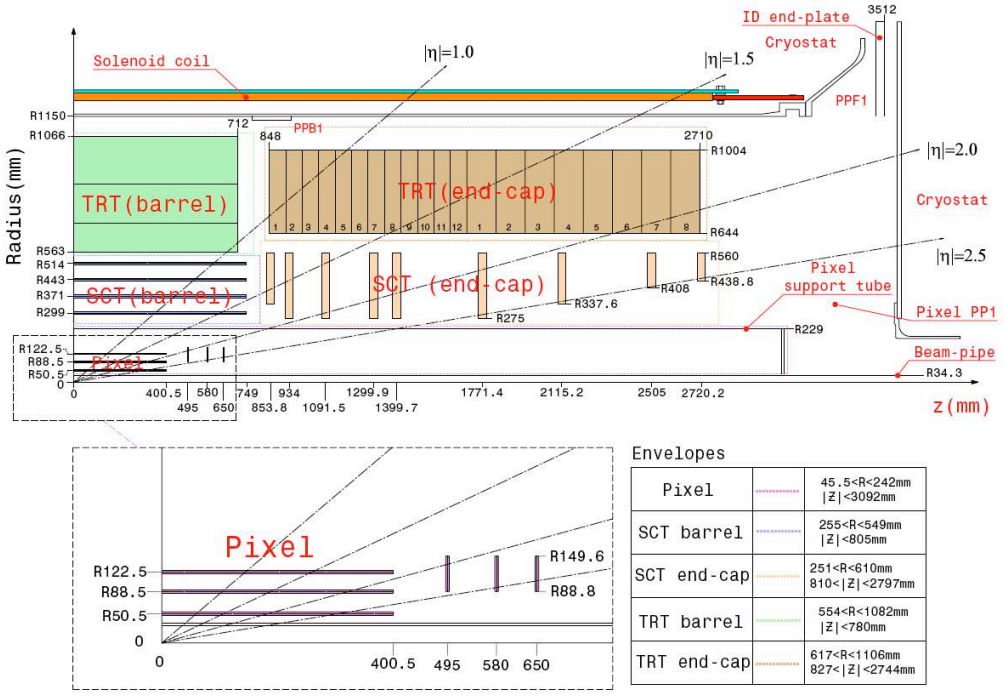

Figure 4.3: View of a quarter of the ID barrel and end-cap subsystems, in the $R-z$ plan. The design of the ID in terms of layers in the barrel and end-cap regions and the separation of these regions is a compromise between available space and the minimal number of hits per charged particle for any kind of direction.

4.2.2 The SCT

The Semiconductor Tracker (SCT) is located after the Pixel detector. It is made of Silicon microstrip sensors. It consists of eight strip layers in the barrel region which produce at most

four accurate 2-D space points (eight 1-D measurements) per charged particle track. The end-caps are made of eighteen forward and backward disks, with strips running radially, located a distance from 80 to 280 cm (from $z = 0$). The microstrip sensors installed in SCT modules consist of 126 mm long chained sensors with a strip pitch of 80 μm. Each module is made of two detectors slightly tilted by 40 mrad stereo angle to measure the z position. 4088 modules are assembled to form the barrel and end-caps for a total area covered by the SCT of 63 m^2. In both the barrel and end-cap regions, a resolution $\sigma_{R-\phi} \times \sigma_z = 580 \times 17\ \mu m^2$ is obtained. In total , there are approximatively 6.3 millions of readout channels in the SCT.

4.2.3 The TRT

The Transition Radiation Tracker (TRT) system is made of straw tubes of 4 mm diameter filled with a gas (made of 70% Xenon, 20% Methane and 10% CO_2). A 30 μm diameter (Au-covered) Tungsten string is disposed at the center of each tube. It constitutes the anode of the system that collects electrons after the gas is ionized by the passage of a charged particle. The barrel part is made of 3 layers of 150 cm height long straws while the end-caps are made of eighteen wheels containing 39 to 55 cm height long straws oriented radially. The TRT coverage enables track trajectory reconstruction up to $|\eta| \sim 2.0 - 2.1$, as shown in Figure 4.3. It provides a measurement of the charged particle trajectory with typically 30-36 hits per track.

The TRT is also used to discriminate the electron from heavier charged particle, as $\pi^{\pm}$ for instance. The energy in transition radiation for signal from electron is larger than particles at their minimum of ionization (MIP) which allows an efficient discrimination. There are in total 351 000 readout channels in TRT.

4.3 The Calorimetry

The electromagnetic (EM) calorimeter of ATLAS, located after the ID, will measure the energy and direction of photons and electrons in a large dynamic range in energy (from few tens of GeV to 2-3 TeV). The hadronic calorimeter follows the EM calorimeter and measures the energy and direction of hadronic jets originating from quarks and gluons. The two calorimeters are separated into a barrel covering $|\eta| \lesssim 1.5$ and two end-caps covering the region $1.5 \lesssim |\eta| \lesssim 3.2$. Dedicated forward calorimeters are used at larger η ($3.1 \leq |\eta| \leq 4.9$), to ensure a full coverage by the calorimetry in $|\eta| \lesssim 5$. The calorimeters are shown in Figure 4.5 and their characteristics (coverage and cells $\eta \times \phi$ size) are listed in Figure 4.4.

4.3.1 The Electromagnetic Calorimeter

The ATLAS EM calorimeter is a sampling calorimeter made of lead absorbers interleaved with Liquid Argon (LAr). An electrode is placed at the center between two absorbers to collect the LAr ionization signal from the passage of a charged particle. The EM barrel calorimeter (EMB) and the two end-caps (EMEC) are in different cryostats at the temperature of the LAr (88.5 K).

The EMB ($|\eta| < 1.4$) is made of two half-barrels symmetric in z having an inner and an outer radius, $R_{in} = 1.15\ m$ and $R_{out} = 2.25\ m$ respectively. Each half barrel is made of 16 modules in ϕ (of size $2\pi/16$) containing 64 3.2 m long absorbers. The modules are made of two

	Barrel		End-cap	
EM calorimeter				
Number of layers and $\|\eta\|$ coverage				
Presampler	1	$\|\eta\| < 1.52$	1	$1.5 < \|\eta\| < 1.8$
Calorimeter	3	$\|\eta\| < 1.35$	2	$1.375 < \|\eta\| < 1.5$
	2	$1.35 < \|\eta\| < 1.475$	3	$1.5 < \|\eta\| < 2.5$
			2	$2.5 < \|\eta\| < 3.2$
Granularity $\Delta\eta \times \Delta\phi$ versus $\|\eta\|$				
Presampler	0.025×0.1	$\|\eta\| < 1.52$	0.025×0.1	$1.5 < \|\eta\| < 1.8$
Calorimeter 1st layer	$0.025/8 \times 0.1$	$\|\eta\| < 1.40$	0.050×0.1	$1.375 < \|\eta\| < 1.425$
	0.025×0.025	$1.40 < \|\eta\| < 1.475$	0.025×0.1	$1.425 < \|\eta\| < 1.5$
			$0.025/8 \times 0.1$	$1.5 < \|\eta\| < 1.8$
			$0.025/6 \times 0.1$	$1.8 < \|\eta\| < 2.0$
			$0.025/4 \times 0.1$	$2.0 < \|\eta\| < 2.4$
			0.025×0.1	$2.4 < \|\eta\| < 2.5$
			0.1×0.1	$2.5 < \|\eta\| < 3.2$
Calorimeter 2nd layer	0.025×0.025	$\|\eta\| < 1.40$	0.050×0.025	$1.375 < \|\eta\| < 1.425$
	0.075×0.025	$1.40 < \|\eta\| < 1.475$	0.025×0.025	$1.425 < \|\eta\| < 2.5$
			0.1×0.1	$2.5 < \|\eta\| < 3.2$
Calorimeter 3rd layer	0.050×0.025	$\|\eta\| < 1.35$	0.050×0.025	$1.5 < \|\eta\| < 2.5$
Number of readout channels				
Presampler	7808		1536 (both sides)	
Calorimeter	101760		62208 (both sides)	
LAr hadronic end-cap				
$\|\eta\|$ coverage			$1.5 < \|\eta\| < 3.2$	
Number of layers			4	
Granularity $\Delta\eta \times \Delta\phi$			0.1×0.1	$1.5 < \|\eta\| < 2.5$
			0.2×0.2	$2.5 < \|\eta\| < 3.2$
Readout channels			5632 (both sides)	
LAr forward calorimeter				
$\|\eta\|$ coverage			$3.1 < \|\eta\| < 4.9$	
Number of layers			3	
Granularity $\Delta x \times \Delta y$ (cm)			FCal1: 3.0×2.6	$3.15 < \|\eta\| < 4.30$
			FCal1: $\sim$ four times finer	$3.10 < \|\eta\| < 3.15$, $4.30 < \|\eta\| < 4.83$
			FCal2: 3.3×4.2	$3.24 < \|\eta\| < 4.50$
			FCal2: $\sim$ four times finer	$3.20 < \|\eta\| < 3.24$, $4.50 < \|\eta\| < 4.81$
			FCal3: 5.4×4.7	$3.32 < \|\eta\| < 4.60$
			FCal3: $\sim$ four times finer	$3.29 < \|\eta\| < 3.32$, $4.60 < \|\eta\| < 4.75$
Readout channels			3524 (both sides)	
Scintillator tile calorimeter				
	Barrel		Extended barrel	
$\|\eta\|$ coverage	$\|\eta\| < 1.0$		$0.8 < \|\eta\| < 1.7$	
Number of layers	3		3	
Granularity $\Delta\eta \times \Delta\phi$	0.1×0.1		0.1×0.1	
Last layer	0.2×0.1		0.2×0.1	
Readout channels	5760		4092 (both sides)	

Figure 4.4: η coverage and cells $\eta \times \phi$ size of the calorimeters.

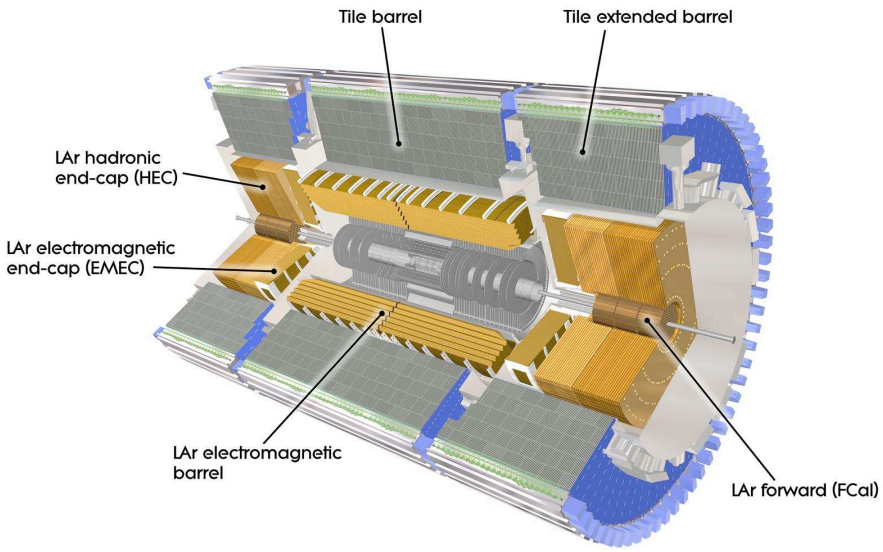

Figure 4.5: View of the ATLAS calorimeter systems. The barrel and end-cap parts of the EM and hadronic calorimeters are shown. As well, the Forward calorimeters are illustrated.

types of electrodes, commonly named electrodes A and B, the 2.5 mm transition region arising at $|\eta| = 0.8$. A high voltage of 2000 V is applied on both sides of the electrode.

The EMEC is made of two 63 cm thickness wheels covering a range in rapidity $1.475 < |\eta| < 3.2$ and having inner and outer radius, $R_{in} = 30\ cm$ and $R_{out} = 2.1\ m$ respectively. Each wheel is actually made of an inner and an outer wheels split projectively in η at $\eta = 2.5$ with different gap sizes of $d = 2.2\ mm$ and $d = 1.7\ mm$ respectively. The inner(outer) wheel contains 32(96) absorbers-electrode samples covering a range in ϕ of $2\pi/8$. The applied high voltage varies in η to compensate the gap increasing with η.

Motivations and Performances

The EM calorimeter of ATLAS have in part been optimized for the search of the Higgs boson through its decay modes $H \to \gamma\gamma$ and $H \to ZZ^{(*)} \to 4e^{\pm}$. In the particular case of the Higgs decay into two photons the Higgs boson is searched in the low masses range where the total Higgs width is very narrow. A crucial point is too precisely reconstruct the invariant mass of the photon pairs to be able to distinguish the signal on top of a large and non-resonant background. The mass and its resolution can be expressed as:

$$m_{\gamma\gamma} = \sqrt{2E_1E_2(1-\cos\theta_{12})} \tag{4.1}$$

$$\frac{\Delta m_{\gamma\gamma}}{m_{\gamma\gamma}} = \frac{1}{2}\left(\frac{\Delta E_1}{E_1} \oplus \frac{\Delta E_2}{E_2} \oplus \frac{\Delta\theta_{12}}{\tan(\Delta\theta_{12}/2)}\right) \tag{4.2}$$

where $E_{1,2}$ are the energies of the photons and $\Delta\theta_{12}$ represents the 3-D separation angle between the photons. The mass resolution relies therefore on a good reconstruction of both the energy and direction of the photons. A large background associated to the photon comes from jets that are reconstructed as photons. The design of the EM calorimeter is also dictated by the requirement of a good rejection of jets.

A synopsis of the performance of the LAr EM calorimeter of ATLAS is given here:

- **Hermeticity and angular coverage:** A good hermeticity of the EM calorimeter of ATLAS is obtained by the accordion shape of the absorbers (section 5.2.1), routing the signal at the rear and back of the calorimeter. The largest possible acceptance is needed to get the best sensitivity to rare physic processes such as $H \to \gamma\gamma$ decay. It is also very important for the measurement of the missing transverse energy.

- **Noise impact:** The $CR-RC^2$ filter shaper located in the Front End boards outside the cryostat minimizes the electronic and pile-up noise (section 5.3).

- An excellent **energy resolution and linearity** is needed to reconstruct the invariant mass of the diphoton (and 4-electrons) system in Higgs search into $H \to \gamma\gamma$ ($H \to 4e^{\pm}$). A stochastic term of $10\%/\sqrt{E}$ and a constant term of 0.7% is expected to contribute to the energy resolution (section 5.1.3). A linearity response better than 0.5% (1%) up to 300 GeV (3 TeV) is required.

- **Position resolution:** the accurate reconstruction of the invariant mass of the diphoton pair in the $H \to \gamma\gamma$ channel relies on an accurate measurement of the photon direction θ. It is measured with a resolution of 50 mrad$/\sqrt{E}$.

- **Particle identification, jets rejection:** an excellent γ/jet and $e^{\pm}$/jet separation is needed to minimize the background associated to the $H \to \gamma\gamma$ channel. A thin granularity is achieved in the main sampling ($\Delta\eta \times \Delta\phi = 0.025 \times 0.025$) to provide an accurate particle identification (and precisely reconstruct the photons direction). A thin longitudinal segmentation is designed in the first layer of the calorimeter in order to separate two overlapping photons from a π^0 decay and a single isolated photon (section 5.2.1).

The LAr EM calorimeter geometry and signal reconstruction scheme are presented in more details in the next chapter.

4.3.2 The Tile Hadronic Calorimeter

The hadronic calorimeter is placed immediately outside the EM calorimeter as shown in Figure 4.6. It comprises of a barrel part covering the rapidity range $|\eta| < 1.0$ and two extended barrels that cover the range $0.8 < |\eta| < 1.7$. It is a sampling calorimeter made of steel as absorber medium and scintillating tiles as active medium, suggesting its name of Tile Calorimeter. It has an inner radius $R_{in} = 2.28\ m$ and an outer radius $R_{out} = 4.25\ m$ for a height $l = 5.64\ m$ and $l = 2.65\ m$ respectively for the barrel and extended barrel part. These are separated by a gap of 60 cm wherein a small Tile subdetector is introduced, made of scintillating tiles only. The tiles of 3 mm thickness and trapezoid form are inserted on 14 mm thickness plates of stell. The Tile is segmented in three layers with a $\Delta\eta \times \Delta\phi$ granularity of 0.1×0.1 in the first two layers and 0.1×0.2 in the third (outermost) layer.
The barrel and extended barrel Tile, have a radial depth of approximatively 7.4 λ, where λ is the interaction length unit. Accounting for the contribution of the EM calorimeter, the calorimeters amount to about 11 λ in total, as illustrated in Figure 4.7. The end-cap hadronic calorimeter (HEC) is a Liquid Argon-copper sampling calorimeter covering the range $1.5 < |\eta| < 3.2$. It is therefore contained in the end-cap cryostat. The HEC consists of an inner wheel, made of

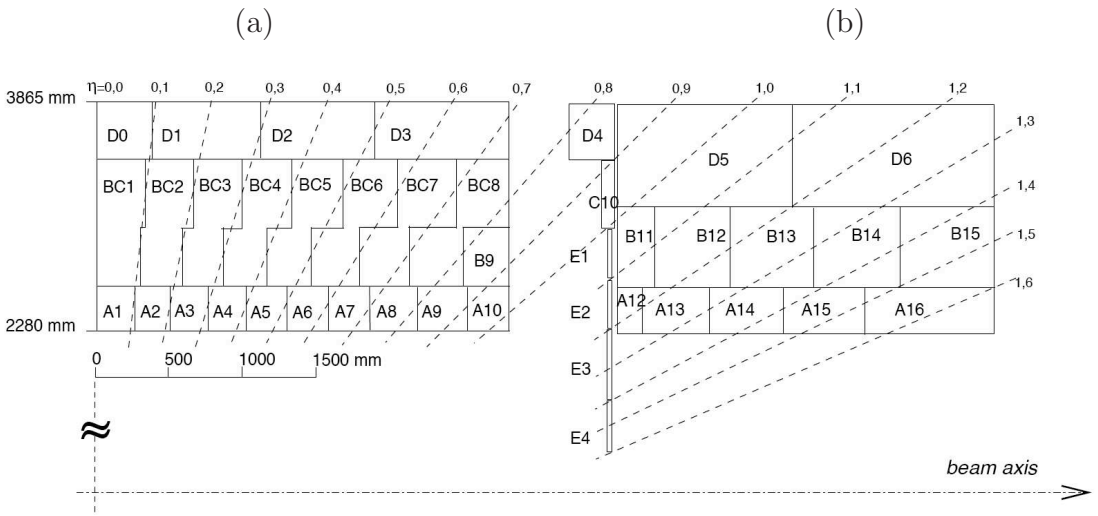

Figure 4.6: Segmentation in depth and η of the barrel (a) and extended barrel (b) of the Tile Calorimeter.

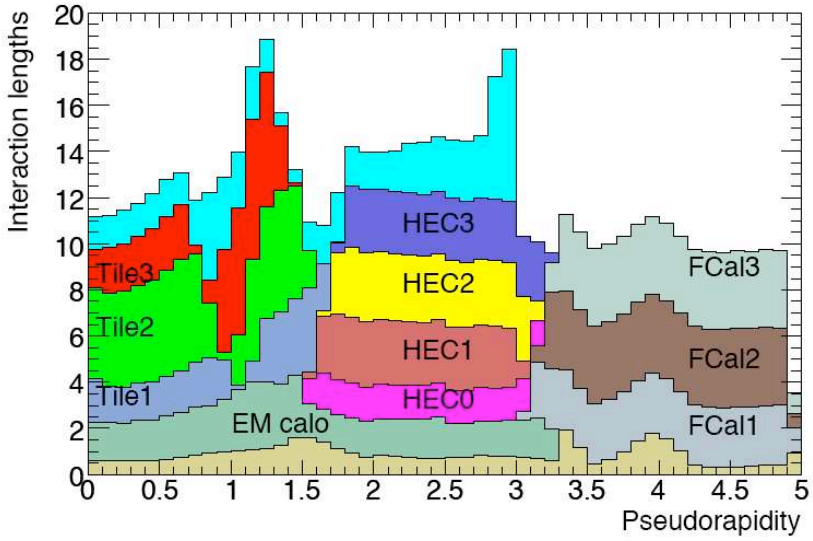

Figure 4.7: Interaction length of the EM calorimeter, the Tile barrel and extended barrel, the HEC and the forward calorimeter as a function of η

25 copper absorbers of 25 mm thickness separated by a Liquid Argon 8.5 mm thickness gap of (three electrodes and four 1.194 mm liquid argon gap actually separates the copper plates), and an outer wheel, made of 17 copper absorbers of twice the thickness of gap. A high voltage of 1800 V is applied in the end-cap wheels.

4.3.3 The Forward Calorimeter

The Forward calorimeters (FCALs) are relatively far from the interaction point (4.7 m) are located in the same cryostat than the EMEC and HEC calorimeters and cover a range in rapidity $3.1 < |\eta| < 4.9$. These detectors are made of three modules which differ in their absorber component and gap size, as illustrated in Figure 4.8(a) and (b). The gaps are smaller than for the other calorimeters to compensate the high multiplicity of charged particles at large

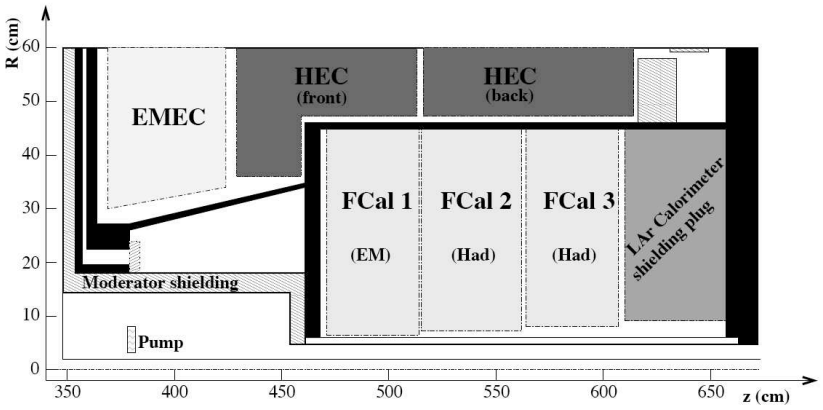

	FCal1	FCal2	FCal3
Function	Electromagnetic	Hadronic	Hadronic
Mass of module (kg)	2119	3826	3695
Main absorber material	Copper	Tungsten	Tungsten
LAr gap width (mm)	0.269	0.376	0.508
Radiation length (X_0)	27.6	91.3	89.2
Absorption length (λ)	2.66	3.68	3.60
Number of electrodes	12260	10200	8224
Number of readout channels	1008	500	254

Figure 4.8: Top: View in the $(R-z)$ plan of the Forward calorimeters. Bottom: Parameters (gap size, absorbers material) of the FCALs.

η. The first module FCAL1, associated to the EM calorimeter receives a HV of 250 V, while the second and third layers FCAL2 and FCAL 3, both related to the hadronic calorimeter, receive respectively 375 and 500 V.

4.4 The Muon Spectrometer

The muon chambers and the superconducting coils constitute the outermost piece of the ATLAS detector and contribute to its impressive size. The muon spectrometer has been designed in the spirit of providing an accurate measurement of the muons momentum in a large dynamic range. A resolution of about 10% is achieved for muons with a transverse momentum of 1 TeV. The spectrometer comprises of a barrel and two end-caps. The magnet system is made of eight 25 m (5m) long super-conductring coils with inner and outer radius $R_{in} = 4.7\ m$ and $R_{out} = 9.4\ m$ respectively in the barrel(end-cap) part delivering a magnetic field of 4 T. The muons are deflected under a toroidal field delivered by superconducting air-core toroid magnets and traverse the muons chambers. In addition to chambers dedicated to precision measurements trigger chambers (Level 1, as detailed in the next section) on the muons are incorporated in the spectrometer.

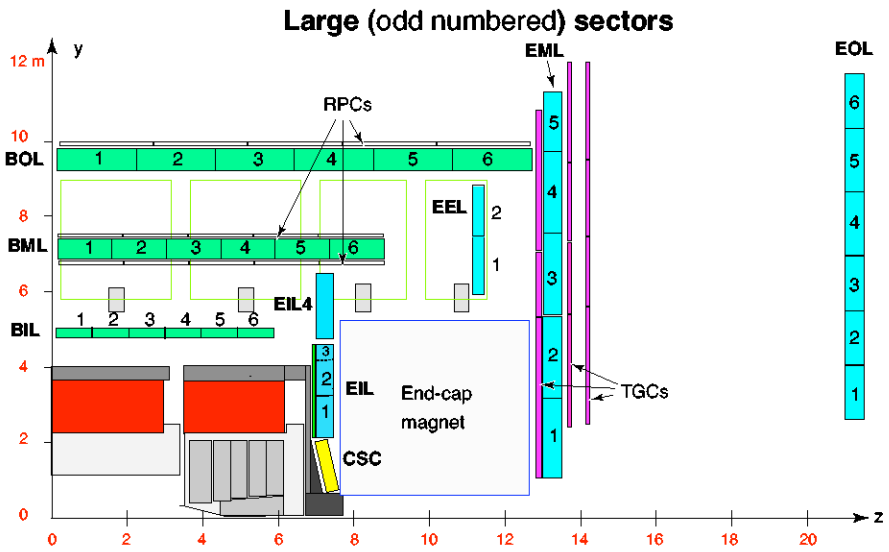

Figure 4.9: Sketch of the muon spectrometer in ATLAS detector. The precision measurement chambers, MDT and CSC, respectively in the barrel and end-cap parts are shown as well as the RPC and TGC chambers, dedicated to the trigger (Level1).

Monitored Drift Tubes (MDT) and Cathode Strip Chambers (CSC) MDT chambers are used in the barrel covering the region $|\eta| < 2.0$, for the measurement of the muons momentum. The MDT consists of two levels of four planes of 3 cm diameter Aluminum drift tubes with a Tungsten string receiving 3 kV. About 1000 chambers (with different geometries) are used for a total surface of 5500 m^2. The chambers are precisely aligned with laser diodes and CCD captors to provide an accurate measurement of the muons trajectory. A resolution of 35 μm is achieved in the z direction. In the end-cap part ($2.0 < |\eta| < 2.7$), a thiner granularity is needed to compensate the higher particle multiplicity. The CSC used in the end-caps are proportional chambers that provide a resolution of 40 μm in R for a resolution of 5 mm in ϕ .

Resistive Plate Chambers (RPC) and Thin-Gap Chambers (TGC) The trajectory measurement is completed with faster chambers that ensure the L1 trigger. In the barrel part, RPC chambers are used, characterized by a response time of 1.5 ns (with respect to the 25 ns nominal interval between beam collisions) and a resolution of 10 μm in z. In the end-cap the TGC chambers are used, with a slightly longer response time (4 ns) and a resolution in R(ϕ) of 2-6 mm (3-7 mm).

4.5 The Trigger System

The trigger system is crucial in the LHC environment where high collision rates are achieved (The frequency corresponding to the LHC beam crossing every 25 ns is 40 MHz). The amount of readout channels is huge, around 10^8 in the ID, 10^5 in the calorimeters and 10^6 in the spectrometer. The amount of information is therefore too important at the initial level to be directly recorded on magnetic tapes. A pre-selection is made through a three-step trigger system that selects interesting event signatures. The trigger architecture is represented in Figure 4.10.

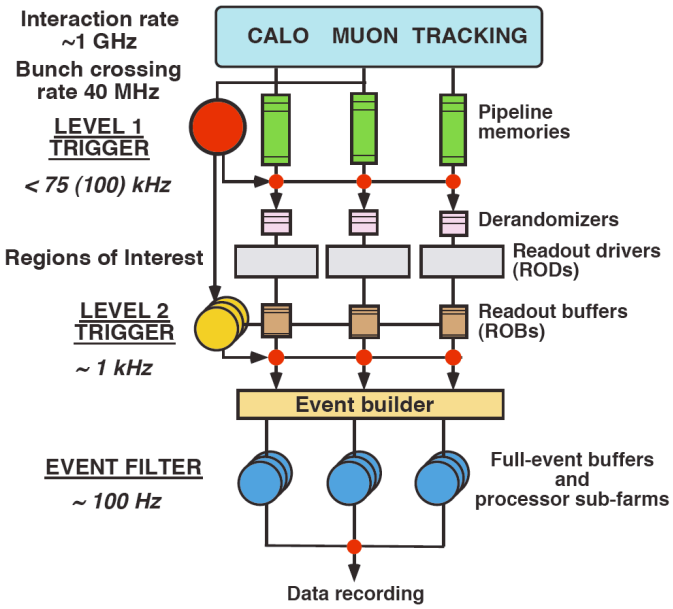

Figure 4.10: Sketch of the trigger levels in ATLAS detector.

1.- **The Level 1** operates at the crossing frequency and is aimed at reducing it to an output rate of 100 kHz (corresponding to a reduction of factor of 400). It is based on calorimeter and spectrometer information where simple criteria are required to create 0.1×0.1 clusters and RPC/TGC coincidences respectively. It has a latency of 2.5 μs which allows to keep the information of about 100 crossing beams in pipelines while the decision is made to keep or not the event.

2.- **The Level 2** is seeded by the Level 1 trigger and defines regions of interest (RoI). The information recorded in the pipeline are put into digital form and the information from the detectors is available with the appropriate granularity. The RoI, that represents around 2% of the detector volume, are split into categories based on different reconstruction algorithms. The ID track information is used. The Latency varies between 1 and 10 ms and the output frequency is about 2kHz (corresponding to a reduction factor of 50).

3.- **Event Filter** corresponds to the complete reconstruction of the events sent to storage farms, leading to a final frequency of about 200 Hz. It corresponds to a reduction factor of 10 (or 10^5 with respect to the initial crossing frequency).

The events are completely reconstructed with a maximal latency of 1s. The trigger system reduces the amount of information put on tapes to 10-100 Hz. This corresponds to an amount of information recorded of about 10 Tbytes/day, requiring powerful processors and dedicated spaces for the data storage.

The **Tier 0**, at CERN, is the location where the data is stored, reconstructed and organized in analysis topics, and redistributed to the **Tiers 1**. The **Tier 1** also ensures the long time storage of a fraction of the data and distributes it to the **Tier 2**. The Tier 1 in France it at the "Centre de Calcul" at Lyon. Finally the **Tier 2** contains data and tools for analysis and MC simulations. Monte Carlo simulations and calibration data constitute an important part

of the data storage, comparable to the collision data. It represents nowadays about 22 and 18 Pbytes respectively on disk and on tape (in the french cloud).

Part I

Drift Time Measurement and Intrinsic Uniformity of the EM Calorimeter of ATLAS

Chapter 5

The EM Calorimeter of ATLAS

In this chapter, the interactions of photons and electrons through matter are briefly summarized, followed by a description of the EM LAr calorimeter of ATLAS. The readout chain of a signal generated by the passage of a charged particle in the LAr is presented, from the ionization signal to the reconstructed energy. Two methods of energy reconstruction are presented. During summer 2004, beam tests were made on barrel and end-cap modules of the EM calorimeter of ATLAS. Some important results from the beam tests on the calorimeter uniformity and energy resolution are highlighted.

5.1 Introduction

Electron and photon interactions with matter are described by ionization and radiative processes. The principle of a sampling calorimeter such as the LAr calorimeter of ATLAS is to generate a cascade of electron and photon interactions, alternating active (light) and passive (heavy) mediums. The electrons and photons interactions with matter are presented in this section. The EM LAr calorimeter of ATLAS is then described.

5.1.1 Electrons and Photons through Matter

The energy lost by a particle when it traverses the matter is described by different phenomena, according to the initial energy of the particle.
Figure 5.1(a) shows the energy lost by a photon as a function of its energy. The cross section of photon interaction with matter is written as [38]:

$$\sigma_{tot} = \sigma_R + \sigma_{p.e} + \sigma_c + \sigma_p + \sigma_{nucl}$$

- The Rayleigh scattering σ_R is the photon elastic scattering. The photon changes its direction by interacting with an atomic electron but does not loose energy in the process. Photon-nuclear (elastic) interactions σ_{nucl} and Rayleigh scatterings are negligible in the following.

- The photoelectric effect $\sigma_{p.e}$ is the photon interaction with an atom which emits an electron. The atom, in an excited state, returns to its ground state by emitting an Auger electron or X-rays. $\sigma_{p.e}$ goes with Z^5 and decreases rapidly with energy (its dependence is as $1/E^3$).

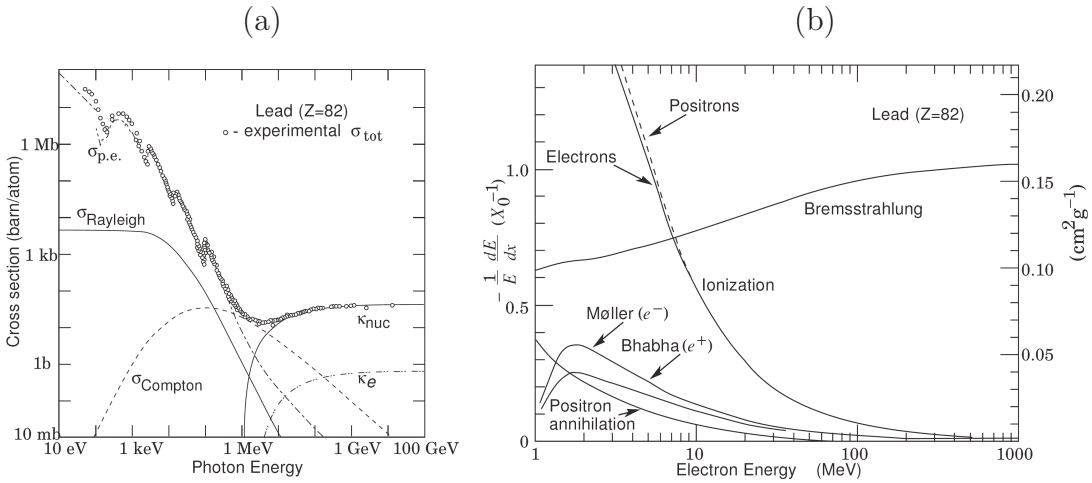

Figure 5.1: (a): Cross section of the photon interaction with matter as a function of its energy. k_{nucl} and k_e correspond to electron-positron pair creation by interaction with a nuclear and an electron, respectively. (b) Processes of electron interaction with matter as a function of its energy, per radiation length.

- The Compton diffusion σ_c is the inelastic scattering between a photon and an electron. It dominates between at few hundred KeV and a few MeV and then decays as 1/E.

- When $E_\gamma > 2m_e c^2$, the process of e^+e^- pair creation in the Coulomb field of an atomic nucleus or an electron is opened. The cross section grows with the energy and dominates above few MeV,where it becomes independent of the γ energy.

Figure 5.1(b) displays the different processes of energy lost by an electron in the lead, as a function of its energy.

- For energies below $\sim 10\ MeV$, the electron mainly interacts by ionization, when it carries enough energy to extract an electron from the coulomb potential of the atom.

- Above $\sim 10\ MeV$ the electron interactions through matter are dominated by radiative processes. The electron loses energy by emitting a photon, resulting from Coulomb interaction with the electric field of atomic nuclei.The phenomena of electron energy lost by photon emission is the so called Bremsstrahlung process.

Above $E \sim 10MeV$, the electron and photon interactions in matter are dominated by radiative processes corresponding respectively to the electron energy lost by Bremsstrahlung and the photon conversion into an e^+e^- pair. The radiation length (X_0) of a material, generally measured in $g.cm^{-2}$, is the average distance traversed by an electron associated to a fraction of its energy lost of 1-1/e ($\sim 63\%$). It is parametrized as:

$$X_0 = \frac{716.4A}{Z(Z+1)ln(287/\sqrt{Z})} \quad (5\%\ accuracy) \tag{5.1}$$

where A is the mass number and Z the atomic number of the material. For photons, the mean free path for pair creation is $9/7X_0$. The distribution of the energy lost per unit of X_0 in the

EM cascade is given by the empirical formula [38]:

$$\frac{dE}{dt} = \frac{E_0 b(bt)^{a-1}e^{-bt}}{\Gamma(a)} \tag{5.2}$$

where $t = x/X_0$, the traversed matter thickness. a and b rely on the material characteristics. This gives as mean position of the distribution maximum:

$$t_{max} = \frac{a-1}{b} = ln\Big(\frac{E_i}{E_c}\Big) + C \quad (C_{\gamma,e^\pm} = 1/2, -1/2) \tag{5.3}$$

E_i and E_c are respectively the initial energy of the electron (or photon) and the critical energy when the Bremsstrahlung and ionization process cross sections coincide. In the lead, $X_0(Pb) = 56\ mm$ and $E_c = 7.3\ MeV$, an EM shower generated by a photon with an initial energy of 10 GeV has a maximum development position at $\sim 7.8\ X_0$. In average, 98% of the EM shower is contained in 20-25 X_0, which fixes the EM calorimeter longitudinal size.

The transverse profile of the EM shower is shaped bye initial high energy electrons that have a longer mean path free than photons at the end of the shower, that are more sensitive to photoelectric effect and the Compton scattering. It is defined by the Moliére radius:

$$R_M = \frac{X_0}{E_c} \times 21.2\ MeV$$

About 95% of the EM shower is contained in a cylinder of radius $2R_M$.

5.1.2 Sampling Calorimeter

The EM calorimeter of ATLAS is a sampling calorimeter:

- The passive medium, or absorber, is made of lead which is a dense material. Photons and electrons loose their energy by Bremsstrahlung radiation and pair creations in the lead. (In the hadronic end-cap calorimeter, copper absorbers are used.)

- The active medium is made of Liquid Argon (LAr) that allows a good resistivity to radiations and a high drift velocity of the electrons[1)]. In the active medium the electrons ionize the LAr and create Ar^+e^- pairs.

Basically, a readout electrode centered in the LAr gap receives a high voltage (HV = 2000 V in the barrel) while the lead plates are grounded. The readout electrode collects the ionization electrons and generates a signal current.
The particle looses energy in both the active and passive medium while only the electrons from the active medium are collected. The fraction of the initial particle energy E_i that is deposited in the active medium by ionization, or *sampling fraction*, is defined by:

$$f_{sampling} = \frac{E_{active}}{E_{active} + E_{passive}}$$

$E_{active,passive}$ is the energy lost in active and passive mediums. A high sampling fraction is needed for an accurate energy measurement.
The visible energy is actually:

[1)] while the ions drift slowly due to the high density of the liquid.

$$E_{meas} = E_i f_{sampling} F_{e/\mu} \ , \qquad F_{e/\mu}/f_{sampling} = 0.6 - 0.8$$

$F_{e/\mu}$ is a correction factor accounting for the difference between a minimum of ionization particle (MIP) like a muon and an electron that can emit low energy photon produced, that can even be absorbed by photo-electric effect. It is called the e^-/μ ratio.

5.1.3 Energy Resolution

The maximal development of the EM shower is defined by the energy of the incident particle E_i and the characteristics of the material, via E_c. The number of particles created in the EM shower also relies on these quantities. The number of particles at the maximum of the shower development is given by:

$$N_{max} = \frac{E_i}{E_c}$$

directly proportional to the initial energy of the particle. The fluctuations on the energy deposited by ionization ΔE relies on the fluctuations on the number of particles produced in the EM shower N.

$$\frac{\Delta E}{E} \propto \frac{1}{\sqrt{E}} \tag{5.4}$$

The energy resolution in the calorimeter decreases as $1/\sqrt{E}$. To account for more effects than statistical fluctuations, the energy resolution can be written as:

$$\frac{\sigma_E}{E} = \frac{a}{\sqrt{E}} \oplus \frac{b}{E} \oplus c \tag{5.5}$$

The first term is the stochastic term, the second term is the noise term and the third term is the constant term.

- The stochastic term corresponds to the statistical fluctuations associated to the EM shower development. The a coefficient is expected to be $\approx 10\%$ in the ATLAS LAr EM calorimeter. In the hadronic end-cap and forward calorimeter it is expected to be about 50% and 100% respectively. The sampling fraction brings a major contribution to a.

- The noise term comprises of the electronic readout chain and the pile-up noises. Method of *Optimal Filtering* and shaping are used to reduce the noise as explained in section 5.3. The $1/E$ dependence implies that this contribution becomes important (and dominates) at low energies.

- The constant term c summarizes all contributions to the non-uniformity of the calorimeter response, that do not depend on the particle energy: material non-uniformity (gaps and absorbers thickness), imperfections in mechanical structures, temperature gradient, radiation damage, energy reconstruction scheme and stability in time... A study presented in the next chapter aims at estimating the gap uniformity in the EM barrel calorimeter of ATLAS and extract a contribution to the constant term. It is expected not to exceed 0.7% while in the hadronic and forward calorimeter it is respectively expected to be around 3 and 10%. During the beam test [39], the response uniformity of the EM calorimeter of ATLAS was measured in four barrel and three end-cap modules and a global constant term of $\sim 0.6\%$ was found.

There are additional effects causing a dispersion in the energy measurement:

- The longitudinal leakage corresponding to showers which are exceeding in length that of the calorimeter, thus leaking outside.

- The lateral leakage at the beginning of the EM shower at the end of the shower where low energy photons are more sensitive to coulomb interaction and Compton scattering, deflecting their trajectory.

- The amount of matter in front of and in the calorimeter, coming from the ID, cables, services and support structures. Also accurately referred, fluctuations in the upstream material induces a degradation of the energy. The presampler is a dedicated small detector installed between the ID and the calorimeter, that aims in estimating the energy lost by electrons and photons before arriving in the calorimeter.

5.2 The LAr EM Calorimeter of ATLAS

5.2.1 Calorimeter Geometry

The EM calorimeter of ATLAS is made of lead absorbers interleaved with readout electrodes wherein Liquid Argon (LAr) is used as active medium. The barrel (EMB) and end-caps (EMEC) are located inside separated cryostats that cool the system at 88.5K, the temperature of the Liquid Argon. The EM calorimeter of ATLAS amazes by its innovative structure, inspired by D. Fournier [40]. The Liquid Argon-lead absorbers sampling in ATLAS has an accordion shape. The choice of a such geometry with respect to standard straight calorimeter segmentation (Figure 5.2(a)) is governed by the idea of getting projective signal towers and a good hermeticity of the cryostat by routing out the signal toward the front or rear faces of the modules, limiting then electronic noise and cables (causing additional matter) in the calorimeter [36]. Figure 5.3

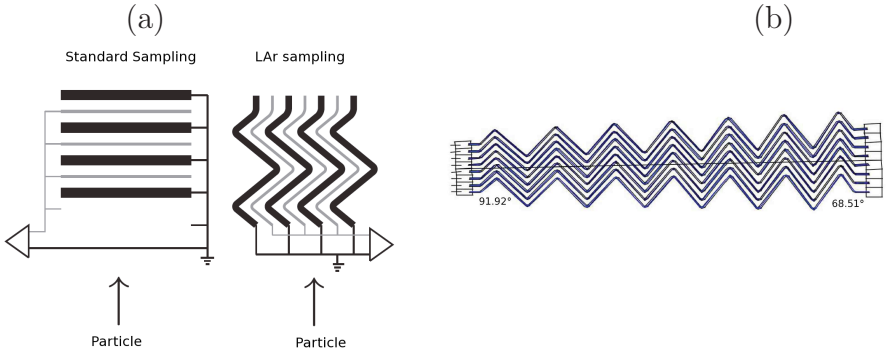

Figure 5.2: (a): Schematic view of the "standard" straight geometry of a sampling calorimeter and the accordion shaped geometry chosen for the EM calorimeter of ATLAS. (b)View of the accordion shape of the absorbers. The waves angle and amplitude vary with depth to provide a constant LAr gap size.

show the transversal view of an EM barrel. The granularity in the (η, ϕ) plane is shown for the three compartments of the EM barrel calorimeter: the Front, Middle and Back. The longitudinal segmentation of the barrel and the end-caps is illustrated in Figure 5.4.

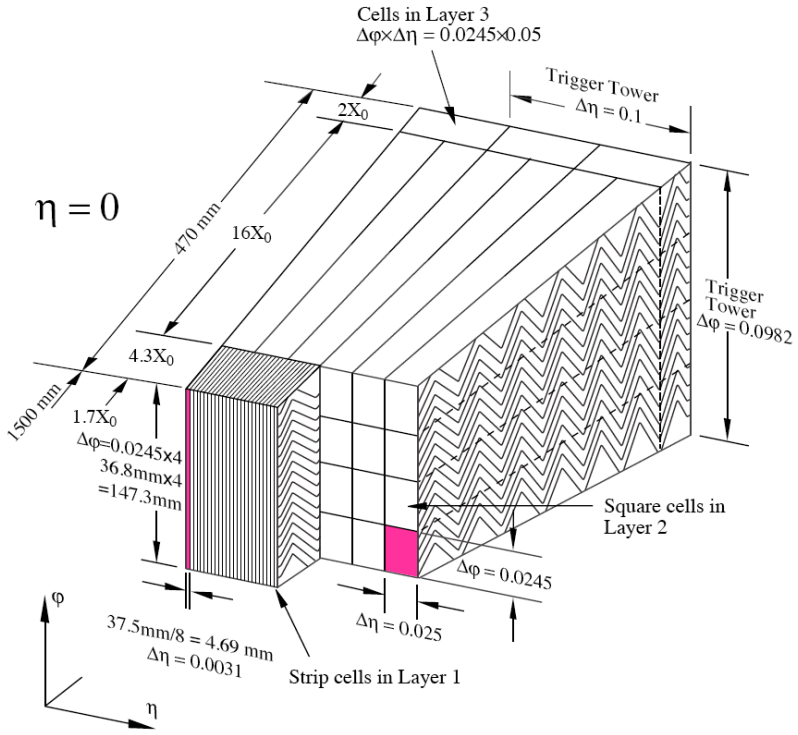

Figure 5.3: Sketch of the transversal segmentation of the EM calorimeter barrel for $\eta = 0$.

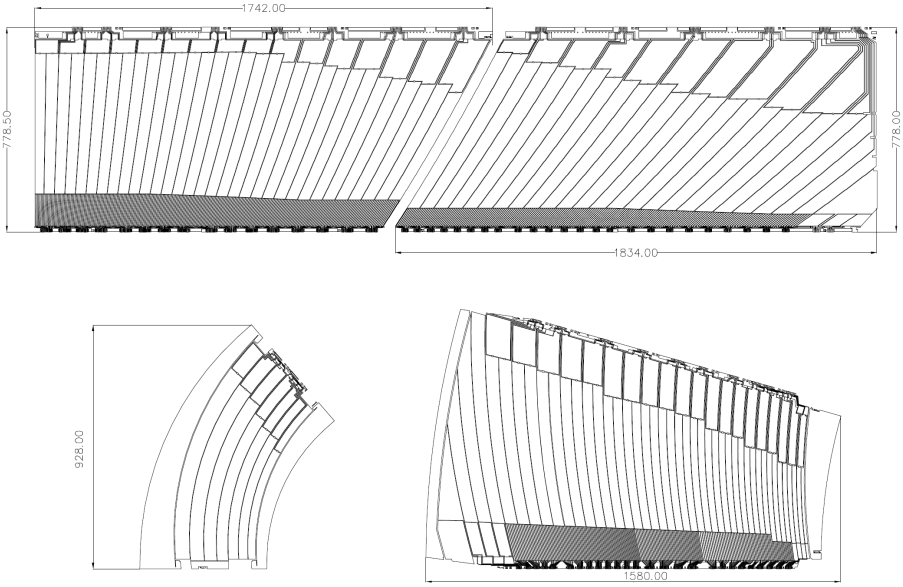

Figure 5.4: (b): Longitudinal segmentation of the EM calorimeter barrel and end-cap.

Figure 5.5 displays a schematic view of the lead-LAr-lead sampling in the straight section. The absorbers are made of lead plates on which two 0.2 mm thickness sheets of stainless-steel are glued to provide the mechanical strength. The plates are separated by a gap of LAr wherein a readout electrode collects the ionization signal induced by the passage of a charged particle.

The LAr gap has a constant width of d = 2.1 mm, ensured by the use of honeycomb which is important to ensure an uniform response in energy. Considering the projective accordion

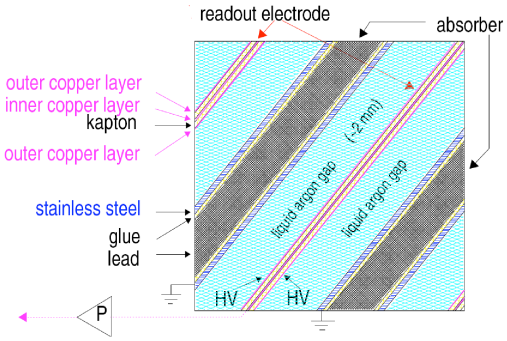

Figure 5.5: Sketch of the lead-LAr-lead sampling in the EMB (straight section).

shaped geometry of the EMB, the angle and amplitude "waves" of the accordion shape vary with η, as illustrated in Figure 5.2(b). The modules are made of two types of electrodes, namely electrodes A and B, the 2.5 mm transition region arising at $|\eta| = 0.8$. The LAr gap and the absorbers are maintained constant in both regions while the lead thickness varies from 1.53 mm in $|\eta| < 0.8$ (electrode A) to 1.13 mm in $0.8 < |\eta| < 1.475$ (electrode B). This allows to compensate for the increased amount of material traversed in the EM calorimeter at large η. The readout electrode is made of three conductive copper layers separated with insulating polyimide sheets (Kapton). A high voltage HV = 2000 V (nominal) is applied in the outer layers while inner copper layer collects the ionization electron. The lead plates are grounded and create an electric field allowing the ionization electrons to drift toward the readout chain. The high voltage granularity in the barrel is $\Delta\eta \times \Delta\phi = 0.2 \times 0.2$ which corresponds to 32 electrodes powered commonly. In the end-cap, the gap is not constant as opposed to the barrel. It varies from 2.8 mm to 0.9mm in the outer wheel and from 3.1 mm to 1.8 mm in the inner wheel. The high voltage is varied with η to approximatively compensate the gap dependence in η and obtain a rather uniform response in that direction . The nominal HV for the barrel and end-cap of the EM calorimeter are shown in Figure 5.6(a) et (b) respectively. The signal

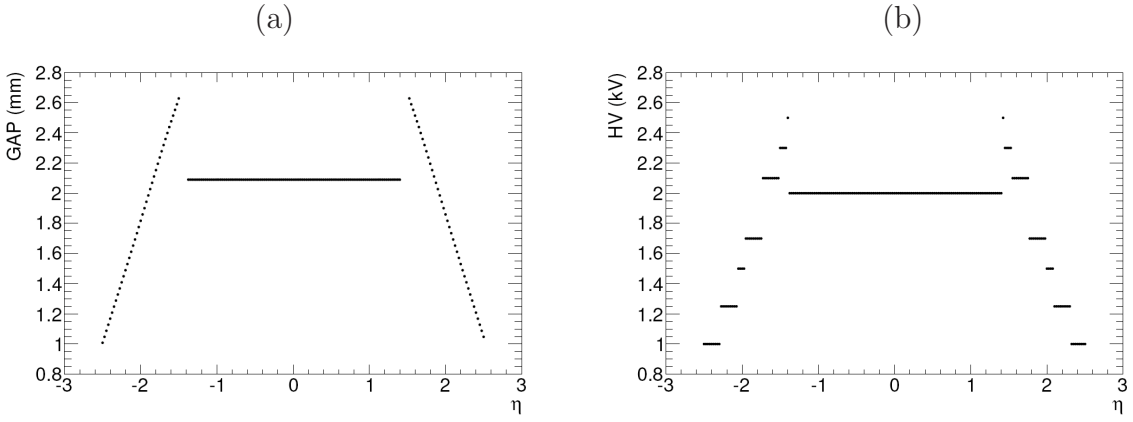

Figure 5.6: Distribution of the LAr gap size (a) and HV applied to the readout electrode in the EMB and EMEC, as a function of η (b).

readout chain is developed in detail in the section 5.3.3.

When the electrons produced at the interaction point reach the EM calorimeter, they have traversed the ID and therefore have lost a fraction of their energy, mostly in the Pixel and SCT detectors. The solenoid installed in the calorimeter cryostat also contributes to the matter seen by the particles and amounts to about 1.5 X_0. Figure 5.7(a) and (b) display the number of radiation lengths in front of the calorimeter and in the different layers, in the barrel and end-caps respectively. To account for the energy lost in front the EM calorimeter, a pre-sampler detector is used, based on a simpler planar geometry.

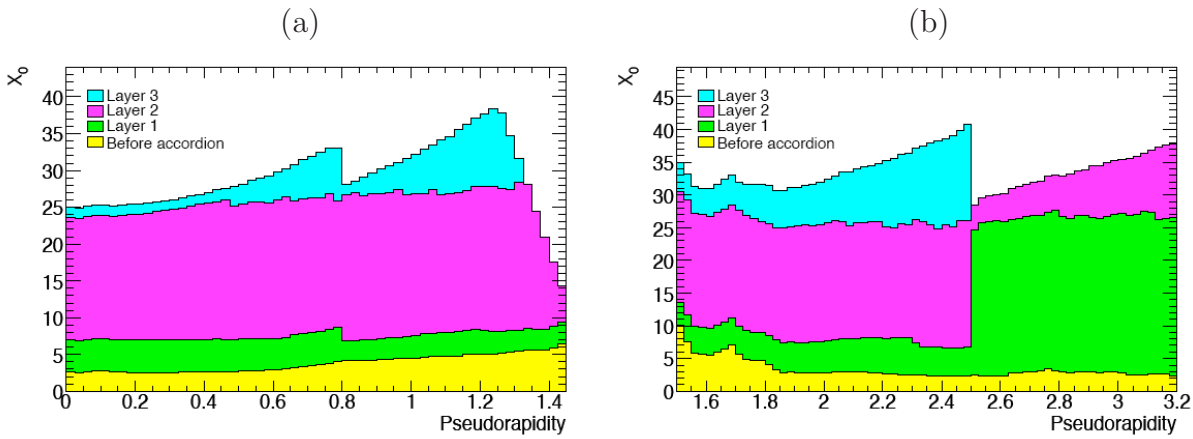

Figure 5.7: Distribution of the radiation length in as a function of η in the front of and in the different layers of the EM calorimeter, barrel part in (a), and end-cap in (b). At the transition between the barrel and end-cap, a large fraction of material causes important degradation in the measure of the energy.

- The *Presampler* detector consists of a thin layer of Liquid Argon (1.1 cm thickness in the barrel and 0.5 cm in the end-cap) and electrodes with a poor segmentation. it covers the rapidity range $|\eta| \lesssim 1.8$. The presampler is aimed at improving the overall energy measurement and in particular to sample the energy lost by the electron and photons in the material in front of the calorimeter.

- The first layer of the ATLAS EM calorimeter, commonly named the *strip* or *front*, is made of narrow strips, as show in Figure 5.3 (in the barrel part). In the central region ($|\eta| < 1.4$) the cells size is $\Delta\eta \times \Delta\phi = 0.025/8 \times 0.1$. The fine longitudinal segmentation provides an accurate η direction measurement and allows for an efficient π^0/γ separation by distinguishing the two energy maxima of the photons originating form the meson decay from the maxima energy of a single isolated photon. As illustrated in Figure 5.7 the Front layer corresponds to 4.3 X_0 at $\eta = 0$ and is relatively constant in η.

- The second layer, commonly called the *Middle*, contains a large fraction of the e^-/γ EM shower energy. It is segmented in squared cells of size $\Delta\eta \times \Delta\phi = 0.025 \times 0.025$, except near the barrel-end-cap transition where the cells are larger. The Middle contributes to 16 X_0 at $\eta = 0$ and varies with η. Typically, the shower of an unconverted photon is contained in a cluster of size 3×5 in the barrel part and that of a converted photon (in the ID) in a cluster of size 3×7. The spread in ϕ being due to the electron and positron

(from the conversion) curvature under the electric field. (In the end-caps, the photons are typically defined in a cluster of size 5×5.)

- The third layer, or *Back* sampling, has the same ϕ granularity than the middle but has twice a coarser granularity in η. It is used to measure the end of the EM shower (it corresponds to $X_0 = 2$ at $\eta = 0$), separate the $e^-\gamma$ from the jets and estimate the EM shower leakage which is approximatively proportional to the energy deposited in the barrel.
  The total thickness of the EM calorimeter is 22 X_0 at $\eta = 0$ and increases to 30 X_0 at the electrode A-B electrodes transition. In electrode B it goes from 24 to 33 X_0 in the η range $0.8 < |\eta| < 1.3$.

5.3 Ionization Signal Readout

When a high energy electron or photon passes through the EM calorimeter of ATLAS, the cascade of Bremsstrahlung emissions and pair conversions in the absorber generates low energy electrons that ionize the Liquid Argon atoms and create Ar^+e^- pairs. The ionization electrons drift under the electric field created by a voltage between the outer copper layers of the electrode and the grounded lead sheets.The inner copper layer collects the ionization charge by capacitive coupling.

5.3.1 Triangular Signal

The electrons from the LAr ionization through the passage of a charged particle drift uniformly towards the electrode under an electric field of 10 kV/cm (in the barrel). The current signal has a triangular shape in time:

$$I(t) = \frac{Q_0}{T_D}\Big(1 - \frac{t}{T_D}\Big) \tag{5.6}$$

where T_D is the average drift time of the electrons, around 450 ns in the 2.1 mm gap of ATLAS LAr barrel, corresponding to a drift velocity of about 4.5 $mm.\mu s^{-1}$. Q_0 is the total deposited charge in the LAr, Q_0/T_D corresponds to the initial current collected. The Ar^+ ions created by ionization drift about a thousand times slower and are collected too late to significantly contribute to the ionization signal. In a first approximation the current signal depends only on the initial current and the drift time T_D. Impurities in the Argon (such as 0_2), recombination of the Ar^+e^- pairs can however create deformations of the triangular shape [41].

The ionization signal collected in the first sampling of the calorimeter is read out from the front of the detector while the signals collected on readout electrodes in the second and third layers are routed towards the back of the detector (which correspond respectively to the inner and outer radius location in the barrel, the smallest and largest z surface in the end-caps). A diagram of the LAR readout electronics is illustrated in Figure 5.8 [42]. The collected current on the readout electrode is routed out of the barrel and end-caps boarders to the summing boards, that sum the signal from nearest neighbor gaps, and to the mother boards, for analogical signal read out in a region $\Delta\eta \times \Delta\phi = 0.2 \times 0.2$. The current signal is propagated forward among the signal cable, of impedance 25 or 50 Ω (respectively for the inner or outer surfaces), and treated in the electronic chain located outside the cryostat.

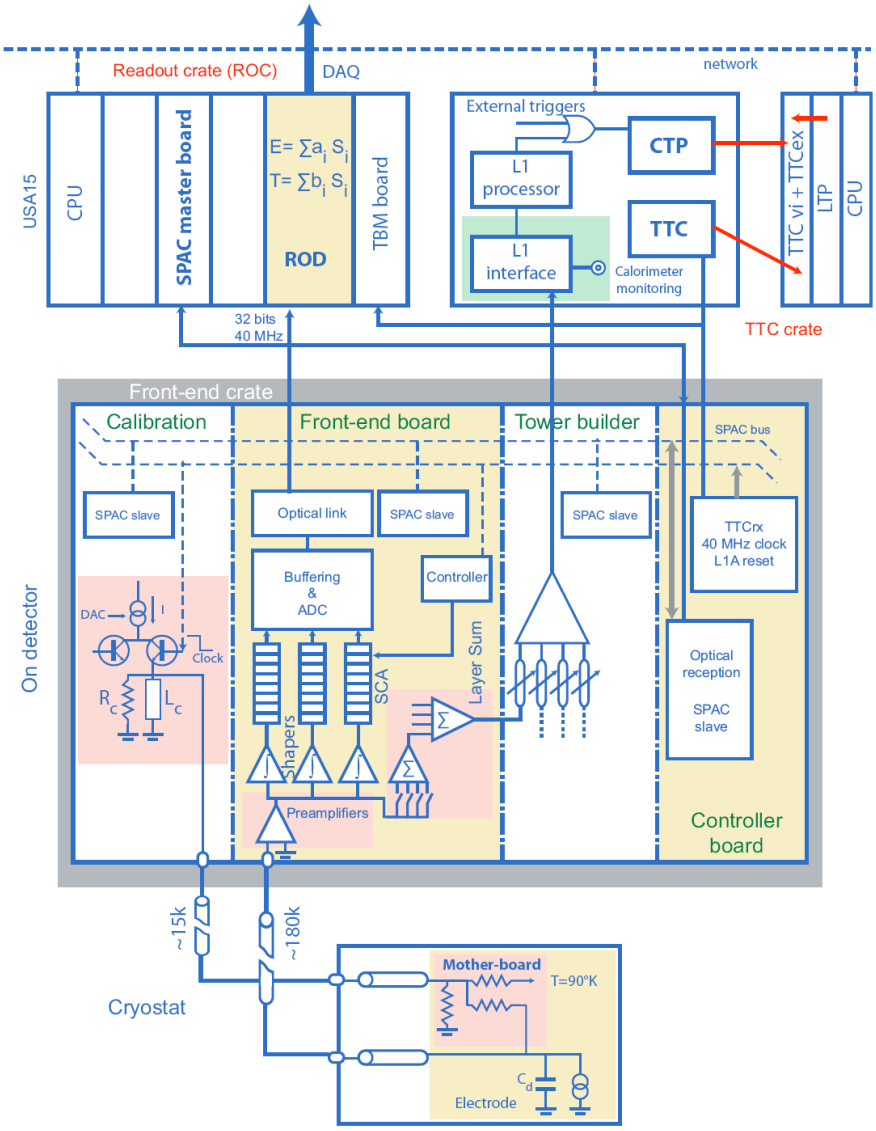

Figure 5.8: Diagram of the readout electronic of the LAr EM calorimeter.

5.3.2 Cryostats and FeedThroughs

The EM calorimeter is immersed in Liquid Argon within a cryostat maintaining a constant temperature of 88.5 K. The cryostat is made of two aluminum vessels: an inner cold vessel (at 88.5 K) and an outer vessel, at room temperature. The solenoid associated to the ID is supported by the inner cylinder of the warm vessel.

The signal and calibration lines are brought outside/inside the cryostat using *Feed-Through* (FT) devices. To minimize the numbers of connexion lines the FT are connected radially to the cryostat. There are in total 2×32 FT in the barrel part of the EM calorimeter (of size $2\pi/32$ in the ϕ direction, corresponding to two modules) and 2×25 FT in the end-cap, achieving 2×61400 and 2×48000 lines respectively. The end-cap cryostat comprises of the LAr EM, hadronic (HEC) and forward calorimeters. A view of the end-cap cryostat and detectors is illustrated in Figure 5.9.

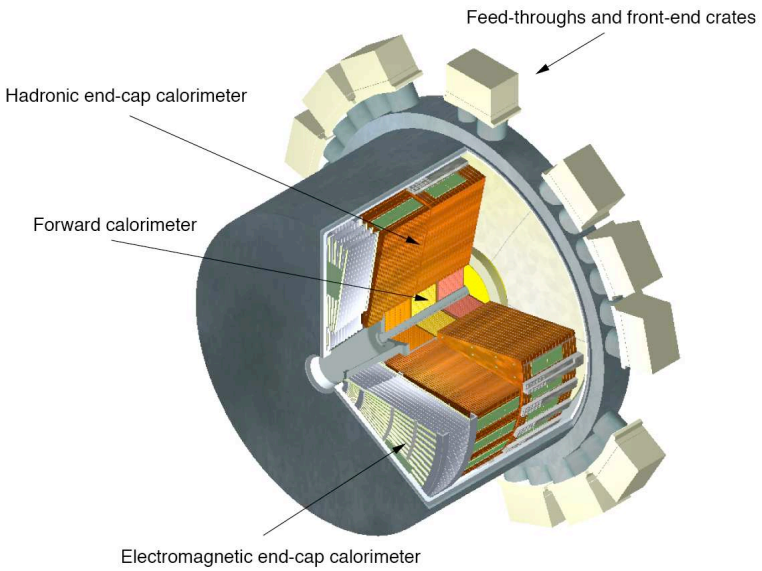

Figure 5.9: View of the end-cap cryostat. The FT are disposed radially. The LAr EM, hadronic and forward calorimeters are shown.

5.3.3 Readout Electronic Chain

Right on top of the FT output are the Front End Crates in which Front End Boards (FEBs) are inserted. Their role is to treat the triangular pulse by pre-amplifying and shaping it through a bi-polar filter of type $CR - RC^2$, with a constant time $\tau = 15\ ns$, yielding a bi-polar signal, as illustrated in Figure 5.8 [42]. The signal bipolar shape is shown in Figure 5.10(a). The

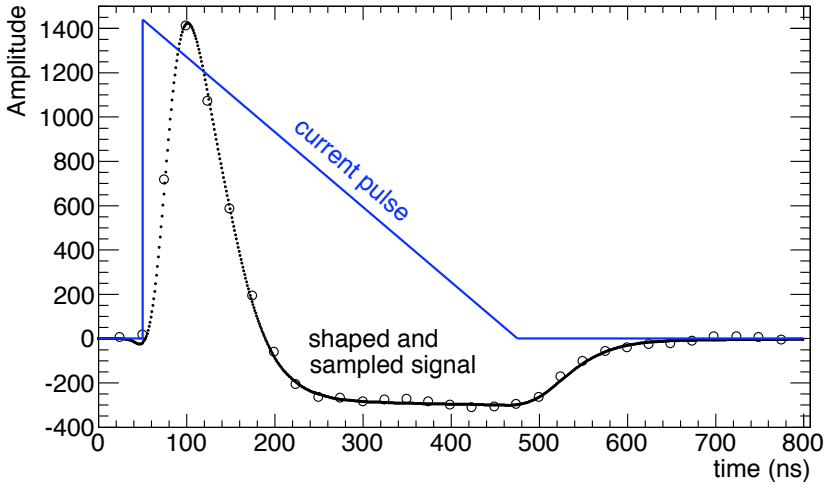

Figure 5.10: Example of ionization current and bipolar shaped sampled signal in time.

main advantage of this procedure is to make the total integral of the signal null. The maximum amplitude of the shaped signal is proportional to the initial current and arises at around 45-50 ns, between the second and third samplings. During the physic runs, 5 samples will be recorded (centered around the sampling with the maximum of amplitude), although dedicated

runs recorded up to 32 samples.

The samples are digitized by an analogical-to-digital converter (ADC). The large range in energy deposited in ATLAS EM calorimeter (between 30 MeV to 2-3 TeV) corresponds to 16 bits, while the ADC converter is limited to 12 bits. To provide an accurate and uniform energy reconstruction the shaper uses different gains. The high/medium/low gain multiply the signal by a factor of 93/9.3/1. The gain is applied to the signal according to ADC thresholds.
The signal samples are then stocked in SCA (Switched Capacitor Array) pipelines.
To properly achieve the correspondence between ADC and current a calibration procedure is performed on the electronic channels of the calorimeter. A calibration signal is generated by the calibration board transformed by a Digital-to-Analogical converter (DAC). The calibration signal is converted through an inductance into a continuous current whose discharge induces an exponential signal. The calibration current is written as:

$$I^{cali}(t) = I_0^{cali}[f_{step} + (1 - f_{step})e^{-t/\tau_{cali}}] \tag{5.7}$$

where τ_{cali} is the constant time, of about 430 ns, and f_{step} is a shift of about 7% introduced to compensate the resistive component of the inductance. The calibration current is then injected

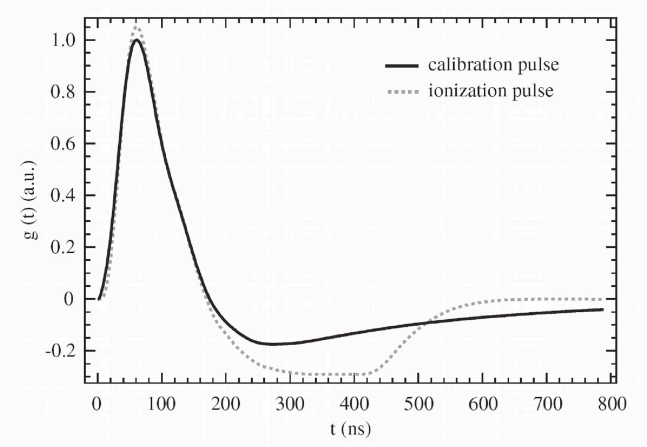

Figure 5.11: Example of calibration pulse shape compared to the ionization signal shape.

to the electrode and passes through all the read-out electronic chain followed by the ionization signal, until it reaches the ADC. The calibration signal mimics the ionization signal, as illustrated in Figure 5.11.

When an event candidate is triggered, the samples are routed to the Read Out Drivers (ROD). The RODs receive the signal samples from the ADC and the information from the calibration board. They perform the *Optimal Filtering* procedure on DSPs (Digital Signal Processors) and send the signal to Read Out Buffer (ROB) modules that send the energy, time and data quality of the signal.

5.3.4 Optimal Filtering

Assuming that the bipolar shaped signal form is known, the observed signal can be written as a function of time:

$$S(t) = \quad Ag(t-\tau) + n(t) \tag{5.8}$$

$$S(t) \approx \quad Ag(t) - A\tau g'(t) + n(t) \tag{5.9}$$

where A is the signal amplitude and τ the phase of the signal with respect to the beam crossing clock. $g(t-\tau)$ is the shaper function and g' its derivate. n(t) is the electronic and pile-up noise. The pile-up part depends on the luminosity (section 3). The electronic noise comes from capacitive, resistive or inductive noise and is reduced by the RC^2 part of the shaper, the two integrations limiting the bandwidth.
Each signal sample, at a time t_i, is written as:

$$S_i = Ag_i - A\tau g'_i + n_i \tag{5.10}$$

A and τ are extracted by properly combining the signal samples. To mimic the effect of noise a discrete convolution between signal samples and a set of optimal weights is made.

$$U = \sum_i a_i S_i \quad , \qquad < U >= A \tag{5.11}$$

$$V = \sum_i b_i S_i \quad , \qquad < V >= A\tau \tag{5.12}$$

The weights a_i and b_i are the so-called *Optimal Filtering Coefficients* (OFC) [43]. Equations 5.11 leads to the set of conditions, considering the noise null in average ($< n_i >$):

$$\sum_i a_i g_i = 1 \quad \sum_i a_i g'_i = 0 \tag{5.13}$$

$$\sum_i b_i g_i = 0 \quad \sum_i b_i g'_i = -1 \tag{5.14}$$

U and V are estimators of A and $A\tau$. Their variance can be written as follow taking into account the auto-correlation of the noise.

$$V(U) = \sum_{i,j} a_i a_j M_{ij} \qquad V(V) = \sum_{i,j} b_i b_j M_{ij} \tag{5.15}$$

M_{ij} are the coefficients of the noise auto-correlation matrix. The OFC are obtained by minimizing the variance of the U and V (assuming 5.13), with the use of the Lagrange multipliers method:

$$a = \frac{(g'.Rg')Rg \ - \ (g.Rg')Rg'}{(g.Rg)(g'.Rg') \ - \ (g.Rg')^2} \quad (R = M^{-1}) \tag{5.16}$$

$$b = \frac{(g.Rg)Rg \ - \ (g.Rg')Rg}{(g.Rg)(g'.Rg') \ - \ (g.Rg')^2} \tag{5.17}$$

The energy deposited in the LAr is then written as:

$$E_{MeV} = C_{ADC \leftrightarrow MeV} \sum_i (s_i - p_i) OFC_i\{a_i, b_i\} \tag{5.18}$$

s_i and p_i being respectively the signal and pedestal amplitude.

5.3.5 Energy Reconstruction

To reconstruct the energy deposited in the LAr gap from the signal samples amplitude s_i measured in ADC counts, correspondence factors are used that translate the electronic chain crossed by the ionization and calibration signals, as illustrated through the following equation:

$$E_{reco} = C_{\mu A \leftrightarrow MeV} . C_{DAC \leftrightarrow \mu A} . \Big(\frac{M_{phys}}{M_{cali}} \Big)^{-1} . \Big[\sum_i (s_i - p_i) OFC_i \{a_i, b_i\} \Big] \tag{5.19}$$

the reconstructed energy relies on the correspondence factors from the electronic chain and on the signal samples amplitude.

- $C_{\mu A \leftrightarrow MeV}$ is the correspondence factor between the current collected by the readout electrode and the energy deposited in the LAr, respectively in μA and MeV.

- $C_{DAC \leftrightarrow \mu A}$ establishes the correspondence between the signal current and the bipolar shaped and sampled signal in ADC counts. It is calculated at the calibration level.

- $\Big(\frac{M_{phys}}{M_{cali}} \Big)^{-1}$ is the correction factor accounting for the different calibration and ionization signal shapes and injection points.

- The last term is the signal amplitude, obtained with the OF procedure, after the pedestal substraction.

5.4 Signal Shape Prediction

The OFC are extracted based on the assumption that the signal shape $S(t)$ is accurately known. In ATLAS two methods are commonly used to predict the physic signal shape. They both use the calibration pulse properties to predict the ionization signal shape and extract the OF coefficients. The calibration signal shape $g^{cali}(t)$ illustrated in Figure 5.11 originates from an exponential current of decay time τ_{cali} that mimics the signal shape S(t) and that is well known (a sample is recorded every 1.04 ns). It is used to correct the cells response and determine the signal shape. It is important to note that the calibration signal is injected outside the cryostat vessel in the Front End crate and is then routed out through the FT toward the detector, following an inductive path, where it joins the ionization signal path. A simplified sketch of the electronic chain is shown in Figure 5.12. The differences between the ionization and calibration signals can however be estimated from the calibration signal itself.

5.4.1 The RTM Method

The *Response fourier Transformation* Method (RTM) [44] is based on the factorization of the readout response. The cell and pulse parameters $\{\tau_{cali}, f_{step}; LC, rC\}$ are extracted from the calibration pulse. The ionization signal shape S(t) ($g^{phys}(t)$ commonly) is written as a function

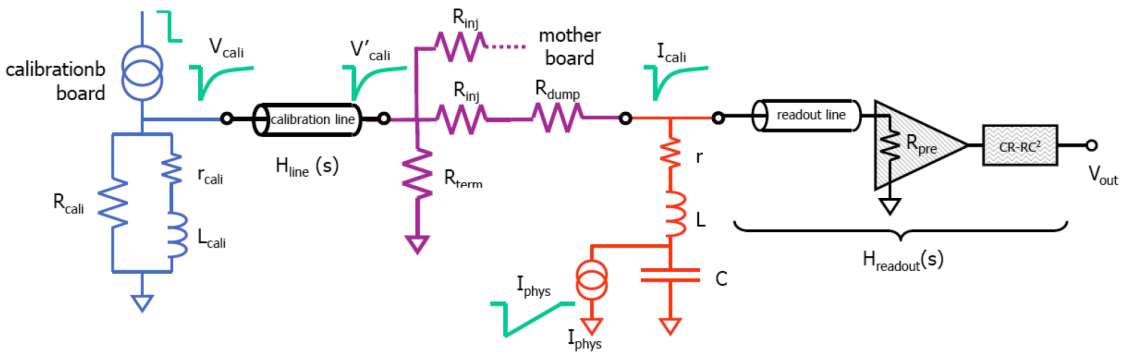

Figure 5.12: Sketch of the electronic chain; the ionization signal is represented by a current I_{phys} following a (r,L,C) circuit; the calibration signal V_{cali} is generated in the calibration board outside the cryostat and routed inside through inductive cables.

of the measured calibration pulse $g^{cali}(t)$:

$$g^{phys}(t) = g^{cali}(t) \otimes \left(\frac{I^{phys}(s)}{I^{cali}(s)}\right) \otimes (g^{CB} \rightarrow g^{det}) \tag{5.20}$$

$$g^{phys}(t) = g^{cali}(t) \otimes L^{-1}\left[\frac{(1+s\tau_{cali})(sT_D - 1 + e^{-sT_D})}{sT_D(f_{step} + s\tau_{cali})}\right] \otimes L^{-1}\left[\frac{1}{1 + s^2LC/srC}\right] \tag{5.21}$$

where $\otimes$ symbolizes a time convolution, L^{-1} the inverse Laplace Transform Operator and s the complex frequency. The first term on the right side of these equations corresponds to the calibration signal pulse, the second term represents the different physic and calibration pulse shapes and the third term reflects the different injection point of the physic and calibration pulses, modeled by a rLC electrical circuit [44]. The prediction of the signal pulse shape uses one additional parameter that is the drift time of ionization electrons in the liquid argon (at the operating temperature of 88.5 K). It is now obtained from measurements of the drift velocity of electrons in the LAr. This method is used in the ATLAS framework, and is applied on both the barrel and the end-caps, to predict the physic pulse shapes and extract the OFC.

5.4.2 The FPM Method

In the *First Principle Method* (FPM) the signal pulse shape is predicted based on an analytical model of the response. It uses the "first principles" of signal propagation through the electronic chain [45].

The amplitude (phase) of the calibration signal is expressed as a product (sum) of terms reflecting the signal propagation through the entire electronic chain. The FT is modeled as a signal propagation cable, defined with its own impedance, skin effect constant, length and speed propagation. They are also decomposed in a sum of direct transmission and back reflection(s) of the signal at the detector transitions. As an example the directly transmitted signal has an

amplitude and phase written as [45]:

$$H_{tot} = H^{FT}_{line}.H^{C}_{line}.H_{cali}.H_{det}.H^{S}_{line}.H^{FT}_{line}.(1 - H_{R1}).H_{trans}.H_{PA}.H_{shp} \quad (5.22)$$

$$\Phi_{tot} = 2\Phi^{FT}_{line} + \Phi^{C}_{line} + \Phi_{cali} + \Phi_{det} + \Phi^{S}_{line} + \Phi_{trans} + \Phi_{PA} + \Phi_{shp} \quad (5.23)$$

The injected calibration signal (H_{cali}) is propagated across the FT (H^{FT}_{line}) and the calibration cable (H^{c}_{line}). It then arrives on the detector (H_{det}) and joins the signal path toward the signal cable (H^{S}_{line}). $(1 - H_{R1})$ represents the fraction of signal passing the FT and H_{trans} is the non reflected fraction that goes to the pre-amplifiers (H_{PA}) and ends on the shaper (H_{shp}). The signal propagation description is expressed in the frequency domain and converted into the time domain using a Fast Fourier transform. In order to drastically limit the number of parameters to be fitted from the pulse shape, a set of direct measurements [46] of the impedance and resonance frequency ($\omega_0 = 1/\sqrt{LC}$) were made for each channel. Measurements on preamplifiers and FT have also allowed for the determination of the propagation speed and skin effect constants of the different cables. Finally the parameters of the calibration signal $\{\tau_{cali}, f_{step}\}$ have been measured during the calibration board production. The time constant of the shaper τ_{sh} and the impedance Z_s of the cold signal cable that propagates the calibration signal inside the detector are the only parameters estimated with FPM by predicting the calibration pulse shape accounting for its electronic pattern. The maximum of amplitude and the timing of the calibration pulse are also let free in the prediction. This notably allows to absorb residual effects that would not be taken into account in the analytical model.

The global amplitude and phase in the method (as described in reference [45]) account for the first and second signal reflection at the signal cable-feedthrough and feedthrough-preamplifier transition. Figure 5.13 illustrates the typical shapes of the direct and reflection components of the calibration signal. The dark blue curve corresponds to the total signal. It sums the directly transmitted signal component (light blue) and the one and two times reflected signal parts (respectively in pink and yellow). Differences between the total and direct signal arise as they cross different electronic paths.

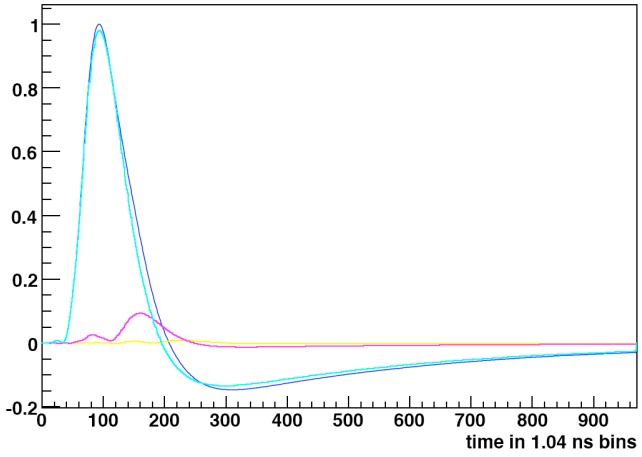

Figure 5.13: Typical calibration signal shape. The direct, first reflection and two reflections components of the signal are illustrated.

In a similar way, the physic pulse amplitude and phase (direct part) are expressed by terms

reflecting its electronic path:

$$H_{tot}^{phys} = H_{phys}.H_{det}.H_{line}^{S}.H_{line}^{FT}.(1 - H_{R1}).H_{trans}.H_{PA}.H_{shp} \quad (5.24)$$

$$\Phi_{tot}^{phys} = \Phi_{line}^{FT} + \Phi_{phys} + \Phi_{det} + \Phi_{line}^{S} + \Phi_{trans} + \Phi_{PA} + \Phi_{shp} \quad (5.25)$$

These expressions are different with respect to the calibration pulse case, as a consequence of their different path through the electronic chain. The τ_{sh} and Z_s parameters extracted from the fit procedure on the calibration pulse are used to predict the signal shape.

As the physic and calibration signals are injected at different points of the electronic chain, the bias in $DAC \leftrightarrow \mu A$ coefficient must be accounted for. This correction is obtained by measuring the amplitude difference observed in calibration and signal pulse for the same initial current. The ratio (M_{phys}/M_{cali}) is extracted for each channel of the different layers of the calorimeter. Figure 5.15 illustrates the ratio measured in FT 21 A (positive z) for the four slots (for each half-barrel and electrode type) of the Middle barrel layer. The red points correspond to the

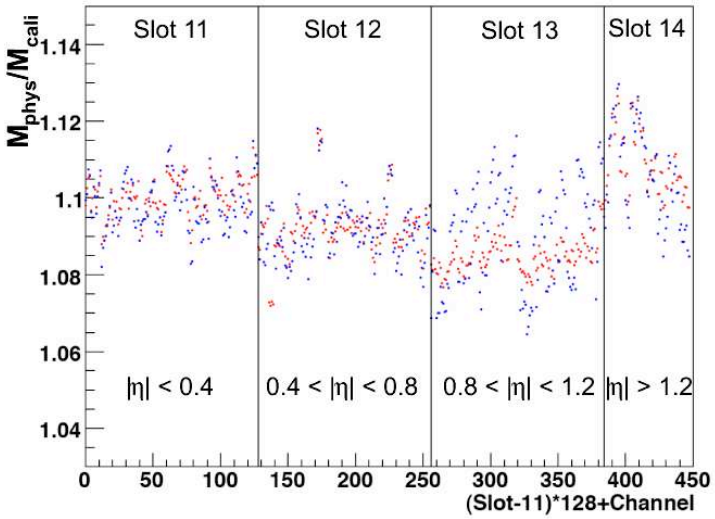

Figure 5.14: M_{phys}/M_{cali} ratio as a function of the channel number, or indirectly the η index of the cells, for the Middle barrel (FT 21 A, $\eta > 0$).

ratio extracted from the FPM method while the black points are the ratio extracted from the RTM method. A slight increase of the ratio is observed with η and discontinuities appear at the transition regions. The two methods agree well; maximal differences of 1.5% appear at large η.

As illustrated in Figure 5.13 the first and second reflexion of the signal significantly contribute to the total signal shape. The cross-talk between neighboring cells also causes deformations of the calibration and physic shape. The different types of cross-talk (resistive, capacitive, inductive or mixed) have been measured during the test beam period [39] in and between the different layers of the EM barrel, as summarized in Table 5.1. The values represent the relative peak-to-peak value. The leading measured cross-talk is a capacitive cross-talk between neighbor cells in the Front layer and it is corrected for in the signal pulse prediction. In other cases, the cross-talk is neglected, its implementation into the calibration signal fit procedure bringing

Layers	Front	Middle	Back
Front	$6.9\%^{2}$	$0.07-0.09\%^{1}$	$0.04\%^{4}$
Middle	$0.07-0.09\%^{1}$	$1.5\%^{2+3}$	$0.5-0.7\%^{3+2}$
Back	$0.04\%^{4}$	$0.5\%^{3+2}$	$1.9\%^{3}$

Table 5.1: Summary of the cross-talks measured in the different layers of the EM barrel. The indexes 1,2,3 and 4 correspond respectively to resistive, capacitive, inductive and mixed cross-talk.

too many additional free parameters.

Both the RTM and the FPM methods uses the calibration pulse properties to predict the ionization signal shape and extract the OF coefficients. The RTM method is based on the factorization of the readout response while the FPM method is based on the analytical model of the response. The only critical parameter that cannot be estimated directly from the calibration pulse and relies on the design of the detector is the drift time of ionization electrons in the calorimeter gaps. In physical mode, only five samples of the ionization signal are recorded, centered around the maximum of amplitude of the pulse. The signal pulse shape in this range of time depends slightly on the drift time. In special cosmic runs, 32 samples are collected that cover the full ionization pulse. In that case the signal shape depends on the drift time. It is possible to predict the 32 samples pulse shape and extract the drift time in each cell of the calorimeter with both the RTM and FPM methods (only for the barrel part in the case of the prediction with FPM). The measurement of the drift time is a very interesting task as it provides an estimate of the gap variation and its impact on the calorimeter intrinsic uniformity. This was already measured during the construction of the modules and used during the test beams to derive the uniformity of the calorimeter, as presented below. The scope of the first part of this thesis is the study of the drift time as measured directly on physics pulses taken in cosmic data.

5.4.3 Test Beam

In summer 2004, when the barrel and end-cap modules of the EM calorimeter of ATLAS were being constructed, a large campaign of beam tests in the H8 and H6 lines of the SpS in the north area of CERN was carried out. Four modules of the barrel and three modules of the end-cap of the EM calorimeter were exposed to the beam. The complete energy reconstruction scheme has been estimated in MC simulations and verified. The uniformity of the calorimeter response in energy has been measured and all contributions to the constant term estimated. (The performances of the modules under magnetic field and with material in front of have also been tested [39].)

The four barrel modules were exposed to 245 GeV electron beams in the H8 line and the three end-cap modules were exposed to 120 GeV electron beams in the H6 line of the SpS. They have all been assembled in the ATLAS EM barrel and end-cap. To change the eta direction of the electrons with respect to the absorbers, the modules were rotated. Chambers were located in front of the virtual interaction point in the beam line to measure the electrons trajectory. Scintillator triggers with 300 ps precision were used to accurately estimate the time interval

between the time trigger and the 40 MHz time sampling.

A brief summary of the main contributions to the constant term is presented in the following [39].

- The non uniformity of the the readout electronic was measured by permuting two neighbor middle cell FEBs in one module and found to be 0.1%. The non uniformity of the summing boards was also measured, as well as the precision of the calibration system, and found to be $\sim 0.23\%$ overall. The ratio of the physic to calibration amplitude M_{phys}/M_{cali} has been measured in the different modules. The variation of the ratio with η is displayed in Figure 5.15(a) for the Front and Middle layers.

- The complete energy reconstruction scheme was verified with data and MC. The signal has been reconstructed with two different methods and the RMS of the average energy difference found to be 0.25%. MC inaccuracies obtained by the difference in the measured energy between data and MC amount to 0.08%.

- The stability in time was measured by looking at the energy reconstruction variation at different time in a period of about one month and found to be below 0.16% in the barrel modules.

- The intrinsic uniformity of the calorimeter was measured during the assembly of the modules and used in test beam to assess the global constant term. It comprises of the variations of the LAr gap and lead plate thickness. The gap variation was estimated by measuring the gap capacitance dispersion in sectors of size $\Delta\eta = 0.2$ (corresponding to eight cells in the Middle layer). In average a gap variation of 0.16% was found. The dispersion of the absorbers thickness has been measured with an ultra sound system in a $5 \times 5\ cm^2$ granularity map and found to not exceed 0.3%, leading to a dispersion of the lead thickness of 0.18%.

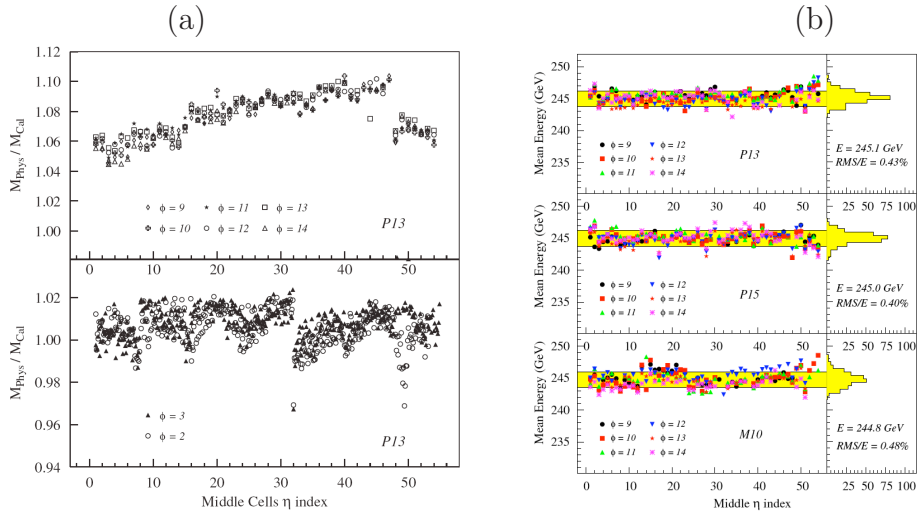

Figure 5.15: (a): M_{phys}/M_{cali} ratio as a function of the η index of the cells for the modules exposed to the test beam, for the Middle compartments on the top and the strips on the bottom. (b): Average reconstructed energy as a function of the η cell index. The RMS of the dispersion is quoted on the right. A dispersion better than 0.5% has been found in the three modules.

The different contributions to the non uniformity of the calorimeter response lead to a local constant term between 0.25% and 0.36% as obtained for the different tested barrel modules. Combined with the non uniformity in energy, as shown in Figure 5.15(b) for the different exposed barrel modules, this provides a global constant term better than 0.6% in average. This result is very important as it confirms that the constant term is below 0.7% expected from the calorimeter design and needed to accurately reconstruct the γ/e^- energy and therefore provide an excellent resolution on the invariant mass of the diphoton system in the $H \to \gamma\gamma$ analysis.

Chapter 6

Study of the Intrinsic Calorimeter Uniformity using the Drift Time Measurement in Cosmic Data

6.1 Motivations

An excellent energy resolution of the photon clusters in the EM calorimeter of ATLAS is essential for a precise reconstruction of the diphoton invariant mass in the $H \rightarrow \gamma\gamma$ channel. Non uniformities in the calorimeter impact the constant term of the energy resolution. Different studies have been done to verify that contributions to the non-uniformity of the calorimeter remind small enough to ensure a constant term below 0.7%, that is expected from the calorimeter design. The calorimeter uniformity has been measured during test beams [39] on barrel and end-cap modules that have been used since for the calorimeter construction. The test beams have assessed the performance of the complete energy reconstruction scheme in the calorimeter. A non uniformity of 0.5% was found for a global constant term c of 0.6% on the energy resolution, in good agreement with expectations [36]. A motivation of this work is to use the cosmic muons data to measure the barrel calorimeter uniformity in the drift time of electrons in the LAr and derive its impact on the intrinsic calorimeter response.

The EM calorimeter construction was completed in the ATLAS cavern at the end of 2006. Cosmic data runs have been taken since this period to commission the associated electronics ($\sim 173k$ channels) and the calibration procedure. Between the end of summer and autumn of 2008, when the calorimeter was fully operational, stable cosmic muons data runs were taken. In particular, runs with 32 samples in the calorimeter were taken (the nominal number of samples is 5), corresponding to the full sampling of the ionization signal. In this work, the signal pulse shape of cosmic data is predicted using the First Principle Method (FPM) [45] and the drift time is extracted from the signal shape prediction.

6.2 The Signal Pulse Prediction

The physics pulse shape is predicted using the FPM method based on first principles of signal propagation, taking into account the entire chain of electronics as seen by the ionization signal. Direct measurements of the different path lengths, impedances, skin effect parameters of cables

and feedthroughs, transfer functions of the shapers and preamplifiers are used as inputs of this method. Only two parameters are extracted in advance cell-by-cell (as described in [45]): the time constant of the shaper τ_{sh} and the impedance of the cold signal cable Z_s. Typically values are $\tau_{sh} \sim 15\ ns$ and $Z_s \sim 25\ \Omega$. These model parameters are extracted from generated electronics calibration pulses and are then used to predict the physics pulse shape. The drift time and shift of the electrode are extracted from this prediction.

The ionization signal in the LAr is parametrized by two triangular signals. Because the calorimeter geometry is such that the electrode is facing two gaps and collects charge from each side, the main triangle corresponds to the normal drift behavior of the cell in its straight sections and is made of the sum of two triangles representing the electrons drift to each outer layer of the electrode. In the bent sections of the accordion electrode, the gap size is no more constant (larger in average) and the electrical field reduced with respect to the straight sections (the picture of the field lines is also more complicated). The ionization current collected in the bent sections is modeled by a smaller triangle with a longer time constant, also made of the sum of two triangles.

In the straight section of the LAr EM barrel, the ionization current is defined by a fast rise ($t < 1$ ns) corresponding to drift time of the initial ionization electrons toward the electrode, followed by a linear decay of duration T_D and amplitude I_0 given by:

$$T_D = \frac{g}{V_D} \quad I_0 = \rho.V_D \tag{6.1}$$

where g is the LAr gap size and ρ the charge density along the perpendicular to the electrode. T_D and V_D are respectively the drift time and velocity of the ionization electrons. ρ relies on the lead absorbers thickness which dispersion in the barrel has been estimated to bring a contribution to the constant term of 0.19%. Since I_0 is the measured current, the contribution to the intrinsic calorimeter uniformity comes from the drift velocity V_D.

The electrical field in the LAr gap is empirically given by the relation $E = HV/g$, which corresponds for a nominal high voltage at 2000 V to $E \approx 2000/2.1 \approx 10\ kV.cm^{-1}$. The drift velocity of the electrons varies with the magnitude of the electrical field at the power α as:

$$V_D = V_D^0\Big(\frac{E}{E_0}\Big)^{\alpha} = V_D^0\Big(\frac{H}{H_0}.\frac{g_0}{g}\Big)^{\alpha} \tag{6.2}$$

V_D^0 is the drift velocity given for a reference electrical field $E_0 = HV_0/g_0$. The empirical exponent coefficient $\alpha = 0.3$ is tuned to yield the most accurate dependence of the drift time with the high voltage as described in section 6.10, where the question of the drift time dependence on HV is investigated.

The signal T_D and amplitude dependence on the gap are then:

$$T_D = \frac{g}{V_D} = Kg^{1.3} \qquad \Big[K = \frac{T_D^0}{g_0^{1.3}}\Big(\frac{HV}{HV_0}\Big)^{-0.3}\Big] \tag{6.3}$$

$$I = \rho.V_D = Bg^{-0.3} \qquad \Big[B = \rho V_D^0\Big(\frac{HV}{HV_0}\Big)^{0.3} g_0^{0.3}\Big] \tag{6.4}$$

illustrating that the drift time is about four times more sensitive to the gap variation than the current amplitude is. The measurement of T_D is therefore a powerful tool to assess the intrinsic uniformity of the calorimeter.

Figure 6.1 displays a typical pulse and the prediction of its shape using the FPM method. The 32 samples signal covers approximatively 800 ns from the rising edge to the end of the pulse. The maximum of amplitude of the pulse relies on the deposited energy by ionization of

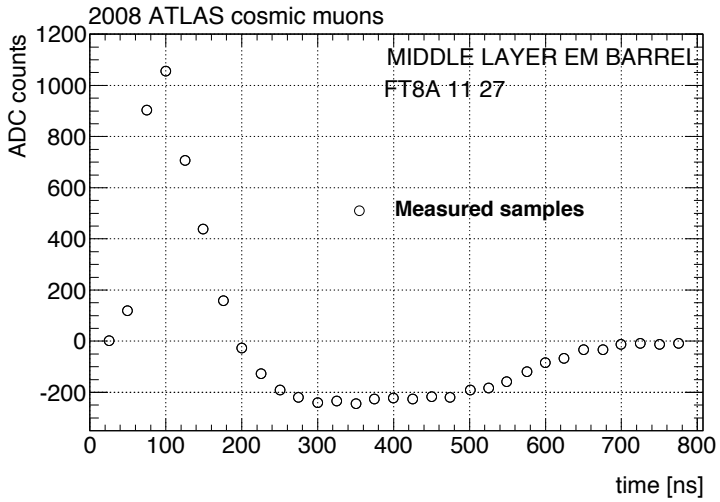

Figure 6.1: Typical 32 samples cosmic muon pulse in the Middle barrel of the EM calorimeter of ATLAS.

the liquid argon. The length of the plateau from the peak position to the beginning of the rise of the pulse corresponds approximatively to the drift time of electrons in the LAr.

LAr-lead absorbers in the ATLAS EM calorimeter are supplemented with the use of stainless-steel 0.2 mm thickness layers glued on each side of the lead plate. Honeycomb is used to keep the electrodes properly spaced in the gap. However, due to mechanical constraints when assembling the modules of the barrel, deformations of the barrel structure under gravity [47], the electrode can move around its centered position changing the relative gaps between two lead plates. When the electrode is mis-centered, the drift time varies on both sides of the electrode inducing two signals with different amplitudes and plateau lengths.

In most of the sectors of the barrel, the high voltage applied on both sides of the electrode was nominal, HV = 2000 V, when the cosmic data were recorded. In some Front End Boards (one FEB corresponding to 0.2×0.2 regions in the (η, ϕ) plane), only one side was at 2000 V and the other side at a lower voltage. In two FEBs also, the high voltage was reduced at 1600 V on both sides. The drift time of the electrons varies with the voltage. When the voltage is asymmetric the two signals have different drift time. The slope of the rise is changed as if the electrode was mis-centered, approximatively modeled by a step corresponding to the sum of the two signal shape having different plateau lengths.

In the straight sections, the two triangles can be described by a drift time TD_i and a current I_i:

$$TD_1 = TD_{2000}\ (1-x)^{1+\alpha}\ (HV_1/2000)^{-\alpha} \quad I_1 = \frac{I_{2000}}{2}\ (1-x)^{-\alpha}\ (HV_1/2000)^{\alpha} \tag{6.5}$$

$$TD_2 = TD_{2000}\ (1+x)^{1+\alpha}\ (HV_2/2000)^{-\alpha} \quad I_2 = \frac{I_{2000}}{2}\ (1+x)^{-\alpha}\ (HV_2/2000)^{\alpha} \tag{6.6}$$

where TD_{2000} and I_{2000} are respectively the drift time value and the collected current at nominal high voltage (2000 V). The difference between the two gaps is modeled in terms of a shift of

the electrode with respect to its nominal central position, which is measured by the relative mis-centering of the electrode $g(1 \pm x)$ compared to the gap g. Figure 6.2 illustrates the form

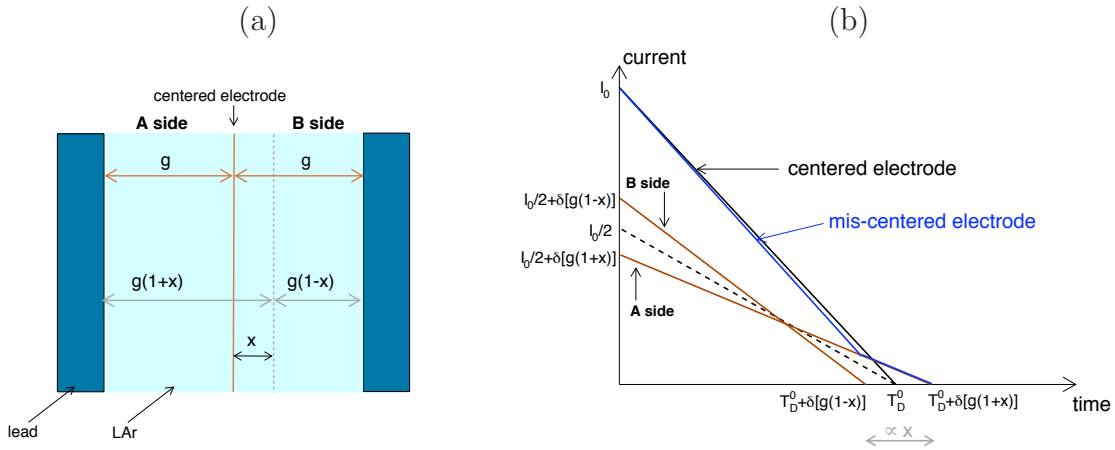

Figure 6.2: (a): Schematic view of the electrode shift (in the straight section) in LAr gap. The gaps are of size $g(1-x)$ and $g(1+x)$, x corresponding to the relative shift of the electrode with respect to its centered position. (b): The current collected by the electrode as a function of time is shown in the case of a centered electrode and when the electrode is shifted, as illustrated in (a).

of the signal current when superposing the triangles from the two straight sections in the cases of a centered or mis-centered LAr-electrode device.

The same dependence on high voltage occurs for the two triangles related to the bent sections that can be parametrized by:

$$TD_3 = TD_{bent}\ (HV_1/2000)^{-\alpha}\ , \qquad I_3 = \frac{I_{bent}}{2}\ (HV_1/2000)^{\alpha}, \tag{6.7}$$

$$TD_4 = TD_{bent}\ (HV_2/2000)^{-\alpha}\ , \qquad I_4 = \frac{I_{bent}}{2}\ (HV_2/2000)^{\alpha}. \tag{6.8}$$

The TD_{bent} and I_{bent} contributions per layer are estimated using the GEANT4 simulation of a uniform charge density in the gap. These values are given in Table 6.1 for the Front, Middle and Back compartments (there are no bent sections in the Presampler)[1)]. The increasing contribution and time associated to the bents from the Front to the Back compartment correspond to the increase in bending angle across the calorimeter.

The fit model used with the FPM method to predict the physics pulse shape is parametrized by:

1. The drift time $T_D = TD_{2000}$ (in ns). If the drift times and amplitudes dependence on the electrode shift and on the high voltage derived in Equations 6.5 is correct, the extracted parameter TD_{2000} should be similar at nominal or lower voltage. The contribution and drift time for the bent sections are fixed to the values given in Table 6.1.

[1)] The normalization is such that $I_{bent} + I_{2000} = 1$).

Layer	TD_{bent} (ns)	I_{bent} (%)
Presampler	-	-
Front	820.	4.9
Middle	898.	7.1
Back	941.	8.5

Table 6.1: TD_{bent} and I_{bent} values for the Presampler and the different barrel compartments.

2. The associated shift of the electrode $SH = x \times 2000$, corresponding to the relative gap shift times the gap size, in microns [2)]; this parameter is in fact only sensitive to the absolute value of x when the high voltage is the same on both sides of electrodes.

3. A global normalization factor A to go from prediction to data.

4. A global timing adjustment ΔT (in ns).

The cosmic data pulses are fitted with this model using the MINUIT package [48]. The result of the fit on a typical pulse in the Middle is displayed in Figure 6.3.

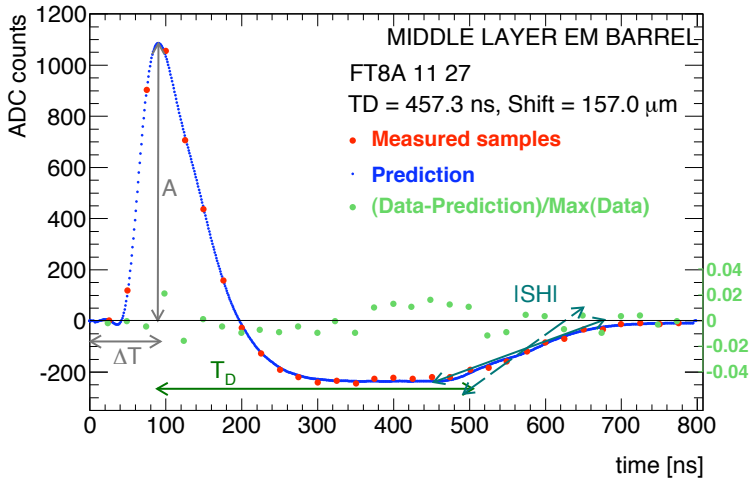

Figure 6.3: Typical pulse in the Middle where the data samples (red points), the prediction (blue points) and the difference $3 \times (data - prediction)$ (green points) are illustrated.

6.3 Event and Pulse Selection

6.3.1 Cosmic Data and Trigger Selection

During the period between end of summer and autumn of 2008 specific cosmic data runs have been taken with 32 samples signal pulses, which is necessary to cover the full signal range in

[2)] The gap size used herein is an approximation of the nominal gap size of 2090 μm. None of the conclusions of this chapter are affected by this approximation. However, for a more accurate estimate of the shift, a 4.5% correction should be applied.

time and extract the drift time in the cells of the EM barrel calorimeter of ATLAS. The events were first triggered and then processed through $L1Calo$ and $L1CaloEM$ streams. The $L1Calo$ ($L1CaloEM$) refers to general (EM) calorimeter trigger and reads the energy deposit in regions of size (0.1,0.1) in the (η, ϕ) plan. The present analysis is based on *Event Summary Data* format files. As the energy deposited by cosmic muons is typically below 20 GeV, the trigger threshold was adapted and almost all statistics in cosmic runs correspond to pulses recorded in high gain. An energy threshold of at 1 GeV on the deposited energy in the LAr is performed to minimize the effect of noise fluctuation on the signal pulse shape. This corresponds to much larger energy than what lost by a minimum ionizing particle. The signal pulses therefore mainly comes from EM shower induced by a photon. The low probability of Bremsstrahlung photon emission by a muon is compensated by the large available statistics.

6.3.2 Data Quality

A lower cut on pulse amplitude maximum ADC counts is applied to select pulses corresponding to an energy deposited in the barrel cells above the threshold. The lower threshold values in ADC counts and the correspondence factor from ADC to MeV (high gain) are given per layer in Table 6.2. Only the pulses recorded in high gain are considered in this analysis as calibration

Layer	Cut value	RMS of the pedestal	$F_{ADC \to MeV}$
Presampler	200 ADC	$\sim$ 8 ADC	$\sim$ 7.0
Front	500 ADC	$\sim$ 8 ADC	$\sim$ 2.5
Middle ($\lvert\eta\rvert \leq 0.8$)	160 ADC	$\sim$ 5 ADC	$\sim$ 10.0
Middle ($\lvert\eta\rvert > 0.8$)	100 ADC	$\sim$ 3.5 ADC	$\sim$ 17.0
Back	160 ADC	$\sim$ 5 ADC	$\sim$ 7.0

Table 6.2: Minimal values for the amplitude maximum of the pulse and RMS of the pedestal, for the Presampler and the three compartments of the barrel calorimeter. The approximated conversion factor $F_{ADC \to MeV}$ from ADC to MeV is also given.

parameters were only available for the high gain.

The low amplitude pulse samples are more sensitive to noise and may fluctuate too much to provide a fit convergence. The lower cut on the pulse amplitude maximum threshold limit the number of fit failures. High amplitude pulse may saturate if the appropriate gain is not applied. Finally there is a fraction of pulses having a non reliable shape. In order to only select cosmic pulses with reliable shapes quality cuts are applied on the pulse shape, as illustrated in Figure 6.4.

1. The bipolar shape of the signal pulse implies a negative undershoot. This is ensured by requiring that at least five samples arising after the sample associated to the amplitude maximum $S_{max}(t_{max})$ of the pulse have a negative amplitude ($S_i - pedestal < 0\ ADC$).

2. The plateau length of the pulse relies on the drift time parameter which corresponds to approximatively a time duration of $450 - 500\ ns$. To prevent pulses with too fast rise (for instance pulses largely affected by cross-talk), it is required that at most 12 samples with time $t(i) > t_{max} + 5$ are near 0, $S_i - S_{max} > -0.1$.

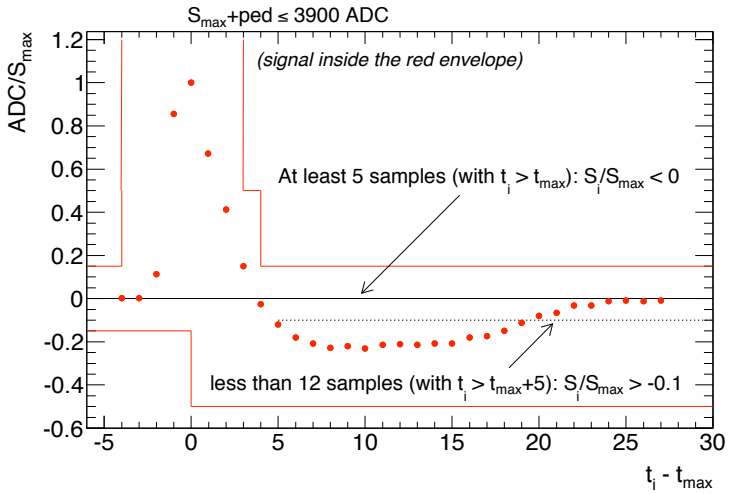

Figure 6.4: Illustration of the quality cuts applied to the pulses shape. The pulse is normalized in amplitude and the time associated to the sample of amplitude maximum t_{max} is set to 0.

An additional (upper) cut on the most energetic sample of the data pulse, namely S_{max} is applied. The difference of thresholds between Electrode A ($|\eta| \leq 0.8$) and Electrode B ($|\eta| > 0.8$) in the Middle is explained by the difference of pedestal RMS ($5/3.5 \approx 1.6$)related to the difference in gain. In the following, the variable A_{max} corresponding to the normalized amplitude corrected for this gain factor, will often be used:

- In the Middle electrode A ($|\eta| \leq 0.8$) $A_{max} = 1.6 * S_{max}$
- $A_{max} = S_{max}$ everywhere else

The cut $A_{max} + pedestal \leq 3900$ ADC counts is applied on the sample of maximum amplitude, to avoid saturated pulses. The *pedestal* value is about 1000 ADC counts. As shown in Figure 6.4 the pulse samples must be contained inside the region delimited by the blue lines. It is required to have at least 5 samples with a time t_i (for the sample i) greater than the time associated to the amplitude maximum sample t_{max} below 0 ADC, ensuring that there is a negative undershoot in the pulse shape. The pulse is also required to have less than 12 samples with $t_i > t_{max} + 5$ above -0.1 ADC/S_{max}, to avoid pulses with too fast rise (as can be the case with cross talk, for instance).

These data quality cuts on the cosmic pulses mildly ensure that the pulse has a well behaved shape.

The number of pulses (N) passing the data quality criteria are shown in Table 6.3. Figure 6.5 illustrates the distributions of the number of pulses per cell in the (η,ϕ) plane when both sides of the electrode are at nominal voltage (2000 V). The unfilled zones correspond to:

- areas of the calorimeter where the high voltage is not nominal on at least one side of the electrodes (in this case, these zones are filled in Figure 6.6)
- areas where no data has been recorded for $[(\eta_1;\eta_2),(\phi_1;\phi_2)]$
  - in the Middle:

Layer	N[HV = 2000 V]	N[HV < 2000 V]
Presampler	20599	204
Front	42692	2165
Middle	330828	19664
Back	79228	5332

Table 6.3: Number of pulses in the Presampler and different layers of the barrel calorimeter after applying the data quality cuts, in the cases of nominal high voltage and lower voltage configuration.

- $[(-1.2; -0.8), (-\pi + 2\pi/16; -\pi + \pi/16)]$ and
- $[(1.2; 1.4), (-\pi + 6\pi/16; -\pi + 5\pi/16)]$,

- and in the Front:

- $[(-1.2; -1), (-\pi + 4\pi/16; -\pi + 5\pi/16)]$,
- $[(0.4; 0.6), (-\pi + 28\pi/16; -\pi + 29\pi/16)]$ and
- $[(1; 1.2), (-\pi + 2\pi/16; -\pi + 3\pi/16)]$.

Given that in the calorimeter the HV is fed from the Back, the areas with non nominal HV are the same in Front, Middle and Back. It should be noted that in the Presampler, the line of alternatively unfilled areas at negative η and ϕ values between 0.4 and 0.6, correspond to the odd channels of one FEB which are noisy and are thus masked. Figure 6.7(a) and (b) show the high voltage mapping in the (η, ϕ) plane for the Presampler and the barrel calorimeter respectively. The red regions correspond to nominal voltage on both sides of the electrode while the colored scale reflects the high voltage applied on one side of the electrode when the other side is at the nominal voltage. The two black boxes in the mapping of the calorimeter correspond to the special case where both sides are at HV = 1600 V.
In the following sections, results on pulses are presented for the nominal case (HV=2000V on both sides of the electrode), except when explicitly mentioned (section 6.10).

Nomenclature Each cell in the Presampler and EM barrel is defined by an unique set of parameters, typically:

$$cell_i = \{FeedThrough, BarAC, Slot, Channel, \eta, \phi\}$$

The cell location is given by its coordinates (η, ϕ), $BarAC$ indicates the concerned half-barrel (It is chosen to be 1 in negative side in z, and 0 in the positive side). The signal is routed out through a given channel to a specific FT located radially (in ϕ). Finally, the slot number indicates the layer and η range to which the cell belongs: Table 6.4 summarizes the main parameters in the four layers.

6.3.3 Fit Quality

In order to get a data sample with well predicted pulses and estimate the efficiency of the fit procedure, a selection is performed based on requirements on the fit precision and description

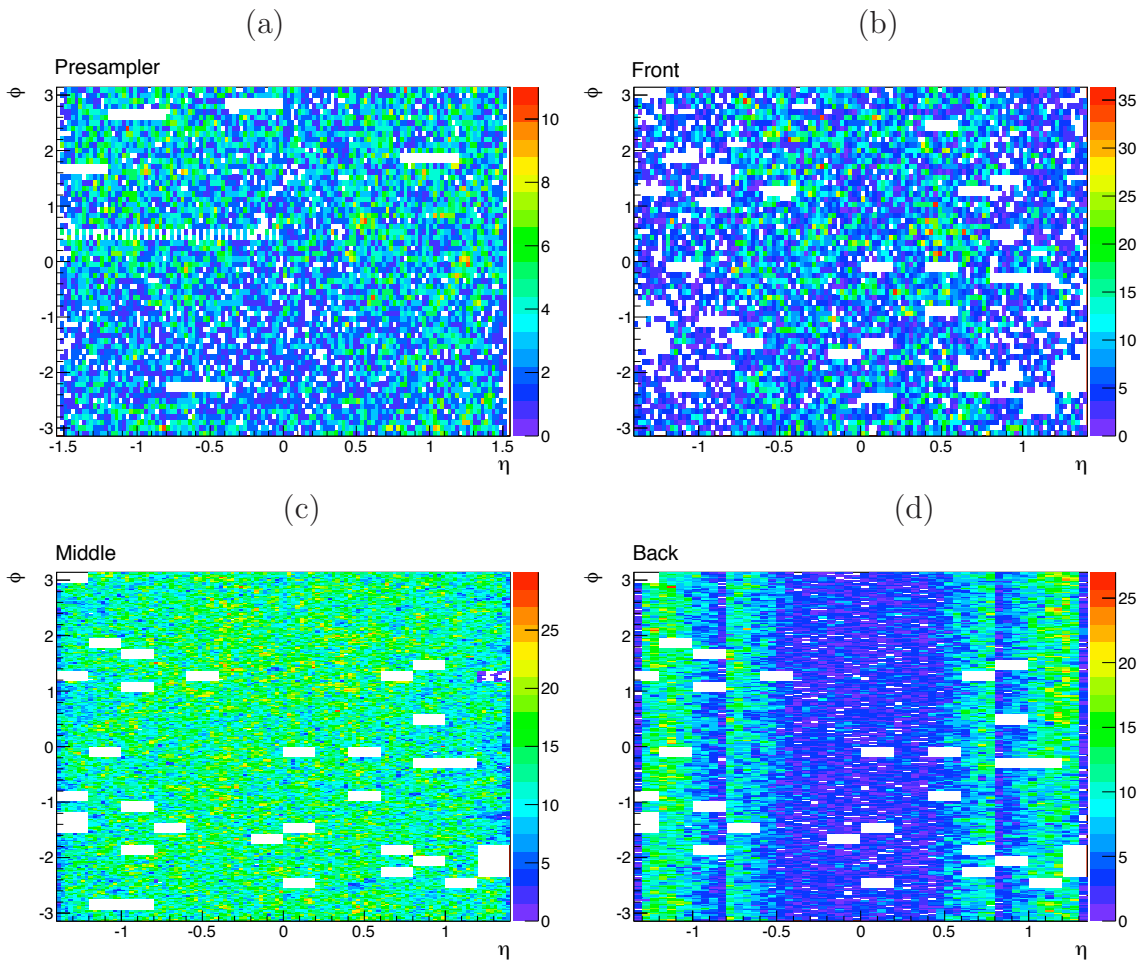

Figure 6.5: Coverage at nominal voltage, in: (a) Presampler, (b) Front, (c) Middle and (d) Back.

Layer	FT	Slot	# channels	η
Presampler	0-32	1	122	$\|\eta\| < 1.55$
Front	0-32	2-8	128	$\|\eta\| < 1.4$
Middle	0-32	11-14	128 (64 in Slot 14)	$\|\eta\| < 1.4$
Back	0-32	9-10	128 -88	$\|\eta\| < 1.35$

Table 6.4: Slot numbers, numbers of channels and η range of the different barrel layers.

of the drift time and shift parameters.

χ^2 of the fit:
The fit performed on data pulses using the FPM method is defined by its χ^2 computed from the amplitude difference between the measured pulse samples $meas(i)$ and the predicted samples

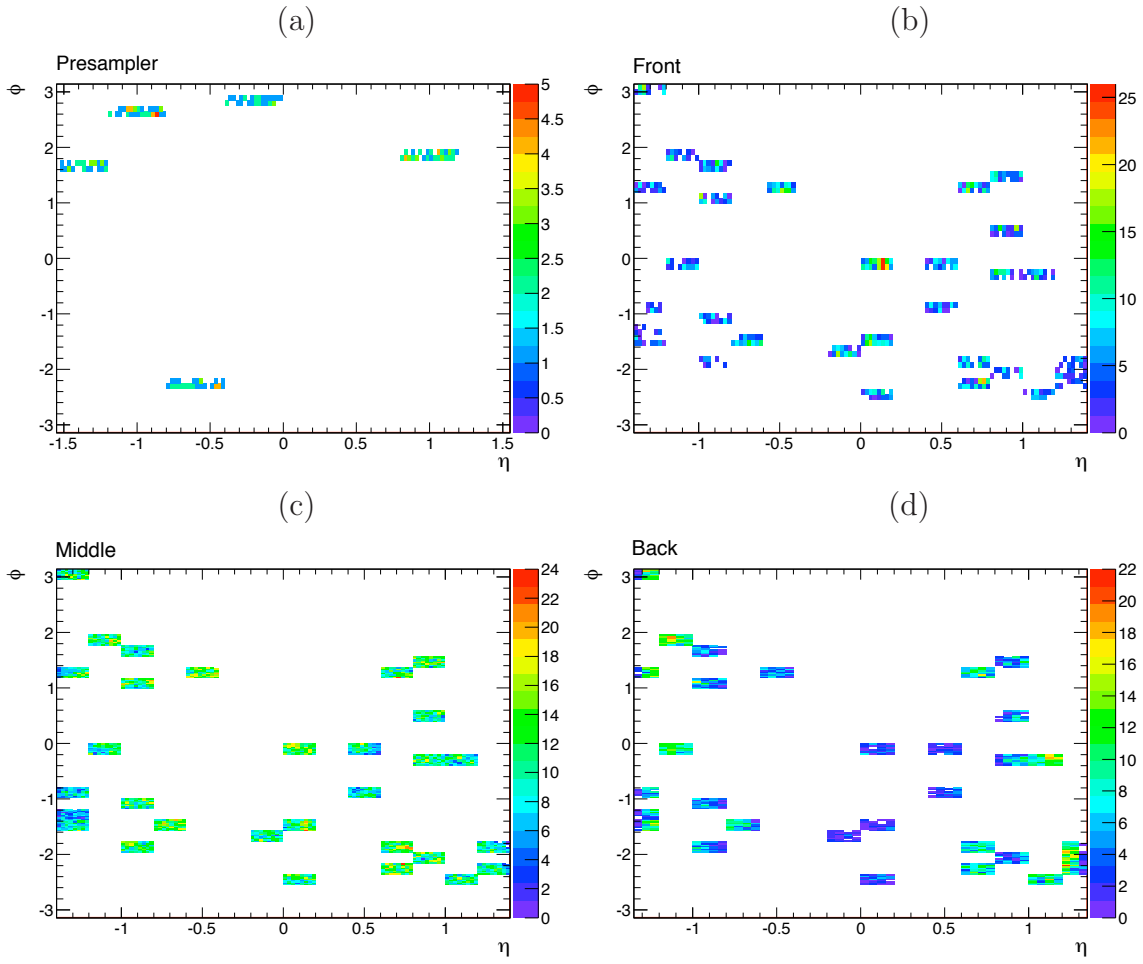

Figure 6.6: Coverage for the the reduced voltage case, in: (a) Presampler, (b) Front, (c) Middle and (d) Back.

$pred(i)$:

$$\chi^2 = \frac{1}{32 - N_{param}} \sum_{i=1}^{32} \frac{(meas(i) - pred(i))^2}{\sigma^2}, \tag{6.9}$$

where $N_{param} = 4$ is the number of free parameters in the fit and σ is the noise term (taken as the RMS of the measured energy in pedestal runs, see Table 6.2). Figure 6.8(a) illustrates the dependence of the χ^2 as a function of the (normalized) maximum amplitude A_{max}. Large signals typically display large χ^2 values. This correlation highlights the systematic limitation of the fit model as it is less adequate for more statistically precise data. In the numerator of equation 6.9, the relative difference between the measured and the predicted samples is proportional to the measured (or similarly the predicted) maximum amplitude, while on the denominator the noise taken as the RMS of the pedestal is independent on the pulse amplitude. To take into account the precision of the model, a normalized χ^2, similar to the one proposed in [49], is considered.

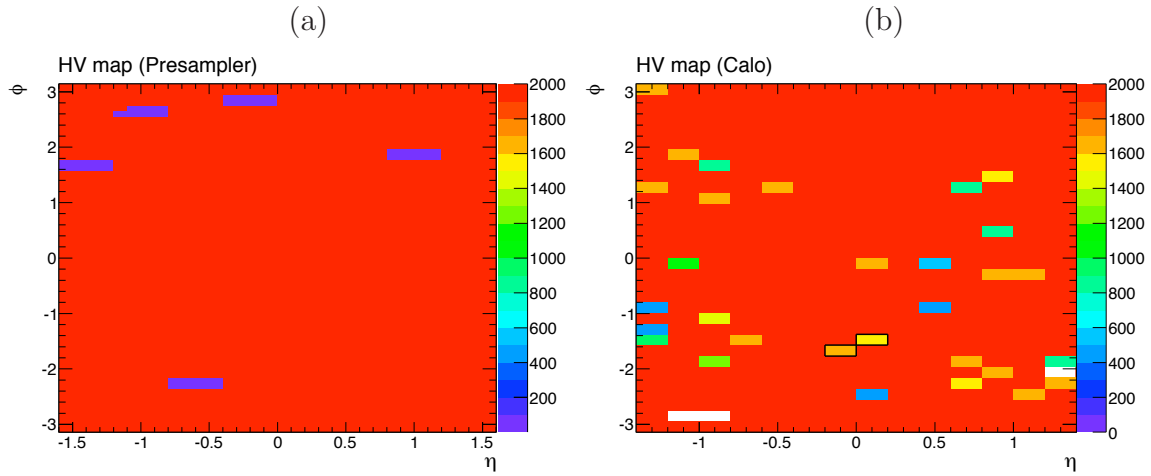

Figure 6.7: HV map in (η,ϕ) for (a) the Presampler and (b) the Calorimeter. Black boxes in b) indicate the region where the HV is reduced on both sides of the electrode, otherwise the second side is always at nominal voltage.

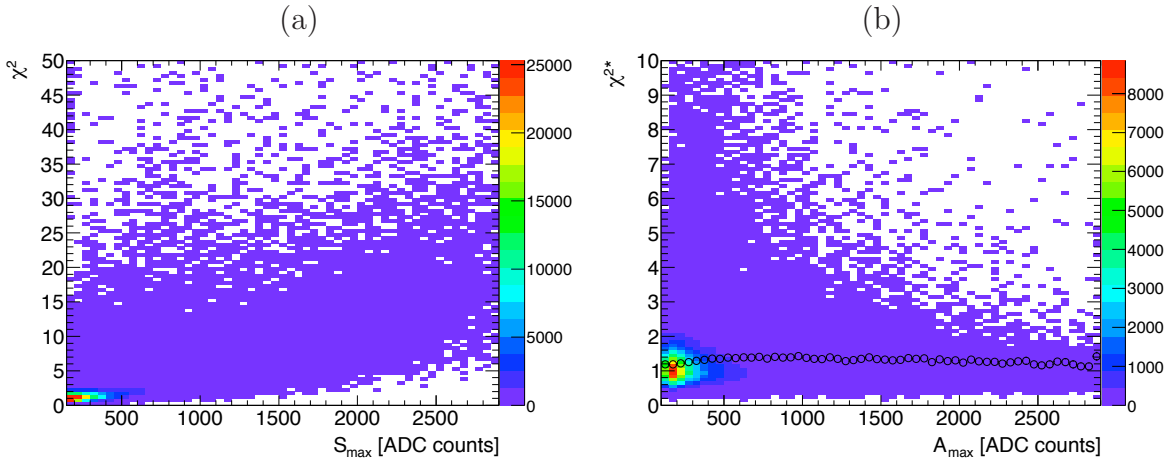

Figure 6.8: (a): Distribution of the fit χ^2 as a function of A_{max}. (b): Distribution of χ^{2*} as a function of S_{max}, both in the Middle.

The normalized χ^2, called χ^{2*} in the following, is defined as:

$$\chi^{2*} = \frac{1}{28}\sum_{i=1}^{32}\frac{(meas(i) - pred(i))^2}{\sigma^2 + (k * S_{max})^2} \tag{6.10}$$

where k represents the relative precision of the prediction. The denominator is replaced by the quadratic sum of the noise and the maximum amplitude of the pulse times the factor k. Figure 6.8 represents the distribution of the χ^{2*} variable in the Middle compartment as a function of the maximum amplitude of the pulses (S_{max}). The profile is relatively flat as expected, reflecting the remaining dependence on the pulse amplitude to the fit precision. As there is no strong reason for the model to have exactly the same precision in each layer of the calorimeter, and similarly to what was done in [49], different k values are estimated for each compartment. The various values of k are obtained by a fit to the χ^2 distribution as a function of A_{max}. The

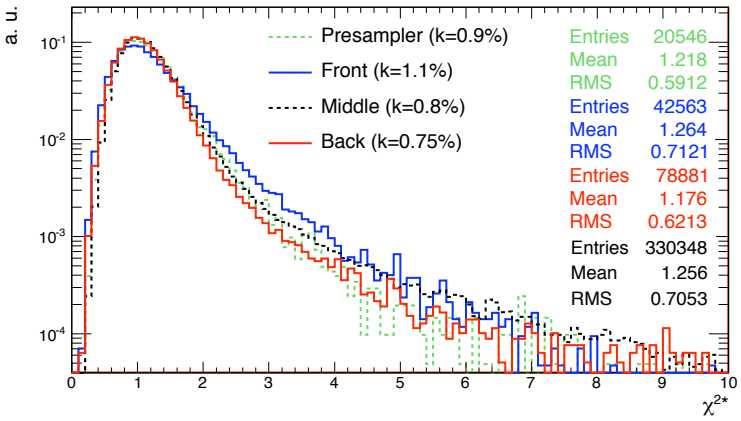

Figure 6.9: χ^{2*} distribution for the Presampler and the 3 layers: in green for the Presampler, in blue for the Front, in black for the Middle and in red for the Back.

values obtained are 0.9%, 1.1%, 0.8% and 0.75% for the Presampler, Front, Middle and Back compartments respectively. The distribution of χ^{2*} for the 4 layers is shown Figure 6.9.

Precision on the drift time and shift parameters

The χ^{2*} variable accounts for the relative difference in amplitude between all predicted and measured samples of the pulse. The four parameters of the pulse prediction are sensitive to different time or amplitude domains on the pulse shape, as illustrated above in Figure 6.3. For the measurement of the drift time and the electrode shift, the last data samples of a pulse associated to the pulse rise are very important. It was noticed that for a small number of pulses the fit converges successfully but the predicted pulse does not succeed in describing the rise of the end of the pulse. This implies an incorrect estimate of both the drift time and the shift. To specifically quantify the quality of the fit at the end of the pulse, the variable Δ_{last7} has been defined, based only on the last 7 samples of the pulse:

$$\Delta_{last7} = \sum_{i=25}^{32} \frac{meas(i) - pred(i)}{S_{max}}. \tag{6.11}$$

Large values of $|\Delta_{last7}|$ single out pulses with erroneous drift time and shift parameters value. This effect is also observed with a toy simulation (see section 6.5), it is therefore an intrinsic feature of the fit model. A large fraction of these pulses ($\sim 3.6\%$ for the Presampler and $\sim 5.3\%$ for the other layers), are found to correspond to secondary minima. The fitting procedure has then been adapted to avoid such unsatisfactory minima. The pulse are re-fitted with Minuit when $|\Delta_{last7}| \geq 0.15$ or $\chi^{2*} \geq 2$ with reduced step on the parameter associated to the time adjustement. This procedure reduces the number of bad fits by retrieving 15.1% of these pulses in the Middle, 3.7% in the Front and 42.4% in the Back.

Figure 6.10 displays the 2D distributions of χ^{2*} versus $|\Delta_{last7}|$ for the Presampler and the 3 barrel compartments. A cleaning selection is applied in the fitted cosmic muon pulses requiring $|\Delta_{last7}| < 0.15$ and χ^{2*} <2.5. This selection is illustrated by the black box, the percentage of events inside this box is given per layer in Table 6.5.

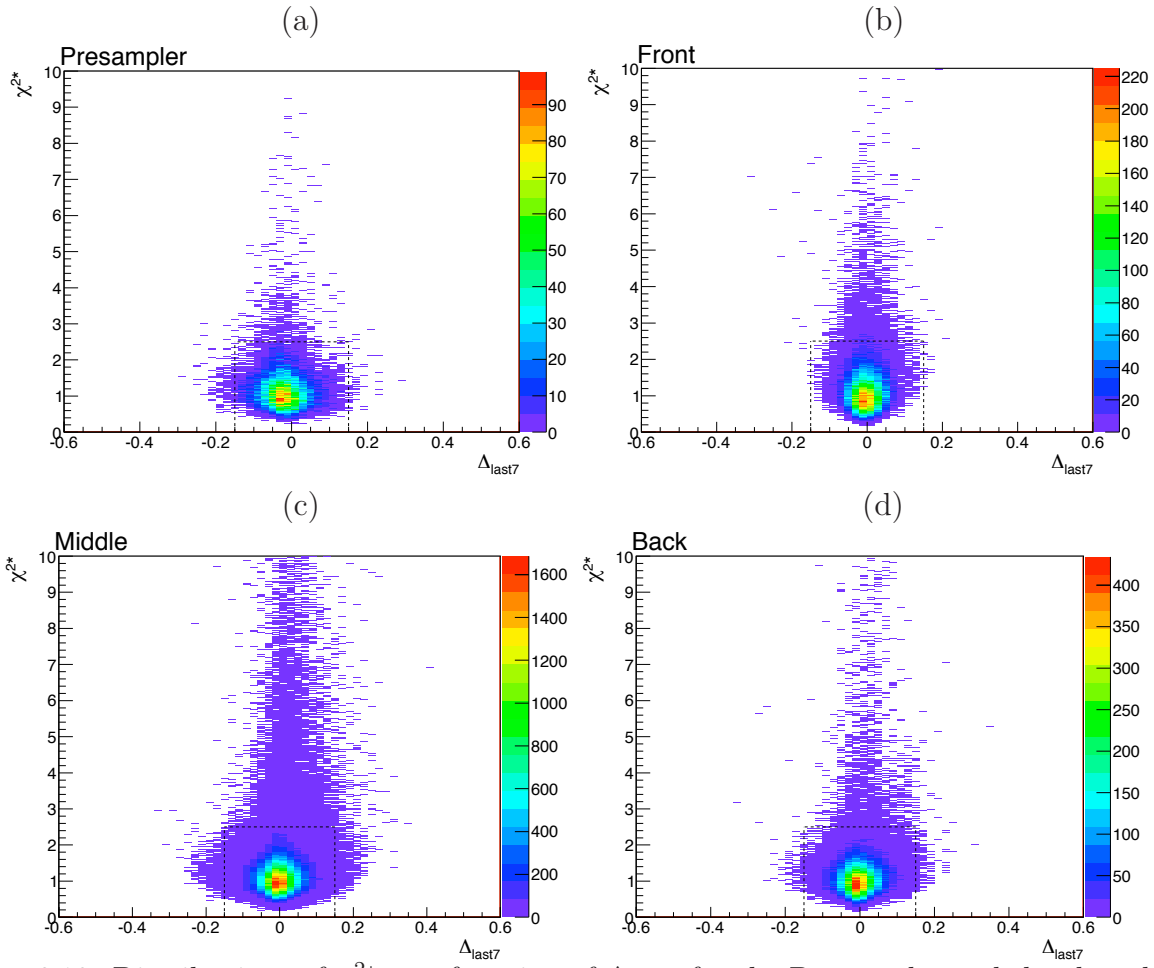

Figure 6.10: Distributions of χ^{2*} as a function of Δ_{last7} for the Presampler and the three barrel compartments. The black boxes represent the events passing the fit quality selection.

Layer	after Δ_{last7} and χ^{2*} cut	after residual cut
Presampler	95.7%	92.7%
Front	94.7%	-
Middle	95.3%	-
Back	96.5%	-

Table 6.5: Percentage of events after applying the fit quality cuts.

A cut on the maximum of residual over the pulse samples i, $max(meas(i) - pred(i))$, is also used to reject small pulses suffering from too much noise fluctuations although passing through the aforementioned selection criteria. The cut is defined by:

- $max(|meas(i) - pred(i)|)/S_{max} < 10\%$,
- if the residual is small ($max(|meas(i) - pred(i)|) < 20$ ADC counts), the cut is relaxed a bit: $max(|meas(i) - pred(i)|)/S_{max} < 20\%$.

It does not impact the pulses selection in the Front, Middle and Back layers. However, this

cut has a large impact on the Presampler, where for some cells a rather small oscillation was observed at a frequency close to the proper cell frequency and of the order of 10 MHz. If a fluctuation occurs in phase with an oscillation of the cell it will more likely be removed. This cut is therefore applied in the Presampler sample, the effect, indicated in Table 6.5, is accounted for in the fit quality selection (Figure 6.10).

6.4 First look at the fit parameters and understanding of the events

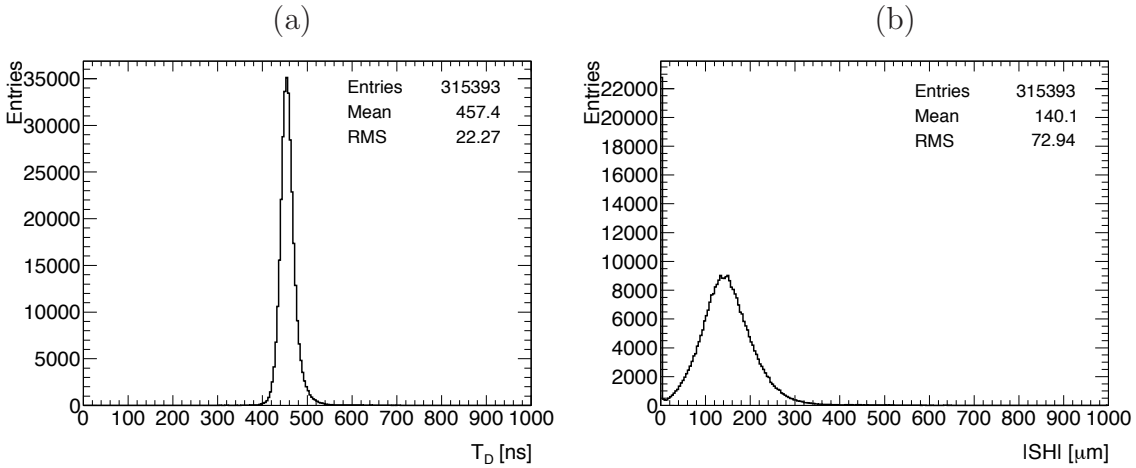

Figure 6.11: (a) T_D and (b) $|SH|$ distributions in the Middle after the cleaning selection (nominal voltage HV = 2000 V).

Figure 6.11(a-b) illustrates the distribution of drift time and electrode shift parameters for all pulses in the Middle layer of the barrel. The mean value of the drift time distribution $< T_D >= 457.4\ ns$ corresponds to what expected from the LAr gap size and HV device. The mean value of the shift distribution $|SH| = 140.1\ \mu m$ corresponds to the expected value from the known mechanical tolerances. This distribution presents a peak at $|SH| \sim 0\ \mu m$ which is mainly due to noise fluctuations. As already mentioned, the slope of the rise at the end of the pulse relies on the electrode shift. When the electrode is mis-centered, the triangles associated to the two sides of the electrode have different slope. The signal pulse is made of the the sum if two bipolar shaped signals having different plateau length and rise time. The shift really measures the deformation of the end section of the pulse searching for a soft step function or a double step structure in the fit. When there is merely no shift of the electrode, as well as when the pulse has a small amplitude and is therefore more sensitive to noise fluctuations, even a small fluctuation upward will force the shift parameter to a value of zero, as the end pulse cannot be made steeper. In the middle layer 7.2% of the events are reconstructed with this feature.

Figure 6.12 displays the drift time and shift distributions and profiles as a function of the normalized signal amplitude A_{max}, after applying the aforementioned selection cuts, in the Middle layer. These average values are quite stable as a function of A_{max}, the dispersions following a reasonable statistical error pattern. The mean value of the shift parameter in the

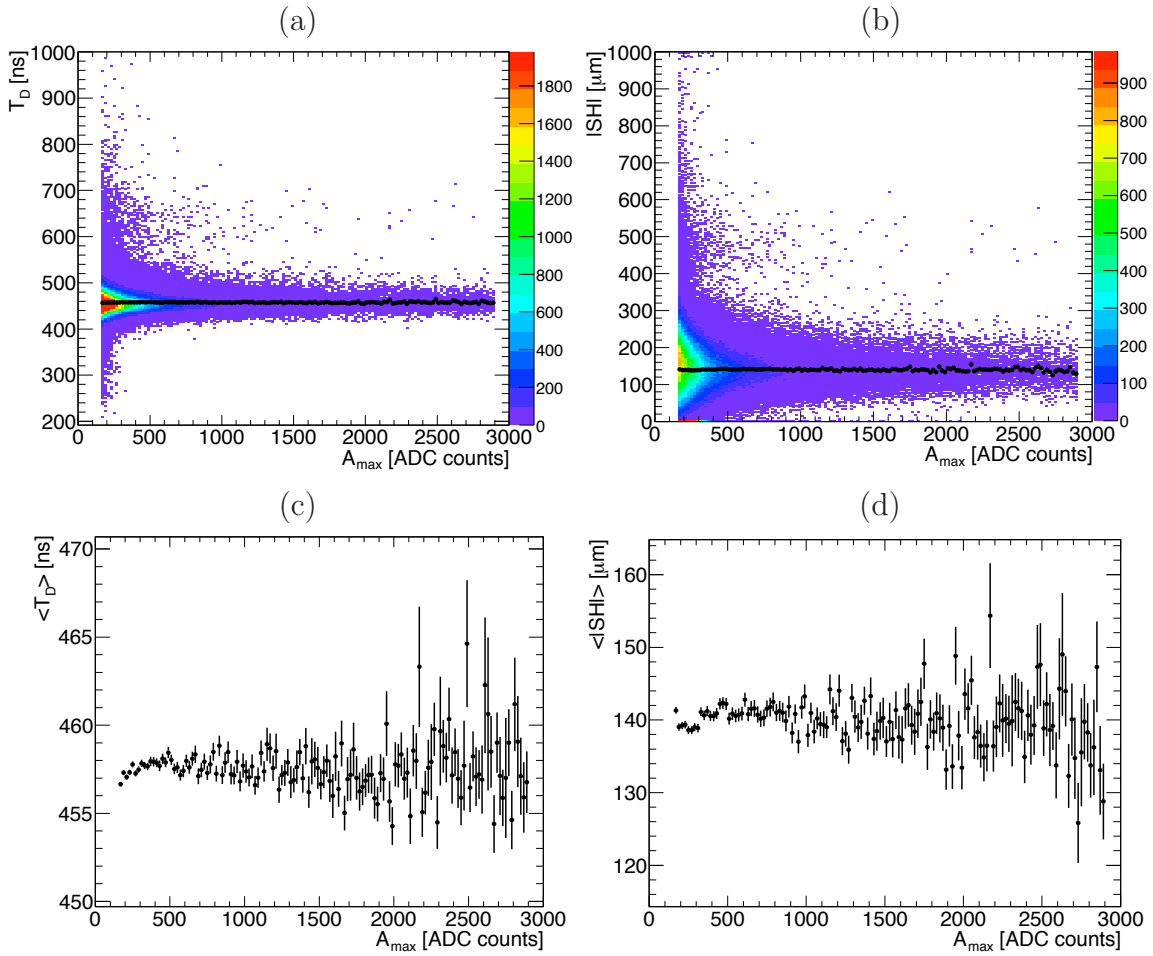

Figure 6.12: (a) Drift time T_D and (b) shift $|SH|$ as a function of A_{max} in the Middle. (c) and (d): profile distribution of (a) and (b), respectively.

low amplitude domain is slightly smaller in average as a consequence of the peak at ~ 0 μm. A closer look at these distributions also indicates the presence of pulses with large drift times (above ∼600 ns) and pulses with large shift values even at large signal amplitudes.

The distributions of the absolute value of the shift $|SH|$ with respect to the drift time T_D in the Presampler and the three layers are illustrated in Figure 6.13. Three regions of drift time appear from these distributions, separated with straight dashed lines, seemingly corresponding to different signal regimes.

1.- The zone I corresponds to the normal regime around the expected drift time where the bulk of the events is fitted with a drift time comprised between 380 and 550 ns. The three layers of the barrel have close mean values $< T_D >$ ($< T_D > = 459.8$ ns in the Front, 457.4 ns in the Middle and 463.0 ns in the Back) while the mean value for the Presampler ($< T_D > = 430.1$ ns) is lower. This observation results in the gap size difference between the Presampler and the barrel (section 6.8.3).
Figure 6.14(a) displays the profile of the residual of the pulses shape in this regions. The profile is obtained by shifting the pulse so that the time corresponding to the amplitude

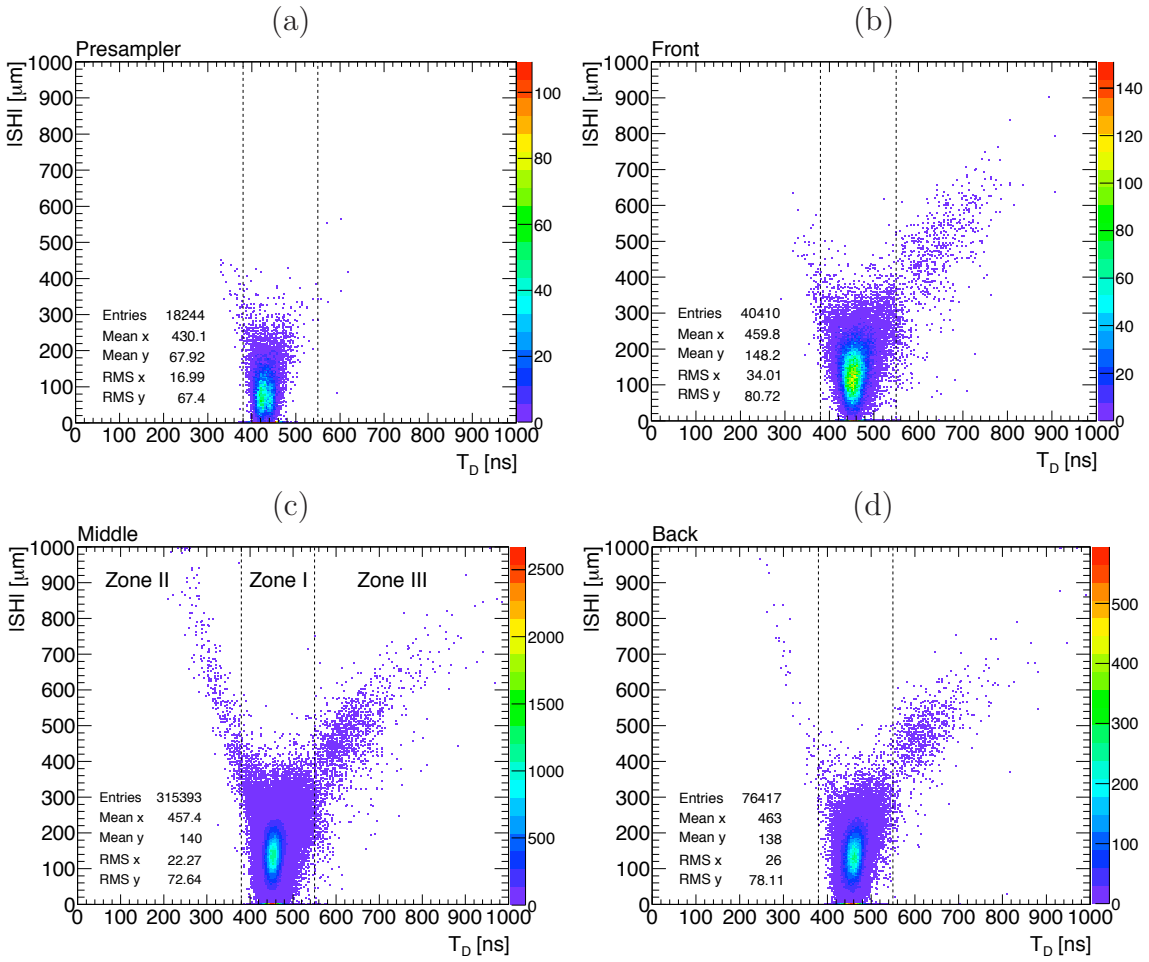

Figure 6.13: Shift $|SH|$ versus drift time T_D in the Presampler and barrel compartments.

maximum is set to 0 and the maximum amplitude of the (predicted) pulses is normalized to 1. The residual shape has a particular behavior, characterized by a "mexican-hat" shape centered at the amplitude maximum of the pulse and an oscillator shape above. This highlights a limitation of the prediction that should be accounted for in the systematic uncertainties. The residual shape is discussed in section 6.12.2, for the middle and the other layers, observing different residual behaviors.

2.- The low drift time region with $T_D < 380$ ns (zone II) of Figure 6.13 is dominated by low amplitude pulses. The presence of much larger residuals could point to an effect due to cross-talk. A closer look at the energy deposited in the neighboring cells show much larger energy depositions therein. Typically signals in excess of $S_{max} > 1500$ ADC counts or cells sampled in medium gain are found as first neighbors, in 80% of cases for the middle layer, thus corroborating the cross talk hypothesis. This is also illustrated by the shape of the residual in Figure 6.14(b).

3.- In zone III (the region with $TD > 550$ ns), some pulses are still significantly negative, more than 700 ns after the time of signal maximum (see Figure 6.14(c)). The large drift time values are a consequence of the long plateau length of the prediction. A possible

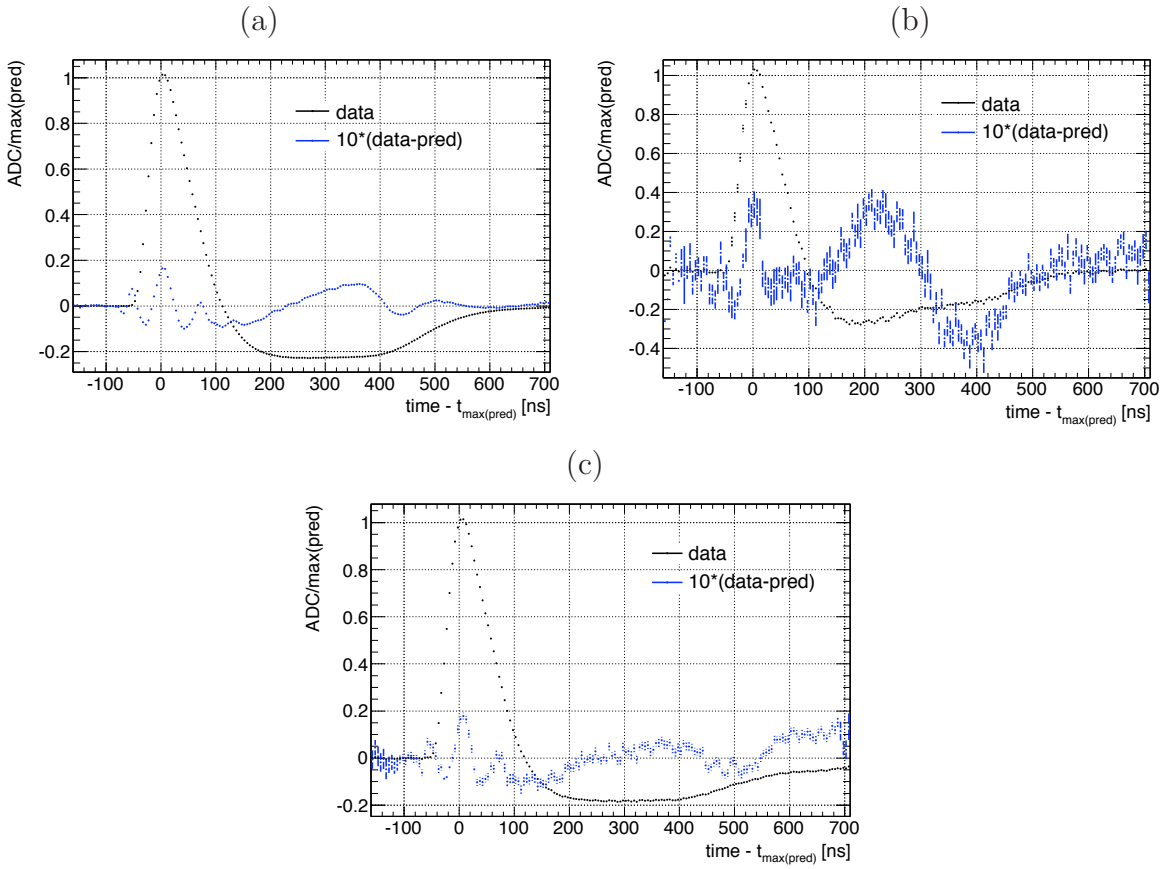

Figure 6.14: Profile of the normalized residuals multiplied by a factor 10 (in blue) as a function of time, to be compared to the normalized data (in black) in the Middle for 3 different T_D zones: (a) $380 < T_D < 550$ ns, (b) $T_D < 380$ ns (bulk of the events) and (c) $T_D > 550$ ns.

explanation is that an energy deposit originating from a photon is emitted along a bent section, thus having an abnormally enhanced bent triangle contribution. Unfortunately the runs taken with 32 samples do not contain the information from the inner tracker which would have allowed for an in depth projectivity study and to determine if the aforementioned hypothesis could be valid. Aside from these catastrophically large drift time pulses, there is a larger class of pulses which are only mildly larger than normal. Figures 6.15 and 6.16 illustrate the η and ϕ distributions of events with $TD > 550$ ns in the Middle and in the Front, respectively. In the η direction a clear structure appears at transition such as the region between the electrodes A and B (at $|\eta| = 0.8$) and at the transition between the two half barrels at $\eta = 0$. Larger drift times are expected from the slight dilution or leakage of the electric field lines due to the separation of the two electrodes, typically of 2.5 mm. In the ϕ direction, it is very interesting to see that a larger drift time is observed for middle cells in the intermodule regions in the upper part of the detector. While the absorbers and electrodes are kept equidistant at the inner and outer radius of the calorimeter, mechanical assembly tolerances allow for a slightly increased gap at the interface between modules (every 64 absorbers), especially in the upper part of the barrel due to gravity. This effect is not obvious in the Front layer and

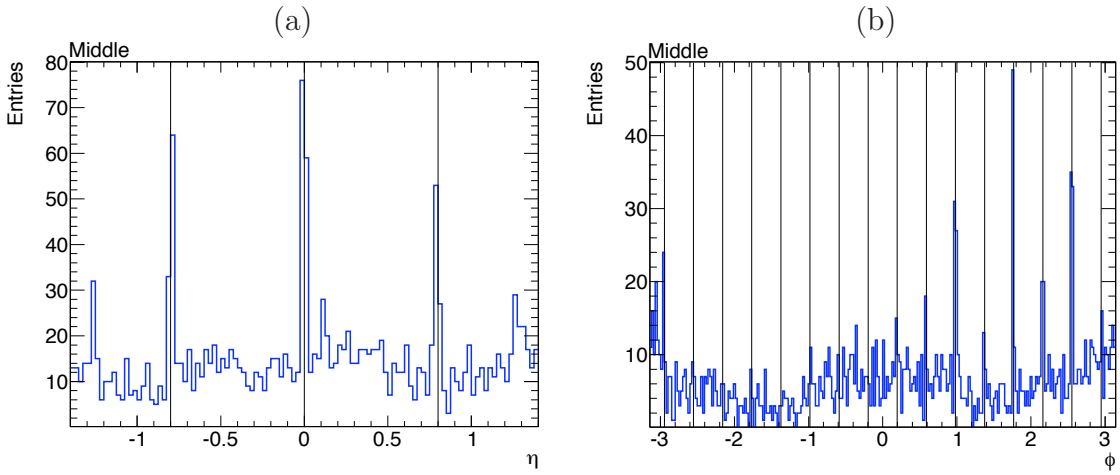

Figure 6.15: η and ϕ distributions in the Middle, for events with $TD > 550$ ns. The black lines represent the electrode and half-barrel transition zones in η and the inter-module separation in ϕ.

not seen at all in the Back, as expected given that the front and the back layers are much closer to the mechanical fixed points [47].

Another interesting feature of Figure 6.15(b) is an apparent modulation in the number of high drift time cells, where the number of high drift time cells is clearly higher near the horizontal plane at $\phi \sim 0$ and π. This structure does not correspond to a plausible mechanical deformation of the detector, but it rather supports the hypothesis that at least some of the tails in drift time are due to energy deposits with a larger fraction of bent sections. Given the anisotropy of the muon flux in the detector (mainly traversing the detector vertically from top to bottom, as most of the cosmic muons collected originate from the cavern shafts) a larger number of radiation deposits with a large fraction of bent sections is expected when the incident muon is maximally non projective *i.e.* essentially in the horizontal plane. Unfortunately the tracking information was not recorded for the cosmic muons data runs used in this analysis. It is therefore not possible to verify such hypothesis.

6.5 Understanding the fit model

A toy Monte-Carlo simulation is devised in order to better understand the features and limitations of the fit model aforementionned. It also allow to understand if the observed effects are physical or detector related or come from the artifacts of the fit.

A large number of "pseudo pulses" are generated for two different cells in the Middle:

$$cell_1 = \{FT\ 21, A, Slot\ 11, Channel\ 14\}$$
$$cell_2 = \{FT\ 21, A, Slot\ 12, Channel\ 40\}$$

according to the following steps.

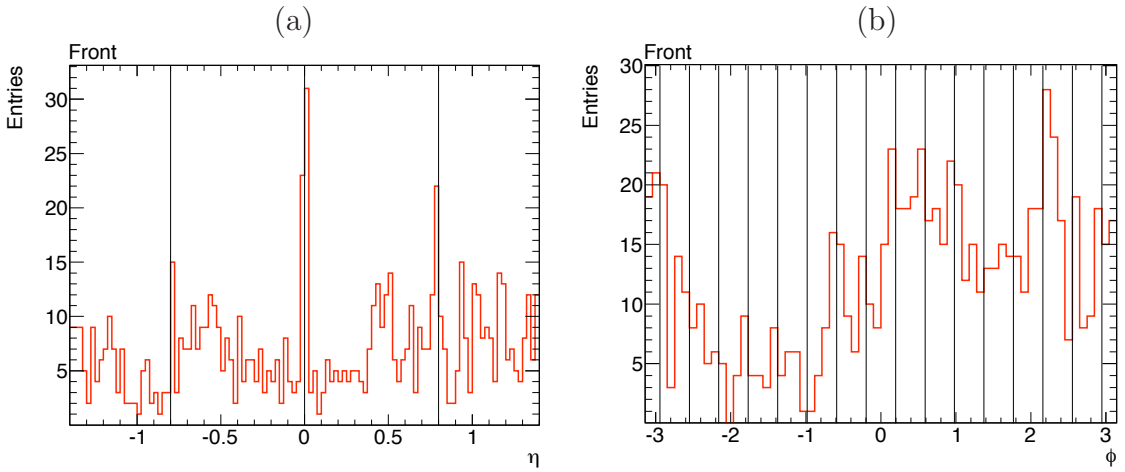

Figure 6.16: η and ϕ distributions in the Front, for events with $TD > 550$ ns. The black lines represent the transition zones in η and the inter-module separation in ϕ.

1. A toy pulse is generated according to the FPM prediction model. The drift time and the shift values are randomly chosen in gaussian distributions centered at 460 ns and 140 μm respectively, with a standard deviation corresponding to what measured in the Middle compartment, respectively of 22.5 ns and 69 μm. The normalization parameter is varied according to an exponential distribution so that a toy Monte Carlo distribution of the amplitude maximum of pseudo data pulses close to that of the data in the region $A_{max} <$ 500 ADC is obtained (see Figure 6.17). The adjustment in time is varied uniformly between -25 and 0 ns, to cover any possible time displacements. The fraction of bent triangles and their time constants are fixed in the model to that of the two chosen cells.

2. Pseudo data are then generated from the predicted pulse each 25 ns to mimic the data sampling frequency and smeared according to a gaussian with a standard deviation corresponding to the measured noise of the two chosen cells. A first round of simulation included the effect of noise auto-correlation. This realistic feature did not impact the results whatsoever and was thus subsequently neglected.

The pseudo data are then fitted using the precise same procedure as for the data pulses.

Figure 6.18(a) displays the χ^{2*} distribution as a function of Δ_{last7} for the toy simulation. The tail at high χ^{2*} values and for $\Delta_{last7} > 0.2$ that was not observed in the data sample emphases the asymmetry in the fit of the last samples of the pulse. When Δ_{last7} is positive, the measured samples tend to be above the prediction and the fit stays negative longer at the end of the pulse. This implies larger fitted drift times and shifts. Such feature of the fit initially occurred in the data samples for a comparable fraction of pulses. A fraction of these badly fitted pulses was removed whit a new fit iteration(section 6.3.3). No refitting procedure has been used in this particular study, indicated a limitation of the fit itself.

Figure 6.18(a) also illustrates that the χ^{2*} values are lower than for what observed in the data which is expected as there is no model precision term in the toy simulation. As a consequence, the residuals profile displayed in Figure 6.18(b) has a smaller amplitude with respect to cosmic muons data. However, a similar behavior of the residuals profile is observed, reproducing the peak at zero. This feature of the fitting procedure is much smaller than the effect observed for

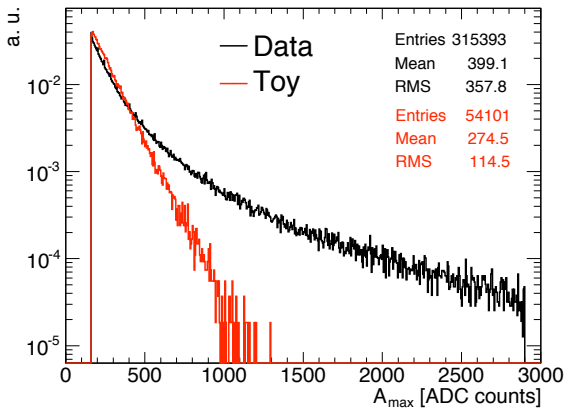

Figure 6.17: Distribution of the amplitude maximum A_{max} in black for the Middle data sample and in red for the toy simulation.

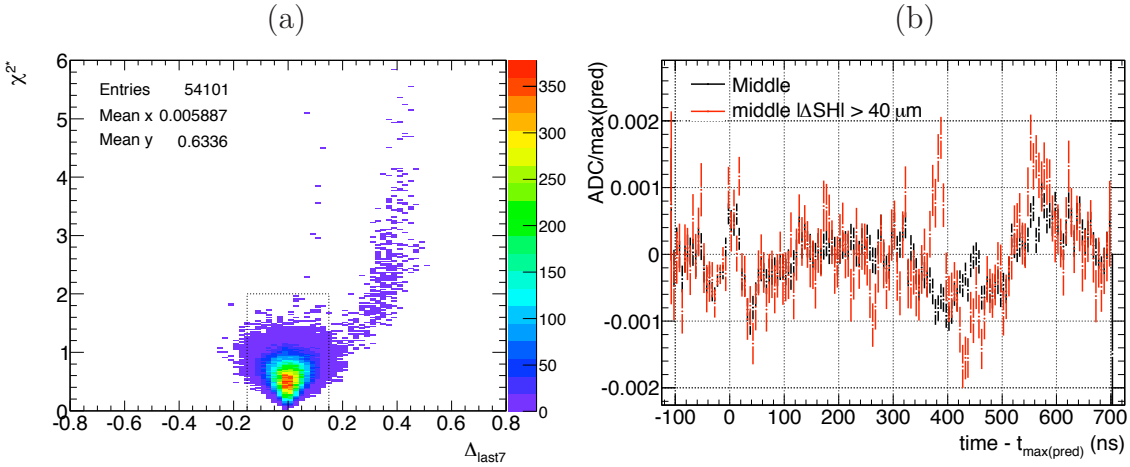

Figure 6.18: (a) χ^{2*} as a function of Δ_{last7}, (b) residuals as a function of the time.

small drift time measurements but could be the scope a future study to better understand the fitting procedure and the impact of the non account for cross-talk effect.

The four parameters extracted from the fit are compared to the generated ones in Figure 6.19 after applying the cut on quality fit, $|\Delta_{last7}| < 0.15$ and $\chi^{2*} < 2$, represented by the black box in Figure 6.18(a). An impressive agreement is found between generated and fitted values of the shift parameter given the simplicity of the model used to generate them. These results also show the linearity of the method. More importantly, as observed in the real data, the fitted shift parameter presents a peak at 0 microns also in the toy simulation. This clearly settles this feature as pertaining to the fitting procedure or the fit model.

The 2D distribution of $|SH|$ versus T_D are illustrated in Figure 6.20(a) for the toy Monte Carlo simulation.

1. No cells are found with drift times in the range TD <380 ns, which further supports the cross talk hypothesis.

2. The bulk of the events are still well within $380 < TD < 550$ ns, but a clear tail appears in

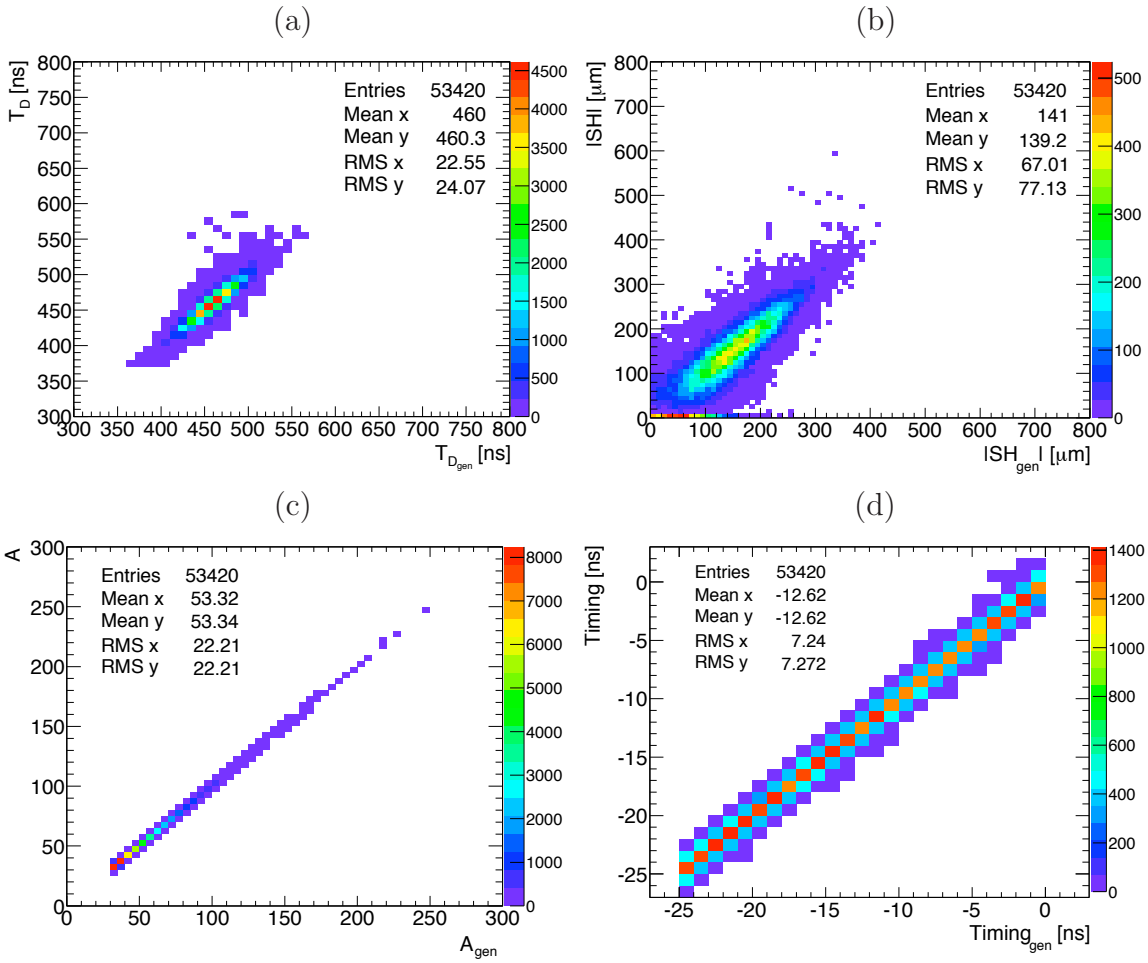

Figure 6.19: Distribution of fitted value with respect to the generated one: (a) T_D, (b) $|SH|$, (c) the normalization and (d) the time adjustment.

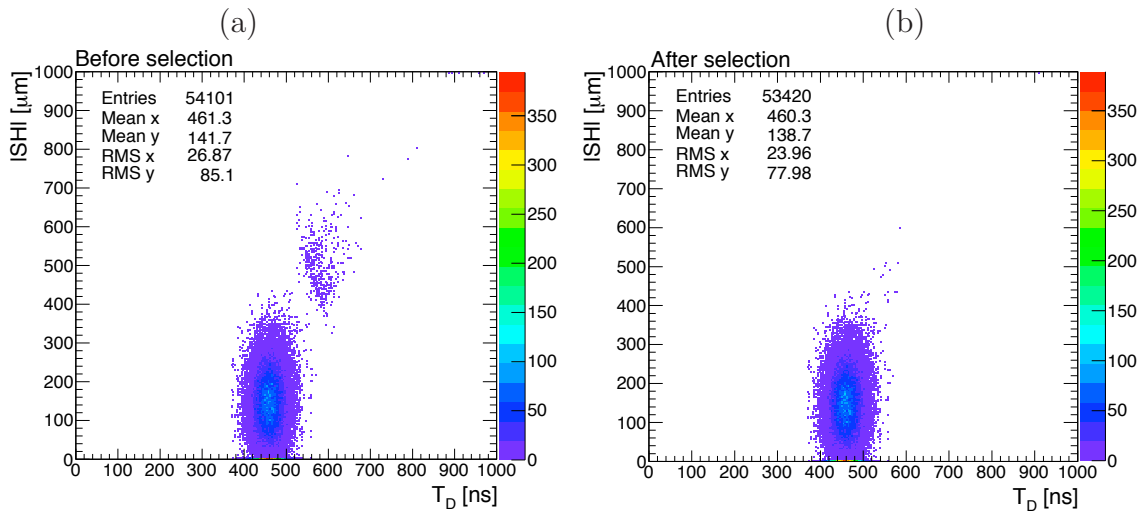

Figure 6.20: $|SH|$ versus T_D (a) before and (b) after cuts on χ^{2*} and Δ_{last7}.

the region $TD > 550$ ns. This further supports the hypothesis of the pulses observed in cosmic muon data with large drift time after the fit quality selection applied are related to detector and mechanical constraints effects.

3. The tail at large drift time and shift values is somewhat disconnected from the bulk of the events. Using the cut on Δ_{last7}, this secondary tail disappears, as shown in Figure 6.20(b).

4. No correlation between the drift time and the shift was introduced in the toy simulation and none appears in the fit result, as illustrated in Figure 6.20.

This study of toy simulation on two random cells in the Middle distinguishes the different features of the signal prediction shape from mechanical effect on the drift time and shift parameters measurement.

6.6 Global Cell Based Fit and Amplitude Weighting

Given the multiple features of the fit and potential unknown physical of detector related effects that could affect the drift time measurement, two ways of enhancing the statistical power of the measurement are presented in this section.

6.6.1 Global Cell Based Fit

As was shown in Figure 6.5(c) in average 12 pulses are found per cell in the Middle layer. An alternative fit procedure is proposed enjoying a more statistical power: all the pulses related to a given cell are fitted simultaneously and an unique value for the drift time and shift parameters is extracted. The "global cell based fit" has been performed on cells from the Middle compartment only. The number of free parameters in the new fit procedure becomes $2 + 2 \times N$, where N is the number of pulses available for each cell, corresponding to:

- 1 drift time T'_D,

- 1 shift parameter SH,

- N normalizations (1 per pulse),

- N time adjustments (1 per pulse).

The χ^2 of the fit (denoted $\chi^{2'}$ to avoid confusion with respect to the standard prediction) is then given by:

$$\chi^{2'} = \frac{1}{32N - (2 + 2N)} \sum_{j=1}^{N} \sum_{i=1}^{32} \frac{(meas(i,j) - pred(i))^2}{\sigma^2} \tag{6.12}$$

A typical output is presented in Figure 6.21, for Middle cell containing 17 pulses. In this representation all pulses are normalized in order to have a maximum value of 1 and the timing is set so as to place the maximum value at 0 ns. This implies that measured samples can have very different relative noise values and therefore weigh very differently in the derivation of the parameters.

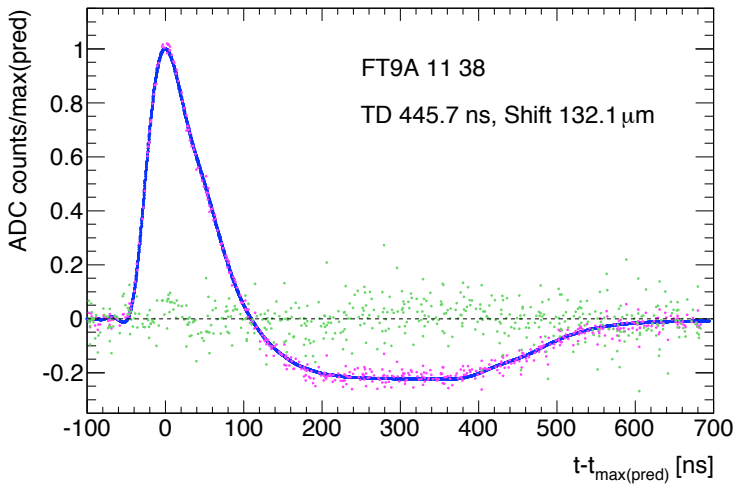

Figure 6.21: Illustration of the global cell based fit for a typical cell in the Middle. 17 pulses have been recorded; the data are displayed in pink after normalization of the predicted amplitude maxima to 1 and time adjustment so that the pulses maximum amplitude and position coincide. The prediction, in blue, is common to the 17 pulses. The differences (data - prediction)*3 are shown in green.

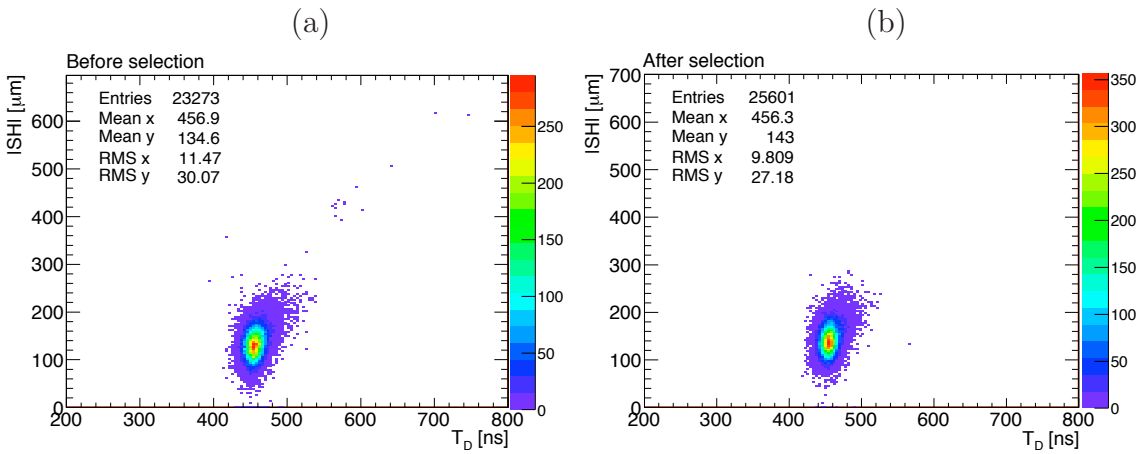

Figure 6.22: $|SH|$ versus T'_D for the global cell based fit with N pulses in the Middle, (a) before and (b) after applying a fit quality selection in the same spirit as what was done in the individual fit case.

A potential problem of this method is that it combines different signals without discrimination. For instance if some of them have a large contribution from the bent section they can affect the fit result in a less transparent way than in the case of individual fits.

Figure 6.22(a) displays the 2D distribution of the shift $|SH|$ and drift time TD' as extracted from the global cell based fit. The region with $|SH| \simeq 0$ microns is reduced with respect to the individual pulse fit case. However, there are still few cells with a shift parameter close to 0 microns. Typically these cells either only have few pulses (Figure 6.23(a)) and/or the pulses have a small amplitude. The number of global cell based fits giving a large drift time is

drastically reduced. Some cells still present a larger drift time as expected from the systematic effects seen at mechanical transitions in the detector and from those cells with small number of pulses.

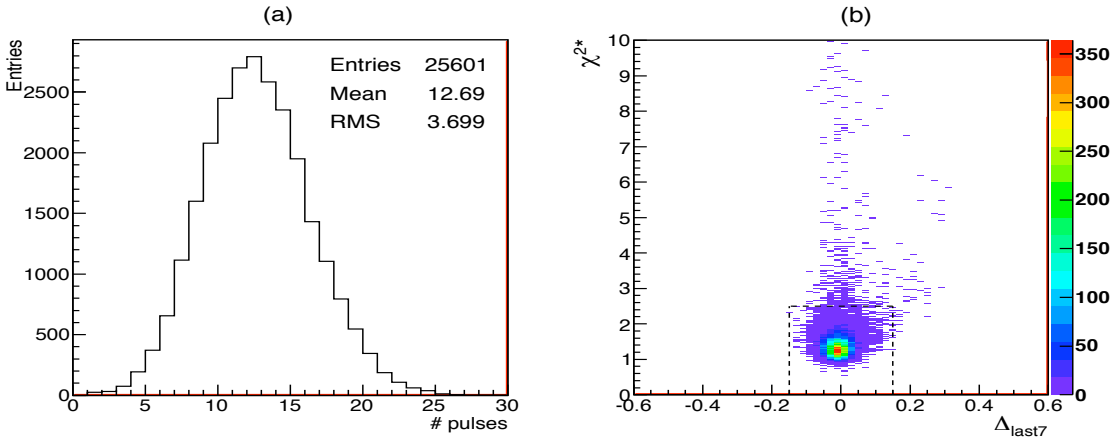

Figure 6.23: Distributions of (a) the number of pulses per cell, and (b) $\chi^{2*'}$ versus $\overline{\Delta_{last7}}$ for the global fits on N pulses.

Nevertheless further cleaning cuts can be applied, as in the case of the individual fits, to force a good description of the end of pulse. For this purpose the average of the Δ_{last7} variable on all the pulses of the cell can be used. A modified χ^2 is defined as in the case of the individual fit, accounting for the maximum of amplitude of the pulses:

$$\chi^{2*'} = \frac{1}{32N - (2+2N)} \sum_{j=1}^{N} \sum_{i=1}^{32} \frac{(meas(i,j) - pred(i))^2}{\sigma^2 + (k * S_{max}(j))^2} \tag{6.13}$$

$$\overline{\Delta_{last7}} = \frac{1}{N} \sum_{j=1}^{N} \sum_{i=25}^{32} \frac{(meas(i,j) - pred(i))^2}{S_{max}(j)} \tag{6.14}$$

with $k = 0.8\%$ for the middle. The 2D distribution of $\chi^{2*'}$ vs $\overline{\Delta_{last7}}$ is illustrated in Figure 6.23(b). Large values of $\overline{\Delta_{last7}}$ are again associated to large values of TD. The black box represents the selection criteria. Figure 6.22 shows the map of the shift $|SH|$ and drift time TD' after applying these cuts. Cells with erroneous drift time and shift are excluded, due to the cut $\overline{\Delta_{last7}} > 0.15$.

Figure 6.24 illustrates the distribution of the χ^{2*} variable in the case of individual and global cell based fits. It is interesting to see that the $\chi^{2*'}$ distribution is narrower as expected from the improved statistical power of the method, but it is also higher in average. This could be explained by a possible increase in systematic effects. Since the pulses in each cell can be very different. the mixture of pulses with normal or larger energy deposits in the bent sections lead to a smaller tail at large drift time but also to an increase in the $\chi^{2*'}$ distribution.

6.6.2 Amplitude Weighting

Another way to enhance systematic effects is to weigh the results of the fit with the inverse of the square of the expected statistical error. In this case the statistical error is proportional to

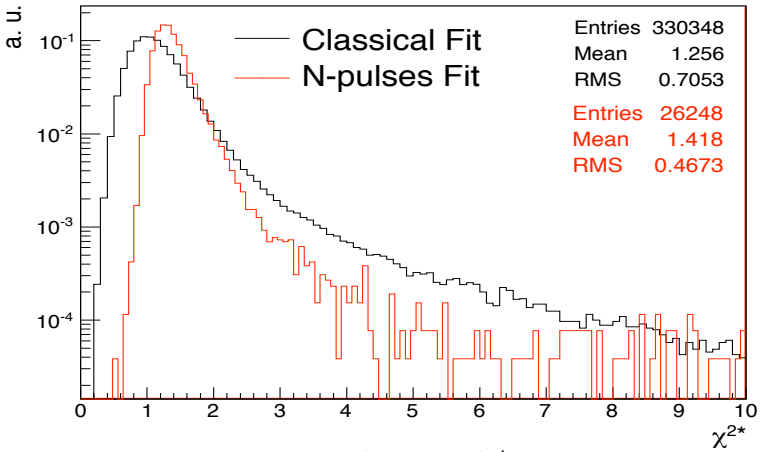

Figure 6.24: *Distributions of the* χ^{2*} *and* $\chi^{2*'}$ *of the normal and global fits.*

the normalized amplitude maximum. A_{max}. The method used in this study proposes to apply a weight defined as A^2_{max} to each individual fitted pulse.

A comparison of the two aforementioned methods with respect to the individual fit case is presented in Figure 6.25(a) and (b) for the Middle; the drift time and the shift distributions are respectively displayed, for the individual fit (without weight), the weighted individual fit, and the global cell based fit. For a fair comparison, only the pulses from a given cell that passes the selection criteria on the N-pulses fit are kept in individual fit cases. The mean values of the drift time distributions are quite close but not fully statistically compatible. The average drift time in the case of the global fit is slightly smaller than the two other average values due to the reduced region with large TD. The average drift time in the case of the weighted individual fit is slightly smaller than in the case without weight ($< T_D >_{wgt}= 457.7\ ns$ with respect to $< T_D >_{wgt}= 457.4\ ns$). This small difference is explained by small amplitude of the pulses with a small drift time (zone II), as was shown in Figure 6.12(a). The statistical power of these pulses is reduced in the weighted drift time distribution, explaining the lower mean value. The distribution of the shift displays as expected from the statistical gain a smaller peak at zero for the cell based fits and even more so for the weighted distribution.

Figure 6.26 illustrates the drift time and the shift distributions of the weighted average of all individual fits in each cell and that of the global cell based fits. Not unexpectedly the drift time mean values are precisely the same as the previous case of individual weighed fits, but the RMS values are much closer although the cell based fit has seemingly a slightly smaller RMS. The average difference is 1 ns and a RMS of 6 ns is found from the distribution of the difference between the drift time extracted from the N-pulses fit and the one from the average weighted individual fit.The peak at 0 microns for the shift distributions is still suppressed, and as for the drift time distributions the average is unchanged from the comparison with the individual weighted fits, and the RMS values are much closer but still the cell based fit presents a slightly smaller RMS.

To further check the choice of statistical weight, Figure 6.27(a) shows the distribution of the inverse of the error $1/\sigma_{TD}$ on the drift time as a function of the amplitude maximum of the pulse A_{max} for the standard (individual pulse) fit. Figure 6.27(b) displays the inverse of the error

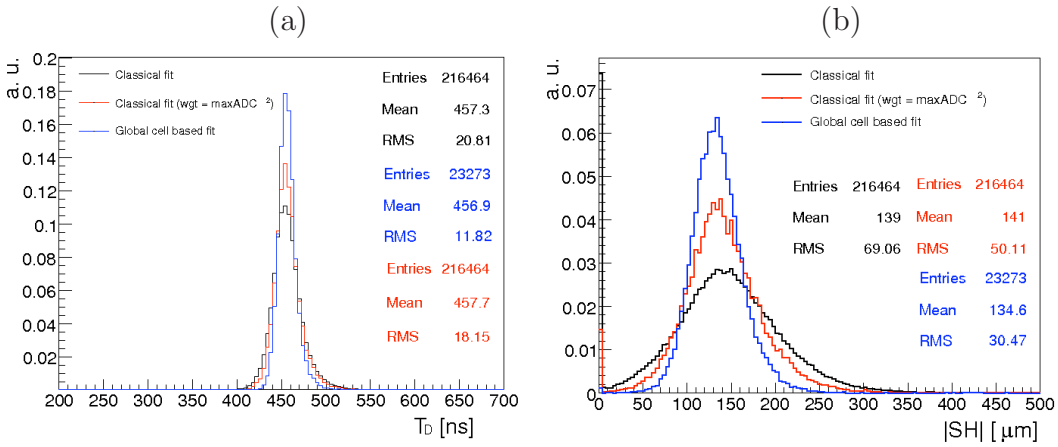

Figure 6.25: Distributions of (a) the drift time and (b) the absolute shift in the Middle, in black for the individual fit, in red for the individual fit weighted by A^2_{max}, and in blue for the global cell based fit methods.

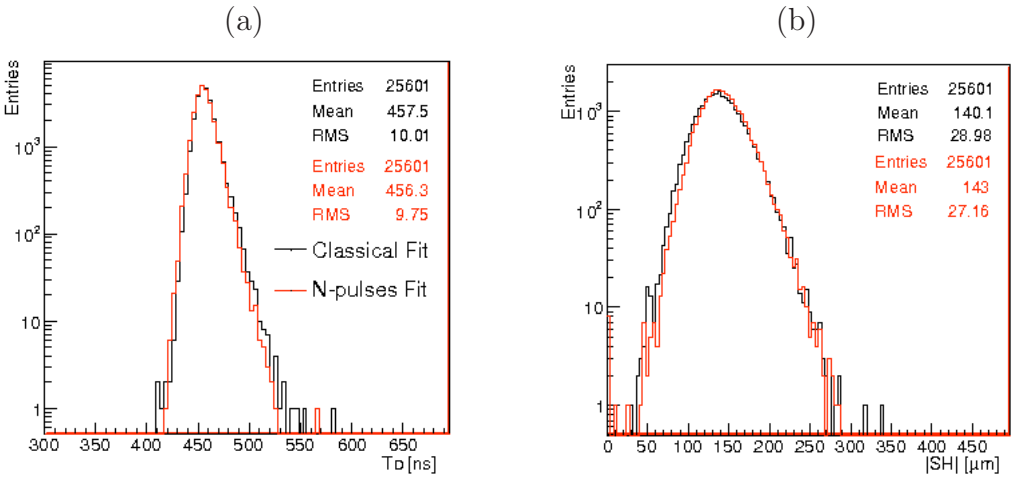

Figure 6.26: Distributions of (a) the drift time and (b) the absolute shift in the Middle, in black for the weighted average of the individual fits belonging to a given cell, and in red for the global fits on N pulses.

$1/\sigma_{TD'}$ from the global cell based fit as a function of $\sqrt{\sum_i A^2_{max_i}}$, the index i corresponding to the pulses in a cell. The Profiles of these distributions are fitted by a polynomial of degree 1 yielding very similar linear behaviors.

Using a global fit on N pulses on a cell basis or performing a weighted average of the individual fits with the weight A^2_{max} leads to similar but not precisely equal results. A further investigation of these small differences would be interesting but beyond the scope of this study. This question will nevertheless be very briefly addressed in section 6.12.1.

In the following sections, the weighted average of individual fits will generally be used. The

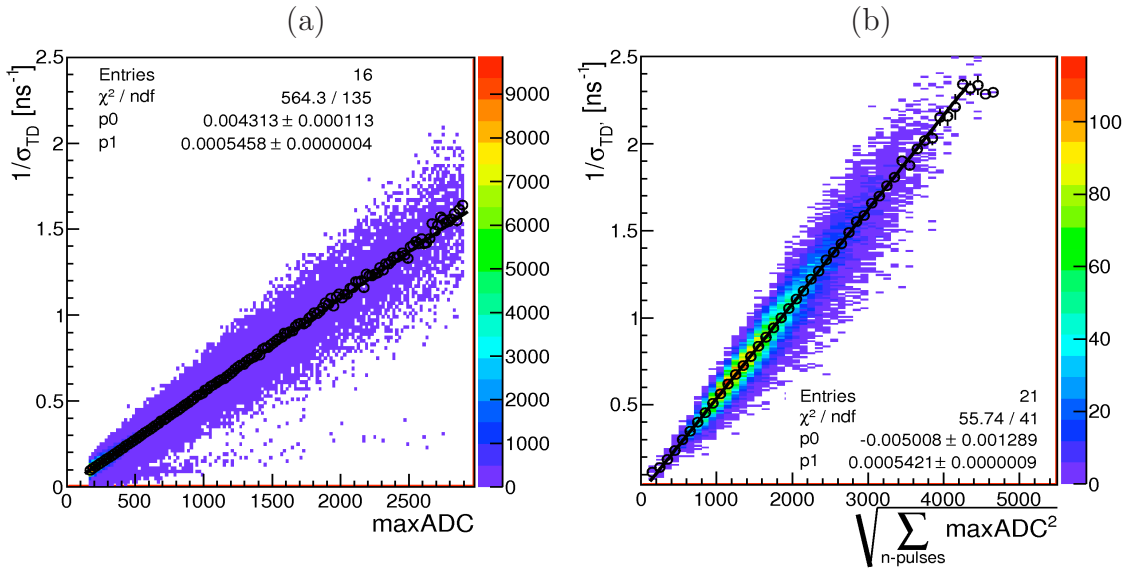

Figure 6.27: (a) $1/\sigma_{TD}$ versus A_{max} for the standard fit, (b) $1/\sigma_{TD'}$ versus $\sqrt{\sum A^2_{max}}$ for the fit with N pulses, in the Middle.

prediction results of the drift time and shift measurements are scrutinized, their uniformity in η et ϕ given for the Presampler and the three barrel layers. In particular the drift time uniformity is measured in the Middle compartment which contains to the most important fraction of the deposited energy and therefore dominates on the impact to the constant term.

6.7 Results for the Middle compartment

6.7.1 Drift Time

Figure 6.28(a-b) displays the 2D distribution of the drift time extracted from the fit as a function of η, in the Middle compartment. The black dots correspond to the mean values per η bins of size 0.1. In addition, the orange line illustrates the prediction of the average drift time deduced from absorber thickness measurements made during the calorimeter construction phase [47]. As was shown in the previous chapter, the angle and amplitude of the waves in the accordion shape of the absorbers varies in η, as well as the lead thickness, to provide a constant LAr gap in depth and similarly an uniform response of the calorimeter. The Absorber-LAr-Electrode-LAr periodic structure is therefore expected to be constant. The fixed pitch is given by (using nominal values):

$$\begin{aligned}\text{Absorber}(2.2\text{mm}) + \text{Gap}(2.09\text{mm}) + \text{Electrode}(0.28\text{mm}) \\ +\text{Gap}(2.09\text{mm}) = (2\pi/1024) \cdot \mathrm{R_i}\theta_\mathrm{i} = 6.66\text{mm},\end{aligned} \tag{6.15}$$

where R_i and θ_i are the average radius and the angle in the radial direction of any of the folds of the accordion shaped absorbers, which are designed in such way that the pitch is constant in depth.
The variation of the absorbers thickness will impose a variation of the gap in opposite direction.

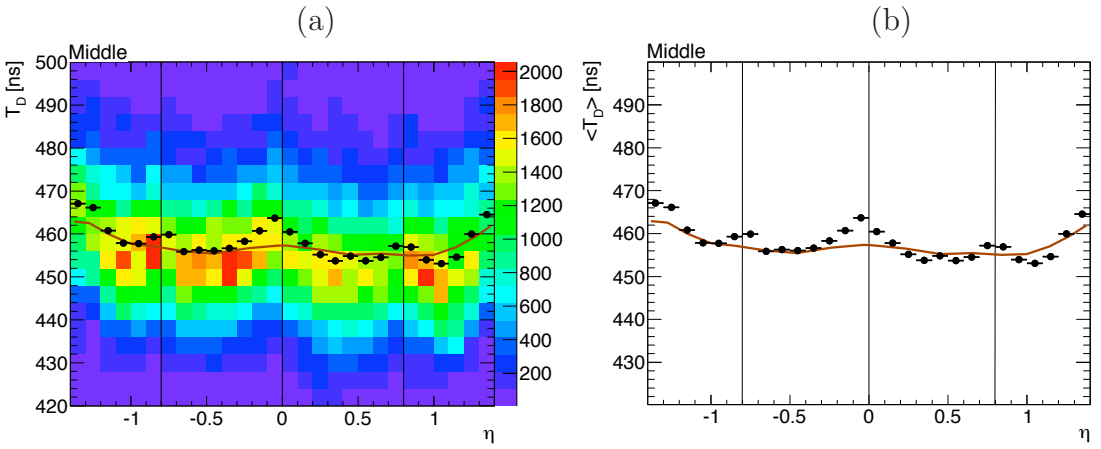

Figure 6.28: Drift time T_D as a function of η in the Middle, in bins of 0.1. Events are weighted by A^2_{max}. The black dots, displayed in (a) and (b), correspond to the Profile of the color plot. The orange line represents the prediction from absorber thickness measurements averaged in ϕ.

The drift time dependence on the gap is given by the relation [50]:

$$T_D = T_D^0 \left(\frac{g}{g_0} \right)^{\alpha+1} \tag{6.16}$$

The drift time variation in η around the average value $T_D^0 =< T_D >$=457.7 ns given by the fit procedure, is then predicted accounting for the variation around the average gap size (2.09mm), given by opposite variation on absorbers thickness. Figure 6.29(a) displays the gap variation as a function of η. The dot points correspond to prediction from the absorbers thickness measurement and the red line is the result of a smooth fit used to derive the gap size in the different cells in η slices.

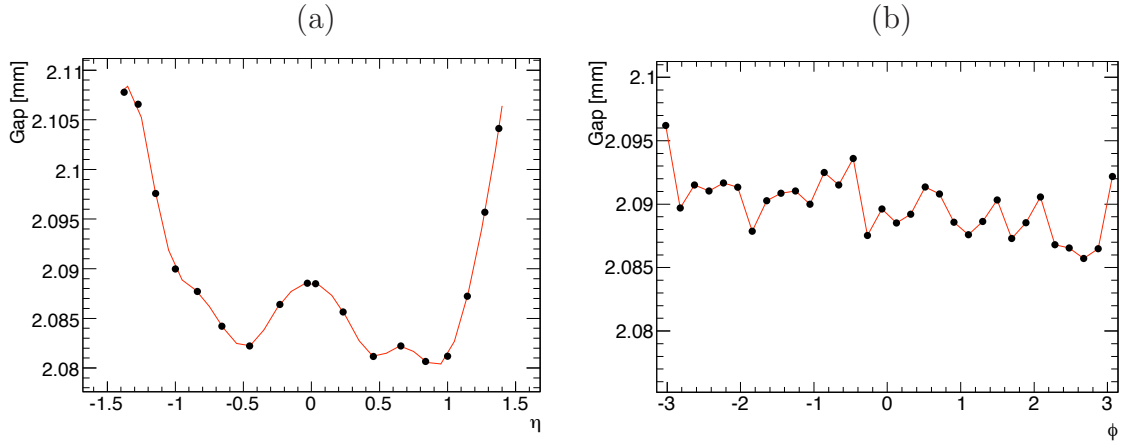

Figure 6.29: Variation of the gap in the Calorimeter along (a) the η and (b) the ϕ directions, calculated from the measured absorbed thicknesses.

The agreement between the prediction and the data is rather good, except in the transition zones around $\eta = 0$, ± 0.8 and perhaps also ± 1.4, where the lower field induces a larger TD.

This effect was already discussed in section 6.4 and is seen more precisely in Figure 6.30 where the η bin size is fixed to the Middle cells size $\Delta\eta = 0.025$. The agreement between the drift

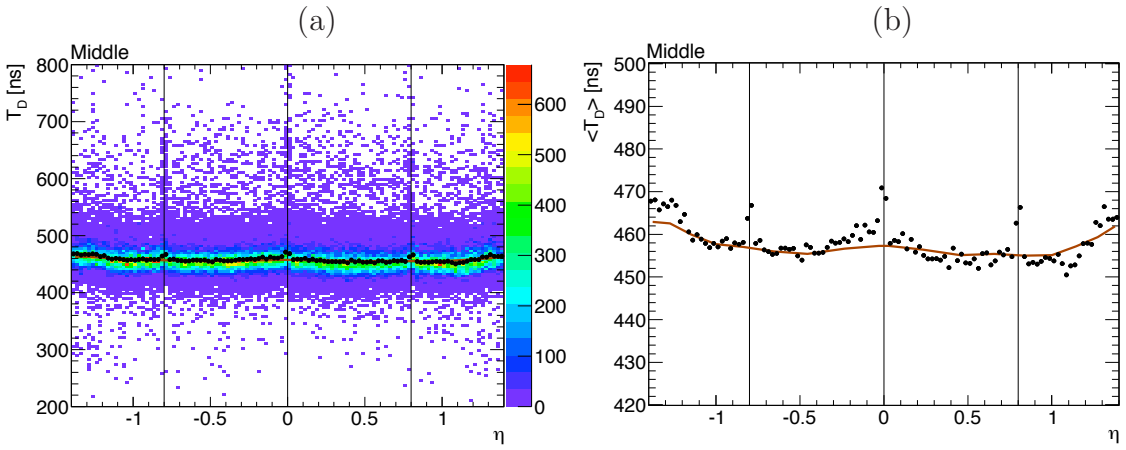

Figure 6.30: Drift time T_D as a function of η in the Middle, in bins of 0.025. Events are weighted by A^2_{max}. The black dots, displayed in (a) and (b), correspond to the Profile of the color plot. The orange line represents the prediction from absorber thickness measurements averaged in ϕ.

time measurement from the fit and the estimate from the measurement of the absorbers is quantified by computing the RMS of the difference between the data points and the prediction. This yields to a RMS of 2.9 ns, when excluding $3 \times 2\Delta\eta$ data points around the transition regions. In comparison, the RMS of the data distribution amounts to 3.7 ns when integrating over the whole η range.

Figure 6.31 displays the drift time distribution as a function of ϕ. No significant variations are expected from the design of the calorimeter (with respect to the transition regions in η). As was shown in Figure 6.15 for the pulses with a large drift time in the Middle, the inter-modules structure is drawn but this is expected to slightly impact the average drift time distribution as a function in ϕ, the pulses from zone III representing a small fraction of the whole statistic. As well, as illustrating in Figure 6.29(b) the absorber thickness measurements do not show significant variations, also a small modulation effect is visible. However, a difference between the upper and lower hemispheres of the calorimeter is observed in Figure 6.31. On average the difference amounts to 1.5 ± 0.1 *ns*, *i.e.* 0.3% relative. This small effect is consistent with the sagging and pear shape deformation of the calorimeter due to gravity and the effect of a small temperature gradient between the upper and lower part of the calorimeter (of about 0.1 K, see [51]).

The two half barrels are displayed separately in Figure 6.32. The distribution of the fits is rather uniform in both cases, with an average of 459.2 ns with an RMS of 2.8 ns for the $z < 0$ half barrel, an average of 455.8 ns with an RMS of 3.1 ns for the $z > 0$ half barrel, and an average value of 457.5 with an RMS of 1.8 ns for the overall ϕ distribution (see section 6.9.1). The fact that the RMS is significantly smaller when the two half barrels are averaged together in η reveals an underlying systematic compensation effect. A closer look at the module construction is very instructive for this matter. Both half barrels are essentially copies of one another, all electrodes were produced with the same master pattern and stacked in similar ways. It is therefore likely

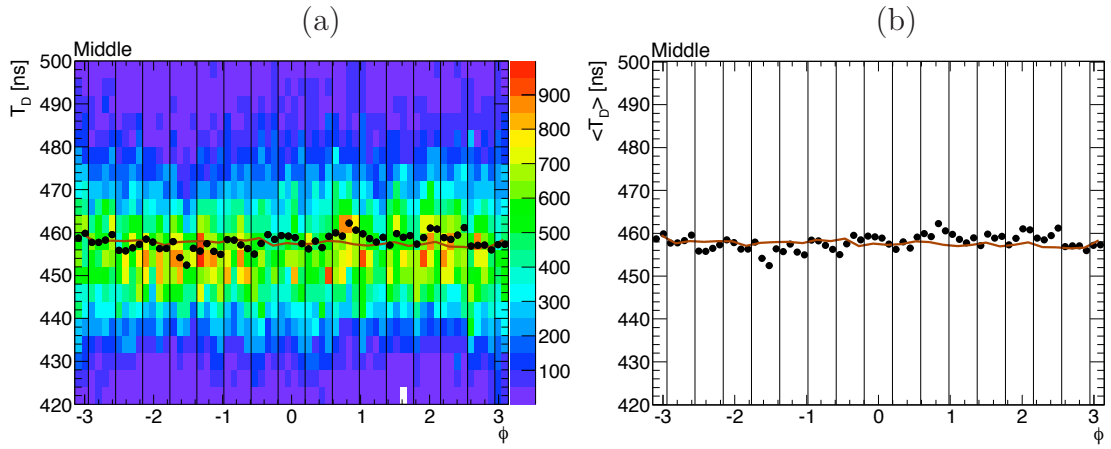

Figure 6.31: Distribution of the drift time as a function of ϕ in the Middle. Events are weighted by A^2_{max}. The black dots correspond to the Profile of the color plot, they are displayed in (a) and (b). In addition, the orange line represents the prediction from absorber thickness measurements averaged in η. The vertical black lines represents the module separations.

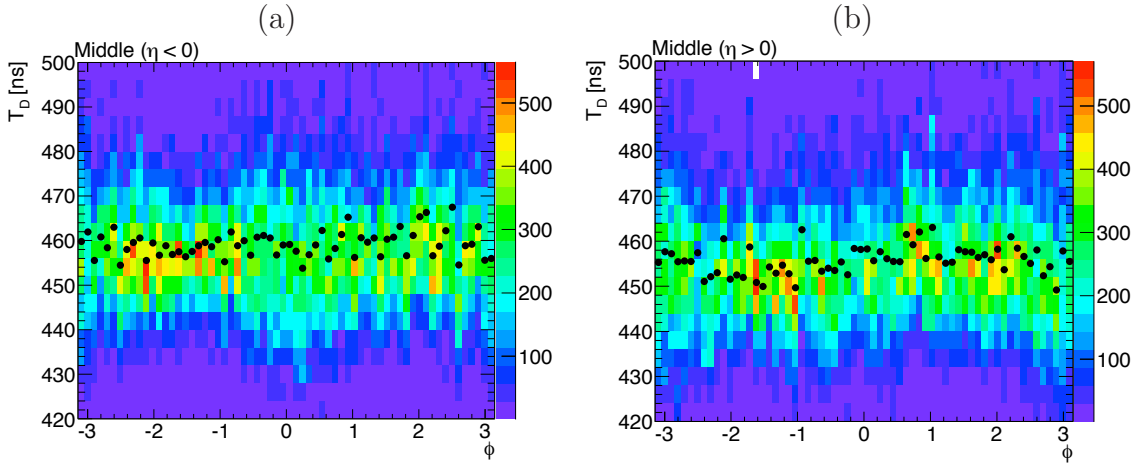

Figure 6.32: Drift time as a function of ϕ in the Middle, for (a) $\eta < 0$ (C wheel) and (b) $\eta > 0$ (A wheel). Events are weighted by A^2_{max}. The black dots correspond to the Profile of the color plot.

that a defect appearing in one also appears in the other. To restore a symmetry in η one half barrel needs to be rotated in the horizontal plane as illustrated in Figure 6.33(a). This implies that at the interface between half barrels the bends are oriented in opposite directions and that the defects are rotated around the vertical y axis. Systematic variations in gap are then likely to be in opposite phase and thus to compensate.

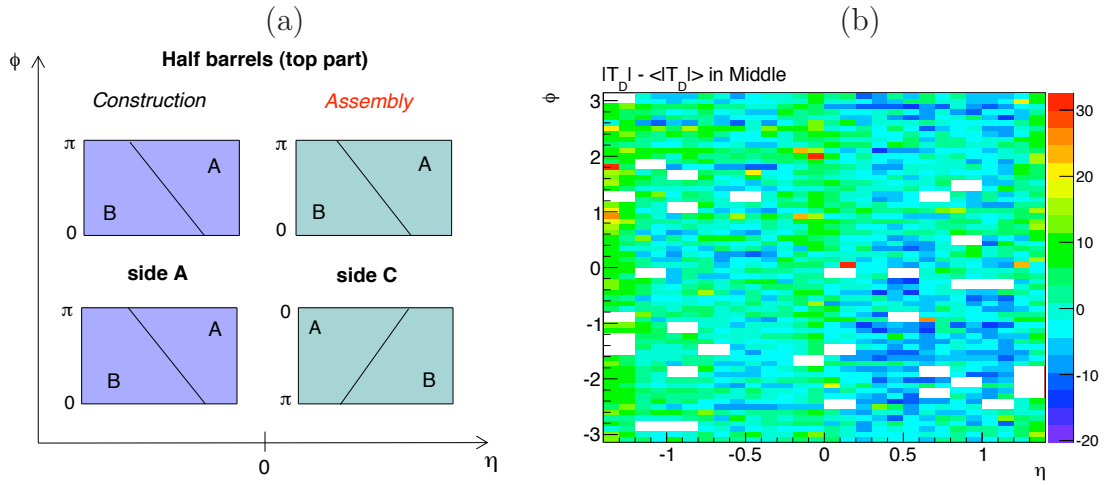

Figure 6.33: .(a):schematic view of the half barrels construction and assembly in the (η, ϕ) plane. (b): (η,ϕ) map in which the difference between the local weighted average T_D and $< T_D >$ the global average is plotted per bin of size $(0.1, 0.1)$. White rectangles correspond to areas where the HV is not nominal or where no data have been recorded.

Figure 6.33(b) represents the variations of the weighted average drift time values around the overall average in bins of (0.1,0.1) in the (η,ϕ) plan. is shown in Figure 6.33. From this illustration, the effects seen in the η and ϕ projections are visible, but a systematic compensation is not obvious. as discussed in section 6.8.2 such effect in seen in the case of the back compartment.

6.7.2 Shift Parameter

The η and ϕ distributions of the absolute shift parameter $|SH|$ are displayed in Figure 6.34(a-b). Some small but rather significant modulations appear in η. No particular structure is observed in the ϕ distribution although discontinuities appear in the module transitions. These

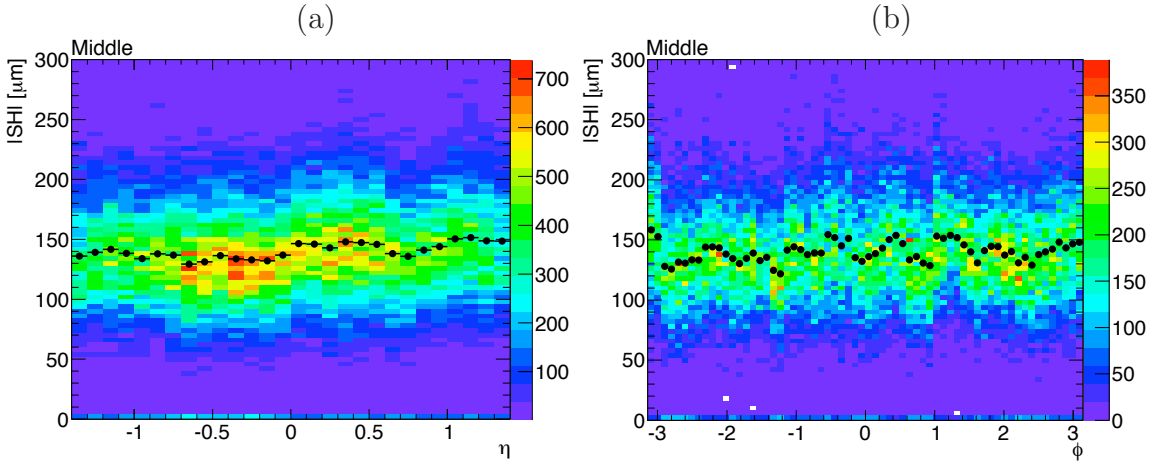

Figure 6.34: $|SH|$ as a function of (a) η and (b) ϕ in the Middle. Events are weighted by A^2_{max}. The black dots correspond to the Profile of the color plot.

effects are more clearer in Figure 6.35 that displays the variations of the local average value per bin of $(0.1, 0.1)$ with respect to the overall average. It indicates that in the negative z side (barrel C), the bottom part (negative ϕ) has shift parameter values somewhat lower than average. Similarly the module in ϕ comprised between $3\pi/16$ and $5\pi/16$ in the barrel A presents also lower shift values. These variations are intricate to interpret, but given their distribution throughout the detector acceptance they are likely to be due to mechanical construction issues.

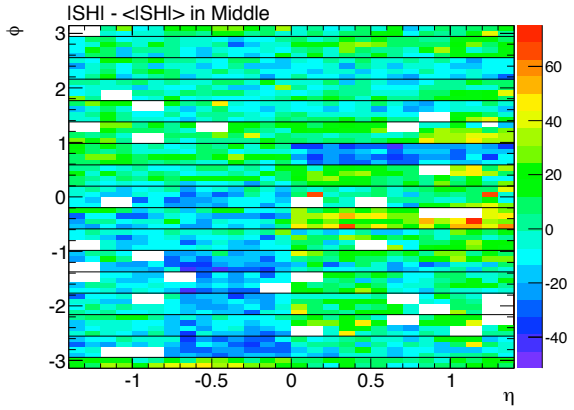

Figure 6.35: (η,ϕ) map in which $|SH| - < |SH| >$ is plotted bin per bin, $|SH|$ being the local weighted average and $< |SH| >$ the global average.

6.7.3 Uniformity of the Drift Time and Intrinsic Uniformity of the Calorimeter

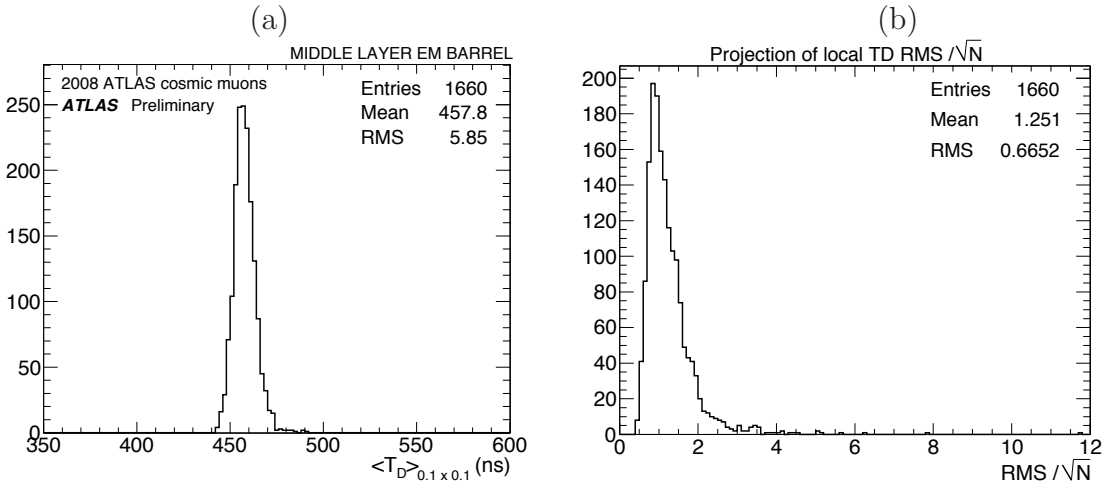

Figure 6.36: (a): Projection of local mean T_D.(b): Projection of local T_D RMS divided by the square root of the number of entries. The pulse drift time are weighted by A^2_{max}.

Figure 6.36(a) displays the distribution of the drift time averaged over $(0.1, 0.1)$ bins in (η, ϕ). The pulses from the bins are all weighted by A^2_{max}. Figure 6.36(b) illustrates the distribution of the error on these local T_D averages obtained by the RMS in.each bin divided

by the square root of the number of entries. The average error of 1.25 ns is well below the dispersion of the local TD averages of 5.85 ns. The available data is therefore accurate enough to reliably estimate the variations of the drift time with respect to the nominal design value. From this measurement the systematic dispersion of the gaps can be estimated and its impact on the response in energy of the calorimeter can be assessed. This study is done only for the Middle layer, which is the main contributor to the energy response of the detector as it represents $\sim 70\%$ of the total signal in the calorimeter.

The drift time uniformity U_{drift} corresponds to the ratio of the RMS and the mean value of the local drift time distribution. From Figure 6.36, it amounts to:

$$U_{drift} = 5.85/457.8 = 1.27 \pm 0.03\%. \tag{6.17}$$

Equations 6.3 (section 6.1) highlight the drift time and signal amplitude dependence on the gap variation. They also Illustrate that the drift time is more sensitive to the gap variation than the current amplitude by a ratio 1.3/0.3. The measurement of T_D is therefore a powerful tool to assess the intrinsic uniformity of the calorimeter.
Using the relation between the drift time and the gap and the gap dependence of the signal amplitude the impact of the gap variation U_C to the calorimeter response is derived from the drift time uniformity.The dispersion of the response due to the barrel calorimeter gap variations amounts to:

$$\left|\frac{\Delta A}{A}\right| \propto \frac{0.3}{1.3} \cdot \left|\frac{\Delta T_D}{T_D}\right| \longrightarrow U_C = U_{drift} \times \frac{0.3}{1.3} = 0.29 \pm 0.01\%. \tag{6.18}$$

Excluding transition zones in η, the gap variations amount to $5.7/457.4 = 1.25\%$ and the impact on the response is of 0.28%.

6.8 Results for the other compartments

The uniformity of the drift time and shift parameters in η and ϕ is presented in this section for the Front and Back compartments of the barrel and ends with the results for the Presampler.

6.8.1 The Front Layer

Figure 6.37(a-b) displays the distributions of T_D as a function of η and ϕ for the Front layer. The dot points represent the profile of these distributions and correspond to the average weighted drift time computed per bin of size $\Delta\eta = 0.1$ and $\Delta\phi = 0.1$. A similar structure as that observed for the middle layer is also present here, although the statistical precision is degraded. The dispersion of the distributions around the mean value of the drift time in the Front are quite equivalent to the Middle. Although not shown here [50] the distributions of TD for the two half barrels taken independently as a function of ϕ have a RMS values of 4.3 ns and 5.4 ns, respectively for the negative and positive half barrels in η. The RMS of the overall distribution is 3.2 ns, again denoting a systematic cancellation effect.

The differences arising (and visible) in Figure 6.37(a) between the profile values and the barycentres of the rectangular colored cells per slice in η is an effect of the asymmetry of the drift time distribution around its mean value. The tail at high T_D which is not present in the

2D plot limited to the interval $420 - 500\ ns$, increase the average drift time computed per η slice. Combined with limited statistics, this explain such differences. Limiting the T_D analysis to the interval $380 - 550\ ns$ (zone I in Figure 6.13(b)) would decrease the profile average T_D value by 3 ns in the Front layer. A similar cut has no visible effect ($< 1\ ns$) in the Middle compartment which enjoy a larger statistics. A same order effect is observed in the Back due to the cells size increase with η which compensate the limited statistics in this compartment.

The $|SH|$ distributions as a function of η and ϕ are displayed in Figure 6.38. Both distributions are rather uniform.

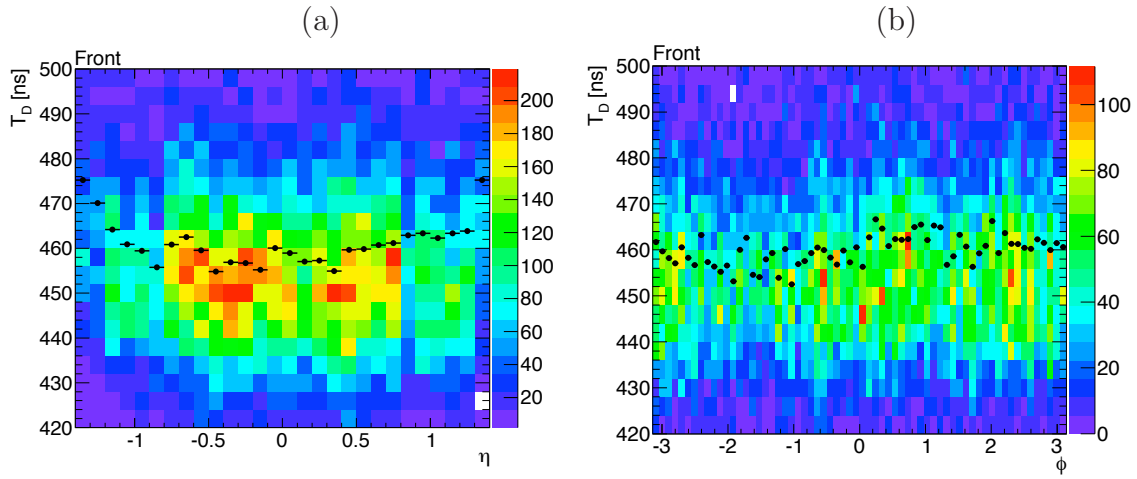

Figure 6.37: Distributions of the drift time as a function of η and ϕ in the Front, with the A^2_{max} weight.

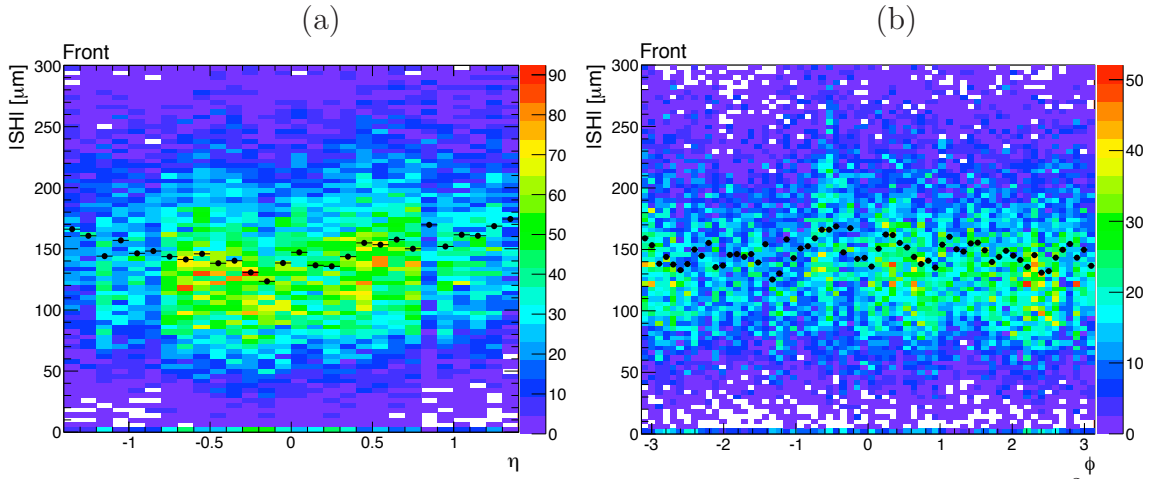

Figure 6.38: Absolute shift $|SH|$ as a function of η and ϕ in the Front, with the A^2_{max} weight.

6.8.2 The Back Layer

The T_D distributions as a function of η and ϕ for the Back layer of the calorimeter are displayed in Figures 6.39(a-b). The non uniform distribution of the event density is a consequence of

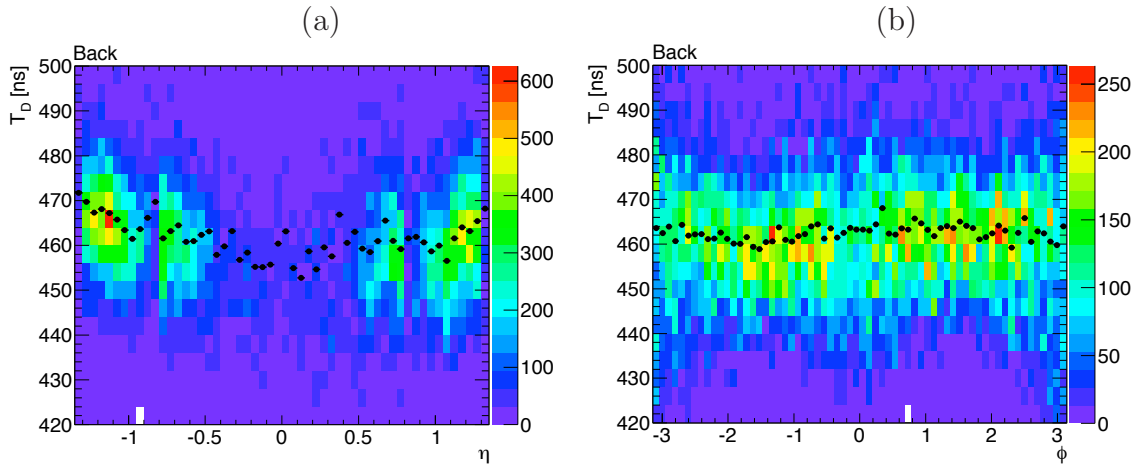

Figure 6.39: Distributions of the drift time as a function of η and ϕ in the Back, with A^2_{max} weight.

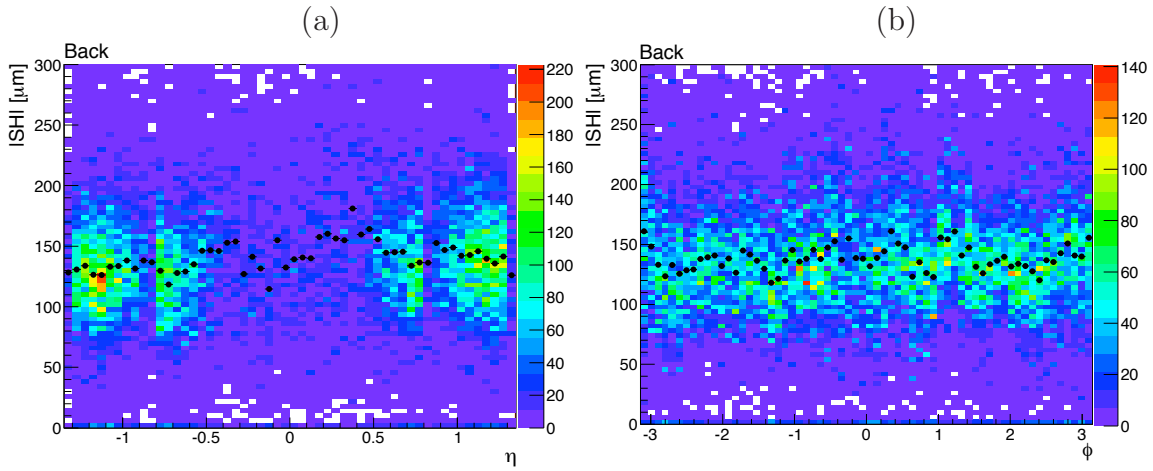

Figure 6.40: $|SH|$ as a function of η and ϕ in the Back, with A^2_{max} weight.

the Back layer projective geometry and reflects the cells size increase with η. The drift time is rather uniform in ϕ, a RMS value of 1.7 is found.
Figure 6.40(a-b) displays the distributions of the shift parameter in the η and ϕ directions. These distributions are rather uniform as well.

Figure 6.41(a) and (b) display the drift time distribution along the ϕ direction for the two wheels separately, in $\eta < 0$ and $\eta \geq 0$ respectively. A clear drift time modulation is observed in both half barrels. This is also visible in Figure 6.42(a) which displays the the variations of the local average value per bin of $(0.1, 0.1)$ with respect to the overall average drift time. As mentioned above (section 6.7.1) this modulation in ϕ is, as expected from the assembly of the calorimeter, opposite from one half barrel to the other, highlighting the rotation of one of the two half barrels along the vertical axis (Figure 6.33(a)) .

The modulation is only seen in the Back, and preferentially for small η values (About 16% of the statistics, $\sim$ 12 500 events, in the Back is contained in $|\eta| \lesssim 0.5$). A possible mechanical explanation of this feature is the presence of fixing points where the modules are clamped together. At the inner and outer edges of the barrel, The position and distance between

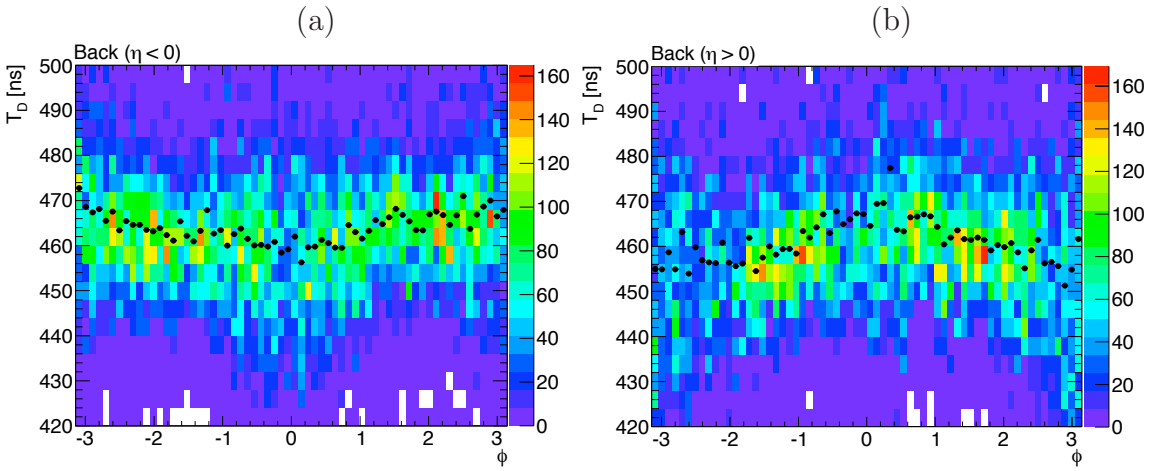

Figure 6.41: Distributions of the drift time as a function of ϕ in the Back, for (a) $\eta < 0$ and (b) $\eta > 0$. Events are weighted by A^2_{max}.

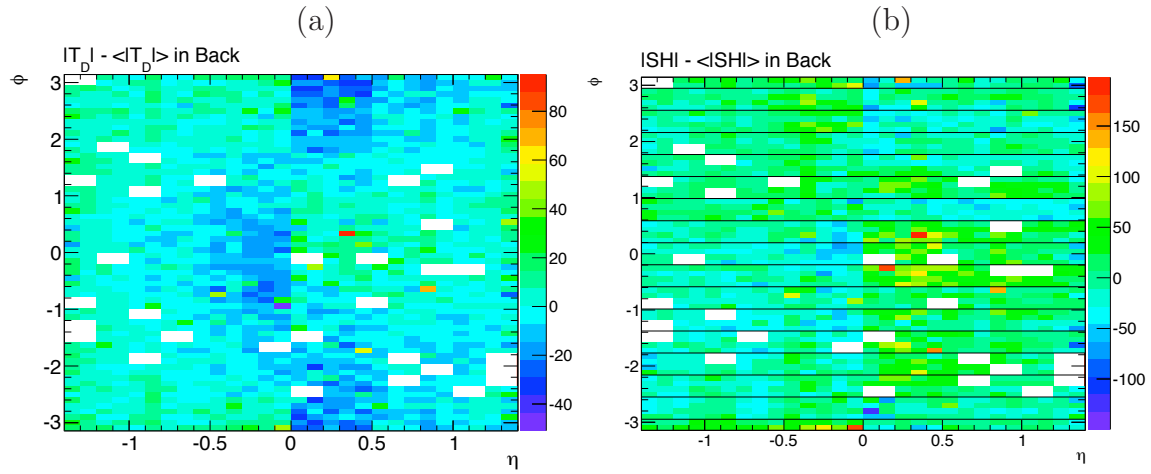

Figure 6.42: (a) $T_D - < T_D >$ and (b) $|SH| - < |SH| >$ in the (η,ϕ) map for the Back layer. These quantities have been estimated using the weight A^2_{max}.

the absorbers is ensured by precisely machined G10 glass-fibre composite bar. The G10 bars are screwed to rings made of stainless-stell that provide the rigidity and define the cylindric geometry of the barrel. Near the regions the absorbers are glued to the rings the gap would be reduced and the drift time lower than its average value, while the relative transverse flexibility of absorbers dilutes the effect away from the Back precision bar explaining why the modulations do not occur in the Middle. The positioning in the Front is less awkward which would also explain why such modulation is not observed in this layer.

Quantitatively, the ϕ drift time modulation of ± 5 ns observed in Figure 6.42(a) induces a gap variation of about 0.7% which corresponds to about 15 μm . Such dispersion is rather large [36] but still plausible. As was the case for the other layers, the overall RMS is significantly smaller than the RMS of the two half barrels independently. (These RMS and mean values of the drift time and shift distributions as a function of η and ϕ are summarized in Table 6.7 for

the Back and the other layers.)

6.8.3 Results in the Presampler

The Presampler, which provides a measurement of the EM shower energy lost in front of the calorimeter, is different from the other layers of the calorimeter by construction. It is made of narrow flat LAr layers (11 mm in depth) and uses the matter in front of the calorimeter as passive medium. The Presampler of made of 32 identical azimuthal sectors per half-barrel (, of 3.1 m long and 0.28 wide), providing a coverage $\Delta\eta \times \Delta\phi = 1.52 \times 0.2$. Each sector is made of heigh modules of different size in order to provide a constant granularity in η of 0.2. Each sector is enclosed by 0.4 mm glass-fibre composite plates. The electrodes are multi-layer circuits made of double sided cathode and three conductive layers anodes. As done in the EM barrel, the outer layers carry the high voltage (HV = 2000 V at nominal value) while the inner layer collects the ionization signal and routs out the signal via capacitive coupling. The electrodes are disposed in the (r,ϕ) plane, inducing an electric field oriented perpendicularly to the calorimeter one. The electrode gap varies from 1.9 to 2.0 mm in η to provide a constant granularity of $\Delta\eta \times \Delta\phi = 0.025 \times 0.1$.

The size of the gaps is slightly smaller than in the barrel layers, leading to values of T_D lower than in the rest of the calorimeter. In addition, this gap varies with η; the values for the 4 regions are given in Table 6.6.

The effect on the fitted drift time can be immediately seen in Figure 6.43(a), where discontinuities occur at the gap size transitions. Considering the gap dependence of the drift time given in equation 6.16, the prediction of the drift time variation between the η regions is derived, taking as reference numbers (g_0,T_D^0) the gap size and the mean T_D measured in the regions $0.8 < |\eta| < 1.2$. The predicted drift times T_D^{pred}, also given in Table 6.6, are illustrated by orange lines in Figure 6.43(a). Table 6.6. A very good agreement is observed between

η region	gap (in mm)	T_D^{pred} (in ns)
$\lvert\eta\rvert < 0.4$	1.966	432.3
$0.4 \leq \lvert\eta\rvert < 0.8$	1.936	423.7
$0.8 \leq \lvert\eta\rvert < 1.2$	2.006	443.8
$1.2 \leq \lvert\eta\rvert$	1.906	415.3

Table 6.6: Gap size values in the Presampler and predicted drift times using the regions $0.8 < |\eta| < 1.2$ as reference.

the measured and expected drift times along the η direction. This is also illustrated in Figure 6.43(b) that displays the the distribution of the drift time normalized to predicted value per η regions, as a function of η. As there is no bent sections in the Presampler, the pulse description is simpler than in the case of the other layers. While the variations in η are large, the ϕ dependence of the drift time is negligible as shown in Figure 6.44(a) and (b), respectively before and after rescaling the drift time values according to gap size variation in the η regions. However a clear difference between the number of events for $\phi > 0$ (corresponding to the top part of the detector) and $\phi < 0$ (corresponding to the bottom part) appears. Such an effect is expected from the amount of material allowing for the radiation of a photon upstream along the path of the cosmic muons.

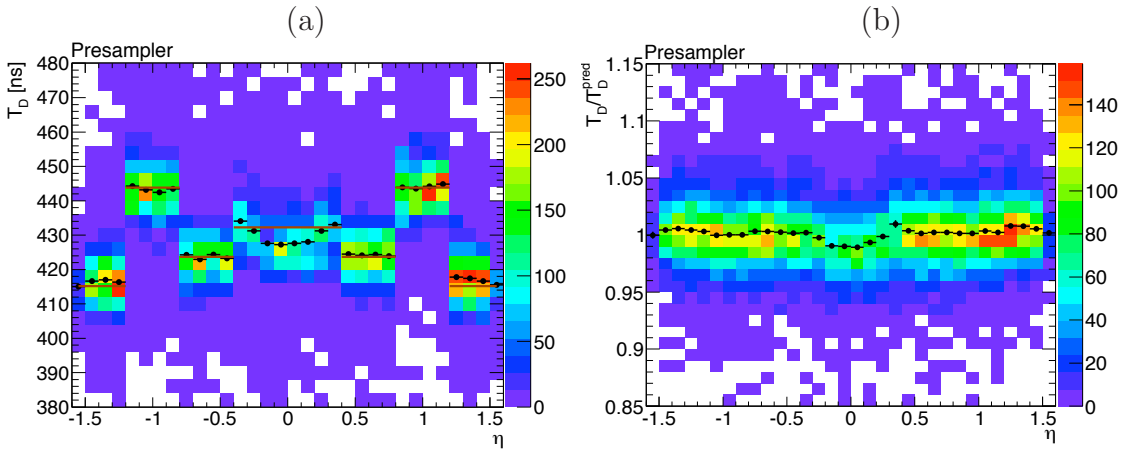

Figure 6.43: (a): Distribution of the drift time as a function of η in the Presampler, with A^2_{max} weight. The black dots correspond to the Profile of the color plot. In addition, the orange line represents the prediction starting from the region $0.8 < |\eta| < 1.2$, using the relation 6.16 and the gap values given in Table 6.6. (b): Distribution of the drift time T_D divided by the predicted value, as a function of η.

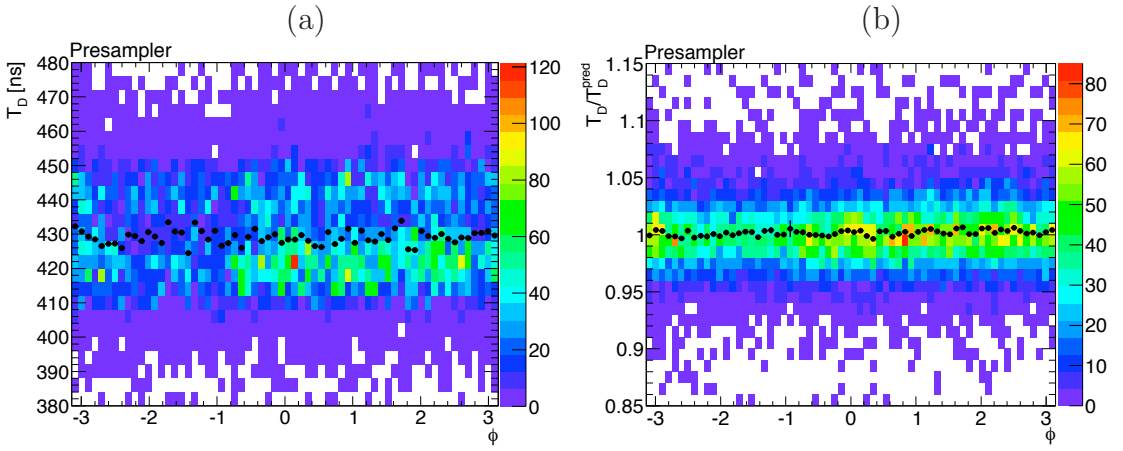

Figure 6.44: (a) Drift time and (b) Drift time divided by the predicted value, as a function of ϕ in the Presampler.

Figure 6.45(a-b) illustrates the distribution of the shift along the η and ϕ directions. Smaller values of the $|SH|$ is observed as compared to the accordion layers. This is expected due to mechanical constraints on the electrodes which are individually glued in between two G10 frames [47]. On average, a mean value of the shift $< |SH| >= 69$ μm is found in the Presampler, as compared to 140 μm in the accordion section. Variations in the average shift value are expected along the η direction, as the gap size varies, although the limited statistics and the large amount of pulses fitted with a shift parameter at ~ 0 μm lead intricate any comparison with expectation. No specific variation is observed as a function of ϕ, as expected from the Presampler geometry.

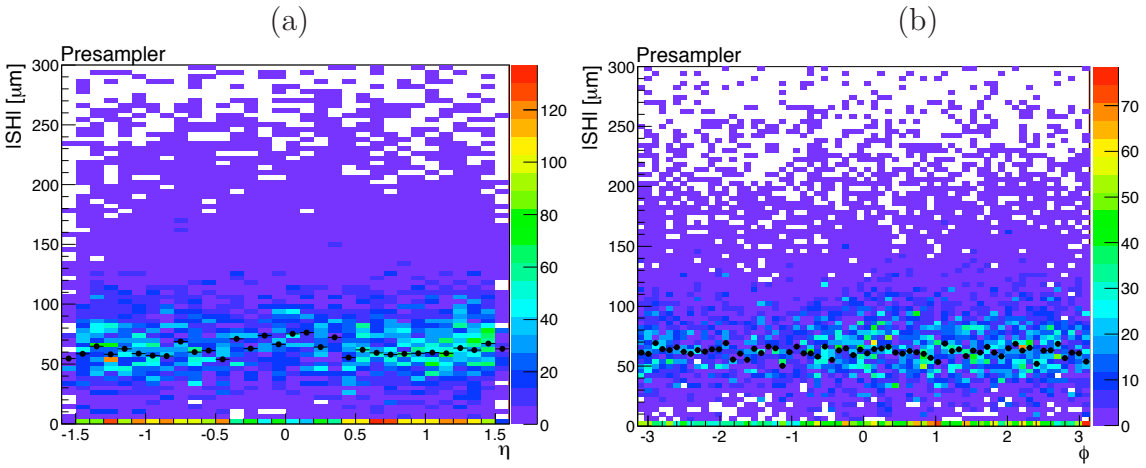

Figure 6.45: $|SH|$ as a function of η and ϕ in the Presampler, with A^2_{max} weight.

6.9 Overall Comparison of Layers

6.9.1 Comparison of the RMS and the Mean values

The profiles of the drift time and shift distributions in both the η and ϕ directions illustrated in the previous section for the barrel layers and the Presampler are used to derive the mean values of these parameters and their dispersion. The numbers for the RMS and mean values of the drift time and shift distributions profiles in η and ϕ are summarized in Table 6.7 for the Presampler and the three layers of the EM barrel.

	Presampler		Front		Middle		Back	
all η	RMS	Mean	RMS	Mean	RMS	Mean	RMS	Mean
T_D (ns) versus η	1.9	428.5	5.1	461.2	3.5	457.8	4.2	461.7
$\|SH\|$ (microns) versus η	5.9	62.5	12.2	149.6	6.3	140.4	12.2	141.1
T_D (ns) versus ϕ	1.9	429.1	3.2	459.8	1.8	457.5	1.7	462.5
$\|SH\|$ (microns) versus ϕ	4.1	61.9	9.7	147.1	8.3	140.0	10.3	138.3
$\eta < 0$								
T_D (ns) versus ϕ	3.1	428.9	4.3	459.6	2.8	459.2	3.3	464.0
$\|SH\|$ (microns) versus ϕ	6.3	61.6	12.9	140.7	11.4	134.9	13.8	132.4
$\eta > 0$								
T_D (ns) versus ϕ	2.7	429.1	5.4	460.1	3.1	455.8	4.7	460.9
$\|SH\|$ (microns) versus ϕ	4.8	62.4	14.9	152.8	13.5	145.9	20.2	145.5

Table 6.7: Comparison of RMS and Mean values for T_D and $|SH|$, between the different layers.

- The T_D dispersion in the η direction is larger than along ϕ in the three layers of the barrel. This is a consequence of the larger average drift times measured in the electrode and half-barrel transition regions (respectively $|\eta| = 0.8$ and $\eta = 0$), where the electric

field is reduced. In the Presampler, the two dispersions are equal (the dispersion in η is obtained after accounting for the size gap variation with η).

- The Front and Back layers have in average a larger drift time than the Middle which was seen in Figure 6.13 by larger tail at high drift time [3)]. This could be explained by the smaller size of these compartments with respect to the Middle, of the order of one absorber wave or less. With an increased contribution of the bent sections, the total (straight and bent sections) signal triangle would have a larger drift time.

These results show consistent and similar uniformity of the drift time and dispersion of the electrode shift. This gives confidence in the contribution of the Front and Back layers to the gap dispersion and its impact on the calorimeter response uniformity.

6.9.2 Drift Velocity

The drift time of the ionization electrons in the LAr gap corresponds to the ratio of the gap width divided by the electron drift velocity in the LAr. During the beam test a map of the absorbers thickness of the exposed modules, with a $5 \times 5\ mm^2$ granularity, was made using an ultra-sound system. The results have been using to derive the opposite impact on the gap size variation in η (average in ϕ). To quantify the consistency of the drift time measurements among layers, the drift velocity is derived accounting for the gap variation in the barrel layers and the Presampler. The drift velocity is a function of the electrical field E applied between the electrode and the lead:

$$V[E] = g/T_D \tag{6.19}$$

For a consistent comparison between the different layers, the drift time measurements should yield similar drift velocities for the various layers per unit field of 1 kV/mm. The drift velocity is normalized through the formula:

$$V[1kV/mm] = \frac{g}{T_D}\Big(\frac{1000\ V.g}{HV.1\ mm}\Big)^{0.3}, \tag{6.20}$$

where the HV dependence comes from equation 6.5 and the gap dependence of T_D from equation 6.16. Figure 6.46 diplays the rescaled drift velocities in the Presampler and three layers (at nominal voltage HV = 2000V). The mean drift velocity for the three layers are in good agreement. The Presampler is however in average 3% lower.

The dependence in η of this normalized drift velocity is displayed in Figure 6.47 for all four layers. These distributions are rather flat and it is particularly interesting to see that the Presampler distribution is also constant, despite the variation of the gaps along the η direction. The small dump visible at the transition regions in the Middle comes from the smaller drift time measured in these regions with respect to predictions, suggesting a larger gap in transitions (similarly lower electric field).

[3)] It has been verified that the weight A^2_{max}, also used for the Front and Back layers, have a consistent impact on the drift time and shift distributions shape and mean value.

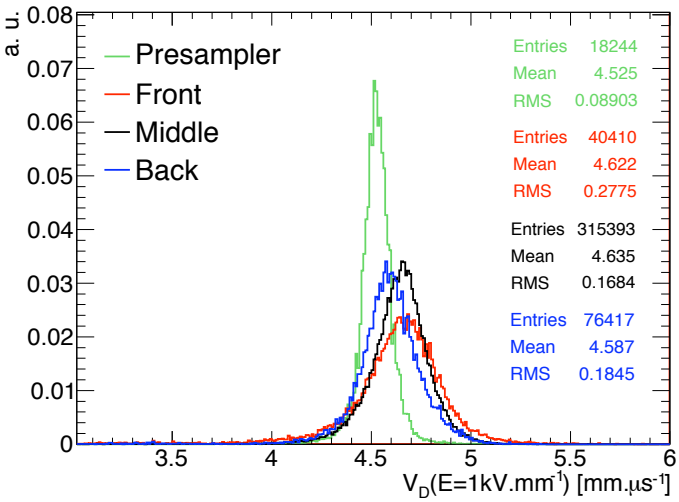

Figure 6.46: Drift velocity rescaled to a field of 1kV/mm, in green for the Presampler, in red for the Front, in black for the Middle, and in blue for the Back. The events used for this plots are at nominal voltage.

6.9.3 Correlation Between Layers

Given that the absorbers and the electrodes are on single support structure throughout the layers a strong correlation should *a priori* appear between layers. Because the absorbers are more rigid than the electrodes such correlation should be stronger for the drift time than for the shift of the electrodes. However because the fixed structure is in the front and on the back of the detector, the results for the front and back layers could somewhat be dissociated from those of the middle layer.

	Front/Middle	Back/Middle
TD	0.114	0.109
$\|SH\|$	0.175	0.217

Table 6.8: Correlation factors for T_D and $|SH|$, between Front and Middle and between Back and Middle.

The standard correlation coefficients between cells from different adjacent layers are reported in Table 6.8. For the Front to Middle comparison, 4 cells in the Middle are grouped in azimuth, and 8 cells of the Front are grouped in η in order to cover the same 0.025×0.1 area, in $\eta \times \phi$ bins. For the Middle to Back comparison cells have been grouped by two in the Middle, in the η direction, in order to cover the same area of 0.05×0.025 as one Back cell. The observed correlations are rather small. Which is somewhat expected from the fact that measurements of drift time and shift have rather large errors compared to the subtle effects that are seeked.

6.9.4 Correlation Between Adjacent Cells in η and ϕ

A relatively large correlation is expected between adjacent cells in η and a weaker correlation between adjacent cells in ϕ. The correlation coefficients of cells adjacent in η and between cells adjacent in ϕ are shown in Table 6.9. As expected the correlations in η are stronger than in

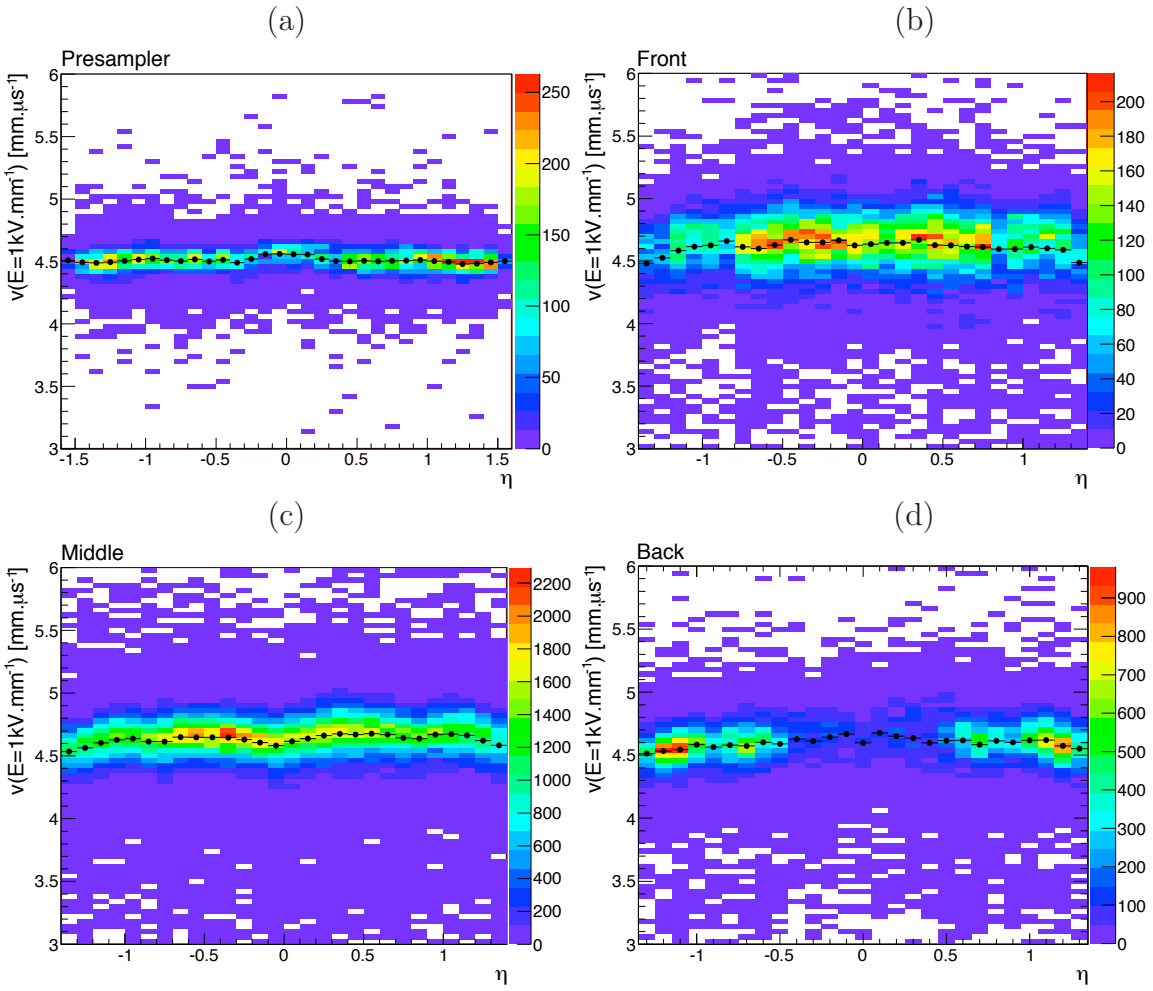

Figure 6.47: Drift velocity rescaled to an electric field E of 1kV/mm in the Presampler and three barrel layers of the calorimeter, as a function of η. The selected events in this plots are at nominal voltage (2000 V).

ϕ and it is particularly large in the middle layer. This strong correlation further confirms the assumption that the observations that are made with the drift time measurements are in fact due to intrinsic mechanical effects in the detector.

6.10 Study with Reduced High Voltage

A small fraction ($\sim$ 5%) of the high voltage sectors (of size 0.2×0.2 in the calorimeter, and 0.4×0.2 in the Presampler) are being operated with a voltage lower than the nominal value. Figure 6.7 displays the (η,ϕ) map of the 4 layers, where the high voltage was lower than the nominal 2000 V value during the data taking period. In general one side of the electrode has a reduced voltage and the other carries the nominal high voltage. This induces two triangles from the ionization of the two LAr gaps on both sides of the electrode with different drift time (as seen in equations 6.5 and 6.6) and a global drift time larger than the average at nominal

	Front	Middle	Back
Correlation between η neighbors			
in T_D	0.200	0.420	0.125
in $\|SH\|$	0.199	0.387	0.198
Correlation between ϕ neighbors			
in T_D	0.050	0.154	0.180
in $\|SH\|$	0.037	0.253	0.209

Table 6.9: Correlation factors for T_D and $|SH|$, between adjacent cells in η or ϕ.

voltage. There are however two zones in $[(\eta_1, \eta_2); (\phi_1, \phi_2)]$:

- $[(-0.2, 0); (-\pi + \pi/16, -\pi + 2\pi/16)]$
- $[(0, 0.2); (-\pi + 5\pi/16, -\pi + 6\pi/16)]$

where the voltage was reduced to 1600 V on both sides. This specific case is discussed first.

6.10.1 Reduced Voltage on both sides of the electrode

The drift time T_D and the shift $|SH|$ are extracted for the zones in the Middle where 1600 V is applied on both sides of the electrode. From the equations 6.5 and 6.6 the value for the T_D is expected to be similar to the previous study at nominal voltage (2000 V on both sides of the electrode). The gap variation is *a priori* independent of the voltage.
Table 6.10 illustrates the average drift time for the Front, Middle and Back layers. A good agreement is observed in each layers despite the limited statistics for the Front and Back. The

Layer	$< T_D >$ for 2000 V	$< T_D >$ for 1600 V	# pulses for 1600 V
Front	459.8 ns	455.2 ns	216
Middle	457.4 ns	457.7 ns	1324
Back	463.0 ns	458.7 ns	114

Table 6.10: Average values of the drift time for HV =2000 V or 1600 V applied on both sides of the electrode. Events are weighted by A^2_{max}. For information, the number of pulses concerned by the case 1600 V is given in the last column.

average drift times measured in FEBs with symmetric voltage at 1600 V and 2000 V agree well in the different layers of the barrel. There is no sector with symmetric voltage at 1600 V in the Presampler.

Figure 6.48 displays the distribution of the shift parameter in the cases of symmetric voltage at 2000 V and 1600 V (respectively (a) and (b)). In the case of nominal voltage on both sides of the electrode, the shift distribution has as expected a symmetric behavior around 0 μm. However, a larger fraction of pulses have a positive shift. The case of symmetric high voltage at 1600 V displays a symmetric distribution as well, centered at 0 μm.This asymmetric events density is a feature of the fit procedure performed within Minuit. As expected from the formula 6.5 and 6.6 implemented in the code to account for the electrode shift and HV dependence on the

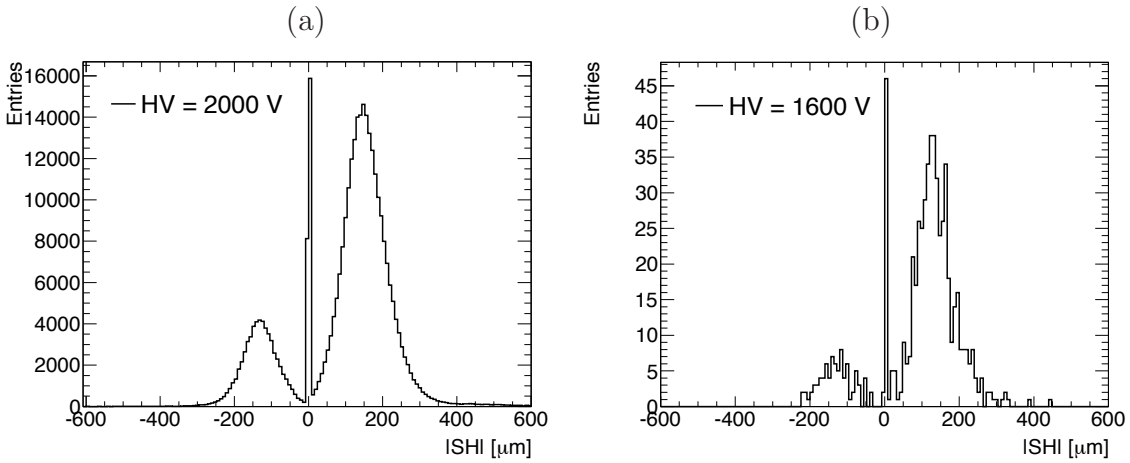

Figure 6.48: Distributions of the Shift parameter ($2000 * x$) in the Middle in the case of (a) nominal voltage and (b) 1600 V on both sides of the electrode.

two drift times, the sign of the electrode shift is imposed in these equations, the electrode is shifted toward the side associated to $(TD_1; I_1)$. The input value for the parameter related to the shift in the fit is fixed at $+150$ μm, based on typical value measured in the calorimeter. When the shift is actually opposite to the arbitrary initial choice, the fit parameter evolutes in the phase space to reach negative shift value, passing through the critical point at 0 μm where secondary minima of the fit χ^2 may arise, inducing the peak observed in the distribution.

6.10.2 Asymmetric HV distribution: nominal on one side and reduced on the other

Equations 6.5 and 6.6 underline the drift time evolution with asymmetric high voltage. The drift time average value found for the different cases of low voltage (between 400 and 1600 V) on one side of the electrode can be rescaled to the drift time at nominal voltage. The drift time uniformity as a function of the HV relies on a good prediction of the value of α.

As mentioned in the introduction, the value $\alpha = 0.3$ has been chosen for this study. Different values of α have been tried though. Initially the value used in the fit prediction was based on measurements in barrel and end-cap modules exposed to electron beams (1999) [52]. The barrel module was exposed to 100 GeV and 245 GeV electrons beams while the end-cap module was tested with 193 GeV. The high voltage was varied from 50 to 2000 V in the barrel. The parametrization [53] was used to extract the electrical field dependence of the drift velocity although it was observed that the description was not accurate in the whole range with a unique value of α. From 1 to 2 kV/cm, the value $\alpha = 0.38 \pm 0.1$ was found in the barrel [52].

The cosmic pulses recorded in FEB where the high voltage is asymmetric (nominal on one side and lower on the other side) are used to estimate the value of α that correctly account for the drift time dependence on HV. However, it has been observed using the parametrization [53] that differences were observed when varying the high voltage range for extrapolation, the value of α increasing with the electric range. Figure 6.49 illustrates the averaged drift time T_D in the Middle as a function of the effective high voltage for different values of the exponent α used in equations 6.5-6.8. The effective high voltage is the applied voltage corrected for the

voltage decrease due to the resistor used the pickup noise filter $HV_{eff} = HV_{app} - R_{filter} \times I$. The value $\alpha = 0.3$ yields the best description of the HV dependence of the T_D measurement in the approximative HV range [800, 2000 V] (corresponding to an electric field range [0.4-1 kV/cm]). This method relies on the fact that the nominal drift time for the cells considered is constant. Of course, with this assumption, the present data is not the most accurate to derive this exponent coefficient. For instance a HV scan within a single cell would have been more precise.

As well, a more precise estimation of the value of α is derived from the comparison between the two symmetric HV cases in cosmic muon data and the result quoted in [53]. Using the parametrization given in [53] for the drift velocity of free electrons in LAr, the value found for α in a small high voltage range (8-12 kV/mm):

$$\alpha = 0.316 \pm 0.030 \tag{6.21}$$

when accounting for the correlation between errors associated to the drift velocity values at the range limits[4)]. The mean value for the drift time found in the case of 1600 V on both sides of the electrode is $< T_D > (1600\ V) = 457.7\ ns$, which is in good agreement with the mean drift time measured in the nominal HV case $< T_D > (2000\ V) = 457.4\ ns$. However as shown in Figure 6.7(a) the two FEBs where the HV is at 1600 V on both sides of the electrode are located at the half-barrel transition region $-0.2 < \eta < 0.2$ (and are neighbors in ϕ around 1.5), where the effective high voltage is lower and the drift time larger of about 2 ns in average. For a proper comparison with the nominal HV case, the mean drift time at 1600 V is rescaled by the this difference of 2 ns, although these 2 ns are accounting for as systematic error on the drift time, and the mean value of the drift time at 2000 V is estimated in the cells that belong to ϕ ring in the η range of the two FEBs at 1600 V (the statistical errors are also included):

$$< T_D > (1600\ V) \rightarrow 459.7 \pm 2.0\ ns \tag{6.22}$$

$$< T_D > (2000\ V) = 460.2 \pm 0.1\ ns \quad (-0.2 < \eta < 0.2) \tag{6.23}$$

Using equations 6.5 and 6.6 in the approximation of small HV variations, the value found for α is:

$$\alpha = 0.295 \pm 0.028 \tag{6.24}$$

which is in good agreement with prediction [53]. The combined result leads to:

$$\alpha = 0.310 \pm 0.020 \tag{6.25}$$

Figure 6.50 illustrates the corrected dependence of T_D as a function of the effective high voltage, for the Front, the Middle and the Back, using the exponent coefficient $\alpha = 0.3$. It corresponds to the mean value found for the drift time for different voltages when extracting TD_{2000} from Equations 6.5.

The drift time dependence seems to be well corrected for in each of the layers. The average drift times for each layer after the correction is applied are reported in Table 6.11.

Fortunately, the Presampler is less affected by high voltage problems. Only five sectors are not at nominal voltage and receive almost no high voltage on one side of the electrode ($HV < 1\ V$ in all cases) while the other side is at 2000 V. This implies that the total signal

[4)] The term of correlation is 1.10, reflecting that the two errors are almost 100% correlated).

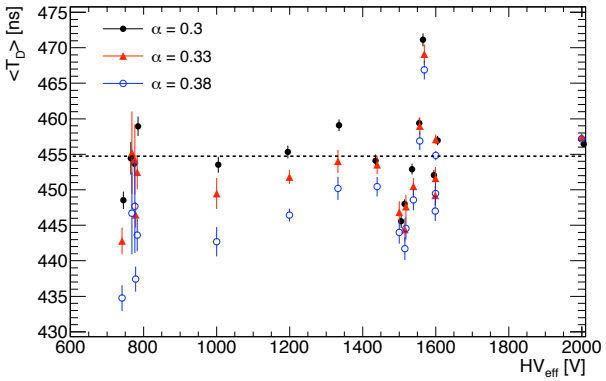

Figure 6.49: Corrected drift time TD as a function of the effective high voltage, in the Middle. The black dots correspond to the case $\alpha = 0.3$ in the relations 6.5-6.8, the red triangles to $\alpha = 0.33$ and the blue open dots to $\alpha = 0.38$.

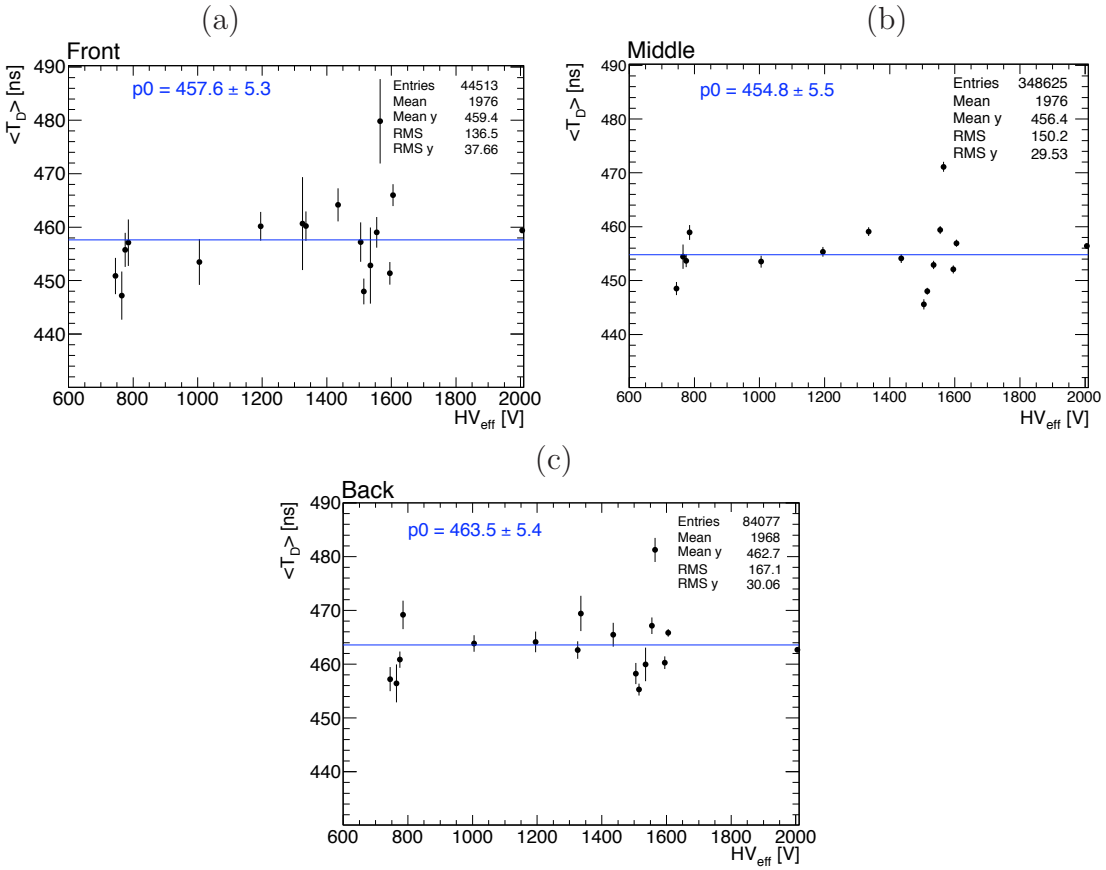

Figure 6.50: Corrected drift time T_D as a function of the effective high voltage with $\alpha = 0.3$ for: (a) Front, (b) Middle and (c) Back.

almost comes from only one triangle, the total amplitude is approximatively reduced by a factor 2. The drift time measure in these sectors should be of the same order of the average value found at nominal HV. However, among the 108 pulses from the five sectors at reduced voltage in the Presampler (passing the selection criteria) it was observed that the drift time was generally smaller or larger than in the case of nominal voltage (average around $\sim 250\ ns$), as illustrated in Figure 6.51. It has been observed that for these cases of very large difference in the HV on both sides of the electrode, the formula 6.5-6.6 used to constrain the pulse shape and extract the drift time and shift parameters are not consistent anymore. The fit however converges and describes well the shape, as illustrated in Figure 6.52(a) and (b) respectively for the pulse with a low and large fitted drift time. Rather "normal" drift time are expected from the pulses shape, confirming that only the side at 2000 V significantly contribute to the total signal. In such extreme case of HV difference, or as was observed in the Front and Middle for asymmetric voltage with 400 V and 2000 V on both sides, the formula should be protected to, the value of α changed so that the drift time and shift parameters value have meaning.

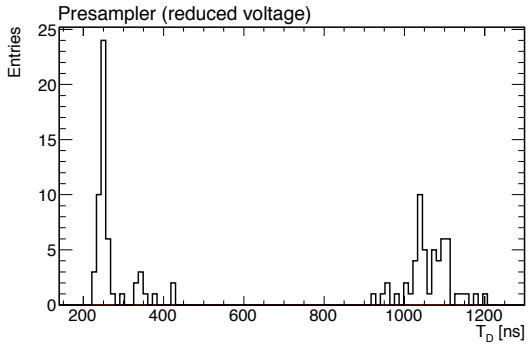

Figure 6.51: Distribution of the drift time in the Presampler in the case of reduced voltage.

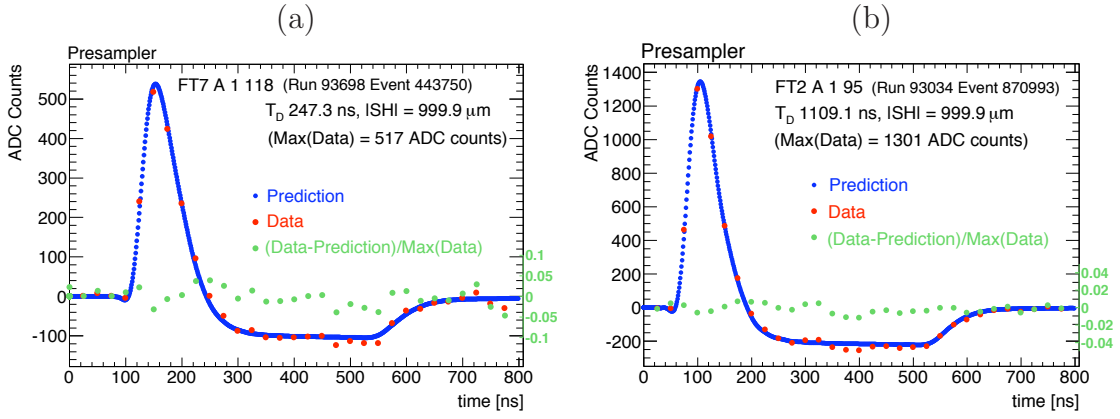

Figure 6.52: Examples of pulse in the Presampler, in the case of reduced voltage. In (a) a low drift time is extracted from the fit while in (b) a large drift time is found, although these two distributions have a normal behavior. The shift parameter reach the fir limit in both cases.

The distributions of the shift parameter are illustrated in Figure 6.53, for different high voltage configurations. These distributions are very different from those for the case of 2000V

Layer	$< TD >$ for 2000V	$< TD >$ from the fit
Front	459.8 ns	457.6±5.3 ns
Middle	457.4 ns	454.8±5.5 ns
Back	463.0 ns	463.5±5.4 ns

Table 6.11: Weighted average values of the drift time for the nominal HV compared to the TD value extracted from a fit of a polynomial of degree 0.

or 1600V as expected from the artificial shift introduced by the asymmetric high voltage. The main reason why they differ is that the HV difference can be interpreted as an intrinsic shift of the electrode. This can be easily seen by comparison of the equations 6.5 and 6.6, which are initially written as two different drift times for different high voltage on both sides of the electrode (straight section) and a shift x of the electrode. When the high voltage is symmetric, the difference between these drift times is proportional to the physical electrode shift. When assuming the electrode centered and the high voltage asymmetric, the difference relies on high voltage ratio between the two electrode sides, at the power α. Solving the drift time difference in these equations yields an equivalent residual shift due to the difference in high voltage (when the electrode is perfectly centered) of:

$$SH_{HV} = 2000 \times \frac{1}{2} \frac{(\frac{2000}{HV})^{\alpha} - 1}{1 + \alpha} \tag{6.26}$$

The dirac function previously at zero in the distribution of the shift, corresponding to a well centered electrode, is now displaced to SH_{HV}. As shown in Figure 6.53, the observation corresponds well to the prediction, represented by red lines. It should also be noted that the distribution is not symmetric around zero anymore but it is around SH_{HV}. It is therefore better illustrated keeping the sign of the shift, even though the sign of the shift is completely arbitrary (the electrode cannot distinguish from which side the ionization electrons are arriving). A larger dissymmetry in events population is observed when decreasing the high voltage one side of the electrode which invert for the cases of HV = 1000 V and below. This is explained by the value of the artificial shift when the electrode is centered that becomes greater than the input value of the shift parameter in the fit for HV below 1200 V ($SH(1200V) \approx 128\ \mu m$ while $SH(1000V) \approx 174\ \mu m$).

6.10.3 All Voltages

6.10.4 The Drift Time

Figure 6.54 displays the distribution of the weighted average drift time in the (η,ϕ) plane for the Presampler and the three layers of the calorimeter with all voltage configurations considered together (computed per bin of size (0.1,0.1)). The drift time value for low voltages are obtained after accounting for the HV dependence of the drift time and are therefore comparable to the nominal case. After the HV correction is applied the values of the drift time are in fair agreement with the overall average in the three layers of the EM barrel. Nevertheless, in some regions where HV is reduced the drift time values are not in complete agreement. In particular, there are three regions in Front and the Middle that show significantly lower TD than average (two of these regions are also visible in the Back). The regions correspond to the specific case with

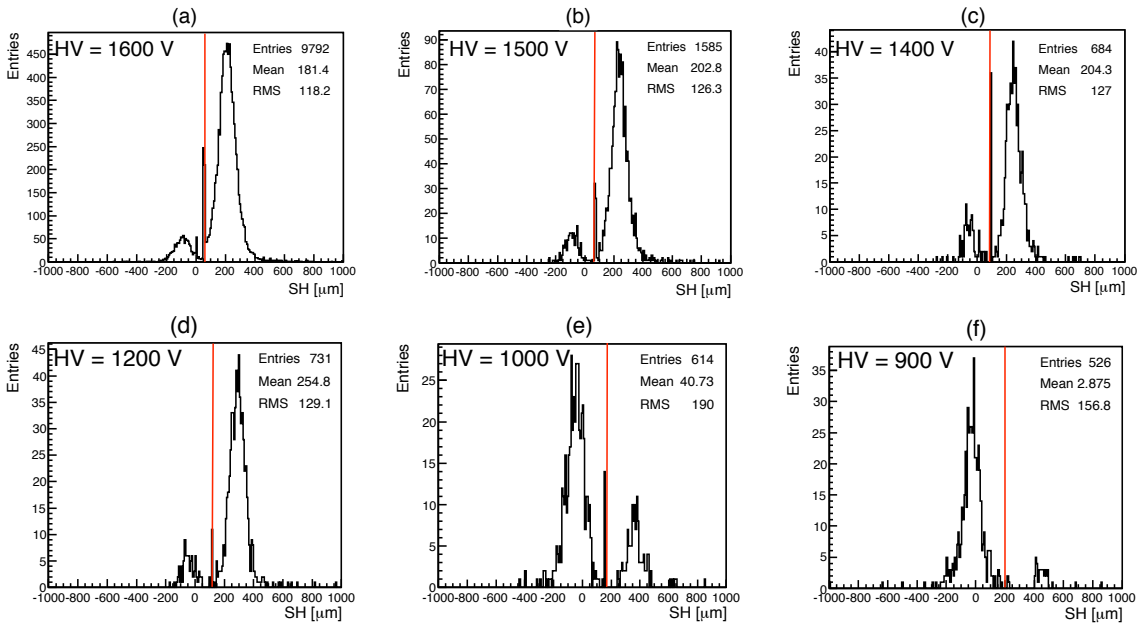

Figure 6.53: Distribution of the shift SH for the different asymmetric HV cases: 2000 V on one side of the electrode and (a) 1600 V, (b) 1500 V, (c) 1400 V, (d) 1200 V, (e) 1000 V and (f) 900 V on the other side.The black line corresponds to the expected peak value (see text for details).

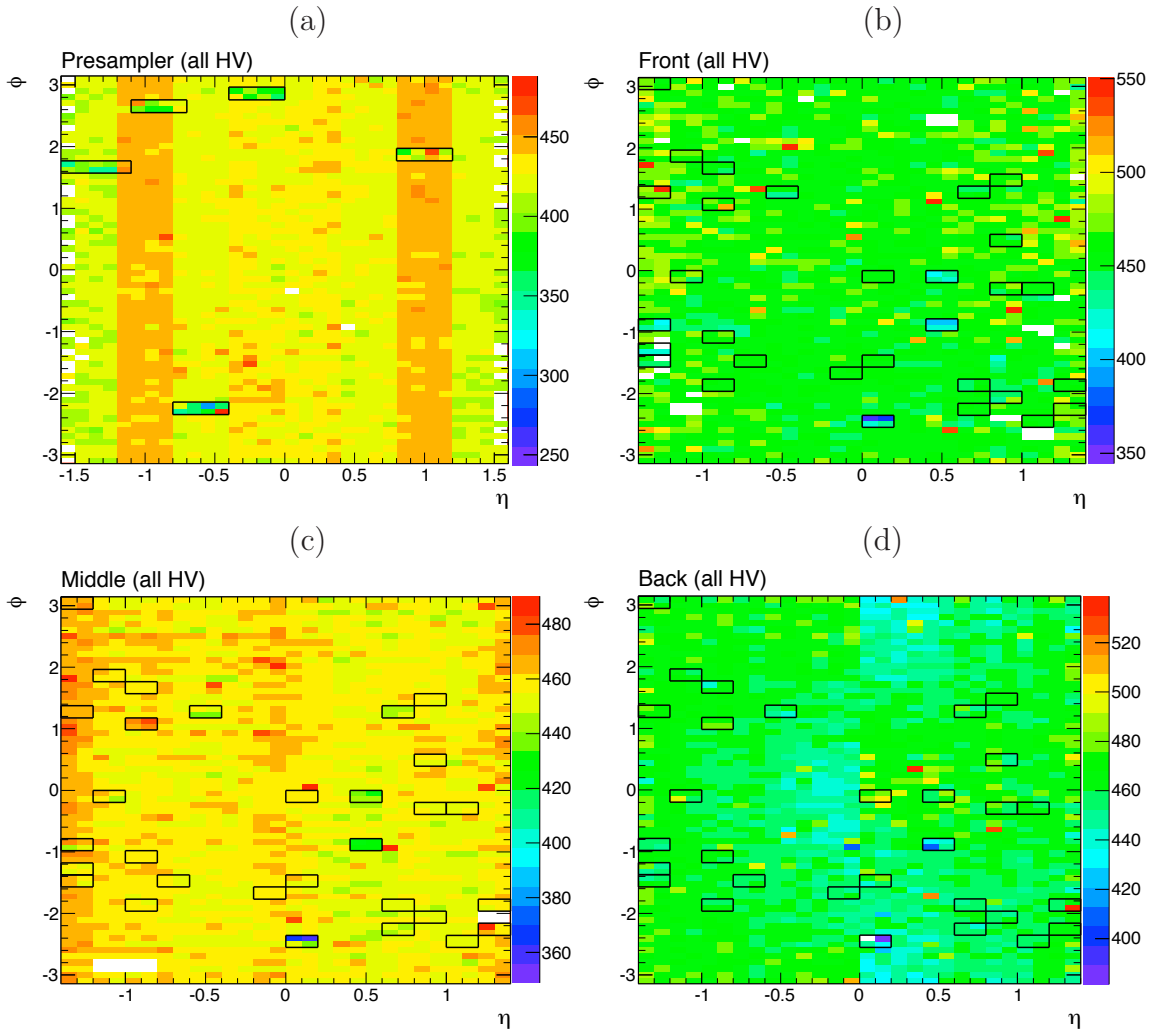

Figure 6.54: (η,ϕ) map for TD (a) in the Presampler, (b) Front, (c) Middle and (d) Back, including all voltage configurations. The regions where the high voltage is lower than the nominal value are surrounded by black boxes. White zones correspond to regions of the detector where no data have been recorded.

a high voltage lower than the nominal value appear to a significantly lower TD than average. These regions correspond to the case of the largest HV difference between the two sides of the electrode, with 400 V on one side and the nominal 2000 V on the other side. As mentioned above, the value chosen for α is no more consistent when considering such HV range. A larger value for α would be expected (from the fit of the drift velocity), which would increase the drift time.

The bands drawn in η for the Presampler reflect the gap variation. This layer shows large discrepancy in the drift time obtained at nominal and low voltage cases. This is explained by the very low voltage value (typically smaller than 1 V) applied on the reduced voltage regions. No reliable results are expected from these regions.

Drift time uniformity Extending the analysis done in section 6.7.3 to all HV configurations, the T_D dispersion in the Middle increases from 5.85 ns (RMS) to 7.36 ns. The estimated impact on the uniformity of the response in energy is degraded to 0.39% from an initial value of 0.29%. This degradation of the results highlights the limitations of the HV correction.

6.10.5 The Drift Velocity

Figure 6.55 displays the distributions of the weighted average drift velocity in (η,ϕ) map, computed per bin of size (0.1;0.1) and using equation 6.20, where the drift time value is already rescaled to HV=2000V and the gap variation with η accounted for, respectively in (a) the Presampler, (b) the Front, (c) the Middle and (d) the Back. These Figures show an overall good understanding of the drift time measurements and the detector description. The visible effects are quite likely due to mechanical deformations or large HV differences.

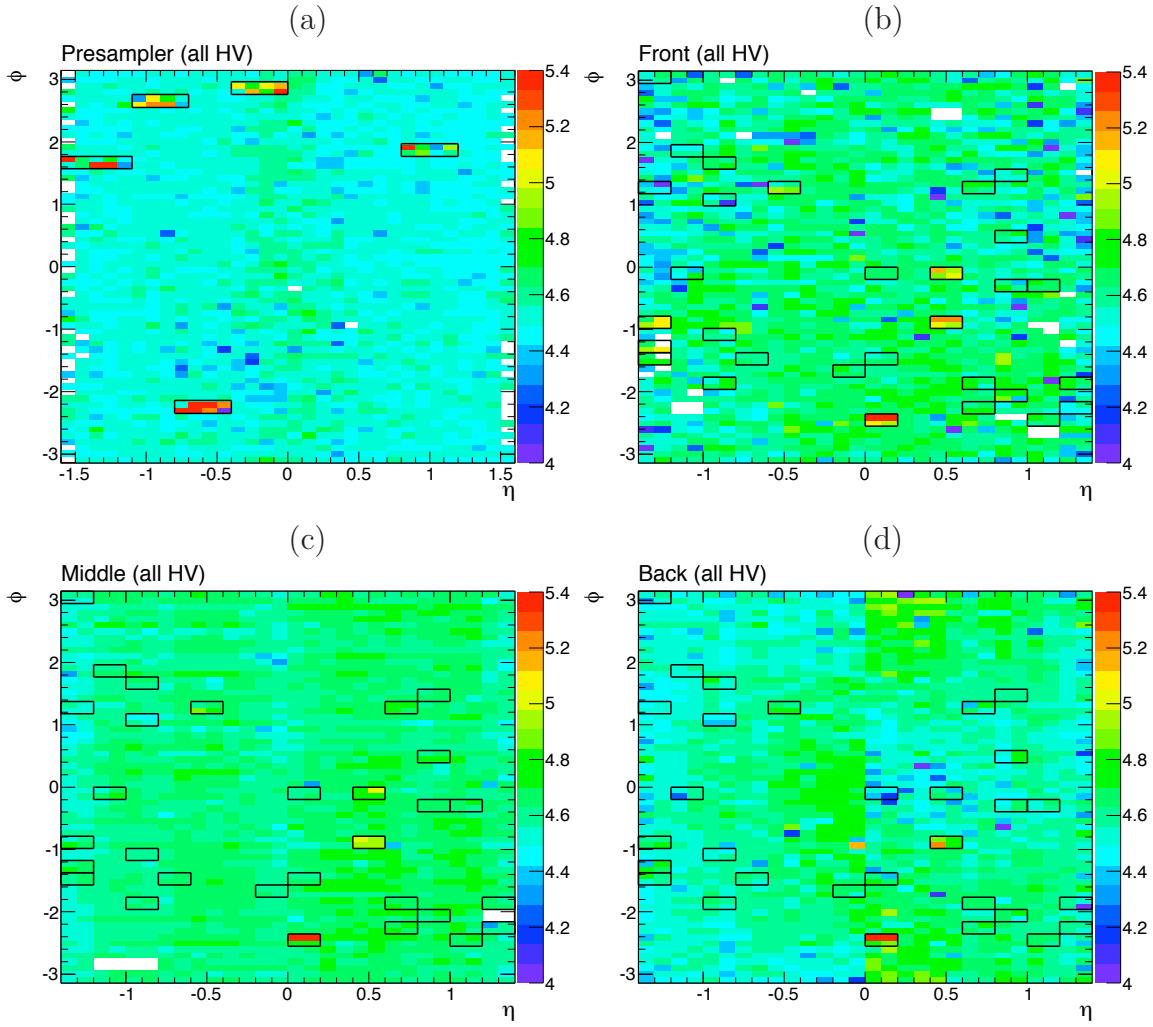

Figure 6.55: (η,ϕ) map for the Drift velocity rescaled to a field of 1 kV/mm, in (a) the Presampler, (b) the Front, (c) the Middle and (d) the Back. The regions where the high voltage is lower than the nominal value are surrounded by back boxes.

6.11 Comparison with the RTM Method

The measurements of the drift time in the EM calorimeter of ATLAS (barrel and end-cap) using the same set of cosmic muons data have also been performed using the RTM method [44]. This method is the official one used in ATLAS for the signal shape prediction. It is based in the signal shape prediction by the convolution of the calibration signal with response transform functions accounting for the amplitude difference and the different injection points of the physical and calibration signals (see section 5.4.1). This method is therefore faster and easier than the FPM although it suffers from uncertainties on the component parameters of the electronic chain, mainly LC and τ_{cali}. The results on the drift time measurements in the different barrel and end-cap layers of the EM calorimeter, the drift time uniformity and its impact on the calorimeter response have been reported in [54]. A comparison between these two methods in the barrel layers have been also done. The main results (reported in [55]) are presented in the following:

- Using the same selection criteria (although the values of k in the normalized χ^2 of the fit are different between the two methods for the each barrel layer), the drift time measurement along the η and ϕ direction have been compared in the three barrel layers. Figure 6.56(a) and (b) display the distribution of the drift time using both the RTM and FPM prediction, in the Middle, along the η and ϕ directions respectively. The prediction from the absorbers thickness measurements is also displayed. A good agreement is observed in Figure 6.56(a) between RTM and FPM although the drift time measured within the RTM method is globally greater in the electrode A ($|\eta| < 0.8$) and smaller in electrode B ($|\eta| > 0.8$). In average a relative difference of 0.2 ns is found with a RMS of 1.2 ns compatible with the precision of the two prediction methods. Both distributions show larger drift time in the transition regions with respect to the prediction. The distributions of the drift time along ϕ are in good agreement, given the larger dispersion observed in both results.

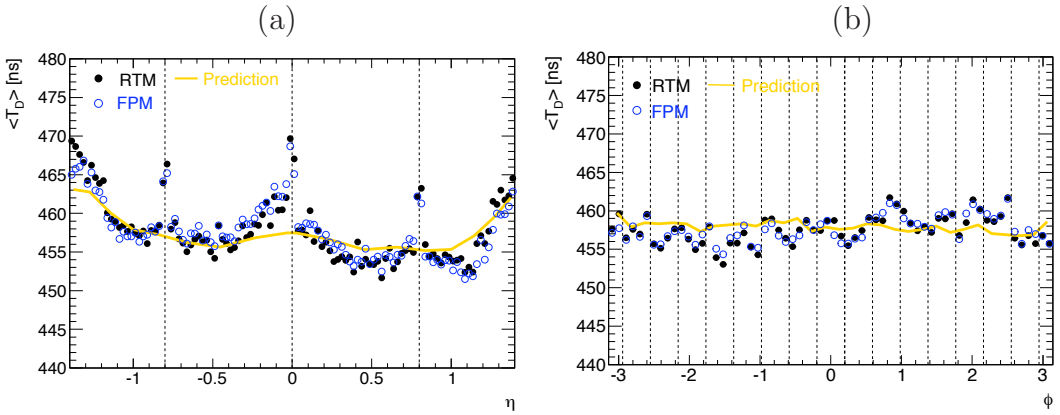

Figure 6.56: Distributions of T_D as function of (a) η and (b) ϕ in the Middle obtained with the FPM and RTM methods. The prediction from absorber thickness measurements is also shown.

- Figure 6.57(a) displays the weighted average drift time distributions as a function of η obtained with the FPM and RTM methods. The distributions have similar dispersion (slightly smaller with the RTM method), a difference in average drift time of 1.3 ns is

derived with a RMS of 3.9 ns of the order of the distributions dispersions. The Front layer is more sensitive to cross-talk effect due to the thin longitudinal segmentation. In particular, the capacitive cross-talk between two neighbor cells in the Front impacts the pulse shape and is accounted for in the cell response. The different approach of the RTM

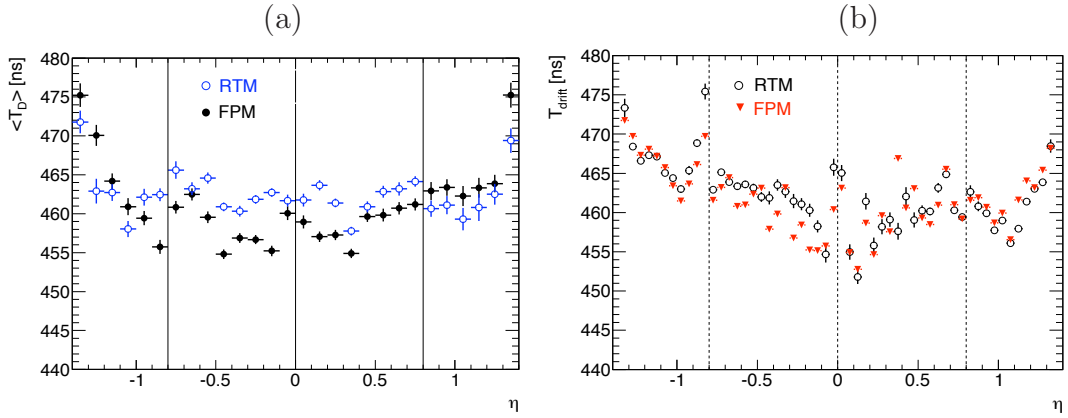

Figure 6.57: Distributions of T_D as function of η in (a) the Front and (b) the Back barrel layers, obtained with the FPM and RTM methods.

and FPM methods to describe the cross talk could explain the difference observed in Figure 6.57(a) between the two methods.

- The good agreement in drift time measurement and the use of the same gap variation with η (from the absorbers thickness measurement) induces compatible results for the drift velocity in the barrel and drift time uniformity. With the RTM method complementarity for the end-cap and given the good confidence level in the results, the impact of speed variation on the uniformity of the full calorimeter response is estimated. Figure 6.58 displays the distributions of (a) the drift time and (b) drift velocity as a function of η in the Middle barrel and end-cap compartment obtained with the RTM method. The drift time decrease with η observed in the end-cap is a feature of the varying HV that compensates the gap size increase. Such effect is not observed in the drift velocity distribution as it is rescaled to $E = 1\ kV/mm$.

The small differences observed between the two methods are accounted for as systematic error on the final result.

6.12 Systematic Studies

The different sources of systematic uncertainties are presented in this section and their contribution to the systematic error associated to the drift time (and drift velocity) estimated.

6.12.1 Fit Strategies related Systematics

Two ways of enhancing the statistical power of the drift time measurement have been discussed in section 6.6: the use of the weight A^2_{max} and the global cell based fit. The first have been chosen

(a)

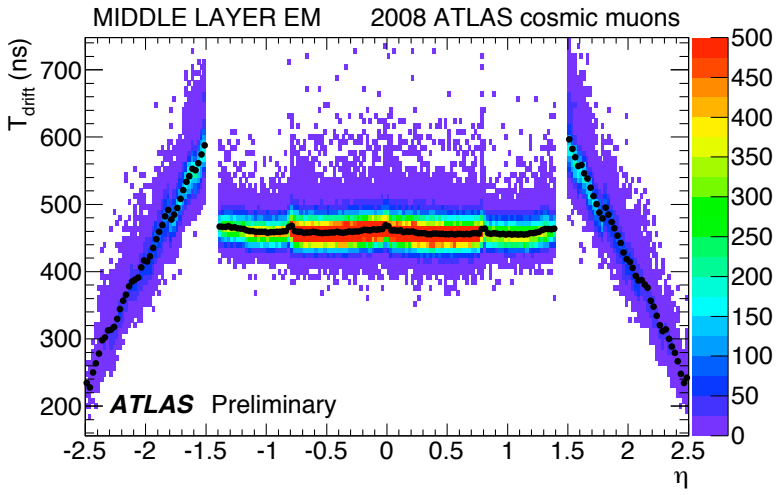

(b)

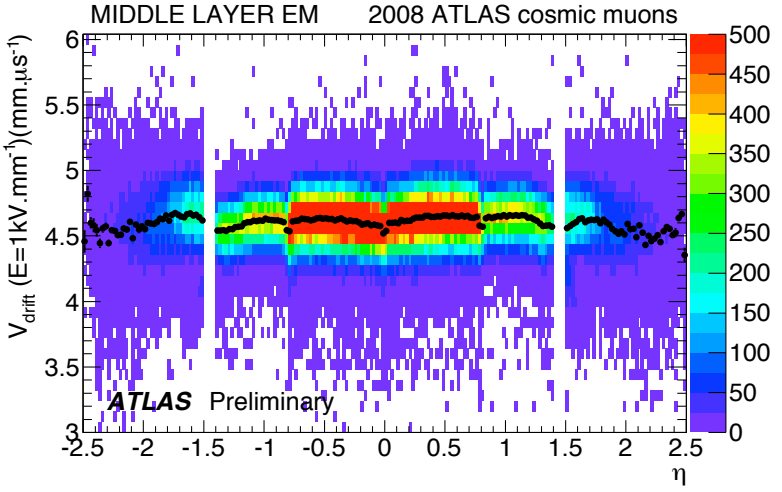

Figure 6.58: Distributions of T_D and V_D in the η directions (per bin of size 0.1) in the Middle barrel and end-cap, using the RTM method.

and used to derive the different results presented above. Figure 6.59 displays the η dependence of the drift time and the absolute shift of the electrode with individual fits weighted by A^2_{max} and the global cell based fits. A nice agreement is observed for the drift time, with a difference of 0.8 ns in average, while there is a sizeable difference for the shift parameter, of 6.4 μm in average, as already mentioned in section 6.6.

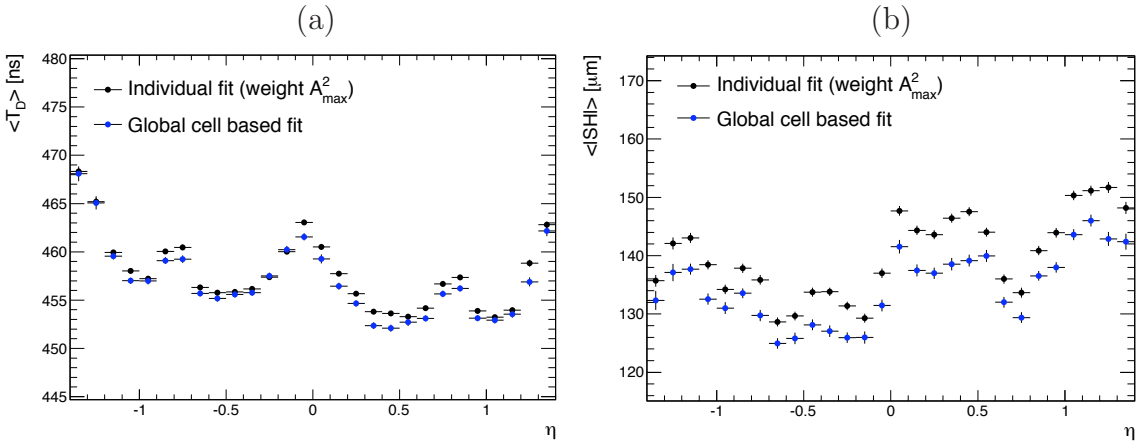

Figure 6.59: η dependence of (a) T_D and (b) $|SH|$, by bins of 0.1; the black dots are for the individual fits and the blue ones for the fits with N pulses.

The relative difference between these two methods on drift time measurement should be accounted for as systematic uncertainty although it is very small (0.2%) and won't impact much the global error.

6.12.2 Model Prediction and Residuals

Figure 6.60 displays the residuals averaged over η and ϕ in each of the 4 compartments. The profiles are made by shifting the maximum of the pulses to the time origin. As was seen in section 6.4 for the Middle, these residuals have a particular shape. Three regions appear in the time domain of the residuals:

- In the region of positive response (between -50 and +100 ns) the residuals are peaking at 0 for the Middle and the Back, while a dip is observed in the case of the Presampler and the Front. This suggests an effect linked to the capacitance of the cells, which are large in the first case, and small in the other. However a test discussed in section 6.12.3 did not confirm this hypothesis. The maximum deviation between the data and the prediction, in the positive region, is in average 2% for Presampler and Front, 1.5% for the Middle, and less than 1% for the Back. Given the oscillatory shape of the residuals, it is expected that the use of Optimal Filtering Coefficients weighting the samples taken every 25 ns will reduce the difference between the data and fit.

- In the region between +100 ns and +400 ns, which corresponds to the flat undershoot (see Figure 6.3), a slope is observed in the Front, Middle and Back compartments (about 2% of the pulse maximum over 300 ns) which indicates that the undershoot is not exactly flat. Electron attachment by impurities could give such a slope, possible consequences of

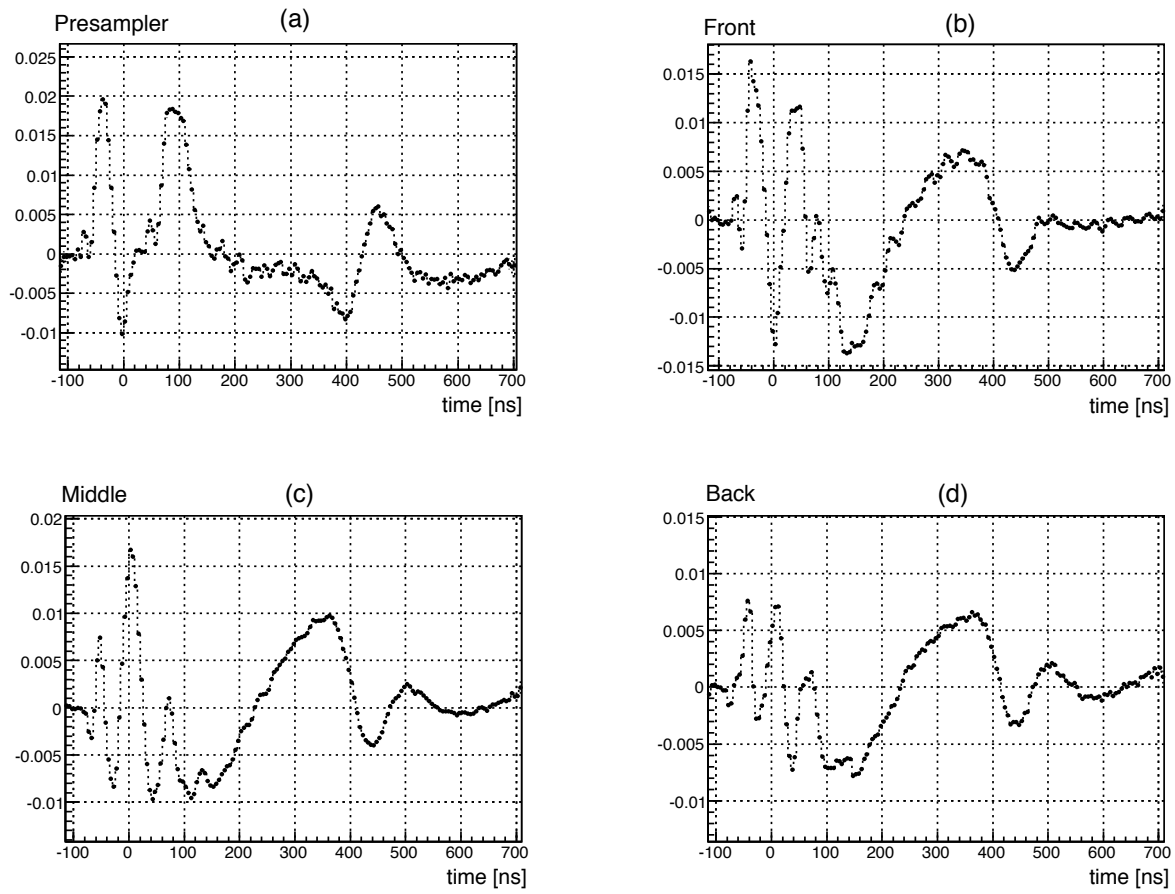

Figure 6.60: Profile of the normalized residuals $(meas(i) - pred(i))/max(pred)$ as a function of time (equal to recorded time - $t_{max(pred)}$) for events at nominal high voltage in: (a) Presampler, (b) Front, (c) Middle and (d) Back.

such an effect have been investigated in section 6.12.4. However an opposite and smaller slope is seen in the Presampler which casts doubt on such an interpretation.

- In the region of the end of the pulse (between 400 and 500 ns), a bump, positive for the Presampler and negative in the three other cases, is observed. This indicates that the parametrization by two main triangles differing by the shift parameter (see equations 6.5 and 6.6) does not perfectly describe the data. The reality is probably closer to the sum of many triangles, each differing slightly from the other, and giving a smoother rise than the one resulting from two triangles only. The description of the bends by a unique additional triangle (weight I_{bent}, length TD_{bent}) is also of course an approximation.

Figure 6.61 illustrates the normalized residuals for the different slots in the Middle. In all these regions the residuals have very similar although not identical shapes, thus confirming a limitation of the prediction. Furthermore, all the above imperfections will result in systematic biases on the values obtained for the drift time and the shift parameters, as discussed in the next sections.

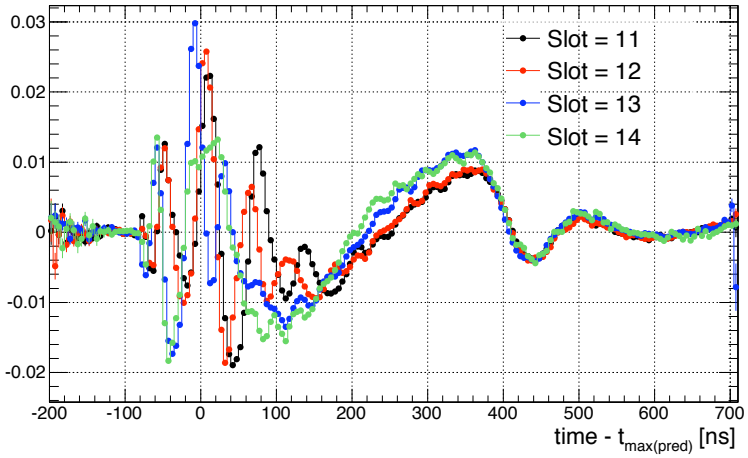

Figure 6.61: *Profile of the normalized residuals* $(meas(i) - pred(i))/max(pred)$ *as a function of Time (equal to recorded time -* $t_{max(pred)}$*) for events with HV=2000V in different slots of the Middle: in black for Slot 11, in red for Slot 12, in blue for Slot 13 and in green for Slot 14.*

Given that the bumps at the end of the pulse are of opposite sign between the Presampler and the Middle, and that the residuals around the maximum of the pulse are also of opposite sign, the systematic error associated to the residuals shape is (+2%,-0%) on the Presampler and (-2%,+0%) on the calorimeter layers.

6.12.3 Variation of the Capacitance

To further understand the residual shape near the amplitude maximum of the pulse, the cells capacitance has been varied in the Middle compartment, for FT 25A ($\eta < 0$). The capacitance is varied by $\pm 5\%$, a new set of parameters τ_{sh} and Z_s is subsequently derived from calibration fits and used in new fits of cosmic muon data. Figure 6.62(a) displays the impact on the weighted average drift time as a function of η. The overall drift time scale is changed slightly, but no significant variation is observed in the drift time dependence in η. It is interesting to note that when varying in both directions the capacitance, the drift times invariably increase.

The residual shapes shown in Figure 6.62(b) for the different capacitance values do not differ from one another. As discussed in [45] using a value of capacitance too low (or too high) is compensated by a larger (smaller) value of the shaper time constant τ_{sh}, giving finally very similar pulse shapes.

The systematic associated to the capacitance variation impact on the drift time measurement is given by the relative difference between the mean value of the drift time in the classical case and in the cases the capacitance is varied by $\pm 5\%$ which leads to a systematic error (+0.44%,-0%).

6.12.4 Effect of Electron Attachment

As mentioned in the previous chapter recombination of the Ar^+e^- pairs and impurities in the Argon (such as 0_2 [47]) can create deformation of the triangular shape [41]. In the LAr, the

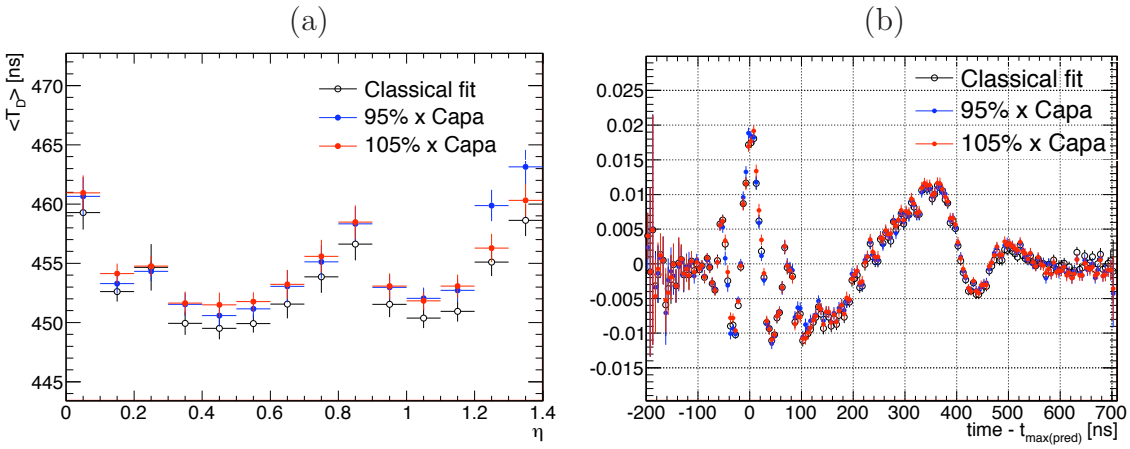

Figure 6.62: (a) Distribution of the average weighted T_D in bin of size 0.1 as a function of η. (b): Profile of the residual shapes, for different assumptions of capacitance for FT 25A in the Middle: in black the classical individual fit case, in blue and red for the capacitance decreased and increased by % respectively.

energy lost by Ar^+e^- pair recombination due to pollution is given by [41]:

$$\Delta E = E\frac{A}{1 + c\frac{1}{\rho}\frac{E}{g}} \tag{6.27}$$

where $A = 1$, $c = 0.0045\ g.cm^{-2}.MeV^{-1}$ and $\rho = 1.396 g.cm^{-3}$.

In the presence of attachment of drifting electrons to impurities, the signal is no longer a triangle but has the form but has the form:

$$I(t) = Q_0/T_D.exp(-t/T_{live}).(1 - t/T_D) \qquad \text{for} \quad 0 < t < T_D \tag{6.28}$$

T_{live} is the associated life time. In the full collection mode and for $T_{live} >> T_D$, the collected charge is reduced by a fraction equal to $1/3(T_D/T_{live})^2$. Using the Fourier transform of $I(t)$, the pulse shape is derived by convolution of the various features affecting the pulse formation and propagation (see [45] for the general case).

The data are then fitted with the additional parameter, T_{live}. Figure 6.63 displays the distribution of the values obtained for T_{live} in the Middle compartment (a) as a function of the new drift time parameter extracted from the five-parameters fit and (b) as a function of the difference between the drift time extracted with and without this new fit parameter. The average value found is 6 μs, with a large dispersion (the RMS is of about 6 μs as well). This new fit procedure was tested in the four layers and no effect was seen in the Presampler although it is made of same active medium. The effect induced by such an average life time would be essentially invisible on the response with a fast shaping, and would be about 2.10^{-3} if the calorimeter was run in the charge collection mode. To prevent effects due to the large tail of T_{live} values, a test has been performed fixing this parameter to the typical value $T_{live} = 5\ \mu s$. As illustrated in Figure 6.64 the slope in the residuals, between 100 ns and 400 ns has now disappeared for the two considered cases, when fitting or fixing T_{live}. The other regions are slightly changed as the expected, although the amplitude maximum of the residual that appear at the pulse maximum amplitude peak is reduced from 1.7% to 1.3% and 1.1% respectively when fixing and fitting T_{live}.

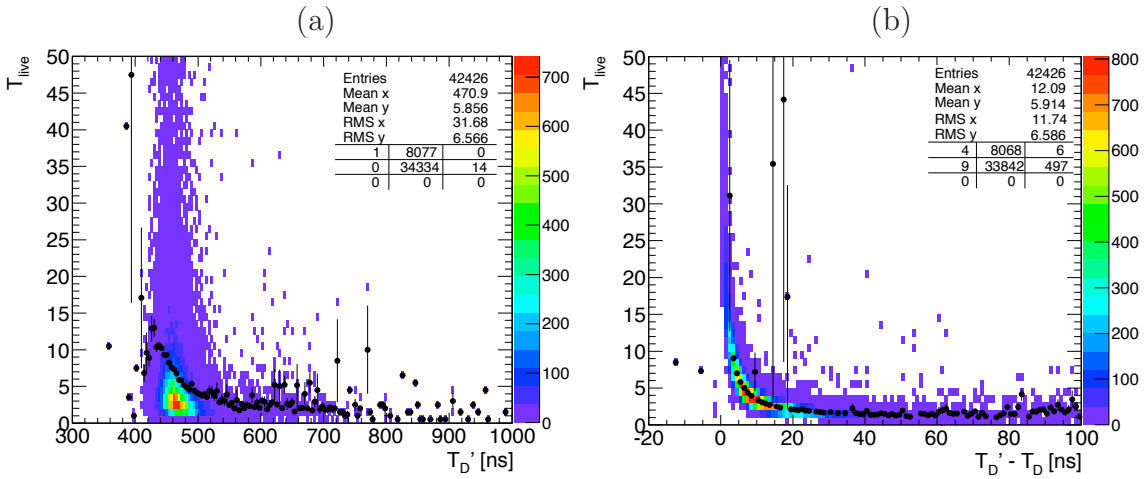

Figure 6.63: (a): Distribution of T_{live} as a function of the drift time T'_D for the the case with a free T_{live}. (b): T_{live} as a function of the difference between drift times with and without this new parameter in the fit.

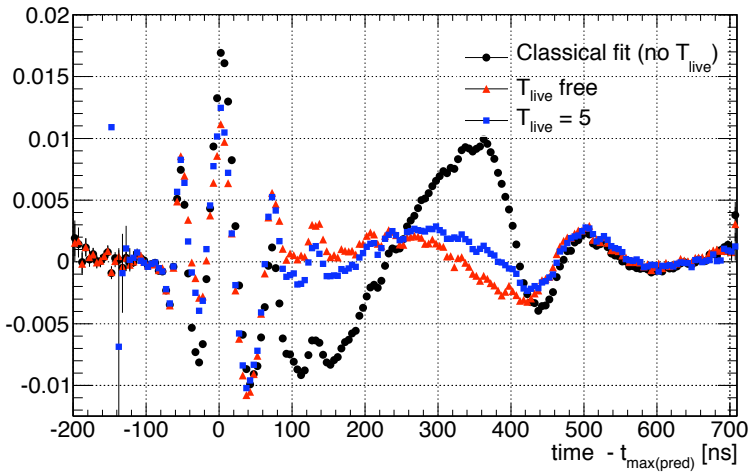

Figure 6.64: Profile of the normalized residual $(meas(i) - pred(i))/max(pred)$ as a function of *time* (the maximum of the pulses are shifted to 0) in the Middle, in black for the standard fit, in red for the fits with T_{live} let free and in blue for the fits with T_{live} fixed to 5.

However, the physical reality of the attachment studied here is debatable for the already mentioned reasons and the fact that the distribution of the drift time values obtained becomes somewhat wider when fitting with attachment, even if its value is fixed to the average value found with the parameter free, as illustrated in Figure 6.65(a) for the Middle.

It is also interesting to check the consistency of the drift velocity among layers when T_{live} is used as an additional free parameter in the fit. As shown in Figure 6.65(b), the drift velocity in the Presampler is essentially unchanged, while, due to the increase in the drift time distribution of the calorimeter layers the drift velocity in all calorimeter compartments is reduced by ∼1.5 to 2%. This makes the Presampler and the rest of the calorimeter more compatible.

Given the uncertainties associated to the introduction of T_{live}, a systematic uncertainty of 100% of the impact of the electron attachment effect, parametrized by T_{live}, on the measurement

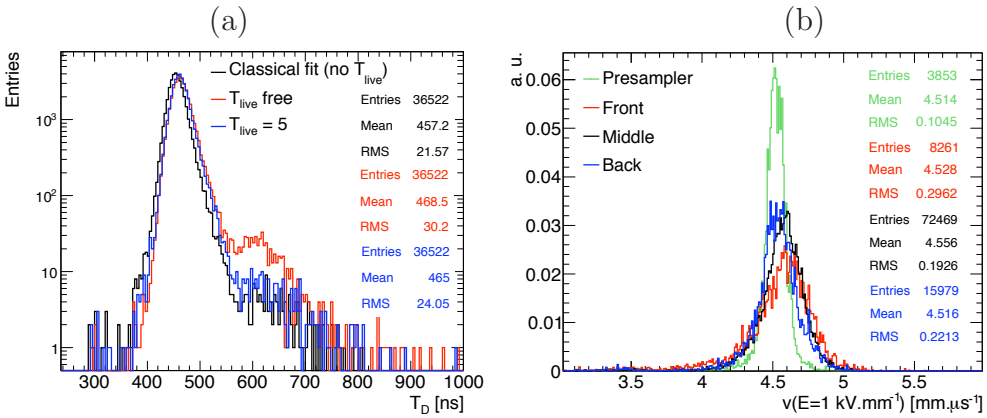

Figure 6.65: (a): T_D distributions: in black for the standard fit, in red for the fit with a free T_{live} parameter and in blue for the fit with T_{live} fixed to 5. (b): Drift velocity associated to a field of 1 kV/mm, for the fit with T_{live} free; in green for the Presampler, in red for the Front, in black for the Middle, and in blue for the Back.

of the drift velocity for the accordion layers is considered. This effect results in a systematic uncertainty of about (+0%,-2.2%) on the calorimeter values.

6.12.5 Variation of the bent triangle contribution

The amount of energy deposited in the liquid argon in the bent sections of the calorimeter is estimated using the simulation. To account for possible differences with the data, a systematic uncertainty related to the estimate of the fraction of signal collected in the bent sections is assessed by varying the contribution of the triangle associated to the bends by ± 20%, for FT25A in the Middle. The resulting systematic variation of the drift time and the shift are illustrated in Figure 6.66 as a function of eta. The drift time variation amounts to ±3 ns and is opposite to that of I_{bent} as expected from equations 6.5-6.8. The fitted T_D parameter corresponds to the drift time in the straight sections TD_{2000} and therefore compensates the absence of the bent sections triangle. It should be noted that the variation of the drift time with different fractions of third triangle are constant throughout the detector which means that an error on the third triangle will not impact the estimate of the intrinsic uniformity. Similarly the shift variations along the η directions are not changed.

The effect of the variations in I_{bent} impact substantially the shape of the residuals at the end of the pulse as shown in Figure 6.67.

As expected the variation of the bent triangle contribution only impact the residual shape in the time domain of the signal pulse rise where the longer triangle from the bent section impact on the slope. The uncertainty induced by the bent triangle contribution leads to a systematic error on the drift time measurement of ±0.65%.

6.12.6 Comparison with the RTM method

The cosmic muon data have also been analyzed using the official method in ATLAS, the RTM method. The signal shape prediction is obtained by the convolution of the calibration signal

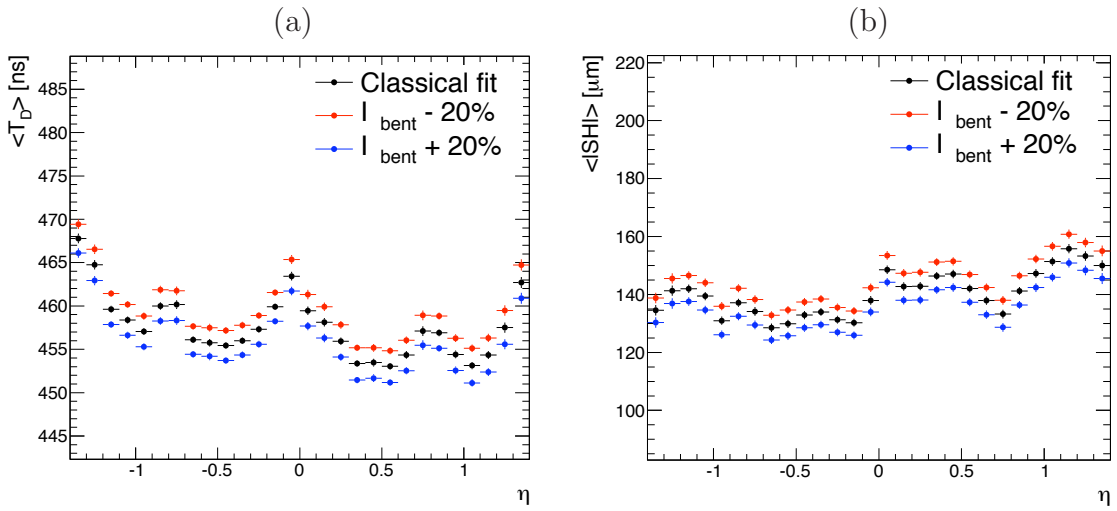

Figure 6.66: *(a) T_D and (b) $|SH|$ as a function of η in the Middle for different I_{bent} configurations: in black the standard case, in blue for $I_{bent} + 20\%$ and in red $I_{bent} - 20\%$.*

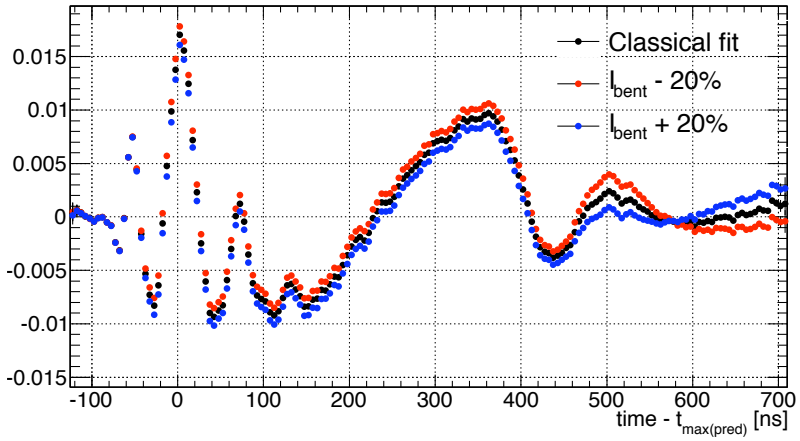

Figure 6.67: Residuals in the Middle for different I_{bent} configurations: in black the standard case, in blue for $I_{bent} + 20\%$ and in red $I_{bent} - 20\%$.

with response transform functions accounting for the amplitude difference and the different injection points of the physical and calibration signal. The shape prediction accuracy relies on the determination of the different parameters involved in the convolution formula (section 5.4.1). The values of LC and τ_{cali} are know with 3% accuracy inducing a systematic error on the drift time measurement of ± 0.1 and ± 0.5% respectively. In the FPM method, the capacitance is varied by ±5% which leads, as mentioned above, to a systematic error (+0.44%,-0%) on T_D.

As discussed in section 6.11 the two methods are compared in the barrel layers. In the Middle and Back layers the drift time distributions well agree, a difference of 0.2 ns is found in average with a RMS of 1.2 ns which is of the order of the precision of the measurement for the two methods. Hence, no significant difference is observed in these compartments. In the Front layer a larger difference is observed between the two methods, of 1.3 ns with a RMS of 3.9 ns. This leads to relative uncertainty on the drift time of ±0.3% in the Front layer only. The Presampler was not studied within RTM.

6.12.7 Summary of the Systematic Studies

In addition to the sources of systematic error on the drift time measurement enumerated above, a systematic error on the value of the gap of 1% for both the calorimeter and the Presampler is added which induces an uncertainty on the drift velocity of ±1.3%.

The drift velocities for each layers are summarized in Table 6.12 and in Figure 6.68 where the reference value [53] is also shown. Our measurements are compatible with the reference, and are actually affected by somewhat less systematics.

Layer	Drift velocity (in mm·μs^{-1} at 1kV/mm)
Presampler	4.52 ±0.001 (stat) $^{+0.11}_{-0.07}$ (syst)
Front	4.63 ±0.003 (stat) $^{+0.06}_{-0.14}$ (syst)
Middle	4.62 ±0.002 (stat) $^{+0.06}_{-0.14}$ (syst)
Back	4.58 ±0.002 (stat) $^{+0.06}_{-0.14}$ (syst)

Table 6.12: Drift velocity at 1kV/mm in the four layers. The systematic uncertainties are also indicated.

Averaging over the Presampler and Middle values, for which most of the systematics are independent (in some cases even apparte) gives as final value:

$$V_D(1\ kV/mm, 88.5\ K) = 4.58 \pm 0.07\ mm.\mu s^{-1}$$

6.12.8 Conclusion

In this study about half a million of ionization pulses (with a threshold of roughly 1 GeV) taken in the Barrel calorimeter - with 32 samples - during the 2008 cosmic muons commissioning campaign are analyzed. Recorded pulses are described with the "First Principle Method" which models analytically the signal propagation and the response of the read-out electronics. Electrical features of cells, and preamplifier, shaper, and transmission cables properties are used to predict the calibration pulse shape. The two only parameters left free and extracted form the fit are the impedance of the cold signal cable Z_s and the constant time of the shaper

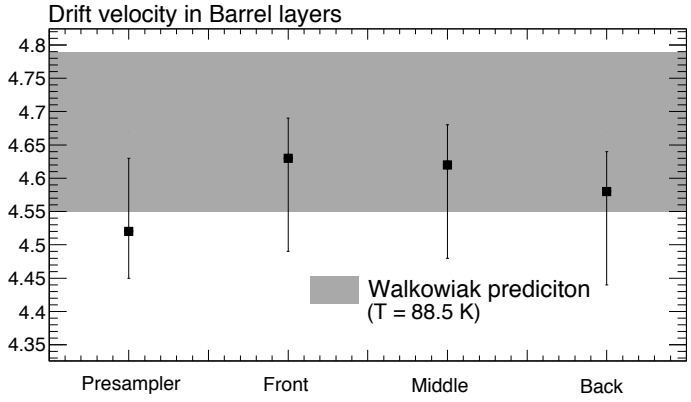

Figure 6.68: The black squares correspond to the drift velocity found in the different layers for an electric field of 1kV/mm, with their associated systematic errors. The grey band corresponds to prediction.

filter τ_{sh}. These parameters are then used to predict the signal pulse shape. The prediction of the signal pulse shape is a four free parameter fit.

The physics pulse of a signal has a triangular shape with time. The model however uses two triangular signals. The main triangle represents the contribution from the straight sections and the smaller (and longer) the contribution for the bent sections of the absorber-electrode device. Because of mechanical tolerances, the main signal triangle is actually the superposition of two triangles with a slight difference of amplitude and duration parametrized by the electrode shift parameter. Furthermore, two triangles are used to describe the contribution of the bends (from both sides of the electrode), of height and duration relative to the two main triangles given by Monte-Carlo simulations.
Besides the drift time and the shift, two more parameters, the amplitude at the peak and the time of the start of the pulse, are used to adjust, the prediction to the data.

In order to assess systematic effects possibly introduced by the fitting procedure and highlight physical or detector related features of the prediction, a "toy model" was devised, which confirmed that the evaluation of the drift time per cell is unbiased.

In order to increase the statistical power of the fit, two methods have been investigated. The global cell based fit, fitting simultaneously all pulses that belong to one cell in the Middle compartment with a common drift time and shift parameters, and the weighted fit, using the square of the amplitude maximum of the pulses, show compatible results and underline the statistical origins of the fit precision limit. The choice was made to use the weight A^2_{max} to derive the drift time measurements in the different layers of the barrel calorimeter and the impact of gap variations on the calorimeter response uniformity.

The drift time measurements presented in this study allowed the observation of known features of the calorimeter.

1. the drift times in the Presampler follow well the expected differences in gap.

2. The overall trend of the drift time measurements in the middle also follows nicely the gap distribution as estimated from the measurement of the absorbers thickness. The larger differences arise in the transition regions in η. A closer look at the tails in the drift time

distribution has shown that a large fraction of them are located in transition regions at 0 and 1.4, that correspond to the transition areas (of the half-barrels), and $\eta = \pm 0.8$ which is the transition from electrode A to electrode B. The electric field is lower than average in these regions explaining larger expected drift time.

3. Beyond these known features of the calorimeter, which allowed to confirm the sensitivity of the method and the accuracy of the model, the drift time measurement showed that the transition between modules in azimuth are visible, in particular on the top of the wheels where a global deformation (pear shape) will tend to open up the gaps. Inhomogeneities of the measured drift times also revealed an azimuthal modulation in the Back compartment of the calorimeter, for small η values ($\eta < 0.4$). This modulation has opposite phases in the two half barrels, and a speculative explanation is that it is due to a construction feature.
   Correlations between cells in adjacent layers, either in η,or azimuth, or in between compartments were investigated. The strongest correlation (close to 50%) was found between cells adjacent in η, reflecting the stiffness of absorbers in the longitudinal direction.

The measurements of the shift parameter are rather homogeneous throughout the calorimeter and in good agreement with the expected mechanical tolerance. The average observed in the Presampler is smaller than that of the other compartments, as expected from the rigid gluing of its electrodes. Correlation between adjacent cells has also been investigated, but as expected from the flexibility of the electrodes, the correlation of the shift values are smaller than that of the drift time.

A small fraction of the high voltage sectors are operated with a voltage lower than the nominal value. This reduced voltage results in a reduced electric field in the gaps, affecting in a correlated way the drift time and the pulse amplitude which are both functions of the drift velocity. The analysis of areas with reduced HV allowed to verify that the power dependence of the speed $V(E) = k \cdot E^{0.3}$ gives a fair description of the observed drift time values in a relatively large HV range. However the prediction model is not adapted for asymmetric voltage with very large HV difference as was observed in the Front and Middle for the low voltage at 400 V and in the Presampler with a very low voltage (HV < 1 V).

To further check the overall consistency of the measurements, in particular in order to compare the Presampler and the accordion calorimeter, the drift velocity rescaled to a fixed electric field value of 1 kV/mm is computed. Systematic errors resulting from mechanical tolerances and effects potentially affecting the measurements such as electron attachment or the relative amount of signal in the bent sections, are estimated. A slightly lower drift velocity is found in the Presampler. The measurements in each layer are nevertheless compatible with each other and compatible with published data. A drift velocity $V_D(1\ kV/mm, 88.5\ K) = 4.58 \pm 0.07\ mm.\mu s^{-1}$ is found in this study which is in good agreement with previously published measurements of the drift velocity of free electrons in liquid argon at the operating temperature of 88.5 K [53].

The drift time depends on the gap to power 1.3 whereas the amplitude relates to the gap to the power -0.3. The uniformity of the drift times will thus measure the impact of the gap variations on the response uniformity with an enhanced sensitivity of $\sim 1.3/0.3 \simeq 4$. Clusters of cells of size 0.1×0.1 are chosen to improve the measurement accuracy (~ 1 ns on the drift time), and have allowed to assess the uniformity of each compartment. For the Middle layer

in which $\sim 70\%$ of the shower energies are located, a drift time RMS dispersion of 5.8 ns for an average value of 457.8 ns is found. This translates into a response uniformity of 0.29%. This result is substantially improved if the result is integrated in ϕ and the η distribution is compared to the expected variations in gap, yielding an overall dispersion of 0.14%. During construction it was estimated [47] that the contribution of gap variation to the constant term of the response of the calorimeter should be around $\sqrt{(0.07\%)^2 + (0.16\%)^2} = 1.7\,{}^0/_{00}$, where the absorber thickness variations account for $0.7\,{}^0/_{00}$ and the gap variations from a sliding average of the cell capacitance measurements account for $1.6\,{}^0/_{00}$. The present measurement confirms, from directly measured ionization data, the excellent quality of the calorimeter construction. Including lead thickness variations of $1.8\,{}^0/_{00}$ (not to be confused with absorber variations which are actually decorrelated from them) the intrinsic barrel calorimeter uniformity amounts to $\sqrt{(0.18\%)^2 + (0.29\%)^2} = 0.34\%$ (0.39% if reduced high voltage regions are included).

This measurement presented illustrates the accuracy achieved within the FPM method using cosmic muon data. The gap dispersion has been re-assessed and can be used to estimate the gap variation impact on the non uniformity of the calorimeter response. This eventually shows a reduced impact on the constant term of the energy resolution. The comparison with results obtained within the RTM method shows compatible results and allows to estimate the calorimeter response uniformity in the end-cap due to the gap variation. A non uniformity of $0.29^{0.05}_{0.04}\%$ and $0.63^{0.06}_{0.04}\%$ was found, respectively for the barrel and the end-cap. Such study should be repeated with LHC collision data, with dedicated 32 samples run. The uniformity of the calorimeter response could also be re-assessed accounting for the projectivity of the events, giving some answers to the features observed in this study.

Part II

Calorimeter Upstream Material Mapping using Conversions

Introduction

An accurate knowledge of the material in the ATLAS detector is crucial for the calibration of the photons and electrons energy reconstruction. This depends on the energy deposited n the active part of the EM calorimeter layers, the material in the calorimeter (sampling fraction) and material in front of the calorimeter that causes loose of energy of initial electrons and photons produced at the interaction point.

The material mapping upstream of the calorimeter is done in ATLAS by measuring the conversion rates in the detector volume. Photons conversions recorded in data at 7 TeV centre-of-mass energy are being used to map the material and compare the measurement with what is expected from the detailed MC simulation of the detector (active part, electronic, cables, services, cooling systems,...).

However, because of the poor knowledge on the initial flux of photons in minimum bias events and the difficulty to rely this to the rate of conversions reconstructed in the Inner Detector (ID) the normalization of the material with data is relative. The normalization of the upstream material is studied using a well known reference piece of a material that is the Beam Pipe (BP). To normalize the BP conversion rate to the initial number of photons, given that a large fraction originate from π^0 mesons, the π^0 Dalitz decays are considered. In this approach, the measurement of the material in the BP can be used for an absolute normalization of the upstream material.

In the study presented here, the BP conversion rate is estimated with data at 900 GeV and 7 TeV centre-of-mass energy. The results are compared with expectation from the MC simulation in order to estimate the relative difference in the amount of material in the BP.

6.13 Minimum Bias events

The minimum bias events are soft interactions in proton-proton collisions, non diffractive inelastic, single and double diffractive events scatterings. These events are characterized by low transverse momenta and a relatively high track multiplicity.

Two simulated Monte Carlo (MC) samples are considered in this analysis in order to derive the BP conversion probability using first data recorded at 900 GeV and data taken at 7 TeV centre-of-mass energy.

1. This study was initially done with a MC sample containing almost ten million of Minimum Bias events at a centre-of-mass energy of 900 GeV. The MC sample has been generated and simulated in Athena release 15.6.1, with an ATLAS geometry flag ATLAS-GEO-08-00-02 [56, 57].

2. A MC sample of about twenty million of Minimum Bias events at a centre-of-mass energy of 7 TeV is also used. It is generated and simulated in Athena release 15.6.7, with an ATLAS geometry flag ATLAS-GEO-10-00-00 (The Beam Pipe layout is unchanged in the ATLAS geometries considered for the 900 GeV and 7 TeV MC samples). Both 900 GeV and 7 TeV MC samples simulate non diffractive scatterings in minimum bias events.

In october 2008, the LHC was fully operational and stable beams were circulating at the SPS energy of 450 GeV. Only in december 2009 collisions at a centre-of-mass energy of 900

GeV occurred. About 700 thousand events have been triggered in ATLAS as minimum bias event (using the Minimum Bias Trigger Scintillator, MBTS). 60% of this statistics was flagged as potential collision candidates, belonging to a good luminosity block, meaning no trigger problem and a good quality of the information of the inner detector tracking system. The data have been recorded with the solenoid field at its nominal current value, 7730 A. *In fine* 384 186 collision candidates are selected and analyzed with the same Athena release and ATLAS geometry configuration used for the MC.

The LHC has produced its first collisions at a centre-of-mass energy of 7 TeV the 30^{th} of March 2010. About 98 million of events triggered with the MBTS system are analyzed in this study which corresponds to data recorded between the 30 of March and 24 of May 2010. 75% of events pass the quality requirements that are stable beams condition and Pixel and SCT detectors green status. The collision data candidates have been processed using the same Athena release and ATLAS geometry tag than what used for the same energy MC sample.

6.14 The Beam Pipe

The structure of the BP in which the proton beams circulate varies in the LHC tunnel. It is the first layer of material seen by the particles produced in the collisions. Near the collision point of ATLAS, it is important that the BP represents the least possible material to reduce the number of interactions with particles before arriving in the ID but solid enough to maintain the vacuum.

6.14.1 Structure

Near the collision point, the BP is made of one layer of Beryllium and additional layers of material added to allow a back-out procedure in-situ [58] and preserve the BP insulation.

- The first layer of the BP is the Getter coating, at a radius R = 28.998 mm, used to remove particles from the vacuum pipe by thermodesorption. It is very thin (2 microns) and barely contributes the BP material; it represents 0.009% of X_0.

- The layer of Beryllium has a thickness of 0.8 mm and contributes to 0.227% of X_0 in the BP material. It constitutes the rigid structure of the BP, separating the vacuum from the detector material.

- A layer of 0.025 mm of Kapton is used to separate the Beryllium from the Heater system. This material contributes to 0.009% of X_0.

- The Heater system is made of a 10 microns layer of Inconel (mainly composed of Nickel and Chrome), defined by a radiation length of 0.064% X_0 and a 0.12 mm Kapton. The heater system allows a back-out procedure done once the BP installed, by heating the Getter to a temperature of 200 degrees Celsius. In the central region, with $|z| < 50\ mm$, there is no Inconel in order to reduce as much as possible the density of the BP.

- The Heater system is followed by a layer of 4 mm of Aerogel, a light material (composed of Quartz and Water) and good insulation system. It notably separates the Heater from the ID, corresponding to a difference in temperature about 210 degrees. The Aerogel

contribution to the BP material is nevertheless of the order of that of the Beryllium layer, 0.267% of X_0.

- Finally, the Aerogel is covered by a layer of 0.12 mm of Kapton and the BP ends with a 50 microns layer of Aluminum (at R = 34.290 mm), with 0.056% of X_0.

The BP structure is illustrated in Figure 6.69, with the thickness of the different materials. The presence or not of Inconel splits the total beam pipe material into two η regions. Given that the Inconel layer is installed at R =29.9 mm, the transition region arises at $\eta =$ 1.287. The BP

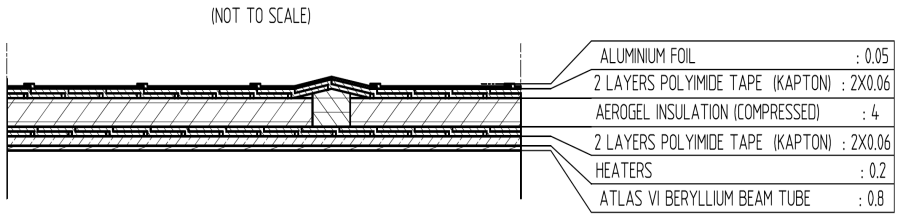

Figure 6.69: Sketch of the Beam Pipe structure at ATLAS position, with the thickness of the different systems.

material [59,60] is in the inner region $\frac{X(\eta=0)}{X_0}(|z| < 50\ mm) = 0.665\%$ and in the outer region $\frac{X(\eta=0)}{X_0}(|z| > 50\ mm) = 0.719\%$, for a total thickness of 5.3 mm. A systematic uncertainty of 3% is taken into account that mainly comes from the heater component, where quantities of Kapton and Inconel are not perfectly known. Figure 6.70 illustrates the BP structure in the inner and outer regions, respectively in red and black. The distributions are obtained with MC Minimum Bias samples by counting the number of true conversions from photon with an initial energy greater than 1 GeV. Small windows are selected in η in order to reduce as much as possible the η dependence of the conversions (see next section). The different components are indicated. The difference between the two distributions at $R \sim 29.9\ mm$ comes from the presence or not of Inconel.

6.14.2 Integrated Beam Pipe conversion probability from First Principles

The conversion of a photon into a pair of electron-positron is possible when its energy is greater than $\sim 2m_{e^-}$. It is the main process of photon interaction through the matter at energy above 10 MeV and it is independent of the energy for photons with an energy above 1 GeV [38]. The conversion probability of a photon through a material of thickness x per unit of radiation length X_0 in the stable regime can be written as:

$$P(x, X_0) = 1 - \exp(-\frac{7}{9}\frac{x}{X_0}) \tag{6.29}$$

The BP conversion probability in the acceptance region $|\eta| < 2.5$ is obtained by integrating this equation over η, accounting for the thickness variation with θ : $x(\eta) = \frac{x(\eta=0)}{sin(\theta)}$, $\theta =$

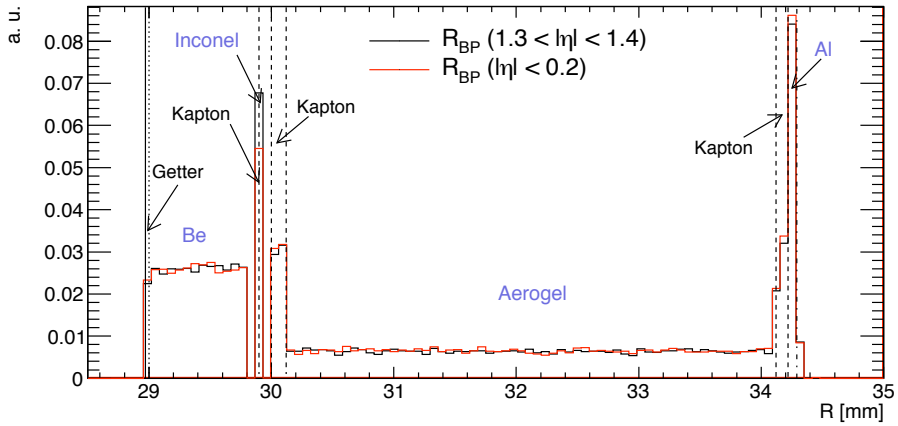

Figure 6.70: Radius of the Beam Pipe obtained with 7 TeV MC samples by counting the number of photon conversions with an energy greater than 1 GeV in red for $|\eta| < 0.2$ and in black for $1.3 < |\eta| < 1.4$. The dashed lines separate the different components of the BP as quoted in the database of ATLAS.

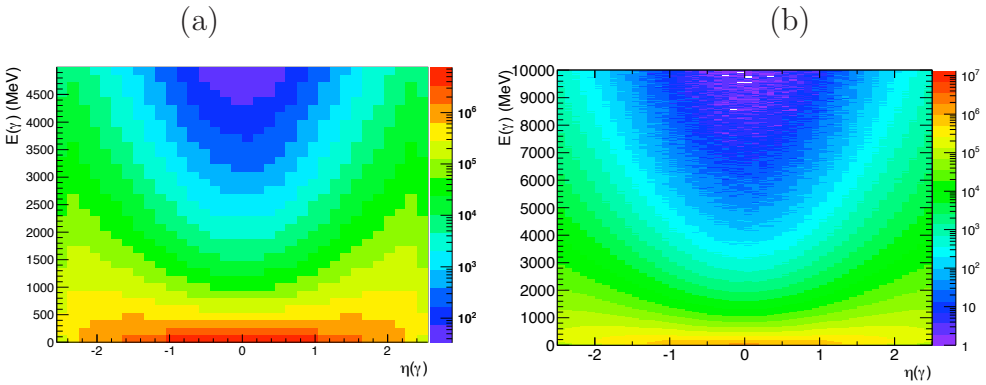

Figure 6.71: Photon energy distribution as a function of its η direction, as generated with the 900 GeV MC sample.

$2 \times \arctan(\exp(-\eta))$. The BP conversion probability integrated in the acceptance range should also account for the photons η distribution. Figure 6.71 displays the photon energy distribution as a function of the η direction of the photon.The higher energy photons tend to be produced at larger η. This behavior originates from the boost of the mesons, mostly π^0, that produces the photons.

the BP conversion probability expression from equation can be written as:

$$P_{BP}(-2.5 < \eta < 2.5, E^{\gamma} > E^{Thr}) = \frac{\int_{-2.5}^{2.5} \left[1 - e^{-\frac{7}{9}\frac{x(\eta)}{X_0}}\right] \rho_{\gamma}(\eta, E^{\gamma} > E^{Thr}) d\eta}{\int_{-2.5}^{2.5} \rho_{\gamma}(\eta, E^{\gamma} > E^{Thr}) d\eta} \tag{6.30}$$

where $\rho_{\gamma}(\eta, E^{\gamma} > E^{Thr})$ is the photon η distribution at a given energy threshold E^{Thr}. In practice, the photon η distribution is fitted for different energy thresholds E^{Thr}. Figure 6.72(a) and (b) display the BP conversion probability found with the MC using the equation 6.30, at 900 GeV and 7 TeV centre-of-mass energy respectively. The prediction is obtained using the BP amount of material given in the two η regions from the layout design and the MC photon η

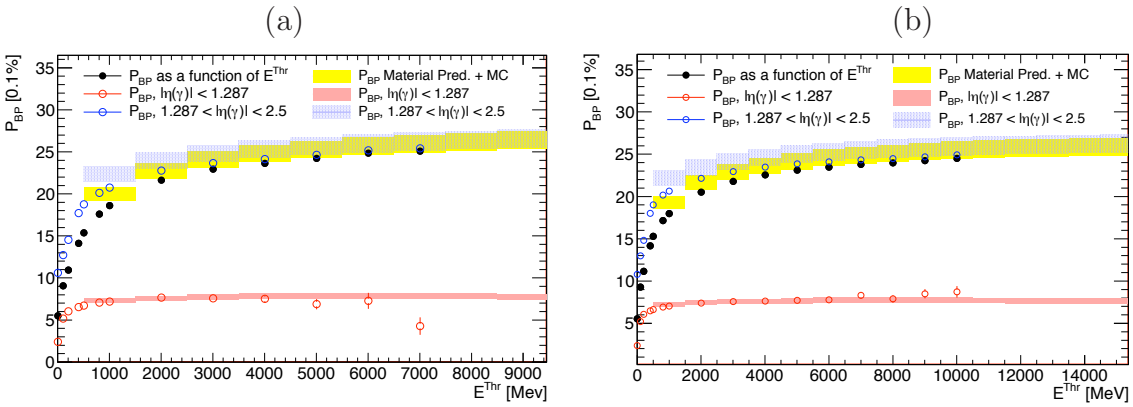

Figure 6.72: BP conversion probability as a function of the photon energy threshold. The yellow line corresponds to the BP conversion probability expected from the beam pipe structure knowledge when accounting for the MC η distribution of photons with energies greater than a given threshold E^{Thr}. The blue and red lines respectively correspond to the expected BP conversion probability in the central and outer region, $|\eta| < 1.287$ and $1.287 < |\eta| < 2.5$.

distribution fitted with a polynomial function of degree 7 for different thresholds E^{Thr} between 1 and 9 GeV at 900 GeV and between 1 and 15 GeV at 7 TeV. The upper limit is given by the weak statistics in photon η distribution fits at high energy. Also shown are the conversion rates estimated, in the acceptance and in the two η regions separately using the truth information from the MC samples, *i.e* by counting the number of true photons that convert in the BP with respect to the initial number of photons produced at the interaction point for different energy thresholds. The black circles correspond to the BP conversion rate estimated in the acceptance region whereas the red triangle and blue open circles correspond respectively the BP conversions rate in the inner and outer η regions. For statistical reasons the BP conversion probability is estimated with the MC samples for photon energy threshold below 8 and 10 GeV only respectively at 900 GeV and 7 TeV. The BP conversion probability estimated in the MC agrees well with the prediction in both 900 GeV and 7 TeV cases although the prediction is slightly larger, especially in the region $1.287 < |\eta| < 2.5$. This discrepancy could be due to the correlation between the photon energy and the photon η direction that is not taken into account in the calculation. The good agreement between prediction and MC indirectly indicates that this correlation is small. The probability reaches a rather stable value above a few GeV. The slight increase observed with the energy is not in agreement with the PDG predictions [38] but is explained by the photon η distribution that is not flat but increases with η, as the thickness of the traversed matter. This comparison verifies that the BP geometry implemented in the MC simulation corresponds to the reference design.

6.15 Towards a Measurement of the BP Conversion Probability

The BP conversion probability is derived using the truth information in MC samples and shown by the markers in Figure 6.72 can be written as:

$$P_{BP}(|\eta^{\gamma}| < 2.5) = \frac{N^{BP}_{TRUTH}(|\eta^{\gamma}| < 2.5)}{N^{\gamma}_{TRUTH}(|\eta^{\gamma}| < 2.5)} \tag{6.31}$$

N^{BP}_{TRUTH} is the number of photons that convert in the BP and N^{γ}_{TRUTH} the number of photon produced at the interaction point in the acceptance region passing the conversion energy threshold. Of course in standard high energy experimental conditions the energy threshold to reconstruct conversions is much larger than the conversion threshold to allow for the tracking to be performed. It is therefore important to investigate the energy dependence of the conversions rates. The estimate of the conversion rates in the BP and upstream material therefore depends on the initial flux of photons that can not be trivially estimated. It also depends on the reconstruction efficiency of the conversions that varies with the photon energy and direction. Up to now the upstream material is normalized relatively to the BP assuming the BP material well known. This study aims at verifying the amount of material in the BP for an absolute normalization of the material. To normalize the BP material we take into account that about 90% of the photons with an energy greater than 1 GeV originate from π^0. The initial number of photons can therefore be normalized to the number of π^0 Dalitz decays . The Dalitz decay mode $\pi^0 \rightarrow e^+e^-\gamma$ is the second decay mode of π^0 meson, after the neutral decay into two photons and its branching ratio is relatively well known, $BR_{Dz} = 1.198 \pm 0.032\%$. The virtual photon decays into a pair e^+e^- in the vacuum that is reconstructed as a conversion that originates from the interaction point, with a vertex radius immediately below the BP conversions. As the other π^0 decay modes are negligible, the number of photons from π^0 as a function of the number of π^0 is given by:

$$N^{\gamma\leftarrow\pi^0}_{TRUTH} \longrightarrow [2 \times (100 - BR_{Dz}) + BR_{Dz}].N^{\pi^0}_{TRUTH} \sim 1.988\ N^{\pi^0}_{TRUTH} \tag{6.32}$$

We can therefore normalize the number of photons to that of Dalitz decays as follows:

$$N^{\gamma}_{TRUTH}(|\eta^{\gamma}| < 2.5) \longrightarrow N^{\gamma\leftarrow\pi^0}_{TRUTH} \longrightarrow N^{\pi^0}_{TRUTH} \longrightarrow \frac{N^{Dz\leftarrow\pi^0}_{TRUTH}}{BR^{\pi^0}_{Dz}} \tag{6.33}$$

The BP conversion probability can be expressed as a function of the ratio of the number of true BP conversions to that of true Dalitz decays. The expression in equation 6.31 becomes:

$$P^{acc}_{BP} = \frac{N^{BP\leftarrow\pi^0}_{TRUTH}(|\eta^{\gamma}| < 2.5)}{N^{Dz\leftarrow\pi^0}_{TRUTH}(|\eta^{Dz}| < 2.5)}.\frac{BR^{\pi^0}_{Dz}}{1.988}.A^{MC} \tag{6.34}$$

where $N^{BP,Dz\leftarrow\pi^0}_{TRUTH}(|\eta^{\gamma,Dz}| < 2.5)$ are the total number of BP conversions and Dalitz decays originating from a π^0 produced in the acceptance. Various MC related factors are extracted in the normalization of the number of photons to that of Dalitz decays as for instance the fraction of photon originating from a π^0 as well as photon and Dalitz acceptance factors. They are

given in the Appendix of this chapter. For reasons of clarity, these factors are combined into a single factor A_{MC} in Equation 6.46.

Once the BP conversion rate is given by the ratio of the number of true BP conversions to that of Dalitz decays, the number of reconstruction BP conversions and Dalitz decays need to be extracted. They will be measured in data and used for the estimate of the BP material.

6.15.1 Selection Criteria

In the ATLAS software the conversion container is filled by looping over the reconstructed tracks and making any possible combination of two tracks that fulfill some conversion criteria such as having a massless vertex with two tracks of opposite charge and with a small angular separation at the vertex perigee. Different variables are used to perform this selection and reject a large amount of combinatorial background [61].

Furthermore, selection criteria based on the vertex and tracks quality are defined to improve the purity of the conversions selection. The following selection cuts are used in this analysis:

1. **Vertex selection:** a quality cut is applied on the vertex, it is required to have a $\chi^2 < 5$. A selection cut is also applied on the reconstructed radius. The BP conversions are required to have a vertex reconstructed with a radius in the range $20 < R_{RECO} < 40\ mm$ while the Dalitz vertices are selected in the range $R_{RECO} < 20\ mm$.

2. **Tracks Selection:** the tracks are required to be in the acceptance region, $|\eta(Trk)| < 2.5$ and have a transverse momentum above the reconstruction threshold $P_T(Trk) > 500\ MeV/c$. A cut on the electron probability of the tracks (standard TRT-PID tool) is also applied. This variable represents the probability of the tracks to be an electron (with respect to a charged pion). It depends of the number of high threshold hits in the TRT and the lost of energy in the Silicon. In this analysis, the standard cut is applied that is $PID(e-) > 0.9$.

The number of reconstructed BP conversions and Dalitz decays are given by the relations:

$$N^{BP\leftarrow\pi^0}_{TRUTH}(|\eta^{\gamma}| < 2.5) = \quad N^{BP}_{RECO} \times \frac{p^{BP}}{\epsilon^{BP}} \tag{6.35}$$

$$N^{Dz\leftarrow\pi^0}_{TRUTH}(|\eta^{Dz}| < 2.5) = \quad N^{Dz}_{RECO} \times \frac{p^{Dz}}{\epsilon^{Dz}} \tag{6.36}$$

where $\epsilon^{BP,Dz}$ and $p^{BP,Dz}$ denote respectively the **reconstruction efficiency** and the **purity** of BP conversions and Dalitz decays.

- $\epsilon^{BP}(\epsilon^{Dz})$ corresponds to the ratio of the number of reconstructed BP conversions (Dalitz decays) originating from a π^0 that pass the selection cuts (detailed in the next section) to that of BP conversions (Dalitz decays) that are potentially reconstructible. The BP conversions (Dalitz decays) are considered reconstructible when the two tracks are in acceptance and have a transverse momentum $P_T(Trk)$ greater than 500 MeV/c. This corresponds to the threshold above which the track reconstruction efficiency is optimal and amounts to about 80%.

- $p^{BP}(p^{Dz})$ corresponds to the fraction of the number of reconstructed and selected BP conversions (Dalitz decays) that come from a π^0 meson. As detailed later, there are different types of fake that contribute to the purity.

Finally, the BP conversion probability is written as:

$$P_{BP}^{acc} = \frac{N_{RECO}^{BP}}{N_{RECO}^{Dz}} \cdot \frac{\epsilon^{Dz} p^{BP}}{\epsilon^{BP} p^{Dz}} \cdot \frac{BR_{Dz}^{\pi^0}}{1.988} . A_{MC} \tag{6.37}$$

The ratio $N_{RECO}^{BP}/N_{RECO}^{Dz}$ will be measured in data while the reconstruction efficiencies and purities, and other terms given in the Appendix rely on the Monte-Carlo.

6.15.2 The Reconstruction Efficiency

When not applying any quality criteria on the reconstructed tracks or vertices, the reconstruction efficiencies for Dalitz decays and BP conversions amount to 30-40%. A small fraction however pass the tracks and vertex selection criteria described above, in particular the cut on the electron PID. *In fine* 264 reconstructed BP conversions and 140 reconstructed Dalitz vertices that match with a truth BP conversions or Dalitz decay originating from a π^0 meson are selected in the 900 GeV MC sample. This leads to global reconstruction efficiencies[5)]:

$$\epsilon^{BP} = \frac{264}{8234} = 3.21 \pm 0.19\% \quad \text{and} \quad \epsilon^{Dz} = \frac{140}{4340} = 3.23 \pm 0.28\%$$

In the 7 TeV sample, the possibility of selecting BP conversions with a reconstructed vertex radius between 20 and 45 mm has been investigated. A motivation for changing the selection of BP conversions comes from the non negligible fraction of conversions in the BP or the inner layer of the Pixel having shared hits between the two tracks. When the conversion happens at low radius and the photon have a relatively high energy, the two charged particles from the decay form tracks with a very small angular separation; the reconstruction of the conversion vertex is more intricate and the vertex can be reconstructed with a larger radius. It was observed that about 80% of the BP conversions that are reconstructed with a radius greater than 40 mm have shared hit(s). Figure 6.73(a) displays the distribution of the truth vertex radius as a function of the reconstructed vertex radius in black for all reconstructed conversions that pass the selection criteria and are matched with the truth conversions, and in red when the tracks share hit(s) in the Pixel layers. As expected the BP conversions with shared hit(s) have a reconstructed radius typically larger. There are also conversions in the B-layer having shared hit(s) that are rather well reconstructed. The upper limit on BP conversions selection at 45 mm instead of 40 mm induces a better reconstruction efficiency ($5.15 \pm 0.09\%$ instead of $4.45 \pm 0.09\%$ at 7 TeV) but degrades the purity due to conversion in the B-layer reconstructed as BP conversions ($72.94 \pm 0.95\%$ instead of $76.69 \pm 0.73\%$ at 7 TeV) which suggests to keep the upper limit at 40 mm.

Figure 6.73(b) displays the distribution of the sum of the reconstructed transverse momentum of the two tracks at vertex and reflects that the conversions with shared hit(s) are rather independent of the photon transverse momentum.

The global reconstruction efficiencies found in the 7 TeV MC sample are as expected greater than what found in the 900 GeV MC sample:

[5)] The numbers at the bottom of these ratios denote the numbers of true BP conversions and Dalitz decays produced in the acceptance which tracks have a transverse momentum greater than 500 MeV/c^2

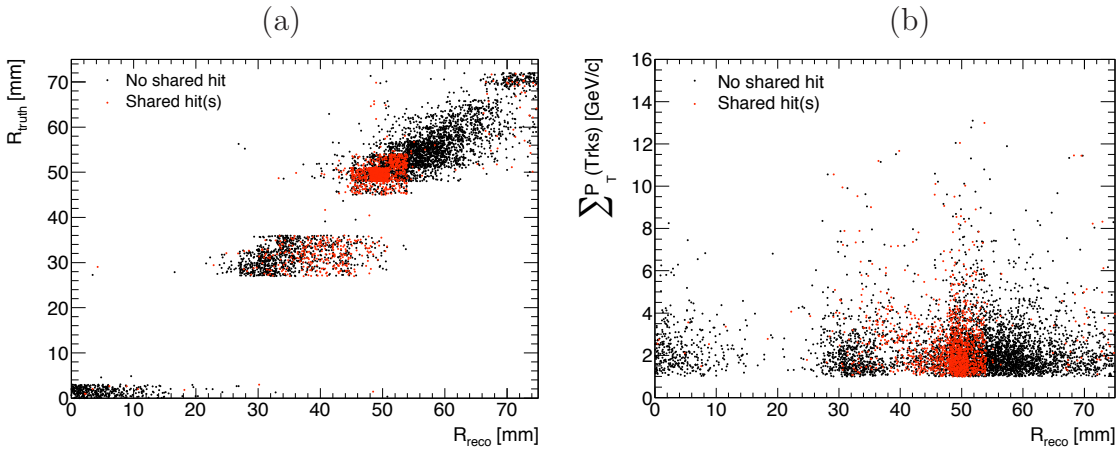

Figure 6.73: (a): Distribution of the truth radius of the Dalitz decays and conversions in the BP (and Pixel inner layer) as a function of the reconstructed vertex radius. (b): Distribution of the transverse momentum of the track pair of the Dalitz decays and conversions in the BP (and Pixel inner layer) as a function of the reconstructed vertex radius. The red points represent the conversions with shared hit(s).

$$\epsilon^{BP} = \frac{2499}{56130} = 4.45 \pm 0.09\% \quad \text{and} \quad \epsilon^{Dz} = \frac{1361}{3036} = 4.49 \pm 0.12\%$$

6.15.3 The Purity and Classification of Fakes

Different types of fakes are considered:

1. $N_1^{BP,Dz}$: the combinatorial background, consisting of any possible combination of two opposite charged tracks, is initially the leading type of fakes. The standard analysis cuts have been optimized in the purpose of reducing these fakes.

2. $N_2^{BP,Dz}$: conversions that are not BP conversions (Dalitz decays) but are reconstructed as.

3. $N_3^{BP,Dz}$: conversions or Dalitz decay that do not originate initially from a π^0. It has been seen in the MC simulations that about 91% of photons with an energy greater than 1 GeV actually come from π^0. The other photons mostly come from other mesons, η and ω. This type of events are not fakes from the reconstruction point of view and the "fake" denomination is not completely correct.

The π^0 BP conversion (Dalitz decay) purity is re-expressed as a function of the number of reconstructed BP conversions (Dalitz decays) matched with a truth conversion and the different types of fake:

$$p^{BP,Dz} = \frac{N_{RECO}^{BP,Dz}(match)}{N_{RECO}^{BP,Dz}} \tag{6.38}$$

$$p^{BP,Dz} = \frac{N_{RECO}^{BP,Dz} - N_1^{BP,Dz} - N_2^{BP,Dz} - N_3^{BP,Dz}}{N_{RECO}^{BP,Dz}} \tag{6.39}$$

$$p^{BP,Dz} = 1 - f_1^{BP,Dz} - f_2^{BP,Dz} - f_3^{BP,Dz} \tag{6.40}$$

where $f_i^{BP,Dz}$ corresponds to the contribution of the fakes of type i to the total number of reconstructed BP conversions and Dalitz decays. The rejection of fakes of type 1 relies on the efficiency of criteria applied on conversion candidates. The fakes of type 2 rely on the reconstruction algorithm performance. The fakes of type 3 arise from the normalization of the total number of photons to that of Dalitz decays that originate only from a π^0 meson. The BP and Dalitz fakes contributions found in the 900 GeV MC sample are listed in Table 6.13. There are relatively more fakes originating from the combinatorial background in the Dalitz

		Fakes 1		Fakes 2		Fakes 3	
energy		#	f_1	#	f_2	#	f_3
900 GeV	BP	12	3.46 ± 0.98%	10	2.88 ± 0.89 %	61	17.58 ± 2.04%
	Dz	13	7.56 ± 2.01 %	0	-	19	11.05 ± 2.39 %
7 TeV	BP	181	5.56 ± 0.40%	90	2.76 ± 0.28%	486	14.93 ± 0.62%
	Dz	192	11.12 ± 0.76%	1	0.06 ± 0.06 %	173	10.02± 0.72%

Table 6.13: Number and contribution of the different types of fake of π^0 BP conversions and Dalitz decays found in the 900 GeV and 7 TeV MC sample.

selection, while there is no fake from the reconstruction for the Dalitz vertices (all vertices are reconstructed with a radius $R_{RECO} < 20\ mm$). After removing the combinatorial background, about 3% of BP conversions are fakes due to a bad reconstruction of the conversion (or Dalitz) vertices radius, mostly conversions arising in the first layer of the Pixel detector. Only one conversion among these ten fakes is a Dalitz decay reconstructed with a larger vertex radius. There are more fakes due to the π^0 identification in the case of BP conversions, as the branching ratio of the Dalitz mode is very small for other mesons than π^0. Photons are also produced by kaons, protons and Bremsstrahlung emissions, adding possible conversions but no more Dalitz decay.

The contribution of the different types of fake obtained in 7 TeV MC sample, also illustrated in Table 6.13, are rather similar to what found in the 900 GeV MC sample. The fraction of fakes of type 1 and 2 are relatively more important than what found in the 900 GeV MC sample for both Dalitz decays and BP conversions while there are less fakes from the π^0 identification.

6.15.4 Summary

Table 6.14 summarizes the numbers of reconstructed BP conversions and Dalitz decays after applying the selection cuts and the associated reconstruction efficiencies and purities found with the MC samples at 900 GeV and 7 TeV. BP conversions and Dalitz have close reconstruction efficiencies and purity which gives confidence in the conversions reconstruction algorithm performance at very low radius. The reconstruction efficiency and purities for both Dalitz decays and BP conversions are very similar at 900 GeV and 7 TeV. The number of reconstructed BP conversions and Dalitz vertices is about ten times what found in the 900 GeV MC sample, while the statistics is enhanced by only a factor 2. The increase of the minimum bias cross section with the energy can not justify such difference. However this is explained by the different kinematic at these energies.

Figure 6.74(a-b) displays the distribution of the (truth MC) tracks transverse momentum P_T(Truth Track) and multiplicity in the two MC samples, in dark for 7 TeV and in red for

energy	terms	Dz	BP	BP/Dz
900 GeV	N_{RECO}	172	347	2.02 ± 0.19
	ϵ_{RECO}	$3.23 \pm 0.28\%$	$3.21 \pm 0.19\%$	0.99 ± 0.10
	p_{RECO}	$81.39 \pm 2.97\%$	$76.08 \pm 2.29\%$	0.93 ± 0.04
7 TeV	N_{RECO}	1727	3256	1.88 ± 0.06
	ϵ_{RECO}	$4.49 \pm 0.12\%$	$4.45 \pm 0.09\%$	0.99 ± 0.03
	p_{RECO}	$78.81 \pm 0.98\%$	$76.69 \pm 0.74\%$	0.97 ± 0.01

Table 6.14: List of π^0 BP conversions and Dalitz decays numbers, reconstruction efficiencies and purities with associated statistical errors found in the 900 GeV and 7 TeV MC samples.

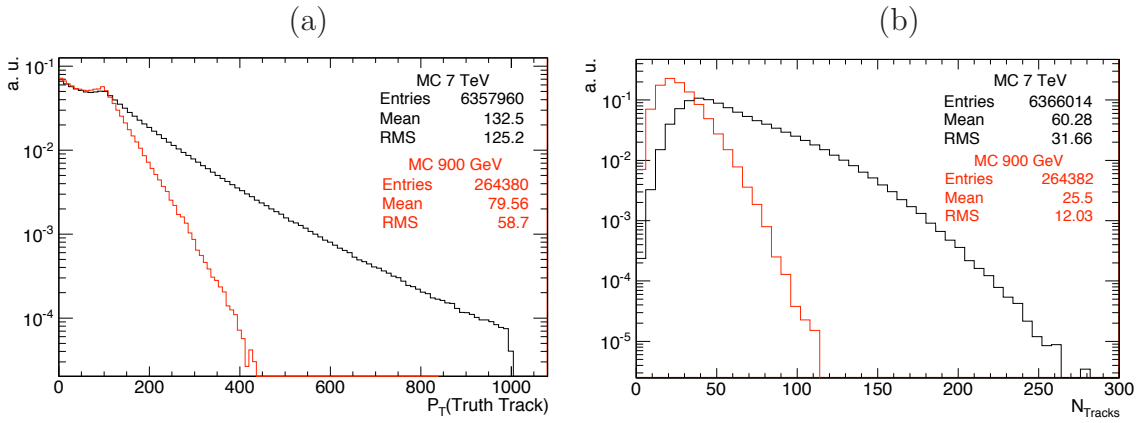

Figure 6.74: Distributions of (a) the transverse momentum and (b) the truth track multiplicity in dark for the MC sample at 7 TeV and in red for the MC sample at 900 GeV.

900 GeV. The distributions are normalized to the unity for a proper comparison, the number of entries are indicated though[6)] . In the range below 1000 MeV/c, the ratio of the number of tracks produced at the interaction point in the 7 TeV sample is larger by a factor $\sim$ 24 to that of the 900 GeV sample, suggesting an increased MB activity with the energy, seen as well in the initial number of π^0 (only reduced by $\sim$ 15% in the 7 TeV sample). The distributions 6.74(b) show a larger multiplicity for the 7 TeV sample. These observations are in favor of the larger number of reconstructed BP conversions and Dalitz with respect to the 900 GeV sample, despite the reduced statistics.

The BP conversion probability estimated with the 900 GeV MC sample when replacing the different terms introduced in Equation 6.50 with the values found in the MC sample amounts to:

$$P_{BP}^{acc}(900\ GeV) = \underbrace{\left(\frac{N_{RECO}^{BP}}{N_{RECO}^{Dz}}\right)}_{2.02\pm0.19} \cdot \underbrace{\left(\frac{\epsilon^{Dz} p^{BP}}{\epsilon^{BP} p^{Dz}}\right)}_{0.94\pm0.11} \cdot \underbrace{\left(\frac{BR_{Dz}^{\pi^0}}{1.988}\right)}_{0.603\pm0.016\%} \cdot \underbrace{A_{MC}}_{\sim 1.625} \tag{6.41}$$

$$P_{BP}^{acc}(900\ \text{GeV, MC}) = 18.60 \pm 0.02\ {}^{0}/_{00}$$

[6)] For technical reasons, only 25% of the statistics is used in the distributions at 7 TeV.

The BP conversion probability found in the 7 TeV MC sample is:

$$P_{BP}^{acc}(7\ TeV) = \underbrace{\left(\frac{N_{RECO}^{BP}}{N_{RECO}^{Dz}}\right)}_{1.88\pm0.06} \cdot \underbrace{\left(\frac{\epsilon^{Dz}p^{BP}}{\epsilon^{BP}p^{Dz}}\right)}_{0.98\pm0.04} \cdot \underbrace{\left(\frac{BR_{Dz}^{\pi^0}}{1.988}\right)}_{0.603\pm0.016\%} \cdot \underbrace{A_{MC}}_{\sim 1.616} \tag{6.42}$$

$$P_{BP}^{acc}(7 \text{ TeV MC}) = 17.99 \pm 0.01\ {}^{0}/_{00}$$

6.16 Results with First Data at 900 GeV

Minimum Bias data at 900 GeV energy in the centre-of-mass have been largely used in ATLAS working groups, notably to check the tracks and conversions reconstruction efficiencies [61] and compare the charged particles multiplicity and spectra with predictions from different Monte-Carlo tuning schemes [62]. A good quality of the data information recorded in the different detectors of the ID and some requirements on the machine reduce the amount of events to 384 186 collision candidates. Theses events are used in this analysis to estimate the BP conversion probability, within the numbers of reconstructed Dalitz and BP conversions.

After all selection cuts are applied, 9 BP conversions and 5 Dalitz vertices have been reconstructed in the data.

The numbers of BP conversions and Dalitz vertices reconstructed in the data leads to the ratio:

$$\left(\frac{N_{RECO}^{BP}}{N_{RECO}^{Dz}}\right)^{900\ GeV,\ data} = \frac{9}{5} = 1.80 \pm 1.00$$

The BP conversion probability estimated from the data is:

$$P_{BP}^{acc}(900 \text{ GeV, data}) = 16.59 \pm 10.52\ {}^{0}/_{00}$$

A good agreement with the MC prediction is found although this result suffers from very large statistical errors. Figure 6.75(a-b) illustrates the reconstructed Dalitz and BP conversion in the data and in the MC. The MC statistics has been normalized to data for a proper comparison. The white region separating the black line from the color filled region corresponds to the fakes in Dalitz decays and BP converisons. In Figure 6.75(a) the fake of type 3 are ignored while in Figure 6.75(b), the π^0 identification is required. The conversions in the first layer of the Pixel detector are also shown, for a radius $40 < R_{RECO} < 75\ mm$. A good agreement is observed although statistically too limited to assess the BP material.

6.17 Beam Pipe Conversion Rate Estimate with 7 TeV Data

Data at a centre-of-mass energy of 7 TeV are being recorded since in ATLAS, increasing daily the luminosity. About 98 million of events are used in this study which corresponds to an integrated luminosity of approximatively $\sim 800\ \mu b^1$.

After all selection cuts are applied, 8463 BP conversions and 4519 Dalitz vertices have been reconstructed in the data. Figures 6.76 and 6.77 display the η and ϕ directions of the

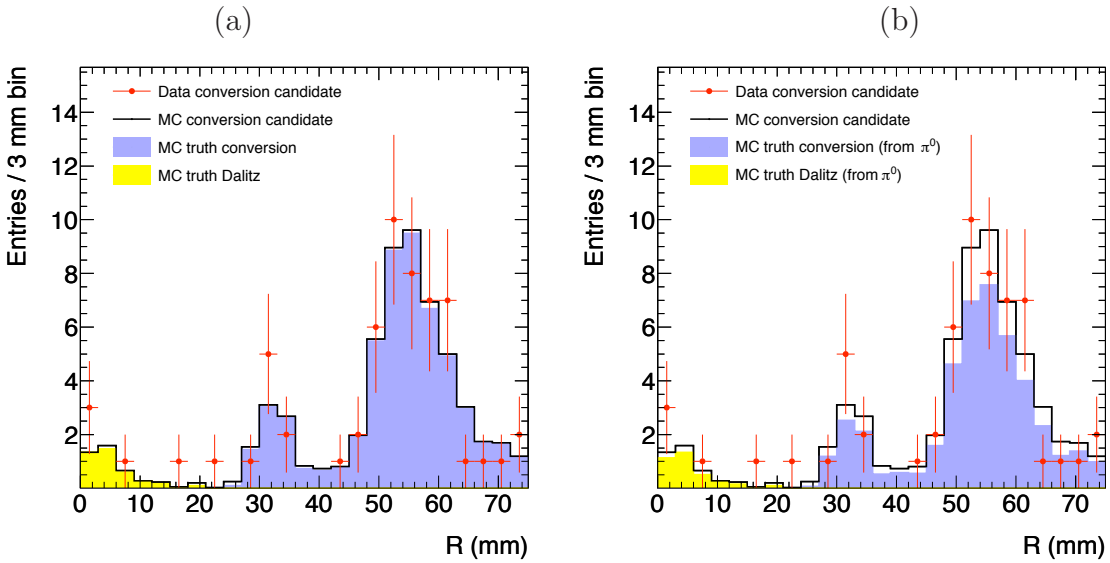

Figure 6.75: Reconstructed radius distribution of the Dalitz vertices and photon conversions, in the BP and the first layer of the Pixel detector. The selection cuts are applied. The red dots correspond to data recorded at 900 GeV. The MC statistic is normalized to data. The black line correspond to all reconstructed conversions while the yellow and blue regions respectively represent the Dalitz and BP conversion matched to a meson decay. In (a), the meson is not specified while in (b) it is required to be a π^0, the difference highlighting the fake of type 3.

reconstructed tracks associated to each BP conversions and Dalitz. The distributions from the MC are normalized to the number of entries in BP conversions and Dalitz for a proper comparison. The distributions for the Dalitz should be flat in the η direction while more BP conversions are expected to be reconstructed at large η due to the larger thickness of material. The data and MC distributions in η are not flat but have the shape of a mexican hat centered at 0. This is due to the presence of dead modules in the Pixel. The data and MC distributions in η for the BP disagree around 0 which is partially understood by the different account for the dead modules in the detector configuration. The same observation occurs in the ϕ distributions.

Figure 6.78 displays the distributions of the transverse momentum of the tracks associated to the BP conversions and Dalitz and shows a good agreement between MC and data.

Using the ratio of the number of reconstruction BP conversions to that of Dalitz found in the data samples at 7 TeV,

$$\left(\frac{N_{RECO}^{BP}}{N_{RECO}^{Dz}}\right)^{7\ TeV,\ data} = \frac{8463}{4519} = 1.87 \pm 0.03$$

the BP conversion probability is found to be:

$$P_{BP}^{acc}(7\text{ TeV, data}) = 17.87 \pm 0.92\ {}^{0}/_{00}$$

in a good agreement with the 7 TeV MC prediction.

Figure 6.79(a-d) display the distribution of the reconstructed Dalitz decays and conversions vertex in the data and in the MC. The MC sample is normalized to 7 TeV data for a proper comparison. The different types of fake associated to Dalitz decays and BP conversions are

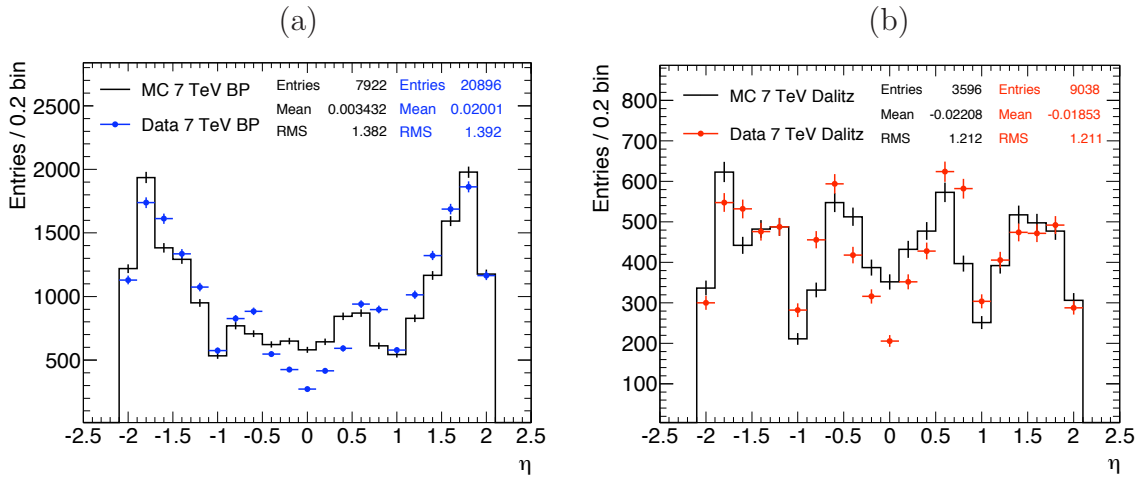

Figure 6.76: Distributions of the η direction at the vertex perigee for (a) the BP conversions and (b) the Dalitz decay at the vertex perigee, for both the MC and data samples at 7 TeV.

displayed. The fakes of type 2 in the Dalitz decays are the fraction of conversions in the BP and in the B-layer reconstructed with a radius below 20 mm. The number of fakes of type 2 in the Dalitz is very small as expected from Table 6.13. The fakes of type 2 in the BP conversions are similarly Dalitz decays and conversions in the B-layer reconstructed with a radius between 20 and 40 mm. Figure 6.79(c) and (d) also display the conversions reconstructed in the B-layer (R $<$ 75 mm). The MC and data distributions agree relatively well at low to medium radius (R $<$ 40 mm). It corroborates the good agreement found in the ratio of the number of reconstructed BP conversions to that of Dalitz decays. As illustrated in Figure 6.79(a) the Dalitz decays and BP conversions are distributed into two well separated regions. The Dalitz to BP transition region is dominated by fakes from the combinatory background. There are however more Dalitz reconstructed at very low radius, as seen in the first bin of the distributions. Small differences are visible in the bump of the BP range; more BP conversions are reconstructed in the data below 30 mm and above 38 mm.The disagreement between data and MC observed above 45 mm, *i.e* in the B-layer, is rather important. It indicates that the material in the B-layer would actually be more important at low radius and decreases more rapidly with R, in the data.

6.18 Systematic Uncertainties

The sources of experimental systematic errors associated to the BP conversion rate are estimated by varying the selection cuts in the 7 TeV MC sample.

1. The χ^2 of the vertex is displayed in Figure 6.80(a-b) for all BP conversions and Dalitz decays, for the conversions that match to the truth in red and for the reconstructed conversions that are not associated to any truth, i.e combinatorial background. The latter distributions are rather flat while the distributions of matched BP conversions and Dalitz follow well a χ^2 distribution. The χ^2 is varied by ± 1 around the cut value chosen in the selection criteria. The variation of the ratio of the number of BP conversions to

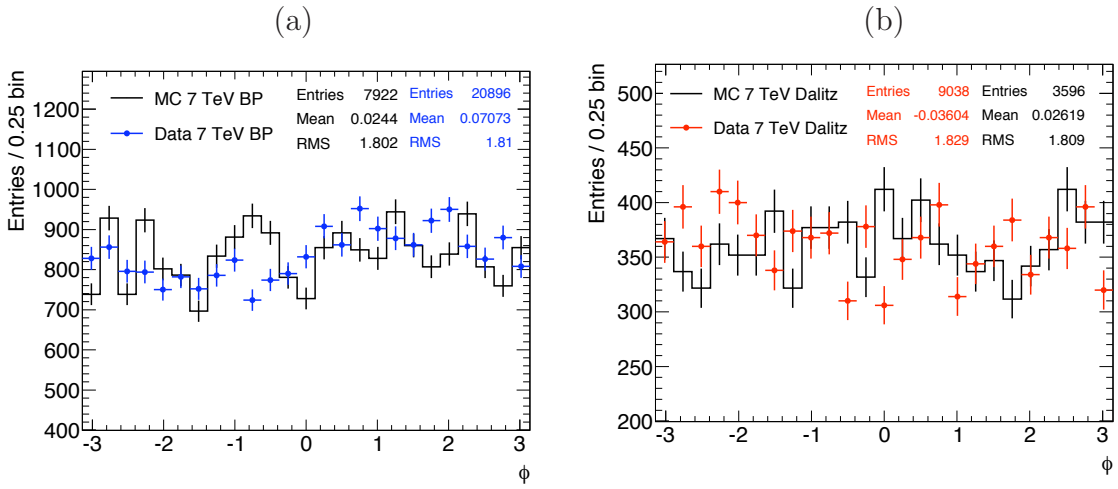

Figure 6.77: Distributions of the ϕ direction at the vertex perigee for (a) the BP conversions and (b) the Dalitz decay at the vertex perigee, for both the MC and data samples at 7 TeV.

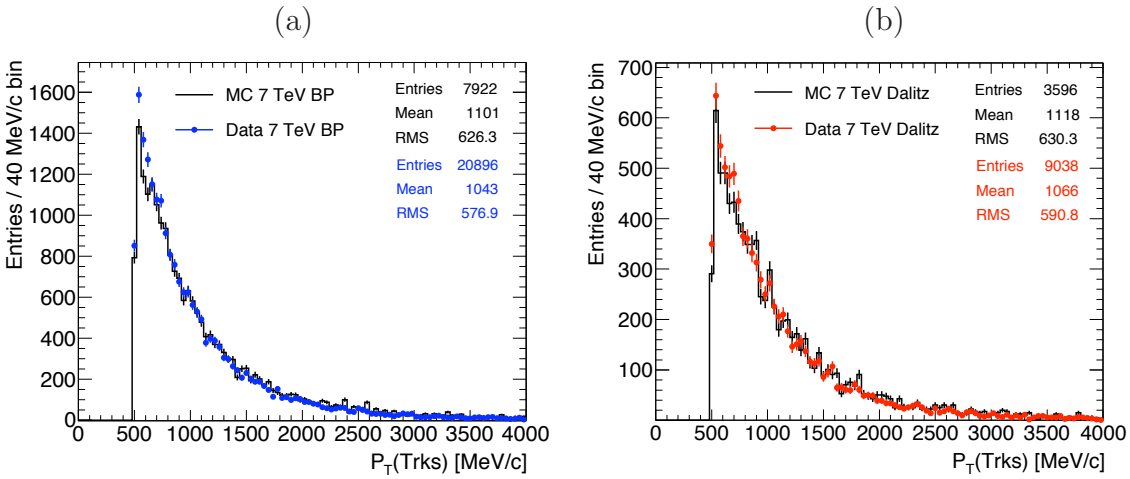

Figure 6.78: Distributions of the P_T of the tracks associated to (a) the BP conversions and (b) the Dalitz decay at the vertex perigee, for both the MC and data samples at 7 TeV.

that of Dalitz measured with the 7 TeV data and of the factors that rely on the MC lead to a relative variation of the BP conversion probability of (-0%,+1.5%).

2. The range of reconstructed vertex radius for BP and Dalitz is varied by $\pm 3\ mm$. The BP conversion probability varies of (-4.2%,+0%) which can be expected from the distributions of the reconstructed vertex radius displayed in Figure 6.79.

3. The track reconstruction efficiency becomes rather flat in P_T for tracks with $P_T > 500\ MeV/c$. The selection is varied requiring the tracks to have a transverse momentum greater than 700 MeV/c. This leads to a relative variation of the BP conversion probability of (-0%,+0.8%) with 7 TeV data.

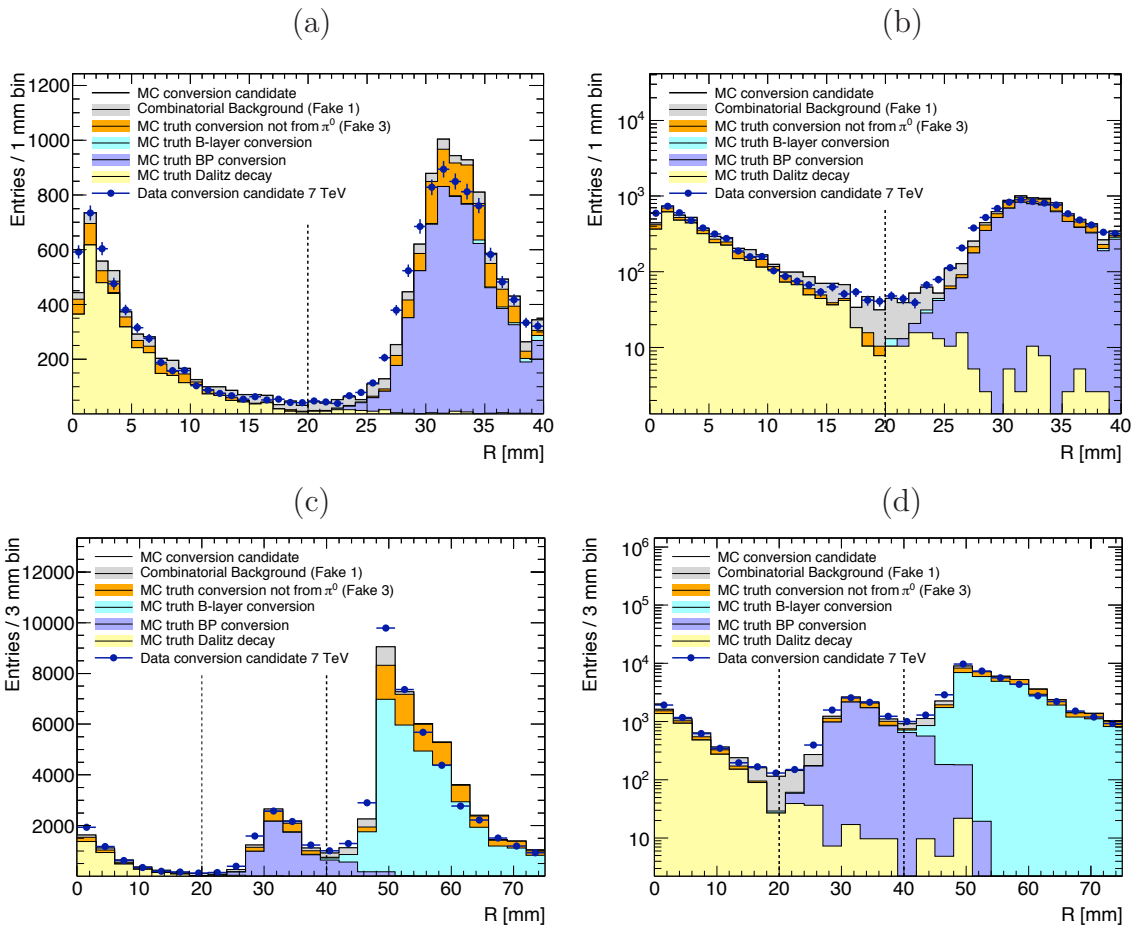

Figure 6.79: Distributions of the reconstructed radius of Dalitz decays and conversion vertices, in the BP and (c-d) the first layer of the Pixel detector, (a-c) in linear and (b-d) logarithmic scale. The selection cuts are applied. The MC statistic is normalized to data recorded at 7 TeV, represented by blue dots. The BP and Dalitz fakes of type 1 and 3 are represented by the colored filled regions, respectively in gray and orange. The reconstructed Dalitz and BP conversions originating from a π^0 are displayed in yellow and light blue, respectively.

This leads to a overall experimental systematic uncertainty on the BP conversion probability of (-4%,+2%). The BP conversion probability estimated:

1. using the BP material given by the layout design and the 7 TeV MC η distribution for photons with energy above the threshold at 1 GeV,
2. with the MC sample and
3. using the MC related factors estimated with the 7 TeV MC sample and the ratio of the number of reconstructed BP conversion to that of Dalitz decays measured in the data

are, with statistical and systematic uncertainties:

$$P_{acc}(\text{Design+MC 7 TeV}) \longrightarrow 19.28 \pm 0.77\ (\text{syst})\ {}^{0}/_{00}$$
$$P_{acc}(\text{MC 7 TeV}) \longrightarrow 17.99 \pm 0.01\ (\text{stat})\ {}^{0}/_{00}$$
$$P_{acc}(\text{data 7 TeV}) \longrightarrow 17.87 \pm 0.92\ (\text{stat})\ {}^{0.36}_{-0.72}\ (\text{syst})\ {}^{0}/_{00}$$

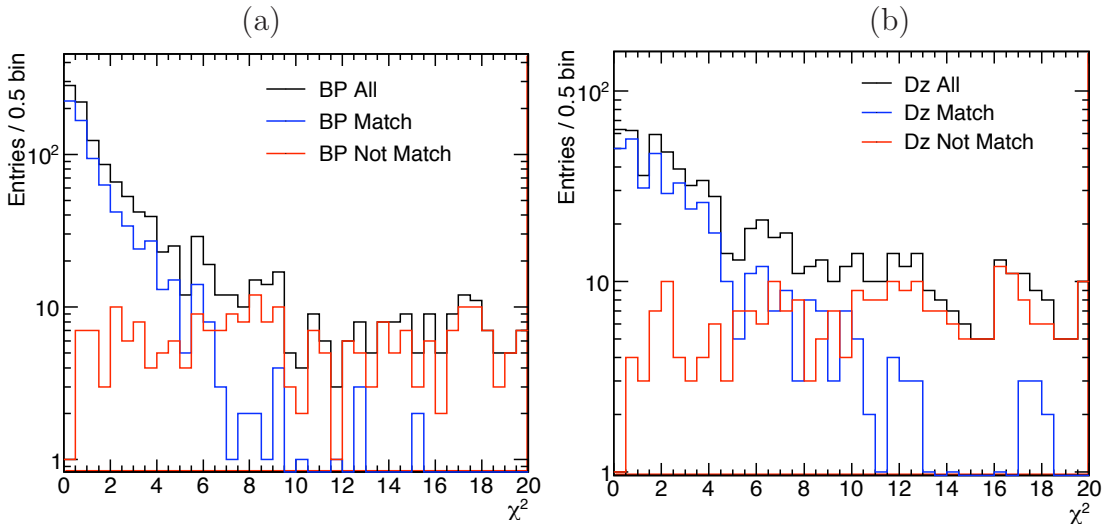

Figure 6.80: Distributions of the χ^2 of the reconstructed vertex of (a) BP conversions and (b) Dalitz decays, in black for all conversions passing the selection criteria, in red for these that match with the truth MC and in blue for the combinatorial background.

The difference observed between the BP rate estimated using the BP material quoted in the design and the rate derived from the MC simulation translates the fact that at the 1 GeV threshold applied on the photon energy the conversion process has not yet reach the stable regime. Elastic and inelastic photon scattering as well as photo-electric process contribute to the cross section of photon interaction with matter. This relative difference of 6.6% gives an indirect estimate of the bias of this method used to extract the material in the BP with data. The relative difference decreases with the photon energy threshold and amounts to 3.8% at 10 GeV energy threshold.

Conclusion

A study of the BP conversion probability with photons from minimum bias events is performed. The ratio of the number of reconstructed beam pipe conversions to that of Dalitz decays is used to estimate the material contained in the BP. 900 GeV and 7 TeV Monte-Carlo minimum bias samples, simulating respectively ten and twenty millions of events, are used to assess the BP conversion and Dalitz reconstruction efficiency and purity. A comparison with photon candidates in the first data recorded at LHC at a centre-of-mass energies of 900 GeV and 7 TeV is made. The following observations are made:

1. As expected reconstruction efficiencies found in the MC samples for the Dalitz decay and BP conversions are very similar.

2. High purities are found for both the Dalitz decays and BP conversions. In particular, as expected a smaller contribution of fakes of type 1 is found in the BP. Very few fakes of type 2 are found in the Dalitz and are identified as BP conversions with a badly reconstructed conversion vertex. For BP conversions, these fakes come from Dalitz ($\sim$ 65%) and conversions in the first layer of the Pixel ($\sim$ 35%). The fakes of type 3 are more

important in BP conversions than Dalitz which can be partially explained by the larger number of photon sources (and the reduced Dalitz branching ratio in other and heavier mesons such as η or ω).

3. The ratio of the number of reconstructed BP conversions to that of Dalitz found in the 7 TeV data, $(N^{BP}_{RECO}/N^{Dz}_{RECO})^{data,\ 7\ TeV} = 8463/4519 = 1.87 \pm 0.03$, agrees well with MC prediction, $(N^{BP}_{RECO}/N^{Dz}_{RECO})^{MC,\ 7\ TeV} = 3256/1727 = 1.88 \pm 0.06$, with similar statistical uncertainties. The distributions of the reconstructed vertex radius show a good agreement between MC prediction and the number of BP conversions and Dalitz decays reconstructed in the data. Using the ratio derived in the data, the BP conversion probability found in the acceptance region amounts to P_{acc}(data 7 TeV) =17.87 $\pm$ 0.92 (stat) $^{0.36}_{-0.72}$ (syst) $^{0}/_{00}$ which is in good agreement with MC prediction: P_{acc}(MC 7 TeV) =17.99 $\pm$ 0.01 (stat) $^{0}/_{00}$.

4. A first and incomplete estimate of systematic uncertainties associated to the BP conversion probability are estimated by varying the selection cuts; these amount to (-4%,+2%). A more thorough estimate of the systematic error is needed.

This study shows that the BP conversion rate can be estimated using the π^0 Dalitz decays. The meaningful observable is the ratio of the number of reconstructed BP conversions to that of Dalitz decays. In this respect the data and the Monte Carlo agree quite well. This shows that on the one hand the amount of material in the simulation agrees with the amount physically present and on the other hand that the physical model of minimum bias events simulated in Pythia is also matching the data. The advantage of normalizing the conversion rate to that of the beam pipe to map the amount of upstream material is that it is independent of the physical model of π^0 prediction; its obvious disadvantage is that it is a relative measurement only. Using Dalitz decays has the advantage not to rely on the amount of BP material, which we have seen to be trivially known, but will rely somewhat on the model of minimum bias events. At the present stage of data taking it is safe to conclude that this measurement corroborates the amount of material of the beam pipe. More specific studies of systematic uncertainties are needed in order to ascertain that the Dalitz decays can be used for an absolute normalization of the upstream material.

6.19 Appendix

In the following the BP conversion probability derived in equation 6.31 is transformed in order to normalize the initial number of photons in minimum bias event to the π^0 Dalitz decays. We first extract the number of photons originating from a π^0 in equation 6.31:

$$N^{\gamma}_{TRUTH}(|\eta^{\gamma}|<2.5) \xrightarrow{A^{\gamma}=\frac{N^{\gamma}_{TRUTH}(|\eta^{\gamma}|<2.5)}{N^{\gamma}_{TRUTH}}} N^{\gamma}_{TRUTH} \xrightarrow{f^{\pi^0}_{\gamma}=\frac{N^{\gamma\leftarrow\pi^0}_{TRUTH}}{N^{\gamma}_{TRUTH}}} N^{\gamma\leftarrow\pi^0}_{TRUTH} \tag{6.43}$$

We have introduced a photon acceptance factor and a factor corresponding to the fraction photons coming from a π^0. The number of photons from π^0 as a function of the number of π^0 is given by:

$$N^{\gamma\leftarrow\pi^0}_{TRUTH} \longrightarrow [2\times(100-BR_{Dz})+BR_{Dz}].N^{\pi^0}_{TRUTH} \sim 1.988\ N^{\pi^0}_{TRUTH} \tag{6.44}$$

This allows the following replacement:

$$N^{\pi^0}_{TRUTH} \xrightarrow{BR_{Dz}} N^{Dz\leftarrow\pi^0}_{TRUTH} \xrightarrow{A^{Dz}=\frac{N^{Dz\leftarrow\pi^0}_{TRUTH}(|\eta^{Dz}|<2.5)}{N^{Dz\leftarrow\pi^0}_{TRUTH}}} N^{Dz\leftarrow\pi^0}_{TRUTH}(|\eta^{Dz}|<2.5) \tag{6.45}$$

where an acceptance factor for the π^0 Dalitz decays is introduced, η^{Dz} being the η of the Dalitz pair e^+e^-.

The BP conversion probability in equation 6.31 becomes:

$$P^{acc}_{BP} = \frac{N^{BP\leftarrow\pi^0}_{TRUTH}(|\eta^{\gamma}|<2.5)}{N^{Dz\leftarrow\pi^0}_{TRUTH}(|\eta^{Dz}|<2.5)}.\frac{BR^{\pi^0}_{Dz}}{1.988}.\frac{f^{\pi^0}_{\gamma}}{f^{\pi^0}_{BP}(|\eta^{\gamma}|<2.5)}.\frac{A^{Dz}}{A^{\gamma}} \tag{6.46}$$

where $f^{\pi^0}_{BP}(|\eta^{\gamma}|<2.5)$ is the fraction of photon conversions in the beam pipe arising in the acceptance region that originate from a π^0:

$$f^{\pi^0}_{BP}(|\eta^{\gamma}|<2.5) = \frac{N^{BP\leftarrow\pi^0}_{TRUTH}(|\eta^{\gamma}|<2.5)}{N^{BP}_{TRUTH}(|\eta^{\gamma}|<2.5)} \tag{6.47}$$

The number of reconstructed BP conversions and Dalitz decays are given by the number of truth BP conversions and Dalitz decays through the relations:

$$N^{BP\leftarrow\pi^0}_{TRUTH}(|\eta^{\gamma}|<2.5) = \quad N^{BP}_{RECO}\times\frac{R^{BP}\epsilon^{BP}}{p^{BP}} \tag{6.48}$$

$$N^{Dz\leftarrow\pi^0}_{TRUTH}(|\eta^{Dz}|<2.5) = \quad N^{Dz}_{RECO}\times\frac{R^{Dz}\epsilon^{Dz}}{p^{Dz}} \tag{6.49}$$

$R^{BP}(R^{Dz})$ is the **reconstruction potential** of the BP conversions (Dalitz) originating from a π^0. This corresponds to the fraction of truth BP conversions (Dalitz decays) that can *a priori* be reconstructed, when the two tracks are in acceptance and have a transverse momentum $P_T(Trk)$ greater than 500 MeV/c. $\epsilon^{BP}(\epsilon^{Dz})$ and $p^{BP}(p^{Dz})$ are the **reconstruction efficiencies** and **purity** of the π^0 BP conversions (Dalitz decays).

Finally, the BP conversion probability is written as:

$$P^{acc}_{BP} = \frac{N^{BP}_{RECO}}{N^{Dz}_{RECO}}.\frac{R^{Dz}\epsilon^{Dz}p^{BP}}{R^{BP}\epsilon^{BP}p^{Dz}}.\frac{A^{Dz}}{A^{\gamma}}.\frac{BR^{\pi^0}_{Dz}}{1.988}.\frac{f^{\pi^0}_{\gamma}}{f^{\pi^0}_{BP}(|\eta^{\gamma}|<2.5)} \tag{6.50}$$

6.19.1 Initial Numbers of γ and π^0

9 728 609 events are analyzed in the Minimum Bias MC sample at 900 GeV. The fractions of photons and BP conversions (in acceptance and with $E(\gamma) > 1\ GeV$) originating from a π^0 are respectively:

$$f_\gamma^{\pi^0} = \frac{133151575}{146214263} = 91.06\% \text{ and } f_{BP}^{\pi^0}(|\eta^\gamma| < 2.5) = \frac{473058}{536827} = 88.12\%$$

19 744 590 events are analyzed in the Minimum Bias MC sample at 7 TeV centre-of-mass energy. The available statistics is therefore enhanced by a factor two with respect to the Minimum Bias MC sample at 900 GeV. The fractions of photons and BP conversions (in acceptance and with $E(\gamma) > 1\ GeV$) originating from a π^0 are respectively:

$$f_\gamma^{\pi^0} = \frac{72746840}{796670068} = 91.31\% \text{ and } f_{BP}^{\pi^0}(|\eta^\gamma| < 2.5) = \frac{1819429}{2048726} = 88.81 \pm 0.02\%$$

6.19.2 Photon and Dalitz Acceptance

The photon acceptance factor derived in equation 6.50 is found to be in 900 GeV MC sample:

$$A^\gamma = \frac{536827}{28854772} \sim 18.60\%$$

To get close acceptances and reconstruction potentials, the π^0 that decay into the Dalitz channel are required to have an energy greater than 1 GeV. This modifies the expression of the BP conversion probability by adding a correction factor c_{cut} to the assumption $N_{TRUTH}^{\gamma \leftarrow \pi^0} = 1.988\ N_{TRUTH}^{\pi^0}$:

$$c_{cut} = 1.988 / \frac{N_{TRUTH}^{\gamma \leftarrow \pi^0}(E(\gamma) > 1\ GeV)}{N_{TRUTH}^{\pi^0}(E(\pi^0) > 1\ GeV)} \approx 1.988/1.353 \approx 1.469$$

The acceptance factor of π^0 Dalitz, for π^0 with an energy greater than 1 GeV, is of the same order:

$$A^{Dz} = \frac{397710}{1180313} \sim 33.69\%$$

The Dalitz acceptance factor is greater than that of the photon which can be expected from the different kinematic of the process: the Dalitz decay arises at the interaction point whereas the conversions rate increases with η.

The photon and Dalitz acceptance factors derived in 7 TeV MC sample respectively amount to:

$$A^\gamma = \frac{113872781}{796670068} = 14.29\% \text{ and } A^{Dz} = \frac{1486526}{5790475} = 25.67 \pm 0.02\%$$

These results are very close to what found in the 900 GeV MC sample. (In the 7 TeV MC sample $c_{cut} = 1.323$)

These different factors strongly rely on the minimum bias events model simulated in the MC. Systematic error associated to these factors needs to be carefully estimated, using different tuned samples of the Pythia MC.

6.19.3 The Reconstruction Potential

Only a fraction of the BP conversions and Dalitz vertices found in acceptance are *a priori* reconstructible, depending the robustness of the tracks reconstruction algorithm. The track reconstruction efficiency is rather stable when tracks are in acceptance ($|\eta(Trk)| < 2.5$) and have a transverse momentum $P_T(Trk) > 500\ MeV/c$.

The BP and Dalitz reconstruction potential found in the 900 GeV MC sample, that correspond to the fraction of BP conversions and Dalitz decays having tracks that fulfill these criteria amount to:

$$R^{BP} = \frac{8234}{473058} = 1.76 \pm 0.02\% \text{ and } R^{Dz} = \frac{4340}{397710} = 1.09 \pm 0.02\%$$

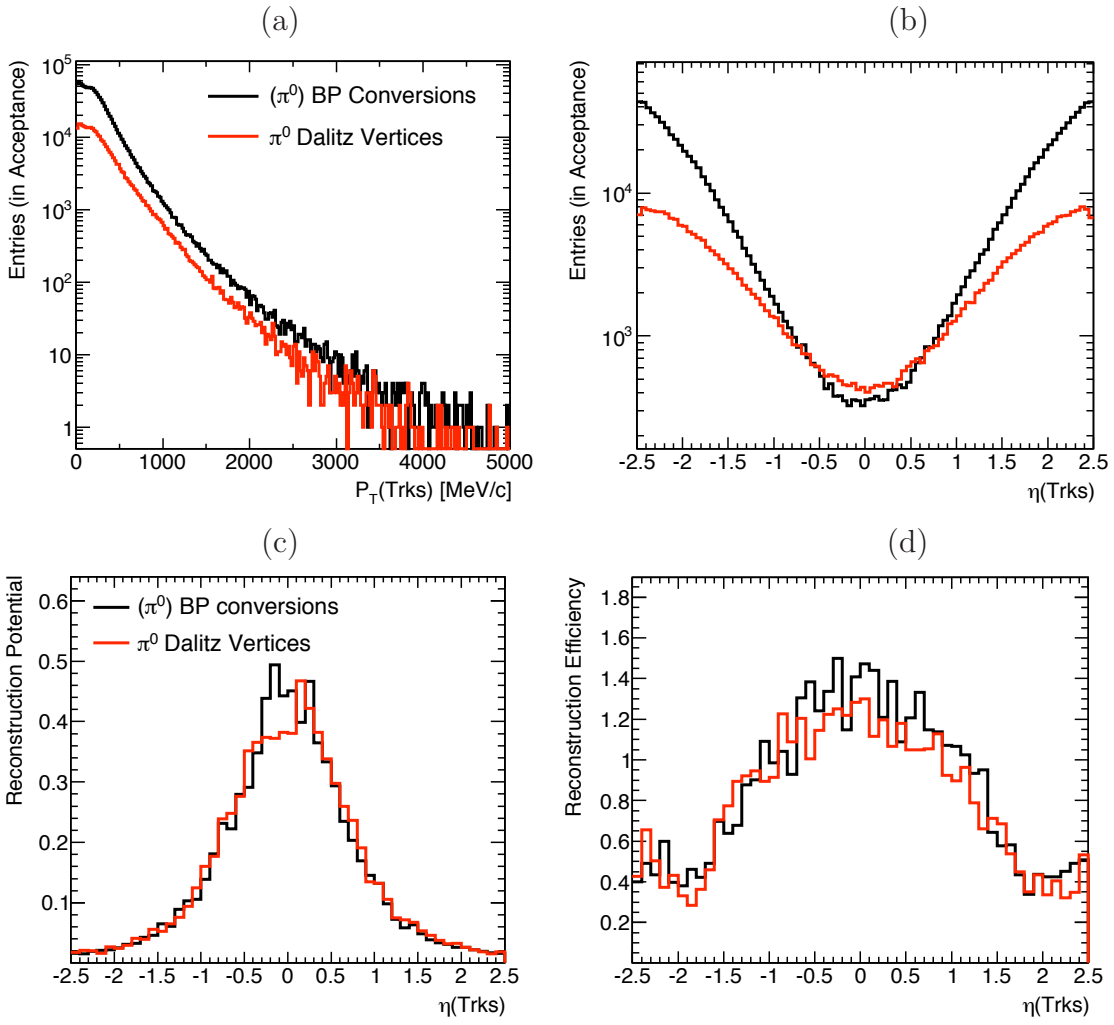

Figure 6.81: Distribution of (a) the reconstruction potential and (b) the reconstruction efficiency as a function of the tracks η for π^0 BP conversion (in black) and Dalitz decay (in red).

Figure 6.81(a-b) shows the (MC truth) η and P_T distributions of the BP conversions and Dalitz tracks. The $P_T(Trks)$ distributions have relatively close shapes. The shape of the η distribution

for the BP conversion is a feature of the BP conversion probability itself: it varies with the quantities of matter traversed which depends on η. The distribution for Dalitz is initially rather flat. The shape distributed in red is obtained after requiring the energy of the π^0 to be greater than 1 GeV. Figure 6.81(c) shows the reconstruction potential of BP conversions and Dalitz from π^0 as a function of the η direction of the tracks. The shapes are close and suggest that the difference between the BP and Dalitz reconstruction potential found in the MC is rather independent of η. Figure 6.81(d) shows the reconstruction efficiency of BP conversions and Dalitz from π^0 as a function of the η of the tracks. Close shapes are observed. The BP and Dalitz reconstruction potential obtained in the 7 TeV MC sample respectively amount to:

$$R^{BP} = \frac{13171}{423461} = 3.11 \pm 0.03\% \quad \text{and} \quad R^{Dz} = \frac{6927}{341550} = 2.03 \pm 0.02\%$$

Part III

Prospects for the Higgs Boson Searches in $\gamma\gamma$ channel

Preamble

The first studies dedicated to the search of the SM Higgs boson in the diphoton decay channel started in 1990 in ATLAS and CMS collaborations. A complete estimate of the sensitivity for discovery through this channel was published in 1999 in the ATLAS *Technical Design Report* [63] for a centre-of-mass energy of 14 TeV. The signal and backgrounds were studied in detail, a Leading Order normalization of the different signal production modes and background processes, irreducible ($\gamma\gamma$), reducible (γ-jet and jet-jet) and $Z \rightarrow e^+e^-$, was derived. The statistical significance of the inclusive analysis was computed for an integrated luminosity of 30 fb^{-1} and 100 fb^{-1}, corresponding respectively to the low and high luminosity scheme initially planed at nominal LHC energy. As a result a statistical significance of 3.9(6.5) σ was expected at 30(100) fb^{-1} for a Higgs mass of 120 GeV/c^2. Exclusive analyses based on the production of a diphoton pair plus one or two jets using the associated production modes and the vector boson fusion production mode of the Higgs were also considered as these provide a powerful statistical significance, having a better signal/background discrimination but a reduced statistics with respect to the inclusive analysis.

During the ATLAS *Computing System Commissioning* exercise [64] started in 2007, the discovery potential of the Higgs search in the diphoton decay channel has been re-assessed. Inclusive and exclusive analyses are studied at a centre-of-mass energy of 14 TeV. The signal and background normalizations have been derived at NLO, leading to an improved statistical significance with respect to the TDR prediction. The statistical significance has been estimated for an integrated luminosity of 10 fb^{-1} using a multivariate maximum likelihood method. Different categories of events have been defined, based on the number of jets produced with the two photons, the η regions of the photons and the conversion of photon. In addition to the diphoton invariant mass the transverse momentum of the diphoton pair and the $cos\theta^*$ (θ^* being the angle between the photon in the centre-of-mass of the diphoton system and the Higgs boost axis) have been used as discriminating variables.
The sensitivity is assessed in a conservative way, based on the inclusive analysis and an events counting in the mass widow of interest, and in more significant ways, using the discovery potential of exclusive analyses, event categories and the discriminating power of the three aforementioned kinematic variables. For a Higgs mass at 120 GeV/c^2, the statistical significance is found to range from 3.2 to 4.1 σ, for a luminosity of 10 fb^{-1}.

Since the first operation of the LHC in december 2008, the energy and luminosity plan for the forthcoming run period have changed. In winter 2009 the LHC plan was to run at 10 TeV for a short period corresponding to a luminosity of approximatively 200 pb^{-1}. The picture has evolved at the 2010 Chamonix workshop where it was decided to start the LHC operation with a first run period in a centre-of-mass energy of 7 TeV. This phase has recently started and is expected to last for approximatively one year and half (until the end of the year 2011). Data

corresponding to a luminosity of about 1 fb^{-1} is expected to be collected during this period of run, followed by a long period of shut-down dedicated to LHC and experiment maintenance. The second phase of run should see collisions in an energy in the centre-of-mass of 14 TeV.

A recent study (2010) of the prospect for the SM Higgs boson exclusion with the energy and luminosity scheme as planed in winter 2009, ($\sqrt{s} = 10\,TeV$, 200 pb^{-1}) has been performed. An extrapolation to the 7 TeV energy case and a luminosity of 1 fb^{-1} have also been done.

Chapter 7

The $H \to \gamma\gamma$ decay channel

At the LHC, the search for the Higgs boson in the $\gamma\gamma$ channel is amongst the most important analyses in the low mass range ($115 < m_H < 150\ GeV/c^2$). In this chapter, we introduce the theoretical features and the phenomenology of signal and background processes associated to the $H \to \gamma\gamma$ channel.

7.1 The Factorization Theorem

The protons are composite objects of quarks and gluons (partons). In a naive picture, the proton is made of three different color quarks, two up quarks and one down quark, of respective electric charge 2/3 and -1/3. The proton is a colorless object of charge +1. The perturbative QCD is no longer valid at the proton scale. The interaction strength between partons increases when they separate and can spontaneously create a quark-antiquark pair. The proton is seen as a gas of partons each carrying a fraction x of the proton momentum. In addition to the three quarks of valence, the vacuum polarization generates gluons and sea-quarks (quark-antiquark pairs). Therefore, heavier quarks, charm and strange quarks (and also bottom quarks) arise in the proton. The proton structure is described by the parton distribution function (PDF) of quarks of valence, gluons and sea-quarks.

The inclusive cross section of any process in LHC collisions $p_1p_2 \to X$ has the following factorization form:

$$d\sigma_{p_1p_2\to X}(\sqrt{S}) = \int_{x_1^{min}}^{1} dx_1 \int_{x_2^{min}}^{1} dx_2\ \phi_{b_1/p_1}(x_1,\mu) d\sigma_{b_1b_2\to X}(\sqrt{s}, x_1, x_2, \mu, \mu_R)\phi_{b_2/p_2}(x_2,\mu) \quad (7.1)$$

The hadronic cross section is made of the convolution of the short distance and the long distance interactions, respectively the partonic process and the PDFs in protons.

1. $\sigma_{b_1b_2\to X}(\sqrt{s}, x_1x_2, \mu, \mu_R)$ corresponds to the cross section of a specific process where b_1 and b_2 are the partons involved at initial-state and X is any final-state; x_i corresponds to the fraction of the momentum of the proton p_i carried by the parton b_i; $\sqrt{s}$ is the energy in the centre-of-mass of the partonic process and is related to the proton-proton collision energy by the relation: $\sqrt{s} = \sqrt{Sx_1x_2}$.

2. $\phi_{b_i/p_i}(x_i,\mu)$ are universal functions that correspond to the probability density of partons b_i in protons p_i. It is function of the fraction x_i of the proton momentum carried by the

parton and of an arbitrary scale μ_F, the so-called factorization scale. It corresponds to the separation scale between the short- and long-distance processes, generally fixed at a physical scale involved in the process.

There is no theoretical formalism in perturbative QCD to fully derive the PDFs in hadron although the work in lattice QCD aims to build one. The PDFs of gluons, valence quarks and sea-quarks in the proton are extracted from both QCD development and experimental measurements. These are extracted with different experiments for a certain range in x and at an energy scale Q_0, and then expanded at an energy Q^2 using the DokshitzerGribovLipatovAltarelliParisi (DGLAP) evolution [65–67].

The HERA machine at DESY [68] has largely contributed to understand the proton function structure and the parton distribution functions inside the proton. 30 GeV electrons collide with 920 GeV protons in deep inelastic scattering (DIS) [69], via neutral and charged courant interactions, respectively $ep \to eX$ and $ep \to \nu X$. Figure 7.1(a) shows the x and Q^2 ranges scanned by HERA and other experiments. Two mains groups have

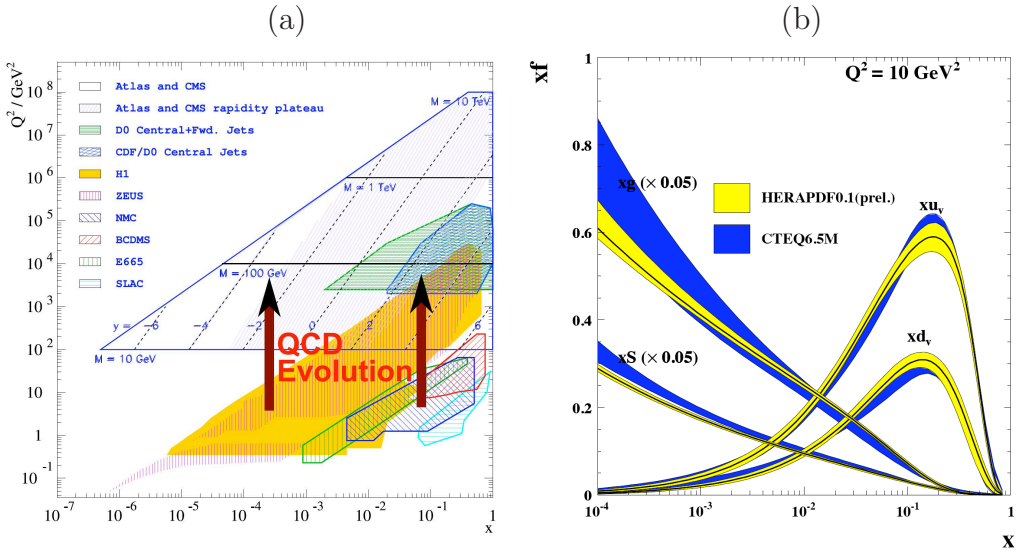

Figure 7.1: (a): region in x and Q^2 scanned by different experiments and prediction for the LHC. (b): Parton density functions measured in HERA H1 experiments compared with CTEQ predictions.

used HERA data and different theoretical assumptions to predict the PDF at the LHC energy:

- The Coordinated Theoretical-Experimental Project (CTEQ) group [70]
- and the Martin-Robert-Stirling-Thorne (MRST) group [71]

They frequently publish updated tables of PDFs. Figure 7.1(b) illustrates the good agreement between CTEQ group predictions and HERA data although discrepancies arise in the small x region. The PDFs obtained with CTEQ predictions [72] for a typical energy expected at LHC are shown in Figure 7.2(a). At high energy and small x fraction of momenta, the gluon density dominates. The large gluonic activity in LHC environment

explains the large cross section of the Higgs boson production through the gluon fusion process despite the small (indirect) Higgs boson coupling to gluons.

In Figure 7.2(b) the PDF from MRST group are normalized to CTEQ prediction [73]. The PDF shapes are close in the small x range while large differences arise at large x. These differences and systematic uncertainties on the PDFs measurement and expansion largely impact the level of precision at which the cross section of a physical process can be predicted.

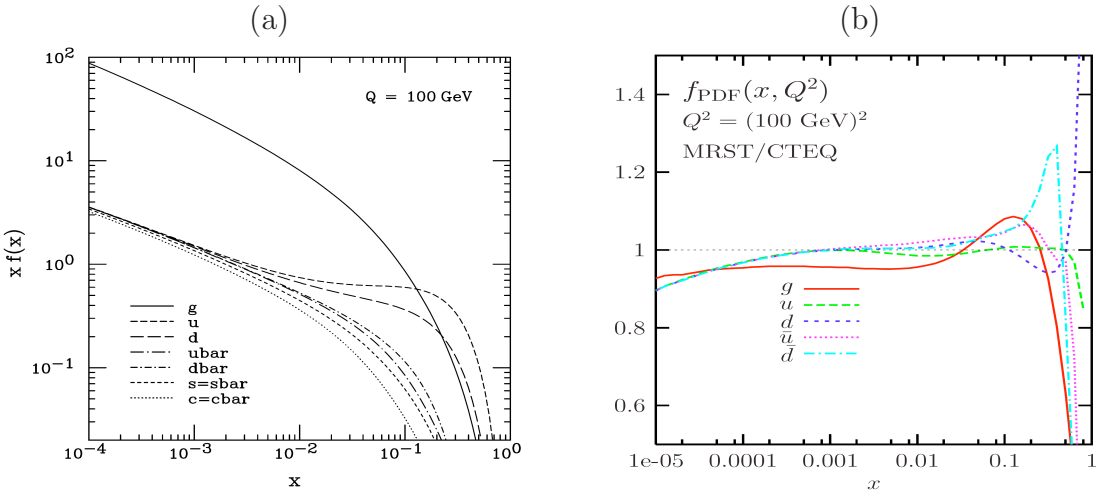

Figure 7.2: (a): parton density functions predicted by the group CTEQ, for a typical energy in the partonic centre-of-mass at LHC, $Q = 100\ GeV$. (b): MRST densities normalized to the CTEQ prediction, for the same energy.

7.2 QCD features

The cross section of a partonic process calculated at the tree-level is represented by the simplest Feynman diagrams possible to describe the process, when the smallest number of particle vertices are involved. It leads to a good but approximative prediction of the inclusive cross section of the hard process in proton collisions. Higher order QCD corrections should be accounted for for a more accurate prediction. These are real emissions of gluons (photons in QED) and virtual loops. Their contribution to the physical cross-section varies with the process and can be of tens of percent. Infinities arise in these corrections and need particular treatments to lead finite the cross section. Infra-Red (IR) and collinear divergences arise when the momentum of the gluon (or photon) tends to vanish. The IR singularities are absorbed by a balance between real and virtual emissions.
The collinear singularities are absorbed in the PDF $\phi_{b_i/p_i}(x_i, \mu)$ from equation 7.1.
Ultra-Violet (UV) divergences are canceled by renormalization. The most common renormalization scheme used is the dimensional regularization [74]. It is based on the idea that the cross section of a process which diverges in the 4 D space-time is finite at another unspecified dimension ϵ. The singular terms are absorbed into the observables of the initial Lagrangian of

the theory- the constant coupling, the particles masses. The limit $\epsilon \to 4$ then leads to a meaningful cross section.These infinities are universal which allows the renormalization procedure although the higher order QCD corrections involve different Feynman diagrams per process which numbers can increase rapidly and limit calculations.

A perfect prediction of the cross section of a process is not possible, the series of corrections term is generally truncated at the Next-To-Leading-Order (NLO) in perturbative QCD. The NNLO corrections have been calculated for some processes, notably involved in the Higgs boson production.

7.3 Associated backgrounds

The main source of background in this channel is the production of two prompt photons in the final state. It is the so-called irreducible background which three main processes at the tree-level are illustrated in Figure 7.3. The diagrams (a), (b) and (c) distinguish in their final-state and power coupling in α_s and α_{EM}, respectively the coupling strength of the strong and EM interactions. The process (a), the Born process, is of the order α_{EM}^2. The process (b), the so-called bremsstralhung process, is of the order $\alpha_{EM}^2\alpha_s$. The process (c), namely the Box process due to the quark Box loop, is of the order $\alpha_{EM}^2\alpha_s^2$ at the LO. Its cross section is relatively small, but is compensated by the large gluon luminosity at LHC.

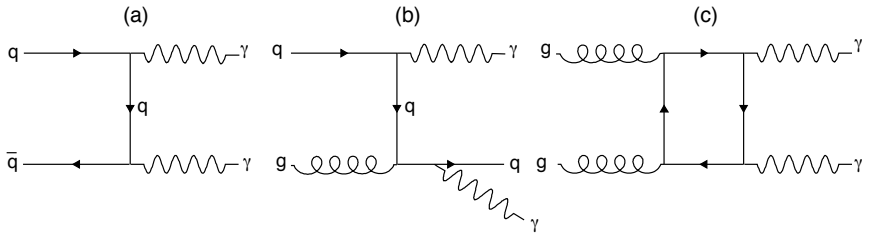

Figure 7.3: Feynman diagrams of di-photon production at the lowest order in α_s.

The other background sources are:

- The semi-reducible background which corresponds to the production of one photon and a jet misidentified as a photon. This occurs essentially when a final-state parton fragments into a leading π^0 or any other meson decaying into photons.

- The reducible background associated to the multi-jet production where two jets are misidentified as photons.

A good rejection of the jets faking photons in the detector is needed to reduce as much as possible the γ-jet and jet-jet backgrounds. After the photon identification (and similarly the jet rejection), these correspond to about half the total background associated to the $H \to \gamma\gamma$ signal.

7.4 Signal properties

The total and $\gamma\gamma$ partial width of the Higgs boson at low masses is small, below the resolution achieved by the EM calorimeter of ATLAS (typically of about 1.5 GeV/c^2). The invariant mass distribution of the signal photon pairs presents therefore a fine resonance which width depends on the photon energy and direction resolution.

The Higgs boson is mainly produced by gluon fusion. At the tree level, when the Higgs boson decays into two photons, the transverse momentum of the process $gg \rightarrow H \rightarrow \gamma\gamma$ is conserved and null. The transverse momentum of the diphoton system is therefore null at the Leading Order (LO) in α_s. Due to the color conservation, NLO corrections to this process come from gluon emissions at initial state and virtual loops. At higher order, the transverse momentum of the diphoton system is equal and opposite (recoil) to the transverse momentum carried by the emitted partons from the hard process. In practice, the $\gamma\gamma$ P_T translates the transversal activity of the hard parton emission from QCD corrections and soft emissions from the shower process.

The Higgs boson being a scalar there is no preferred direction for photons direction with respect to the Higgs boson flight axis (or any longitudinal axis of reference). The distribution of the $cos\theta^*$, where θ^* is the angle between one photon and the Higgs boost axis in the centre-of-mass frame, is expected to be flat.

The distribution of these variables are related to the signal properties. The background processes have different structures and the distribution of these variables are *a priori* expected to contrast with the signal. For instance, the irreducible background is the non-resonant production of photon pairs, the invariant mass shape will therefore be uniform. Also, the leading irreducible background process, the bremsstrahlung process represented in 7.3(b), is realized through the intermediary of a quark, of spin 1/2, that suggests that the $cos\theta^*$ of the diphoton system is not especially uniform. Finally, it is natural to expect difference in the diphoton transverse momentum distribution, related to the QCD evolution of each process. It should be noted for instance that the transverse momentum of the diphoton system in the bremsstrahlung process is non null at LO but equal to the transverse momentum carried by the remnant of the parton which emits the photon.

7.5 The resummation formalism

The invariant mass of the diphoton system is obviously an important observable in the search for the Higgs boson through its decay into two photons.

Other variables are considered to increase the discovery potential of the Higgs boson through the $\gamma\gamma$ channel. The transverse momentum of the diphoton system is a variable presenting an interesting discriminating power. Natural difference are expected between signal and background $P_{T\gamma\gamma}$ (Q_T in the following). In the high Q_T region, the spectrum is well described by the perturbative QCD. In the low Q_T region ($Q_T < 20\ GeV/c$), colinear and IR divergences impact the spectrum shape. In addition, initial-state multiple soft gluons emission introduces logarithmic divergences when $Q_T \rightarrow 0$. The Collins-Soper-Sterman (CSS) soft gluon resummation formalism is used to absorb these singularities and provide a smooth and reliable $P_{T\gamma\gamma}$ shape. A detailed description of the CSS formalism can be found in reference [75].

The factorization theorem is used to write any cross-section of a physic process as the

convolution between a short-distance process and a long-distance process. The partonic cross section in equation 7.1 could for instance represent the Born process $qq \to \gamma\gamma$, of differential cross section:

$$\frac{d\sigma_{Born}}{dQ^2 dy dQ_T^2} \propto \int_0^1 dx_1 \int_0^1 dx_2 T_{Born}(Q_T, Q, x_1, x_2, \mu)\phi_1(x_1, \mu)\phi_2(x_2, \mu) \tag{7.2}$$

The Born cross section T_{Born} is calculated order by order in perturbative QCD and can be written in the compact form:

$$T_{Born}(Q_T, Q, x_1, x_2, \mu) = \sum_{n=0}^{\infty} \Big(\frac{\alpha}{\pi}\Big)^n T_{Born}^n(Q_T, Q, x_1, x_2, \mu) \tag{7.3}$$

At any order n in α_s^n, T_{Born}^n can be split in the sum of a singular and a regular part:

$$T_{Born}^n = T_{Born}^{n,\delta}\delta(Q_T) + \sum_{m=0}^{2n-1} T_{Born}^{n,m} \frac{1}{Q_T^2} ln^m\Big(\frac{Q^2}{Q_T^2}\Big) + R_{Born}^n \tag{7.4}$$

The term R_{Born}^n corresponds to the regular terms and represents the perturbative part. Singular terms arise in the cross section when the transverse momentum becomes much smaller than the invariant mass of the diphoton system. The singularities are contained in the asymptotic part $T(\delta)$ and in the term $\frac{1}{Q_T^2} ln^m\Big(\frac{Q^2}{Q_T^2}\Big)$. The Collins-Soper-Sterman resummation formalism is used to absorb these singularities due to the multiple emission of soft gluons. The cross section is transformed as follow:

$$\frac{d\sigma_{Born}}{dQ^2 dy dQ_T^2} \propto \int d^2b e^{i\vec{Q_T}.\vec{b}} W(b, Q, z_i, z_j) + Y(b, Q, z_i, z_j) \tag{7.5}$$

The part Y contains the regular terms:

$$Y(b, Q, z_1, z_2) = \int_0^1 dx_1 \int_0^1 dx_2 \sum_{n=0}^{\infty} \Big(s\frac{\alpha_s}{\pi}\Big)^n \tag{7.6}$$

$$R_{Born}^n(Q_T, Q, x_1, x_2, \mu, \phi_1(x_1, \mu)\phi_2(x_2, \mu) \tag{7.7}$$

The W term contains the large logarithms, of the form $ln(b^2/Q^2)$. A Fourier transformation is used to preserve the transverse momentum $\vec{Q_T}$ conversation. The large logarithms $\alpha_s^n \frac{1}{Q_T^2} ln^m\Big(\frac{Q^2}{Q_T^2}\Big)$, $m = 0..2n-1$, associated to the effect of soft gluons emission at the order α_s^n, are resummed in W function by Sudakov exponentiation, yielding to a regular and well behaved differential cross section when $Q_T \to 0$. The resummed prediction of the diphoton invariant mass spectrum is however equivalent to the fixed order. Only the rate is enhanced by the higher order contribution of integrated logarithms.

7.6 The fragmentation

The resummation formalism treats the singularities due to the emission of soft gluons at the initial state. Collinear singularities also arise in the final-state, when the photon is collinear to

one of the partons, as for instance in the bremsstrahlung process. Based on the factorization theorem formalism, the collinear divergences are absorbed in the same spirit in empirical fragmentation functions $D^{\gamma}_{q,g}(z, \mu_f)$ which are of order $O(\frac{\alpha_{EM}}{\alpha_s})$ in terms of power counting. The z parameter represents the fraction of momentum carried by the photon with respect to the emitting parton and μ_f is the fragmentation scale.

The magnitude of the photon fragmentation contribution strongly depends on the isolation criteria, the allowed amount of hadronic activity in the direct neighborhood of the photon. To efficiency identify photons and reject jets a small activity around the photon is required that reduces the photon fragmentation contribution.

7.7 Pile up and underlying event

Some others and important aspects occur in the topology of proton-proton collision that should be accounted for in Monte-Carlo simulation to get a reliable prediction of the event signature in the ATLAS detector.

1. *Beam remnants et multiple interaction:* The confinement in the strong interaction creates tensions between the quarks and gluons involved in the hard process and the protons remnants. The proton beam remnants are no more colorless objects and are color-connected to the hard process. As the partons inside the proton carry a small transverse momentum, typically of $\theta(200 - 300\ MeV/c)$, the recoil of momentum is given to the proton beam remnants. Secondary interactions between the proton remnants may also arise complicated the color tension picture.

2. *Pile-up*: At the LHC the proton beams are bunches containing a large amount of protons ($\sim 10^{10} - 10^{11}$). In principle, more than one proton-proton collision can arise per bunch crossing. The number of *pile-up* events depends on the LHC luminosity. In high luminosity schemes ($\sim 10^{34}\ cm^{-2}.s^{-1}$), about 20 events of pile-up are expected at each bunch crossing. In precision measurements such as the reconstruction of the Higgs mass peak in the diphoton channel, tools are being developed to discriminate the primary vertex from secondary ones and accurately reconstruct the photon direction [76].

7.8 Monte-Carlo Simulation/Programs

There are different types of tools used to predict physics at LHC experiments.

- **Monte Carlo Generators** are powerful tools to predict event signature in the detector. They have been developed to assess the complex path connecting QCD interactions to the final observables measured in the detector. The commonly used MC generators for ATLAS simulations are Pythia [77] and Herwig [78].

  The partonic cross section in MC generator is generally calculated at the lowest order in perturbative QCD. The strength of these generators relies on the description of the proton beams collision. A careful treatment of the color-tension due to *multiple interaction* (underlying event) and the *beam remnants* is performed. The generators implement initial and final-state radiations from the hard process. These emissions are described by

splitting kernel $P_{a\to bc}(z)$, function of the fraction z of the mother a momentum carried by the daughter b. The successive cascade of partons radiations are described in separate initial and final state showers.

The QCD perturbative theory which describes quarks and gluons interaction is valid in high energy (in short distance process). Because of the confinement regime, the perturbative theory breaks down at long-distance. The colored parton objects from the hard process as well as from the beams remnants of the parton shower are transformed into colorless hadrons. Phenomena of partons fragmentation, parton combination and unstable particles decay are contained in the hadronization step in generators. At the end of the generation chain, stable particles, colorless mesons and baryons, and leptons are formed and interact with the detector.

- **Programs** (of cross section calculation) predict the cross section of a hard process, generally with a good precision. Focused on the proton-proton collision, the hadronic cross section is made of the convolution of the partonic cross section and the PDFs, the aspect of beam remnants and multiple interactions are ignored. First (and second) higher order corrections are often implemented leading to an accurate prediction of the hard process cross section. As the perturbative series is truncated, cut-off are applied to preserve finite the cross section. Some QCD effects described above (fragmentation, resummation) may also be accounted for to predict reliable difference cross sections shapes. The program are often used to estimate the contribution of QCD corrections with respect to the tree level process. These corrections are used to rescale the LO cross section as predicted by the MC generators, although the kinematic of a process may evolve at higher order suggesting a more elaborate procedure to account for such corrections.

Chapter 8

Irreducible background and signal studies in the $H \to \gamma\gamma$ analysis

Introduction

At the LHC, the search for the Higgs boson in the $\gamma\gamma$ channel is amongst the most important analyses in the low mass range ($115 < m_H < 150\ GeV/c^2$). The strength of this channel relies on the ability of the ATLAS Electromagnetic Liquid Argon calorimeter to accurately measure the energy of the photons and their direction, which are essential ingredients for a precise reconstruction of the invariant mass. However, this channel suffers from a small signal branching ratio and a rather large background. The irreducible background, comprising inclusively of all production processes with two prompt photons in the final state, is the leading background after the photon identification that largely reduces the fraction of jets faking photons. The purpose of this study is to identify each contribution to the irreducible background and evaluate its normalization and the behavior of its differential cross section, based on a comparison of various Monte Carlo (MC) programs. A study of the signal is also presented in contrast to the background in order to asses the discriminating power of relevant kinematic variables and their correlations. Systematic uncertainties to the overall background and signal cross sections are also detailed.

8.1 Analysis Strategy

Aside from the optimization of the photon identification, energy and direction reconstruction, various ways to improve the statistical power of the analysis have been explored. Among them is the use of discriminating variables. Those which have most widely been studied are the P_T of the diphoton system and $cos\theta^*$. The θ^* angle is defined as the angle between the photon and a reference axis in the diphoton rest frame. In the particular case of $P_{T\gamma\gamma}$, which measures the transverse momentum of the system recoiling to the two photons, an accurate prediction is far from straightforward due to the difficulties to model both the infrared and collinear behaviour of the parton emission and the higher order corrections of the processes involved. In order to define a sound analysis strategy using discriminating variables, it is very important that these variables are well modeled and that the degree to which they can be trusted is assessed. To this end the valuable features and imperfections of the available MC programs are studied in

detail. Another way of improving the statistical power of the analysis is to separate events into categories with different sensitivities. All categories are eventually combined. Typically events are categorized based on the quality of the energy measurement of each photon and on the number of jets in the event. A particular attention will be given to the simulation of the number of jets.

The Signal In *pp* collisions at LHC energies, the four main production processes are: the gluon fusion (mainly through a top quark loop), the vector boson fusion (VBF), and the associated production with either a W or Z boson or a top quark pair. Given the large gluon luminosity at the LHC, the Higgs boson production is dominated by the gluon fusion process. This study concentrates on the normalization of the signal cross section in the gluon fusion production mode.

The Higgs boson decay into two photons is mediated by loops of W boson and charged fermions. The partial decay width has the following form [2]:

$$\Gamma(H \to \gamma\gamma) = \frac{G_\mu \alpha^2 M_H^3}{128\sqrt{2}\pi^3} |\sum_f N_c Q_f^2 A_{1/2}^H(\tau_f) + A_1^H(\tau_W)|^2 \tag{8.1}$$

$A_{1/2}^H(\tau_f)$ corresponds to the form factor associated to the fermion loops and $A_1^H(\tau_W)$ to the one associated to the W boson loops. As the $Hf\overline{f}$ is proportional to the mass of the fermion m_f, the loops through light fermions are negligible and the Higgs boson decay into two photons is mainly made through top quark and W boson loops, which tree-level Feynman diagrams are illustrated in Figure 8.1. The W boson and the top quark loops interfere destructively, leading

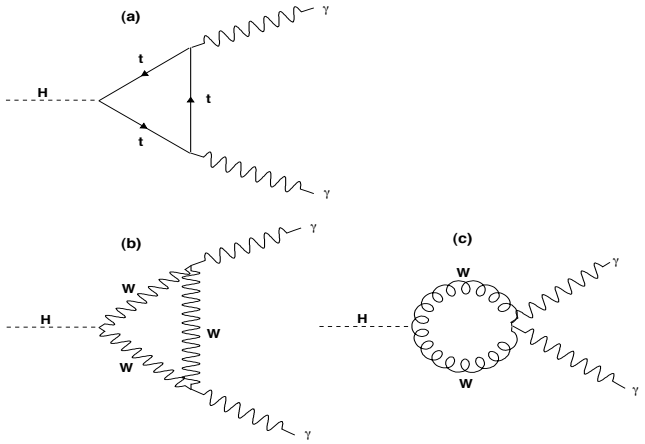

Figure 8.1: Feynman diagrams of Higgs boson decay into two photons.

to a very small branching ratio, of about 0.2%, known with 5% of relative precision.

The irreducible background There are three main processes contributing to the irreducible background at tree level:

(i) The Born process $q\overline{q} \to \gamma\gamma$, illustrated in Figure 8.2(a). In terms of power counting in α_s this tree level process is of $O(\alpha^2)$.

(ii) The Bremsstrahlung process (brem) $qg \to q\gamma\gamma$ of order $O(\alpha_s\alpha^2)$ (Figure 8.2(b)).

(iii) The Box process $gg \to \gamma\gamma$ of order $O(\alpha_s^2\alpha^2)$ (Figure 8.2(c)) which corresponds to the gluon fusion via a quark loop.

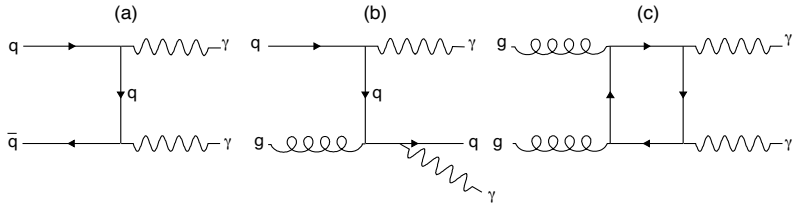

Figure 8.2: Example of Feynman diagrams of photon pair production, at the lowest order (LO) in terms of α_s.

The processes (i) and (iii) are relatively straightforward, whereas the process (ii) necessitates a particular treatment due to the presence of a collinear and infrared divergence in the photon emission. Although it should naturally be accounted as a Next-to-Leading Order (NLO) process as those shown in Figure 9.5, it is treated as a LO process due to its intrinsic connection with the fragmentation process (Figure 8.4(a)). As there is no possible way to discriminate between a parton fragmenting into a leading photon and a direct photon, photons produced either directly or in fragmentation processes are called prompt photons. The irreducible background comprises of all processes with two prompt photons in the final state. It can thus arise from three generic classes of production processes, the two direct photons, the single photon-plus-jets, or the multi-jets, with respectively none, one or two partons fragmenting into a leading photon. Table 8.1 displays which processes contribute to which class of backgrounds. The main fragmentation diagrams contributing to the irreducible background are shown in Figure 8.4.

	irreducible	semi-reducible	reducible
$\gamma\gamma$	direct	-	-
γ-jet	1 frag.	direct	-
jet-jet	2 frag.	1 frag.	direct

Table 8.1: List of the process contributions to the various background categories.

A contribution to the irreducible background which is neglected here since the main topic of this work is the inclusive search of the Higgs boson, is the double parton scattering (DPS). It corresponds to two partonic interactions occurring in the same proton-proton collision during one beam crossing. The latter should not be neglected when considering for instance the VBF channel exclusively [79].

Resonance-continuum Interference Another contribution which is seldom taken into account is the resonance-continuum interference occurring in the $gg \to \gamma\gamma$ processes involving the Higgs boson production and the box irreducible background processes. It has been calculated [80] for standard kinematic cuts used in ATLAS. Although such interference term would intuitively be expected to be barely perceivable, it has been shown that it is destructive and corresponds to almost -3% of the signal for $M_H = 120\ GeV/c^2$. As this effect is not completely negligible it must eventually be taken into account in the overall signal normalization.

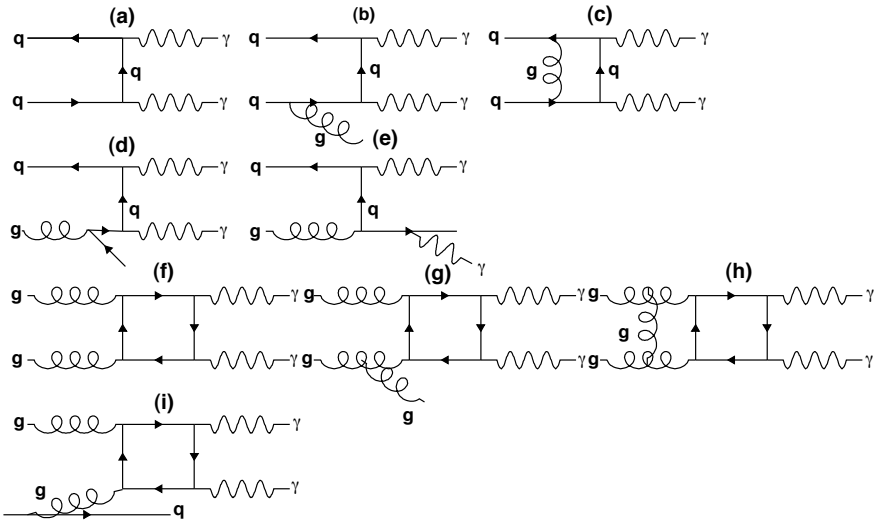

Figure 8.3: Example of Feynman diagrams corresponding to the irreducible background $\gamma\gamma$ production at NLO.

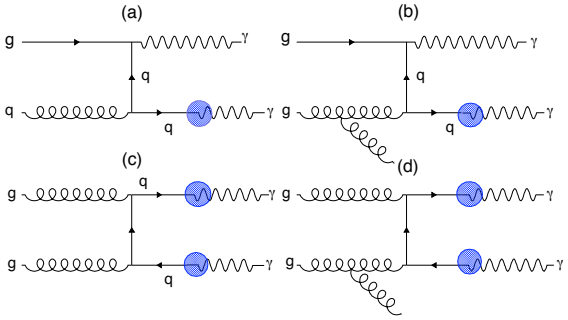

Figure 8.4: Feynman diagrams of the fragmentation contribution to the irreducible background, at LO and NLO.

Kinematic variables The inclusive analysis strategy most commonly used as in [64], is to take advantage of the discriminating variables such as the transverse momentum of the di-photon pair or $cos\theta^*$. These and other discriminating variables are considered, their discrimination power is studied and the precision with which the shapes are modeled is discussed in this study. The variables that will be considered are the following:

1. $P_{T\gamma\gamma}$: the transverse momentum of the photon pair, which is largely due to parton radiation and is for this reason intricate to simulate.

2. $cos\theta^*$: the cosine of the angle between the photon pair and a predefined axis in the photon pair rest frame. Two definitions will be considered here. The first and most commonly used is the boost axis (BA) of the diphoton system. The second, more intricate, the so-called Collins-Soper (CS) frame [81], is defined by the initial-state hadron momenta ($\vec{P}_1$ and $\vec{P}_2$) in the $(x0z)_{CS}$ plane where z_{CS} is the axis which bisects the momenta ($\vec{P}_1$ and $-\vec{P}_2$) as illustrated in Figure 8.5.

   In the CS frame another potentially interesting variable is the angle ϕ^*, defined as the angle between the x axis and the photon momentum projection in the $(x0y)_{CS}$ plane.

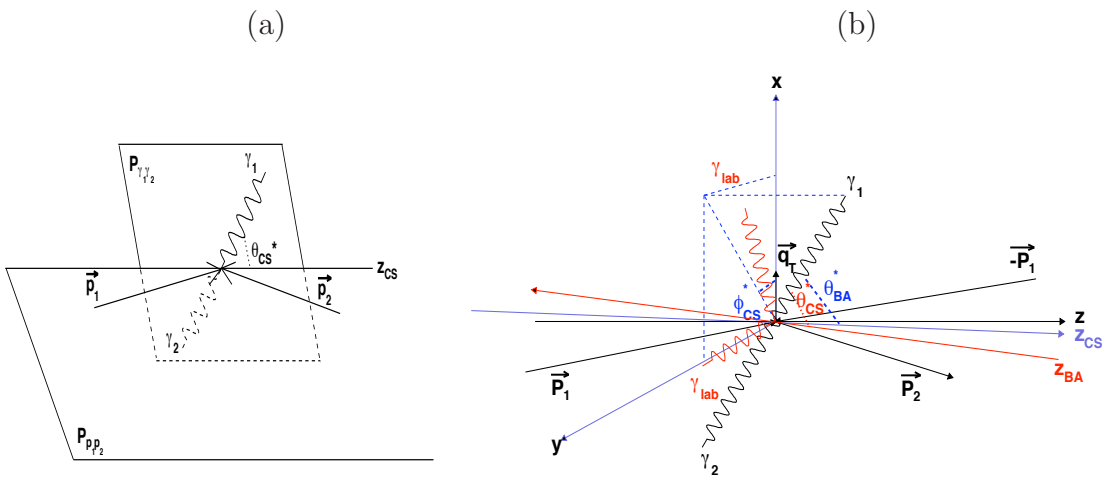

Figure 8.5: (a): Definition of the Collins-Soper (CS) polar angle θ^*_{CS}. z_{CS} bisects the protons direction. $P_{\gamma_1\gamma_2}$ and $P_{p_1p_2}$ correspond respectively to the plan of the two photons in their rest frame and of the two protons. (b): The CS and boosted axis (BA) frame. θ^*_{BA} corresponds to the polar angle in the BA frame. ϕ^*_{CS} corresponds to the azimuthal angle in the CS frame.

3. $\Delta\phi_{\gamma\gamma}$: the difference in azimuthal angle between the two photons.

4. $P_{L\gamma\gamma}$: the longitudinal momentum of the photon pair.

5. P_{Tmax} and P_{Tmin}: the transverse momenta of the leading and sub-leading photons.

The difficulty in defining an analysis strategy making use of discriminating variables is the need of an accurate knowledge of differential cross sections in order to assess the worthiness of their use for discriminating purposes. Particularly given the general framework where even the overall normalizations of both the signal and backgrounds are difficult to predict. For these reasons, systematic studies are extremely important and their outcome should be taken into account in defining the analysis strategy.

8.2 Background and Signal Simulation

8.2.1 Pythia

Pythia [77] is a general purpose Leading Order (LO) generator with parton shower (PS) and a string based hadronization model. Its underlying event model is rather sophisticated and can be thoroughly tuned. It implements all the signal and irreducible background processes illustrated in Figures 2.1 and 8.2. It was used in the CSC note [64] for the simulation of the box diagram di-photon, the semi-reducible γ-jet and the fully-reducible di-jet production processes.

8.2.2 Alpgen

Alpgen [82] is a more specific generator which implements the Matrix Element (ME) $2 \to \gamma\gamma+n$ processes. It is therefore particularly well suited to simulate exclusive samples in terms of the

number of jets. The parton showering process is performed with Herwig [78]. It was used in the calculation of the irreducible background production at the tree level (Figure 8.2 a and b) in [64]. Although Alpgen can also simulate events from the semi-reducible background, it has not been used for this purpose yet. The Higgs boson production by gluon fusion and VBF are also simulated in Alpgen. The combination of the ME and the PS requires a matching between events with final-state jets obtained directly from the ME calculation and jets coming from the PS. The MLM prescription for matching is used [83] to avoid the double counting of event.

8.2.3 Resbos and Diphox

Resbos The Resbos [84] program implements a full NLO ME calculation applying a NLL resummation formalism (which absorbs initial-state singularities due to the emission of soft or collinear gluons) to yield differential cross sections for both the signal production by gluon fusion and the irreducible background. In addition to the processes illustrated in Figure 9.5, Resbos includes the one photon fragmentation of a final-state parton at LO (diagram 8.4(a)). Its main advantage is the use of the resummation formalism which gives an accurate description of the lower part of the $P_{T\gamma\gamma}$ spectrum. It was thoroughly tested at the Tevatron [85] in particular in the inclusive Z production.

Diphox Diphox [86] is a fixed order program of ME calculation almost fully at NLO (the box process is implemented at LO only), including the fragmentation into a leading photon of one or two final-state partons. Its main advantage is the NLO calculation of the three contributions to the irreducible background listed in Table 8.1. Its treatment of fragmentation is also particularly accurate. Despite the absence of treatment of the soft emission which may imply discontinuities in the description of physical observables, Diphox provides meaningful differential cross sections [87].

Pseudo experimental isolation The treatment of infrared and collinear divergences in the photon emission by a parton is intricate. The interplay between diagrams 8.2(b) of the direct and 8.4(a) of the one photon fragmentation contributions which illustrate essentially the same physical process is one aspect of the difficulty in yielding a consistent result. The direct case explicitly displays the necessity of a particular treatment of the collinear and infrared divergence in the photon emission. The fragmentation case illustrates the collinear approximation where the final-state quark is neglected in the picture. In the first case the problem is solved by means of a pseudo-experimental isolation where the photons are required to be isolated at the parton level. A photon is considered as isolated when the transverse energy deposited in a cone ΔR around its direction is smaller than a fixed value E_T^{max}. This implicitly requires that the two photons are separated by ΔR. Since for background rejection reasons photons will need to be experimentally isolated (experimental isolation criterion typically use reconstructed charged particle tracks or energy deposition in a cone around the reconstructed photon) applying a parton level isolation criteria is fine provided that the efficiencies and rejections of the two criteria agree. In the second case, the difficulty is the treatment of what is left within the isolation cone in particular when most of the energy is carried by the photon. In this respect Resbos and Diphox have different approaches. Resbos computes the actual cross section of the Bremsstrahlung process using an auxiliary regulator to treat the collinear and infrared

divergences. An example of auxiliary regulator is the smooth cone, where the isolation criteria varies with respect to the energy of the parton which emitted the photon. In this scheme the energy lower bound on the parton is smoothly varying with a predefined function with the Δr between the photon and the parton. The criterion is chosen to match the primary isolation and allow infrared and collinear events. Diphox instead uses empirical fragmentation functions $D^{\gamma}_{q,g}(z, \mu_f)$ which are of order $O(\frac{\alpha}{\alpha_s})$ in terms of power counting. The z parameter represents the fraction of momentum carried by the photon with respect to the emitting parton and μ_f is the fragmentation scale. Varying μ_f strongly influences the direct and fragmentation cross sections separately but barely alters the total cross section. The two approaches were compared and found to be compatible [85]. Figure 8.6 illustrates the $M_{\gamma\gamma}$ distributions of Diphox for the direct and fragmentation contributions, separately and combined. In Figure 8.6(a) the differential cross sections have been generated with the standard isolation criterion, $E_T^{max} = 15\ GeV$ and $\Delta R = 0.4$, while in Figure 8.6(b) no isolation selection is applied. When applying isolation cuts, the one fragmentation typically decreases from 60% to 40% the total cross section and the two fragmentations contribution decreases from 30% to 3%. The Collins Soper frame is well

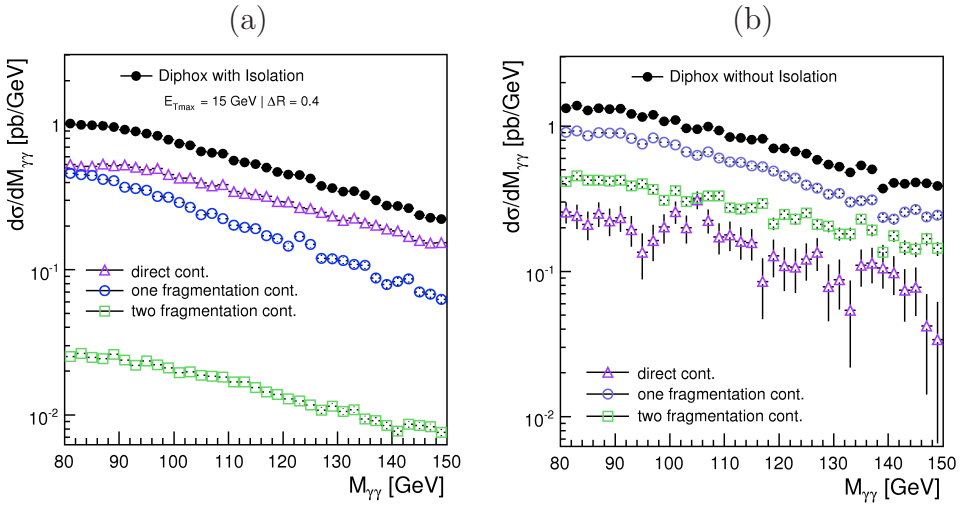

Figure 8.6: $M_{\gamma\gamma}$ distributions for the different contributions to Diphox: (a), an isolation selection $E_T^{max} = 15\ GeV\ \Delta R = 0.4$ is required. The fragmentation contributions are reduced with respect to case without isolation requirements, (b).

defined when soft gluon radiation is taken into account. In the case of a simulation program that does not include this feature (as for Diphox), the CS frame cannot be completely defined (expect for the bremsstrahlung process). In particular the angle ϕ^* cannot be defined in this limit.

8.2.4 MC@NLO

MC@NLO [88] is an event generator which implements the full NLO QCD corrections to specific processes and performs the showering process of Herwig in a consistent way, i.e avoiding the double counting of events and computes rates to NLO accuracy. Although other Higgs boson production modes are implemented in MC@NLO, only the gluon fusion is studied in this analysis.

8.2.5 HNNLO

HNNLO [89] is a fixed order program which calculates gluon fusion Higgs boson production at the Next-to-Next-to-Leading Order (NNLO). Being a fixed order calculation it involves certain non physical behaviors in differential cross section, in particular in the low $P_{T\gamma\gamma}$ region. Since no estimation at the NNLO level of the backgrounds is available, it has not been taken into account for a consistent estimation of observation or exclusion sensitivities. It is nevertheless interesting to compare its predictions to those of the available NLO generators.

8.2.6 Summary

The main characteristics of all the generators and Monte-Carlo programs used are summarized in Table 8.2. This table shows that the most accurate description of the irreducible background is given by the cross section estimation programs, in particular Resbos. This is mainly why the Resbos normalization and $P_{T\gamma\gamma}$ differential cross section were used in [64] to reweight the Alpgen and Pythia samples in the case of the irreducible background. For the simulation of signal events MC@NLO was used without further corrections.

For all studies presented here and unless otherwise stated the factorization, fragmentation and renormalization scales are set to the invariant mass of the diphoton system.

	Generators				MC Programs		
	Alpgen	MC@NLO	Pythia		Resbos	Diphox	HNNLO
			$\gamma\gamma$	γ-jet			
born	LO	-	LO	-	NLO	NLO	-
box	-	-	LO	-	NLO	LO	-
brem.	LO	-	-	LO	NLO	NLO	-
one frag.	-	-	-	LO	LO	NLO	-
two frag.	-	-	-	-	-	NLO	-
gg	LO	NLO	LO	-	NLO	-	NNLO
VBF	LO	-	LO	-	-	-	-
resummation	-	-	-	-	yes	-	-
PS	yes	yes	yes	yes	-	-	-

Table 8.2: List of the main characteristics of the Monte-Carlo programs used to evaluate the irreducible background and the signal.

8.3 Event Selection

The inclusive search for the Higgs boson is based on the identification of two photons and very simple acceptance and selection cuts. Most of the difficulty resides in identifying the photons while rejecting as much as possible fakes. The acceptance and selection cuts are the following:

$$P_{Tmin} = min(P_T^{\gamma 1}, P_T^{\gamma 2}) > 25\ GeV/c$$
$$P_{Tmax} = max(P_T^{\gamma 1}, P_T^{\gamma 2}) > 40\ GeV/c$$
$$|\eta_{\gamma^1,\gamma^2}| < 2.5$$

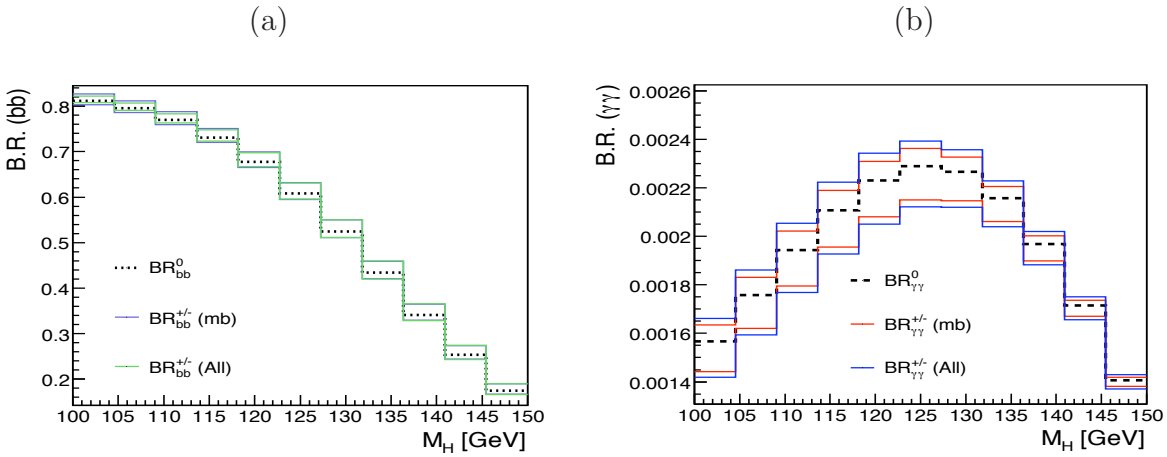

Figure 8.7: Branching ratio of the $b\bar{b}$ (a) and $\gamma\gamma$ (b) Higgs boson decay channels as a function of the Higgs boson mass.

where $P_T^{\gamma 1,2}$ and $\eta_{\gamma^{1,2}}$ are the transverse momenta and pseudo-rapidities of the two photons. In the following these cuts will be applied at the generator level. To further restrict the two photons invariant mass range to the region of interest, the selection $80 < M_{\gamma\gamma} < 150\ GeV/c^2$ is also applied. Slightly different kinematic selection cuts are applied in the exclusive jet categories [64].

8.4 Signal description

Simulating the signal is fairly simpler than estimating the backgrounds, largely because it does not have to deal with the question of fragmentation and its connection with Bremsstrahlung. The decay of the Higgs boson into two photons is well known and a NLO event generator for the gluon fusion process is available. In this section a general comparison of all signal generators is presented.

8.4.1 Decay Branching fraction

The two main contributions to the decay of the Higgs boson into two photons are the W boson and the top quark loops. These contributions compete destructively and leave a rather low branching fraction of 0.2%. This fraction has been estimated with a relative precision of 5%, as illustrated in Figure 8.7. The HDecay program [90] is used to compute the $b\bar{b}$ and $\gamma\gamma$ branching ratios of the Higgs boson including two-loop QCD corrections, in the $t \to \infty$ limit. Table 8.3 lists the Standard Model parameters used and their variations to estimate the associated systematic uncertainty. The quark masses correspond to the perturbative pole mass [90]. The variation of the b quark mass is the main contribution to the systematic uncertainty ($\sim 80\%$) ad is indicated by (mb) in Figure 8.7. The global uncertainty is obtained by combining all variations of the same sign. For $m_H = 120\ GeV/c^2$, the $\gamma\gamma$ and $b\bar{b}$ branching ratio are:

$$BR_{\gamma\gamma} = 0.002231^{+0.000113}_{-0.000179} \qquad BR_{b\bar{b}} = 0.677^{+0.058}_{-0.099}$$

Standard Model param.	central value	variations
$m_{u,d,s}$	190 MeV/c^2	-
m_c	1.4 GeV/c^2	± 0.1 GeV/c^2
m_b	4.6 GeV/c^2	$^{+0.1}_{-0.2}$ GeV/c^2
m_t	172 GeV/c^2	± 2.1 GeV/c^2
m_Z	91.187 GeV/c^2	-
m_W	80.41 GeV/c^2	± 0.025 GeV/c^2
Γ_W	2.08 GeV/c^2	± 0.03 GeV/c^2
α_s	0.118 GeV	± 0.001

Table 8.3: Set of SM parameters and their variation used in the evolution of the Higgs boson $b\bar{b}$ and $\gamma\gamma$ branching ratios.

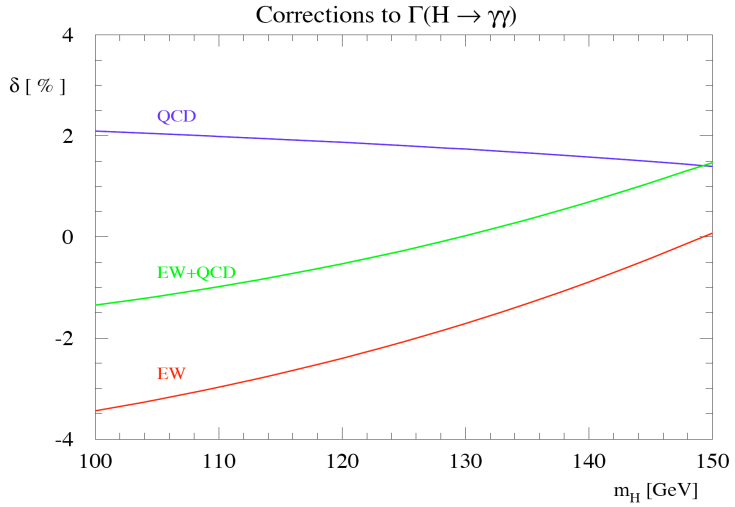

Figure 8.8: NLO percentage corrections to the partial width $\Gamma(H \to \gamma\gamma)$.

QCD and EW corrections have been computed at NLO respectively in [91] and [92, 93]. As illustrated in Figure 8.8 these two corrections almost compensate in the range of mass of interest ($m_H < 150$ GeV/c^2). The resulting total correction $|\delta_{EW+QCD}|$ is found to be smaller than 1.5 %. For $m_H = 120$ GeV/c^2, it is estimated to be approximatively $\delta_{EW+QCD} \sim -0.5\%$.

8.4.2 Resummation versus Parton Shower: Resbos and MC@NLO

The difference in normalization between Resbos and MC@NLO is roughly 10%. It is a rather large difference given that both programs are supposed to estimate at NLO the same process. The main difference between the two approaches comes from the Next-to-Leading Logarithms (NLL) resummation for Resbos and the PS for MC@NLO. The $P_{T\gamma\gamma}$, $P_{Tmin}(P_{Tmax})$, $cos\theta^*_{CS}$, $cos\theta^*_{BA}$, $P_{Tmin}/M_{\gamma\gamma}$ and $P_{Tmax}/M_{\gamma\gamma}$ distributions for the gluon fusion process as simulated by MC@NLO and Resbos are illustrated in Figure 8.9(a-f).

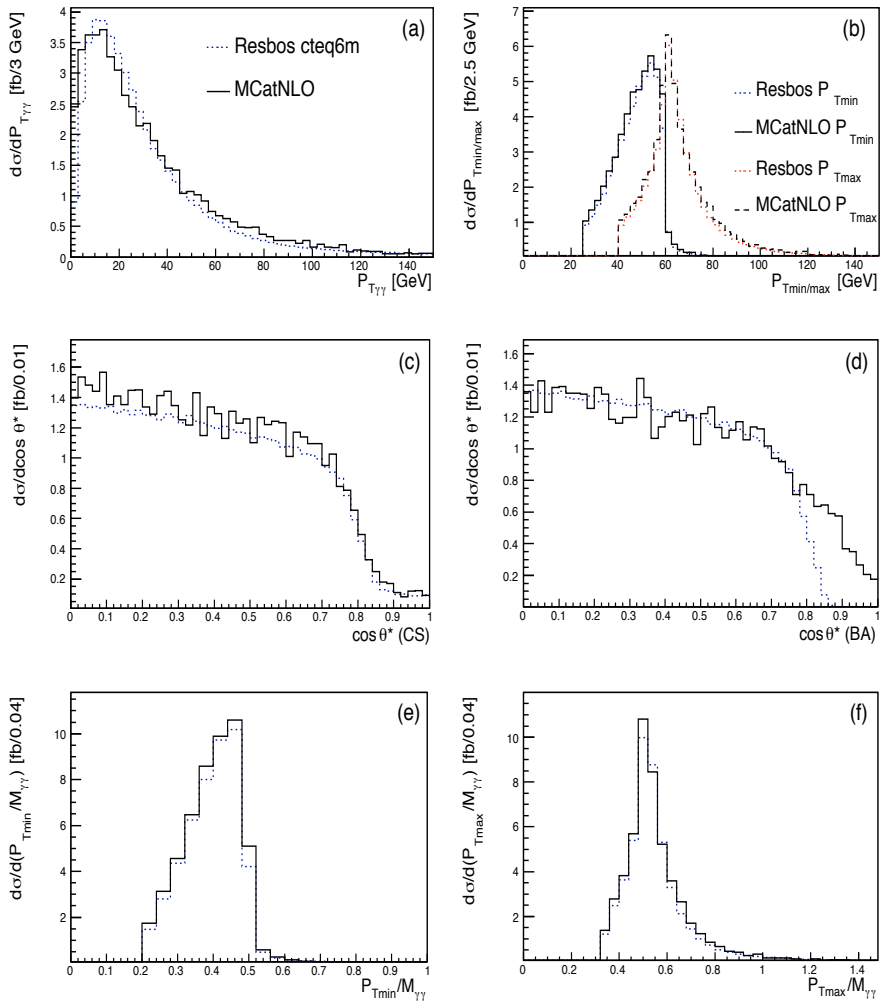

Figure 8.9: $P_{T\gamma\gamma}$, $P_{Tmin}(P_{Tmax})$, $cos\theta^*_{CS}$, $cos\theta^*_{BA}$, $P_{Tmin}/M_{\gamma\gamma}$ and $P_{Tmax}/M_{\gamma\gamma}$ distributions for the gluon fusion process as simulated by MC@NLO and Resbos. The NLO PDF CTEQ6M is used for both Resbos ad MC@NLO.

8.4.3 The Pythia and Alpgen specificities

Only Pythia simulates the four processes of the Higgs boson production. Figure 8.10 illustrates the Pythia $P_{T\gamma\gamma}$ distributions for these four independent processes. The relative event rates for each production process is $\sim 74\%$ for the gluon fusion, $\sim 17\%$ for VBF, $\sim 7\%$ and $\sim 2\%$ for the associated production respectively with a weak boson or a top quark pair. The harder $P_{T\gamma\gamma}$ spectrum observed in the VBF and associated production modes with respect to the gluon fusion is due to the transverse momentum carried by the jets produced with the Higgs boson decay products.

Figure 8.11(a) displays the $P_{T\gamma\gamma}$ distributions obtained with Resbos, Alpgen, Pythia and HNNLO (at NLO) for the Higgs boson produced by gluon fusion only.

The specificity of Alpgen, and the reason why it was officially used in [64] is that it simulates events with partons in the final state using the ME. It is thus expected to most accurately describe the number of events in the exclusive channels with jets in the final state.

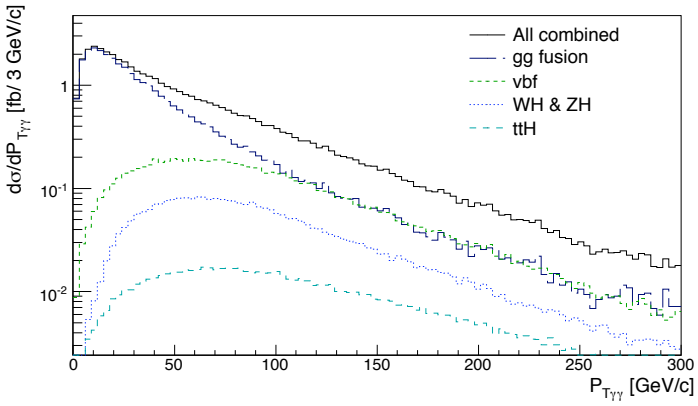

Figure 8.10: Pythia $P_{T\gamma\gamma}$ distributions for the different Higgs boson production channels with $m_H = 120\ GeV/c^2$.The LO PDF CTEQ6L1 is used for all simulated processes.

In the low $P_{T\gamma\gamma}$ region ($P_{T\gamma\gamma} \leq 50\ GeV/c$), only the Resbos, Alpgen and Pythia distributions can be compared since HNNLO is a fixed order calculation program. It is interesting to see that Pythia and Alpgen agree rather well over the entire spectrum. Resbos instead displays a different behaviour in the low $P_{T\gamma\gamma}$ region. This highlights the differences between the NLL resummation and the parton shower models (it should also be noted that the LO parton distribution functions (PDF) CTEQ6L1 are used for Pythia, with $\alpha_s = 0.129$, while the NLO PDF CTEQ6M [72] are used for Resbos with $\alpha_s = 0.118$). The resummation is expected to give a more accurate description. This motivates the reweighting of events as a function of $P_{T\gamma\gamma}$ in [64]. However this difference is rather surprising given the tuning of Pythia parameters using Tevatron data which agree well with Resbos [85]. As a result there is a large difference in the cross sections as illustrated in Table 8.4. It is also interesting to see that in the high $P_{T\gamma\gamma}$ region, all predictions agree quite well, which is expected since this region is dominated by the perturbative part of the parton emission. HNNLO however tends to slightly favor the high $P_{T\gamma\gamma}$ events. But the relative difference between the cross sections is small, around 6%.

Concerning the HNNLO prediction, two PDF sets are used for the NLO distributions, CTEQ6M and MRST2004 [94] ($\alpha_s = 0.121$) while only the NNLO PDF MRST2004 ($\alpha_s = 0.116$) is used for the NNLO distribution. These distributions are illustrated in Figure 8.11(b). The shapes of the NLO distributions are strikingly similar, with a relative difference between their cross sections around 2%. These shapes have also a relatively similar behaviour compared to the NNLO distribution, as illustrated in Figure 8.12.

Given the HNNLO cross section as listed in Table 8.4 the NNLO/NLO k-factor amounts to about 1.15. As shown in Figure 8.12 the NNLO/NLO ratio is rather flat in the high $P_{T\gamma\gamma}$ region which seems to indicate that a simple factor could be used if necessary. However given that non of the backgrounds have yet been estimated at NNLO, such a factor cannot yet be used. When the background will be normalized in the data, the NNLO normalization will be used. The ratio of the NNLO to Resbos NLO distributions illustrates the large differences between the two approaches.

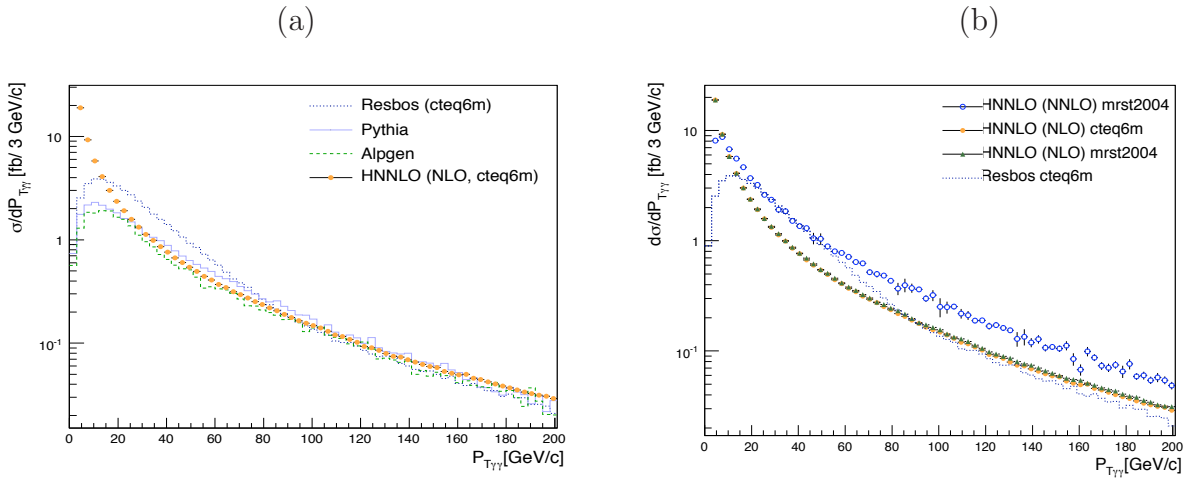

Figure 8.11: (a): $P_{T\gamma\gamma}$ distributions obtained with Pythia, Alpgen, Resbos and HNNLO (at NLO). The LO PDF CTEQ6L1 is used for Alpgen and Pythia distributions. The PDFs used for the other distributions are precised in the legend. (b): The NLO distributions of HNNLO are illustrated for two PDFs, CTEQ6M and MRST2004(NLO), and the NNLO distribution for the MRST2004(NNLO) PDF only.

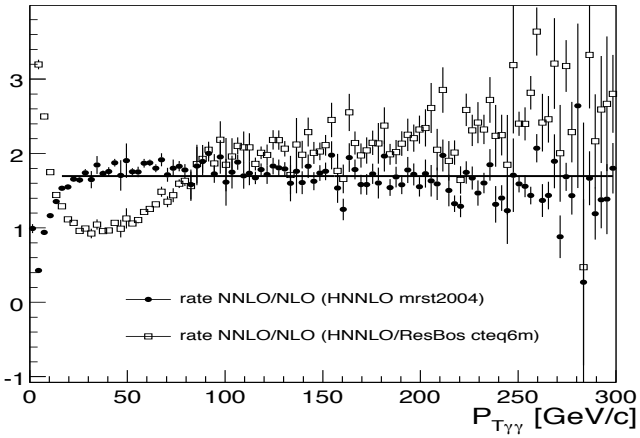

Figure 8.12: Ratios of the NNLO $P_{T\gamma\gamma}$ distribution as generated with HNNLO over the Resbos and the NLO HNNLO distributions.The PDF CTEQ6M is used for Resbos, the NLO(NNLO) PDF MRST2004 is used to generate the NLO(NNLO) distribution with HNNLO.

8.4.4 Estimating the number of jets

The knowledge of the distribution of the number of jets for each signal and background processes is a fundamental information in the framework of exclusive analyses. It primarily relies on the number of partons in the final state, but it also depends on the fragmentation and hadronization processes and eventually on the jet reconstruction algorithms. It is therefore a very intricate observable which cannot be easily estimated without a full simulation. It is interesting to compare the outcome of the available generators. At reconstruction level the threshold on the jet transverse momentum is $P_T^{jet} > 15\ GeV/c$. The Pythia and Alpgen generators can be compared both for the gluon fusion and the VBF processes as illustrated in Figure 8.13(a-c).

cross section (fb)	$m_H = 110\ GeV/c^2$	$m_H = 120\ GeV/c^2$	$m_H = 130\ GeV/c^2$
σ_{Pythia}(CTEQ6L1)	29.0	31.8	28.7
σ^{LO}_{HNNLO} (CTEQ6L1)	22.9	24.1	22.2
σ_{Resbos} (CTEQ6M)	45.4	48.3	44.7
σ^{NLO}_{HNNLO} (CTEQ6M)	49.7	51.3	46.5
σ^{NLO}_{HNNLO} (MRST2004)	48.7	50.2	47.7
σ^{NNLO}_{HNNLO} (MRST2004)	56.9	57.8	53.8

Table 8.4: Resbos, Pythia and HNNLO cross sections of the $H \to \gamma\gamma$ channel with a Higgs boson produced by gluon fusion for three Higgs boson masses.

Exclusive samples in terms of final-state jets have been simulated with Alpgen using a fast detector simulation. For the gluon fusion process, samples with $n = 0, 1, 2, \geq 3$ jets have been produced while for the VBF process, only samples with $n = 0, \geq 1$ jets, in addition to the two jets induced by the two final-state partons produced in association with the Higgs boson, have been produced. A fast detector simulation has also been used for the (inclusive) samples simulated with Pythia. Table 8.5 lists the relative proportions of events corresponding to each exclusive sample with none (**S0**), one (**S1**) or two (**S2**) jets reconstructed in the final state and the inclusive sample with at least three jets (**S3**) observed with the two photons. The distributions of the number of jets as simulated with Pythia and Alpgen differ mostly in the low jet multiplicity region. More events with no jets and less events with one jet are present in Alpgen. A large difference is also observed in the relative number of two jets events in the VBF process. This difference has an overall smaller impact due to the smaller rate of such events.

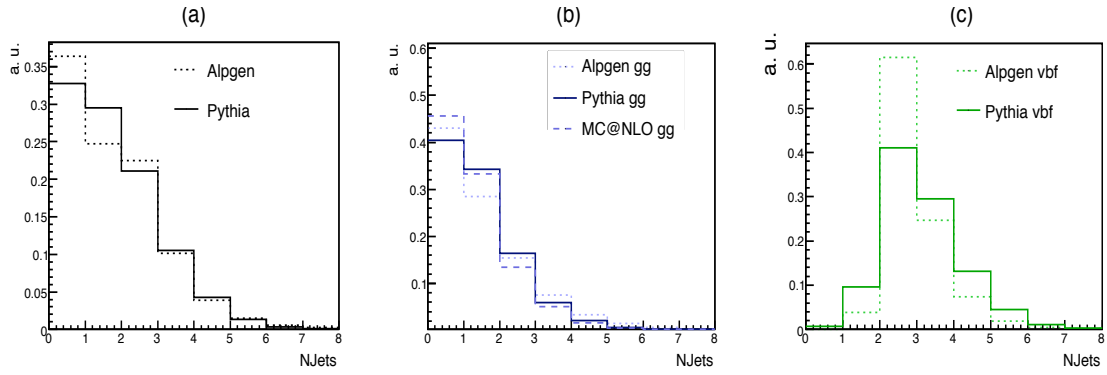

Figure 8.13: Pythia, Alpgen and MC@NLO number of jets distributions for the gluon fusion and VBF (except MC@NLO) processes. All distributions are normalized to unity.

It is however quite remarkable that Pythia and Alpgen have rather similar distributions of the number of jets distributions for the gluon fusion process. Instead, different number of jets distributions are observed for the VBF process.

The Alpgen, Pythia and MC@NLO $P_{T\gamma\gamma}$ distributions corresponding to the samples **S0**, **S1** and **S2+S3** are illustrated in Figure 8.14(a) and (b) respectively for the gluon fusion and the VBF processes. The Pythia and Alpgen distributions are rather similar for the gluon fusion process (Alpgen slightly favors the higher $P_{T\gamma\gamma}$ region). The MC@NLO distribution associated to the sample **S0** has a similar shape but a greater cross section with respect to Alpgen and

samples	0 jet	1 jet	2 jets	$\geq$ 3 jets	σ^{TOT}
Pythia					
gg fusion	40.3%	34.2%	16.3%	9.2%	31.8 fb
VBF	0.7%	9.6%	41.0%	48.6%	7.6 fb
WH & ZH	10.43%	21.2%	33.7%	34.6%	3.0 fb
ttH	0.05%	2.5%	1.5%	98%	0.8 fb
all combined	31.6%	28.3%	21.6%	19.5%	43.2 fb
Alpgen					
gg fusion	42.9%	28.5%	15.1%	13.4%	26.8 fb
VBF	$\sim$ 0.1%	3.8%	61.5%	34.7%	4.9 fb
all combined	36.3%	24.7%	22.2%	16.7%	31.7 fb
MC@NLO					
gg fusion	45.6%	33.3%	13.5%	7.6%	51.6 fb

Table 8.5: Cross section of the Higgs boson decay into the di-photon channel with Alpgen, Pythia and MC@NLO. The relative proportions of events with n final-state jets $n = (0, 1, 2, \geq 3)$ are listed for the different production modes.

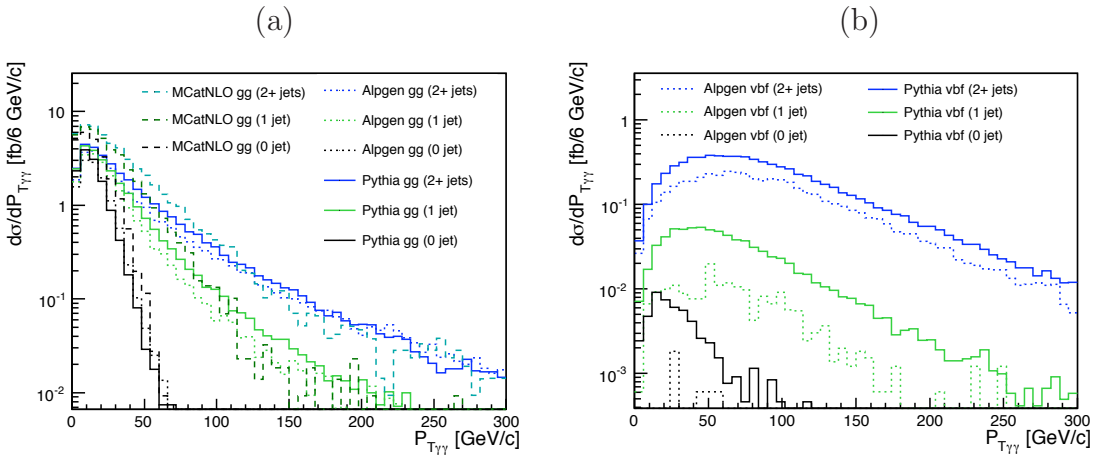

Figure 8.14: Alpgen and Pythia $P_{T\gamma\gamma}$ distributions for the gluon fusion (a) and the VBF (b) processes. The MC@NLO distribution for the gluon fusion is also shown. The distributions of the sample **S1** correspond to the sum of the samples **S0** and **S1** distributions and the inclusive sample **S2+S3** distributions correspond to the sum of the samples **S1** and **S2+S3** distributions.

Pythia. It is interesting to note that the spectra corresponding to the **S1** and **S2+S3** samples are softer than both these of Alpgen and Pythia. For the VBF process quite large differences are observed in the exclusive samples **S0** and **S1** distributions.

8.5 Comparison of Resbos and Diphox

The Resbos and Diphox programs are the most complete programs to evaluate the irreducible background total and differential cross sections. The main differences are (apart from the implementation of the resummation formalism) that Resbos has the NLO ME calculation of the box process and that Diphox calculates the photon fragmentation of one or two final-state partons at NLO while Resbos limits its calculation of one photon fragmentation at LO. These programs are compared and the outcome is used to assess a systematic uncertainty on the background normalization.

8.5.1 Box subprocess

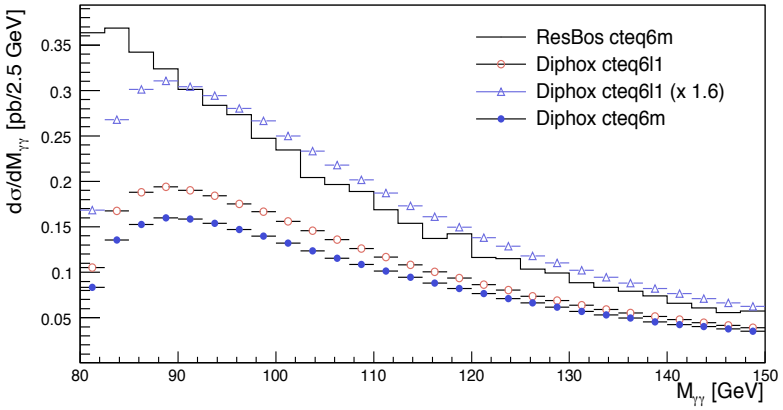

Figure 8.15: $M_{\gamma\gamma}$ distributions for the box contribution at NLO in Resbos and LO in Diphox using both LO and NLO PDFs.

The box process at LO (Figure 9.5(d)) is, strictly speaking NLO process due to the presence of the quark loop. This could lead to an ambiguity when choosing the set of PDFs to use [95]. The Resbos cross section is calculated using the NLO PDF CTEQ6M, while the Diphox cross section is calculated with both the LO PDF CTEQ6L1 and the NLO PDF CTEQ6M. Figure 8.15 illustrates the $M_{\gamma\gamma}$ distributions for Diphox and Resbos. At small values of $M_{\gamma\gamma}$ Resbos and Diphox cannot be compared because of a cut off in the Diphox distribution due to the absence of treatment of the soft radiation (where for any process at LO the 40 GeV/c cut on the transverse momentum of the photon translates directly on a cut at 80 GeV/c^2 in the di-photon mass).

In the medium-high $M_{\gamma\gamma}$ region ($M_{\gamma\gamma} > 100$ GeV/c^2), a good agreement between Diphox and Resbos is observed if a factor of around 1.8 (1.4) is applied to the Diphox distribution generated with NLO (LO) PDFs. In the full mass range, a k-factor of 1.6 is found as the ratio of the NLO cross section (with the NLO PDF CTEQ6M) over the LO cross section (with the LO PDF CTEQ6L1). This factor is in good agreement with the one calculated in [95]. The Diphox and Resbos cross sections for the box sub-process are given in Table 8.6.

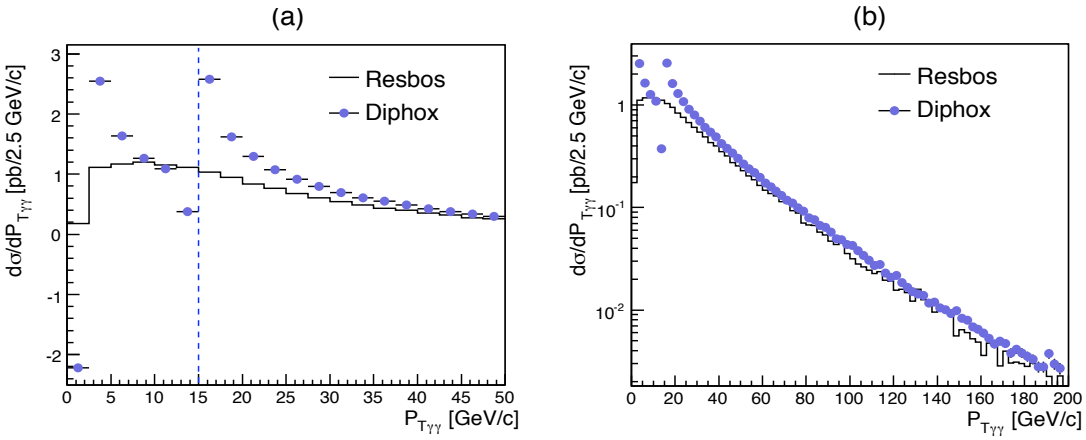

Figure 8.16: Diphox and Resbos $P_{T\gamma\gamma}$ distributions for the $q\overline{q} + qg$ processes in linear (a) and logarithmic (b) scale.

program	σ_{box} (pb)	$\sigma_{born+brem}$ (pb)	σ_{tot} (pb)
Resbos	4.9	16.7	21.6
Diphox	2.3	19.7	22.0

Table 8.6: Resbos and Diphox cross sections for gg and $q\overline{q} + qg$ contributions. The Diphox box cross section increases from 2.3 to 3.1 pb when using the LO PDF.

8.5.2 Fragmentation and Resummation

The Resbos and Diphox $P_{T\gamma\gamma}$ distributions for the so-called born and bremsstrahlung $q\overline{q} + qg$ contributions with fragmentation are illustrated in linear scale in Figure 8.16(a). These processes are of very different nature but are bound together in the Resbos program, they will thus be treated jointly here. In the Diphox distribution, a singularity occurs when $P_{T\gamma\gamma} \rightarrow 0\ GeV/c$ which is due to the fixed order calculation. The NLO shape is characterized by a first negative weight bin and a discontinuity appearing around $P_T^{\gamma\gamma} = 15\ GeV/c$. This discontinuity occurs at E_T^{max}, the upper limit on the transverse momentum carried by the remnants of the fragmenting parton when its separation with the photon is smaller than the isolation cone. In the low $P_{T\gamma\gamma}$ region the difference between Diphox and Resbos is small despite the very different behaviors of the differential cross sections(for $P_{T\gamma\gamma} \leq 20\ GeV/c$, $\sigma_{Resbos} = 7.89\ pb$ and $\sigma_{Diphox} = 8.42\ pb$). This good agreement is reassuring given that the differences in fragmentation models between the two calculations. For the high $P_T^{\gamma\gamma}$ region the two estimates are in good agreement as well, as illustrated in Figure 8.16(b). In the $P_{T\gamma\gamma} > 20\ GeV/c$ region, $\sigma_{Resbos} = 8.51\ pb$ et $\sigma_{Diphox} = 10.97\ pb$.

The total cross sections of the born and bremsstrahlung processes are indicated in Table 8.6. A relative difference of about 16% is observed.

The total Resbos and Diphox $M_{\gamma\gamma}$ distributions are displayed in Figure 8.17. The Resbos box process contributes to about 22% of the total cross section. Since the box process has generally a softer spectrum compared to that of the $q\overline{q} + qg$ contribution (in particular to that of the bremsstrahlung process), given that Diphox has a smaller contribution from the box sub-process, the Resbos overall spectrum is softer than that of Diphox.

The differences between Resbos and Diphox will be accounted for as a systematic uncertainty

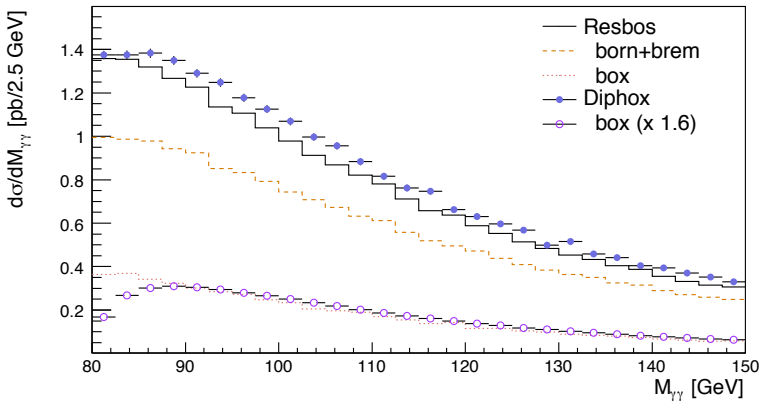

Figure 8.17: Diphox and Resbos distributions of $M_{\gamma\gamma}$.

(section 8.11.1).

8.6 Confronting Pythia to Resbos

Pythia is able to fully simulate all three basic irreducible background processes (Figure 8.2). The born and box processes can be straightforwardly simulated. For the bremsstrahlung and fragmentation processes the simulation is more delicate because Pythia needs to generate a very large sample of photon-jet events to allow to collect a small sample of bremsstrahlung events where a parton emits a photon which needs to satisfy the same parton isolation criteria as those imposed in Resbos[1)]. It then needs to be properly normalized to account for NLO corrections. For a fair comparison, the events of the Pythia bremsstrahlung sample have the same partonic isolation cuts as those applied in Resbos (see section 8.8). The $P_{T\gamma\gamma}$, $M_{\gamma\gamma}$, $cos\theta^*_{CS}$, $cos\theta^*_{BA}$, ϕ^*, P_{Tmin} and P_{Tmax}, $P_{Tmin}/M_{\gamma\gamma}$ and $P_{Tmax}/M_{\gamma\gamma}$ distributions for the box process as simulated by Pythia and Resbos are illustrated in Figure 8.18(a-h). For all these variables Pythia and Resbos agree well. As was the case for signal events Resbos favors small values of $P_{T\gamma\gamma}$ but in this case the total cross sections are quite similar which is interesting since in this case no k-factor seems to be needed contrary to the comparison of Diphox and Resbos for the box process ($\sigma_{Pythia} = 5.23\ pb$ and $\sigma_{Resbos} = 4.92\ pb$). This is worth noting since the official normalization scheme uses the Pythia box process cross section.

The same distributions as in Figure 8.18 but for the born and bremsstrahlung processes are illustrated in Figure 8.19. The Pythia sample corresponding to the qg initial-state process is normalized by a k-factor of 1.7. The $q\overline{q}$ initial-state process sample is not renormalized. The agreement in the overall number of events is fair. The disagreement in the $P_{T\gamma\gamma}$ somewhat similar to what was observed for the box and signal processes, although in this case the Pythia distribution seems to favor the higher transverse momenta with a slight shift. The agreement for the other distributions is also only very moderate. In particular it is interesting to point out a disagreement in the ϕ^* distribution. For the Resbos contribution a slight peak appears at a value of about 0.4 which probably is due the effect of the isolation cone cut on bremsstrahlung events. Although they are quite substantial, the differences observed here will not be taken

[1)]It precisely corresponds to the class of events excluded from this sample when evaluating the gluon and quark rejection factors used in the semi-reducible background rate.

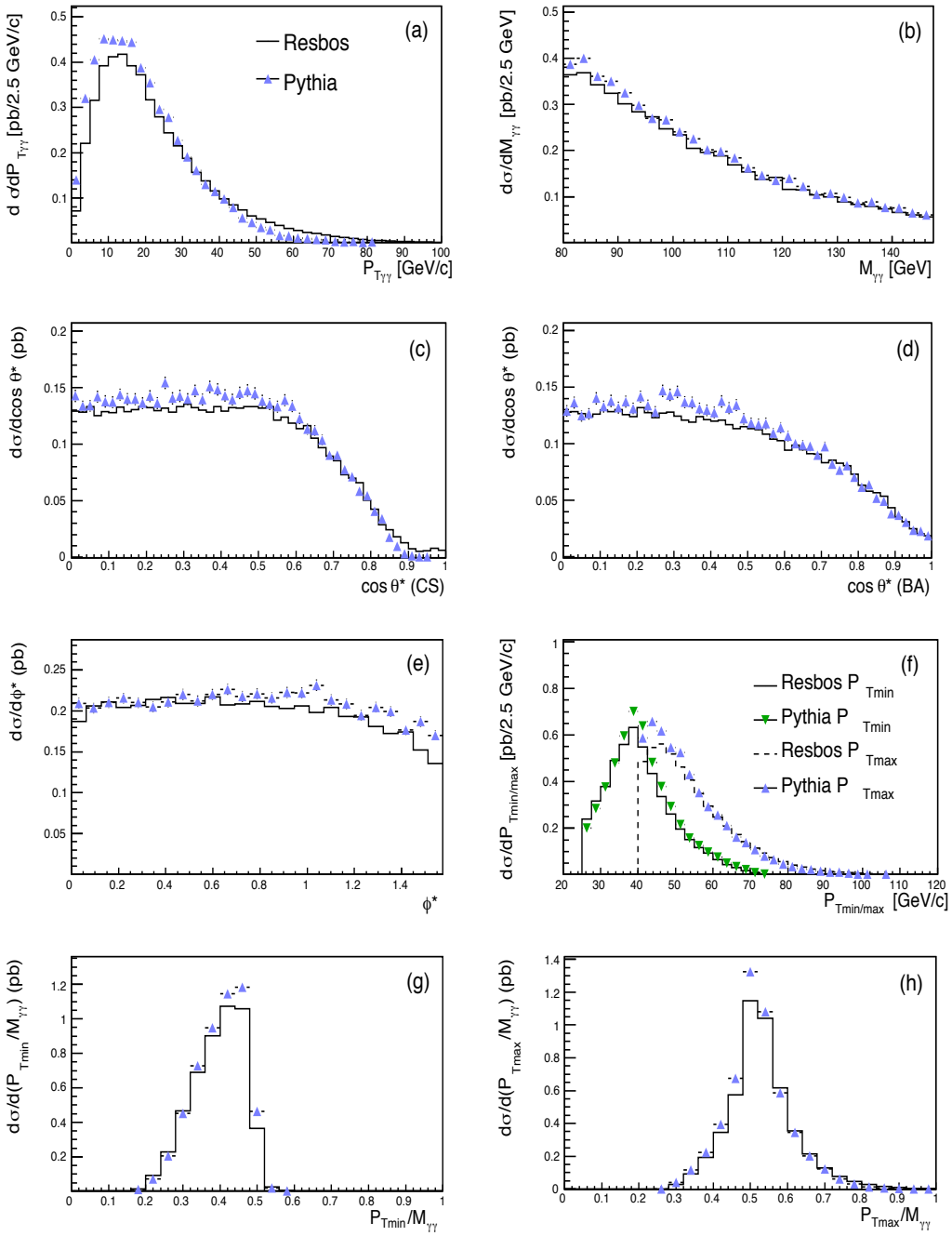

Figure 8.18: $P_{T\gamma\gamma}$, $M_{\gamma\gamma}$, $cos\theta^*_{CS}$, $cos\theta^*_{BA}$, ϕ^*, P_{Tmin} and P_{Tmax}, $P_{Tmin}/M_{\gamma\gamma}$ and $P_{Tmax}/M_{\gamma\gamma}$ distributions for the box process as simulated by Pythia and Resbos.

into account as systematics uncertainties because on the one hand the normalization scheme uses the Resbos sample which was corroborated independently and on the other hand because the Pythia sample suffers from low statistics.

The distributions for the total irreducible background are shown in Figure 8.20.

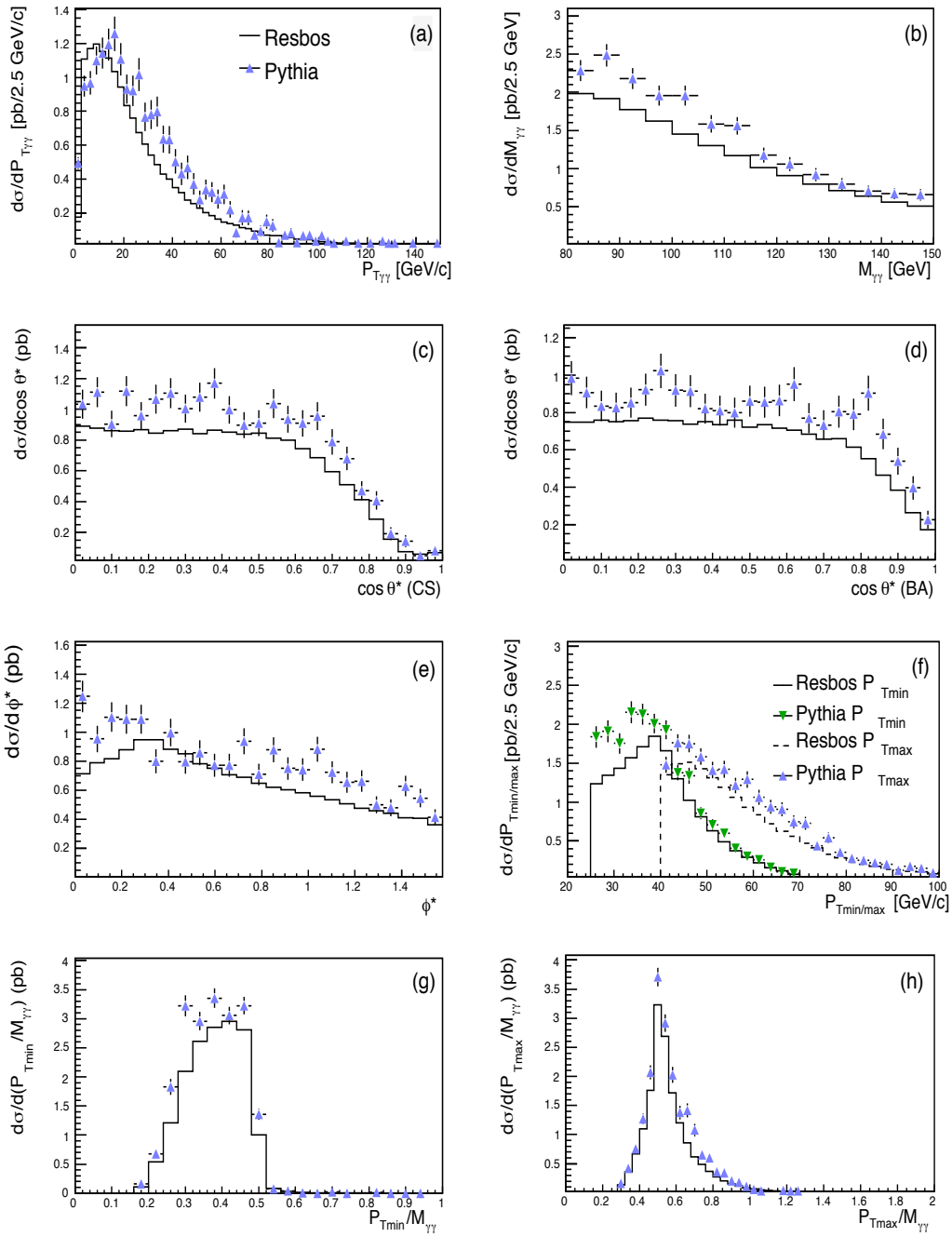

Figure 8.19: $P_{T\gamma\gamma}$, $M_{\gamma\gamma}$, $cos\theta^*_{CS}$, $cos\theta^*_{BA}$, ϕ^*, P_{Tmin} and P_{Tmax}, $P_{Tmin}/M_{\gamma\gamma}$ and $P_{Tmax}/M_{\gamma\gamma}$ distributions for the born and bremsstrahlung processes as simulated by Pythia and Resbos.

8.7 Reweighting Alpgen

8.7.1 Comparison with Pythia

Before discussing the details of the reweighting procedure of Alpgen it is interesting to first compare its outcome with that of Pythia. Considering that Alpgen does not simulate the box process, the two generators are compared only for the born and bremsstrahlung processes.

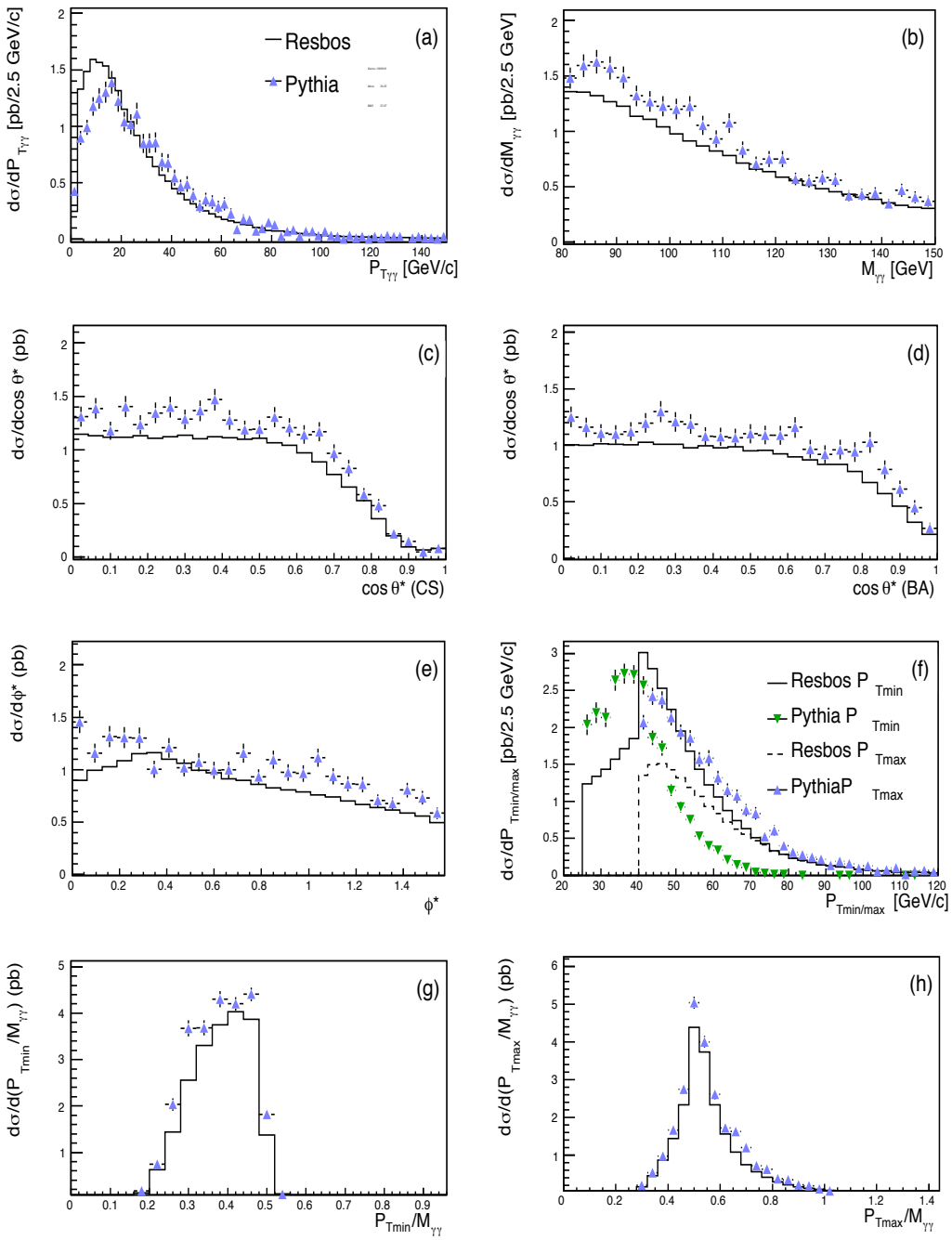

Figure 8.20: $P_{T\gamma\gamma}$, $M_{\gamma\gamma}$, $cos\theta^*_{CS}$, $cos\theta^*_{BA}$, ϕ^*, P_{Tmin} and P_{Tmax}, $P_{Tmin}/M_{\gamma\gamma}$ and $P_{Tmax}/M_{\gamma\gamma}$ distributions for all processes (box, born and brem) as simulated by Pythia and Resbos.

Figure 8.21 displays the $P_{T\gamma\gamma}$, $M_{\gamma\gamma}$, $cos\theta^*_{CS}$, $cos\theta^*_{BA}$, ϕ^*, P_{Tmin} and P_{Tmax}, $P_{Tmin}/M_{\gamma\gamma}$ and $P_{Tmax}/M_{\gamma\gamma}$ distributions for both generators. Contrary to the previous comparison between Pythia and Resbos, in this case no k-factor is applied to the qg initial-state process. A pseudo-isolation is applied in Pythia to mimic the isolation applied in Alpgen, when a separation between the photons and between the photons and the jets greater than $\Delta R_{\gamma\gamma} = \Delta R_{\gamma j} = 0.4$ is required. A relative difference in cross sections of about $\sim 13\%$ is found ($\sigma_{Pythia} = 13.12\ pb$, $\sigma_{Alpgen} = 11.49\ pb$). A large difference is observed between the two predictions in the low $P_{T\gamma\gamma}$

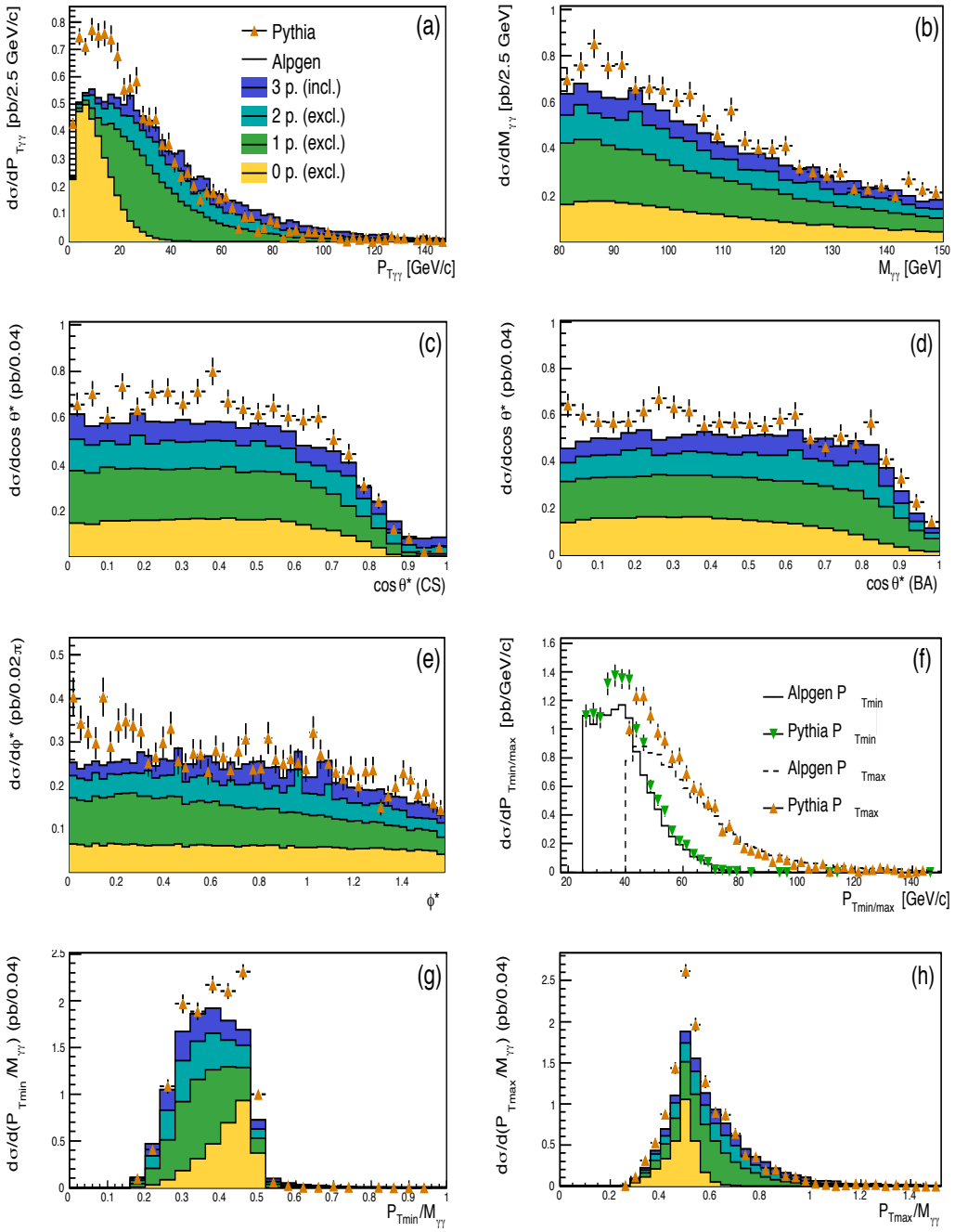

Figure 8.21: $P_{T\gamma\gamma}$, $M_{\gamma\gamma}$, $cos\theta^*_{CS}$, $cos\theta^*_{BA}$, ϕ^*, P_{Tmin} and P_{Tmax}, $P_{Tmin}/M_{\gamma\gamma}$ and $P_{Tmax}/M_{\gamma\gamma}$ distributions for the born and bremsstrahlung processes as simulated by Pythia and Alpgen. The colored regions, denoted n $p.$ correspond to the contribution of the Alpgen samples, simulating the tree-level process $2 \rightarrow \gamma\gamma + n$ $partons$, $n = (0, 1, 2, \leq 3)$.

region. Such difference was not observed in the comparison of Pythia with Resbos, neither when Pythia and Alpgen were compared for signal events. For all the other variables, a fair agreement is observed.

8.7.2 The Reweighting Procedure

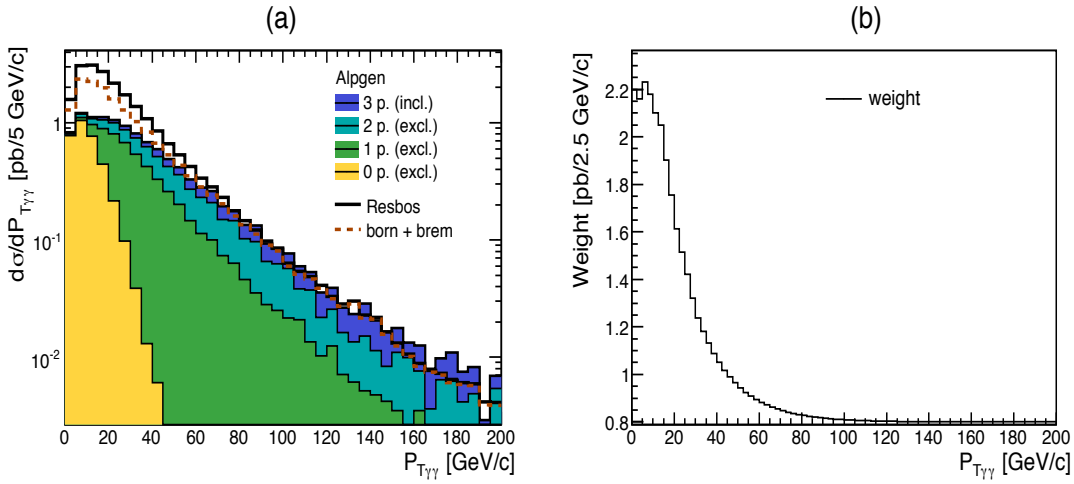

Figure 8.22: (a): $P_{T\gamma\gamma}$ distributions for Alpgen and Resbos. (b): Distribution of the weight used to reweight Alpgen as a function of $P_{T\gamma\gamma}$.

To account for the more accurate features of Resbos using Alpgen as a generator a reweighting procedure based on the generated $P_{T\gamma\gamma}$ was devised [64]. Such method is commonly used at the Tevatron. The Resbos and Alpgen $P_{T\gamma\gamma}$ distributions are illustrated in Figure 8.22(a). However, given the correlation between the $P_{T\gamma\gamma}$ and the distribution of number of jets the reweighting procedure will inevitably affect the relative amounts of events in each category of events in terms of number of jets. The distribution of the number of reconstructed jets

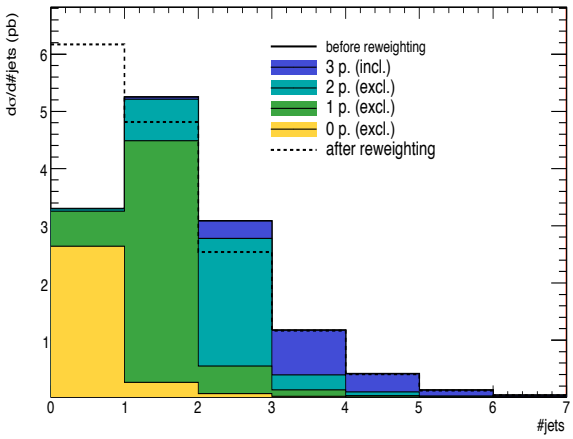

Figure 8.23: Distributions of the number of jets as simulated by Alpgen, before and after the reweighting step.

simulated by Alpgen before and after the reweighting procedure is illustrated in Figure 8.23.

As expected the relative amounts of events with no jet is increased (29.2% $\rightarrow$ 40.4%). The relative contribution of events with one or two jets are reduced (respectively 35.1% $\rightarrow$ 31.5% and 20.3% $\rightarrow$ 16.6%).The difference between the un-weighted and weighted categories could be taken into account as a systematic uncertainty on the exclusive background estimation.

8.8 How "experimental" is the pseudo-experimental isolation ?

The pseudo-experimental isolation criteria is based on parton level selection cuts that conveniently avoids divergences and emulates the actual isolation criteria used in the experimental data. Using the Pythia photon-plus-jet sample it is possible, despite the rather low statistic, to check how "experimental" the criterion really is, i.e. how the parton level cuts compare to the reconstruction level requirements. To emulate the partonic isolation criteria (IsoP), the partons originating from the quark (or gluon) which radiates the bremsstrahlung photon are added into a four-vector. The partonic isolation is then applied requiring that if the separation between the photon and the aforementioned four-vector is smaller than 0.4 and the four-vector transverse energy is in excess of 15 GeV, the event is rejected. When applying the same cuts as those applied in Resbos, most of the events remaining in Pythia are Bremsstrahlung-like events, i.e. where a photon was radiated from a quark of the hard process. Table 8.7 illustrates all the possible origins of the radiated photon in Pythia. The class $qg \rightarrow \gamma\gamma$ corresponds to events with the radiated photon coming from a quark of the hard process (Figure 8.24(a) and (b)). As mentioned above these events correspond to 93% of all events selected. The class of events $qg \rightarrow (q \rightarrow q\gamma)\gamma$ corresponds to those events with the photon radiated by the final state quark (Figure 8.24(a)).

For the born and box samples, the average reconstruction photon identification (IsEm) effi-

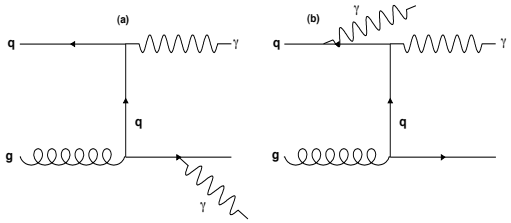

Figure 8.24: Example of Feynman diagrams for Bremsstrahlung processes

ciency is around $\epsilon_{\gamma}^{IsEm} \sim 80\%$ and the efficiency due to the track isolation criterion (IsoTr) is almost fully efficient $\epsilon_{\gamma}^{IsoTr} \sim 99\%$. These efficiencies are in good agreement with those of [96]. The identification efficiency is slightly smaller for the prompt photon of the bremsstrahlung sample and reduced by about 30% for the bremsstrahlung photon ($\epsilon_{b}^{IsEm} \sim 64\%$). As expected a much lower isolation efficiency is found for the bremsstrahlung photon, $\epsilon_{b}^{IsoTr} \sim 72\%$. The efficiency corresponding to the isolation performed at the partonic level is $\epsilon_{b}^{IsoP} \sim 85\%$.

selection	$q\overline{q}$	gg	brem. background					
			All		$qg \to \gamma\gamma$		$qg \to (q \to q\gamma)\gamma$	
			dir. γ	rad. γ	dir. γ	rad. γ	dir. γ	rad. γ
evts	16105	17681	1699		1586		1127	
IsEm	81.3%	81.1%	77.5%	65.3%	77.4%	64.4%	75.8%	60.1%
IsoTr	99.1%	99.3%	99.2%	74.8%	99.2%	73.4%	99.4%	65.6%
IsoP	-	-	-	85.8%	-	85.1%	-	79.7%
IsEm & IsoTr	80.8%	80.7%	76.9%	56.9%	76.7%	55.6%	75.4%	49.07%
IsEm & IsoP	-	-	-	60.1%	-	59.1%	-	52.9%
IsoTr & IsoP	-	-	-	70.1%	-	68.6%	-	58.38%
IsEm & IsoTr & IsoP	-	-	-	54.4%	-	53.0%	-	45.7%

Table 8.7: Photon Identification, experimental and partonic isolation efficiencies calculated with Pythia samples. These efficiencies are estimated for the direct (dir.) photon and for the radiated (rad.) one separately. The $qg \to (q \to q\gamma)\gamma$ process corresponds to the case when the photon is emitted in the final state.

8.9 The Bremsstrahlung and Fragmentation processes Normalization

Reweighting a given Monte-Carlo by a cross section that accounts for NLO corrections and the fragmentation process is a procedure that can lead to very large biases. Because the reweighting is done at the differential cross sections level, the effect of experimental selection cuts is not taken into account. In the case of parton radiation in the final state and fragmentation, a particularly important criteria is the isolation. For instance if a Monte Carlo such as Pythia is reweighted, the total cross section will be that of the direct and fragmentation processes, but only born or box process photons will be actually simulated. When applying selection cuts the amount of background events will then be over-estimated since for instance fragmentation photons have a lower efficiency. A similar situation occurs in [64] where the irreducible background is reweighted using the di-photon transverse momentum spectrum of Alpgen to the corresponding distribution generated with Resbos, for the born and bremsstrahlung contribution. For the box process, the Pythia distribution is used and its cross section is normalized to that of Resbos. The final total cross section (σ^f) is therefore essentially the total cross section of Resbos.

$$\sigma^f = \frac{\sigma^R}{\sigma^A} \times \sigma_r^A \sim \sigma^R$$

where σ^R corresponds to the Resbos cross section and σ^A and σ_r^A correspond to Alpgen cross sections respectively at the partonic and reconstruction (fast simulation using ATLFAST [97]) level. To account for the experimental isolation and identification efficiencies of the photons, the total cross section is multiplied by a factor ϵ^2 where ϵ corresponds to the photon efficiency, estimated with Pythia to be around $\epsilon \sim 80\%$.

$$\sigma_r^A \sim \epsilon^2 \sigma^A$$

At this level, two features have been neglected:
1.- In Resbos, a pseudo-experimental isolation is applied, which emulates the experimental isolation.
2.- The efficiency ϵ is estimated with Pythia for direct photon (i.e photons from born or box processes). In the case of the bremsstrahlung process, a lower efficiency is obtained for the radiated photon, as illustrated in Table 8.7.
A more accurate normalization accounting for these features can be written as:

$$\sigma^f = \epsilon^2 \times \frac{\sigma^R}{\sigma^A} \times \sigma_r^A = \epsilon^2 \times \frac{\sigma_1^R + \sigma_2^R}{\sigma^A} \times \sigma_r^A$$

where σ_1^R and σ_2^R correspond to Resbos cross section respectively for the born and bremsstrahlung contributions. As those processes cannot be generated separately in Resbos, the cross section corresponding to the born process is estimated with Diphox ($\sigma_1^R \sim \sigma_1^D$) and the cross section for the bremsstrahlung process is obtained using the difference $\sigma_2^R \sim \sigma^R - \sigma_1^D$. To account for the effect of the different efficiencies for the bremsstrahlung and fragmentation processes, the aforementioned study made with Pythia is used. The refined normalization scheme is written as:

$$\sigma^f = \frac{\epsilon^2 \sigma_1^D + \epsilon \epsilon_b \sigma_2^{R'}}{\sigma^A} \times \sigma_r^A$$
$$\sigma_2^{R'} = \sigma_2^R / \epsilon_b^{IsoP}$$

where ϵ is the isolation and identification efficiency of the prompt photon given in the fourth line of Table 8.7 for each process and ϵ_b is the isolation and identification efficiency of the bremsstrahlung radiated photon. ϵ_b^{IsoP} is the partonic isolation efficiency calculated for the radiated photon of the bremsstrahlung process. Using the cross sections given by Resbos and Diphox and the efficiencies listed in Table 8.7:

$$\sigma_1^D = 7.8\ pb \qquad \sigma^R = 16.7\ pb$$
$$\epsilon_\gamma^2 \sim (0.807)^2 \sim 0.651$$
$$\epsilon_\gamma \epsilon_b / \epsilon_b^{IsoP} \sim (0.767 \times 0.556)/0.851 \sim 0.501$$

the refined normalization decreases by $\sim 12\%$ compared to the original one.
This normalization is more accurate but still not extremely precise. 100% of the relative effect is thus accounted for as a systematic uncertainty on the overall normalization.

8.10 Discriminating Variables

The irreducible background is mostly called irreducible because of the presence of two isolated prompt photons in the final state, but potential discriminating properties such as the specificities of the production mechanisms and the spin properties of the signal, are not included in this designation. In fact, in the Higgs boson search various kinematic variables are used to further discriminate the signal from the background in order to gain statistical discovery power. The most prominent discriminant property which is always implicitly used and without which this channel would not be considered, is the narrow width of the Higgs boson (in the rather low mass range) which implies that when decaying into two photons the Higgs boson mass can be

accurately measured. Then in trying to take advantage of the differences in production mechanisms, the $P_T^{\gamma\gamma}$ variable is also used. Most of the previous comparisons presented in this study were devoted to clarify our present knowledge of this variable and the systematic uncertainties related to it. The other variable used in the official analysis [64] is $cos\theta^*$, which is related to the spin-0 property of the Higgs boson. With these variables most of the possible distinguishing properties are used. However, numerous other variables are proposed [85]. In the following the discrimination power of these variables is discussed in the light of their correlations. For all plots in this section the differential cross sections are normalized to unity for comparison of their respective shapes.

8.10.1 The di-photon Transverse Momentum ($P_{T\gamma\gamma}$)

The $P_{T\gamma\gamma}$ distributions for both the signal (gluon fusion only) and the irreducible background generated by Resbos are illustrated in Figure 8.25(a). The $P_{T\gamma\gamma}$ distribution for the signal simulated by MC@NLO is also shown. In the low $P_{T\gamma\gamma}$ region the distribution of the gluon fusion signal and the irreducible background are quite similar. In Figure 8.25(b), the correlation

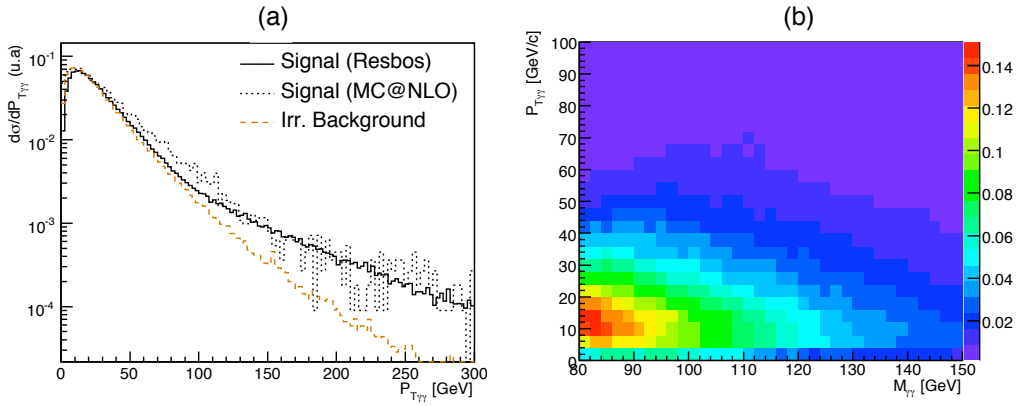

Figure 8.25: (a): $P_{T\gamma\gamma}$ distribution is generated by Resbos for both the irreducible background and the signal (gluon fusion). The MC@NLO distribution is also shown for the signal. (b): Correlation of $P_{T\gamma\gamma}$ versus $M_{\gamma\gamma}$ as generated with Resbos.

between the reconstructed mass and the di-photon transverse momentum is shown for the Resbos background. As expected, the two variables are not correlated.

8.10.2 The Higgs Boson Decay axis in its rest frame ($cos\theta^*$)

As previously discussed, the $cos\theta^*$ variable can be defined in two different axis definitions of the Higgs rest frame, the Collins-Soper (CS) and the Boost Axis (BA) frame. Figure 8.26 displays the $cos\theta^*$ distributions for both the signal and the irreducible background, defined in the CS (a) and in the BA (b) frames. The limited range of the $cos\theta^*$ variable is mostly due to the kinematic requirements on the photons P_T. No discriminating power is observed at this level. It should be noted that no mass window cut is applied.
A non-trivial correlation between $cos\theta^*$ and $M_{\gamma\gamma}$ is observed as shown in Figure 8.28. These distributions indicate that some additional statistical discrimination may still be gained. This can be illustrated when restraining the background distribution within a small mass window.

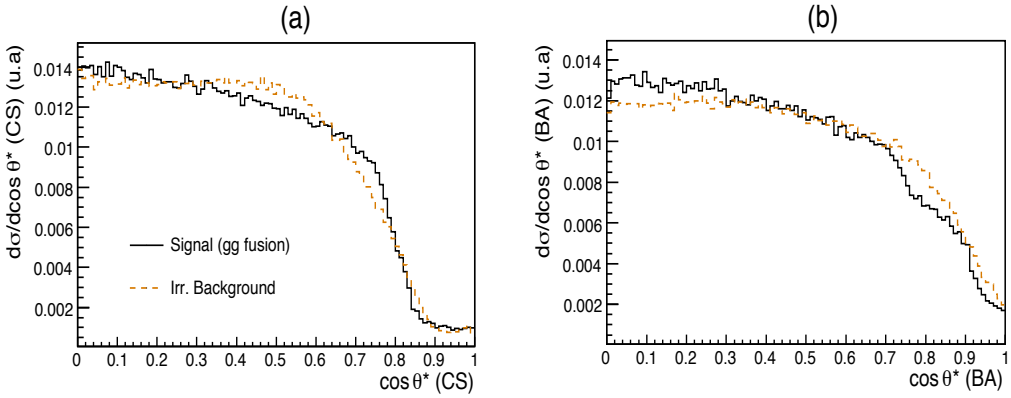

Figure 8.26: $cos\theta^*_{CS}$ (a) and $cos\theta^*_{BA}$ (b) distributions for the signal and the irreducible background with Resbos.

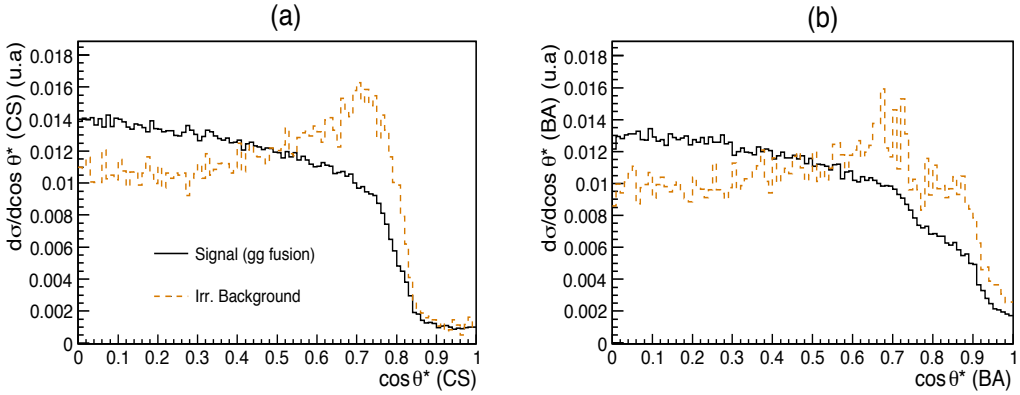

Figure 8.27: Resbos $cos\theta^*$ distributions for the signal and the irreducible background within a small mass window $118 < M_{\gamma\gamma} < 122\ GeV/c^2$.

Figure 8.27 illustrates the two $cos\theta^*$ distributions when replacing the mass range by a small mass window around the Higgs boson mass (used for the signal): $M_{\gamma\gamma} \in [118, 122]\ GeV/c^2$. A sizeable

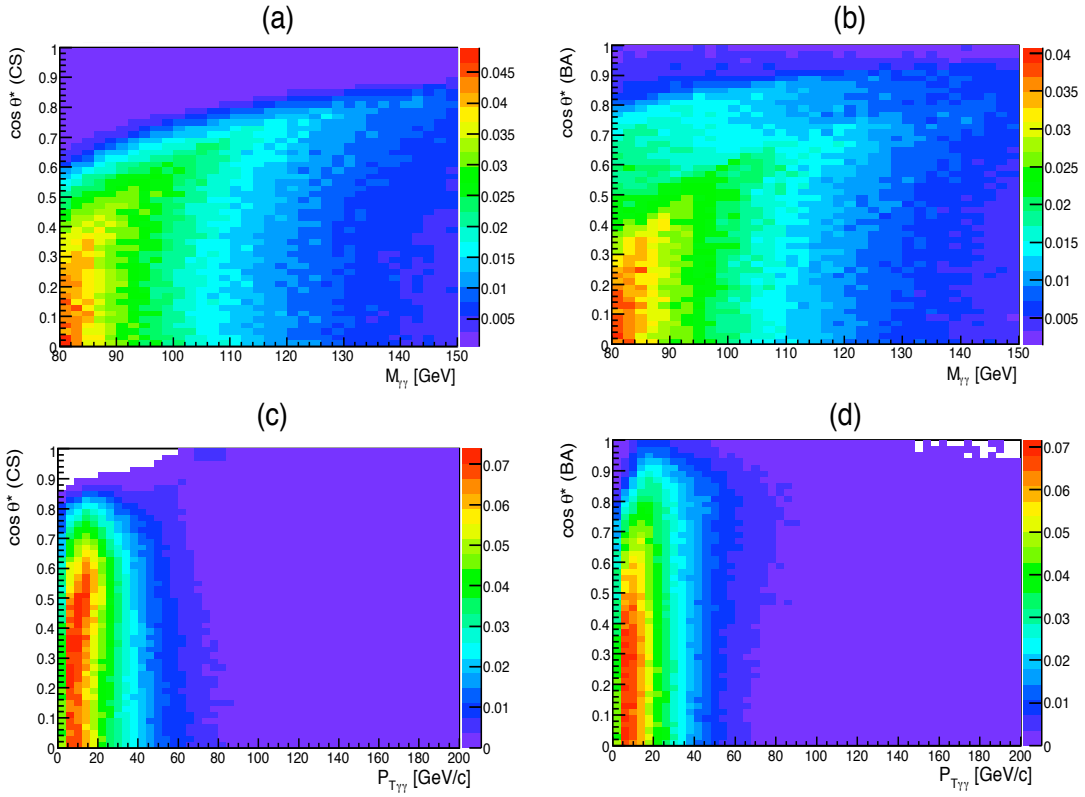

Figure 8.28: $M_{\gamma\gamma}$ correlations with $cos\theta^*_{CS}$ (a), $cos\theta^*_{BA}$ (b) and $P_{T\gamma\gamma}$ correlations with $cos\theta^*_{CS}$ (c), $cos\theta^*_{BA}$ (d) for the background.

discrimination is observed for the two definitions, although a slightly stronger discriminating power is obtained for $cos\theta^*_{CS}$. Such cut would naturally take place in a side band analysis.

8.10.3 The Collins-Soper azimuthal angle (ϕ^*)

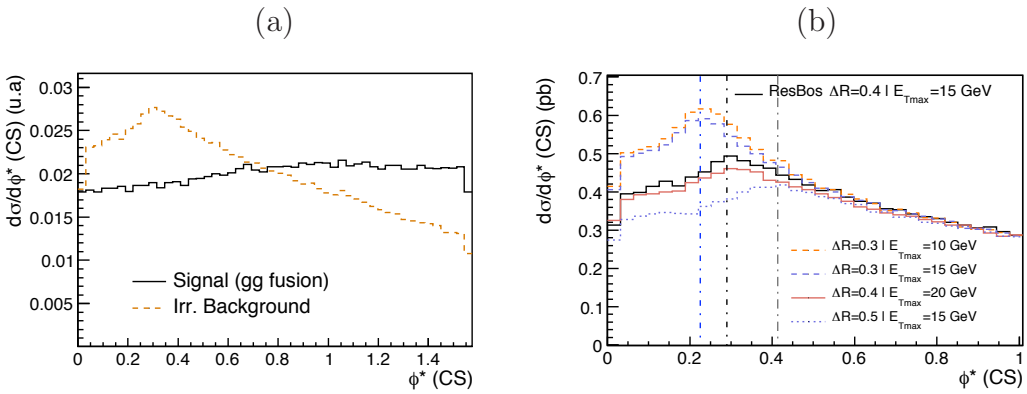

Figure 8.29: (a): ϕ^* distributions for the signal and the irreducible background with Resbos. (b): ϕ^* distributions for the background $q\bar{q} + qg$ contribution of Resbos, for various isolation criteria ($\Delta R, E_T^{max}$).

The angle ϕ^* signal and background distributions are displayed in Figure 8.29(a). A rather flat distribution is observed for the signal while the background distribution is characterized in some cases by a peak arising around 0.3. The presence of this peak is debatable as its presence is not confirmed by all simulation programs. In this case, the mass range has no particular

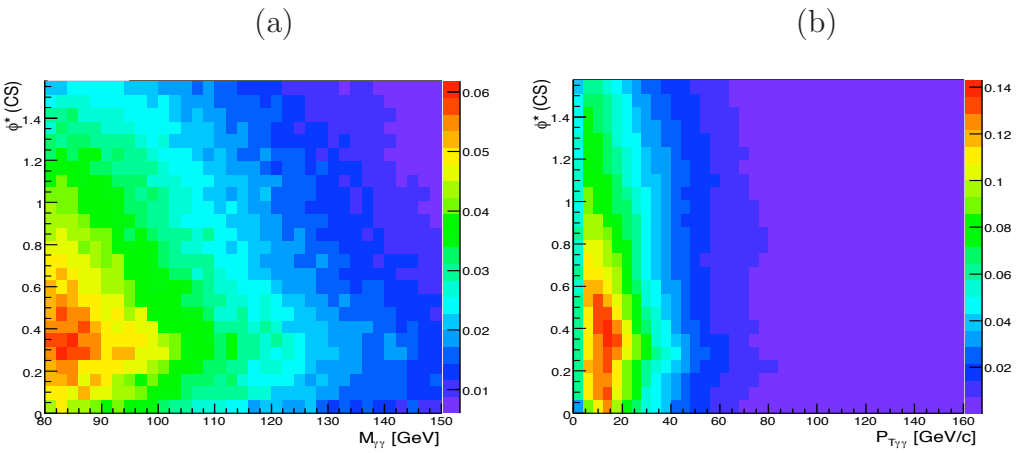

Figure 8.30: ϕ^* correlation with $M_{\gamma\gamma}$ (a) and $P_{T\gamma\gamma}$ (b) for the irreducible background.

effect on the shape, as shown in Figure 8.30(a).
This discriminating shape is due to the $q\bar{q} + qg$ contribution in Resbos. A flat distribution is observed for the box contribution. The physical interpretation of this variable is not straightforward. However, as shown in Figures 8.32 and 8.33, its correlation with the $cos\theta^*$ BA variable with an *acos* function overlaid suggests that the angle ϕ^* in some cases follows the angle between the photon and the boost axis. The low ϕ^* values mainly corresponding to low θ^* (BA) indicate that the peak may be due to the qg contribution only. The peak and its position likely result from the isolation requirement. This could be intuitively understood given that for bremsstrahlung events the boost axis is defined by the quark at LO. Figure 8.29(b) illustrates the angle ϕ^* distribution (only for the $q\bar{q} + qg$ contribution) for various isolation criteria. The

E_T^{max} parameter has no particular effect on the shape while the ΔR parameter modifies the peak position in the expected way.

8.10.4 $cos\theta^*_{CS}$ versus $cos\theta^*_{BA}$

The choice of reference axis for the definition of $cos\theta^*$ is not trivial. As shown in Figure 8.31 the two variables are not very strongly correlated. However, the Collins Soper frame offers a second variable which may have additional discriminating power. It is the frame chosen to

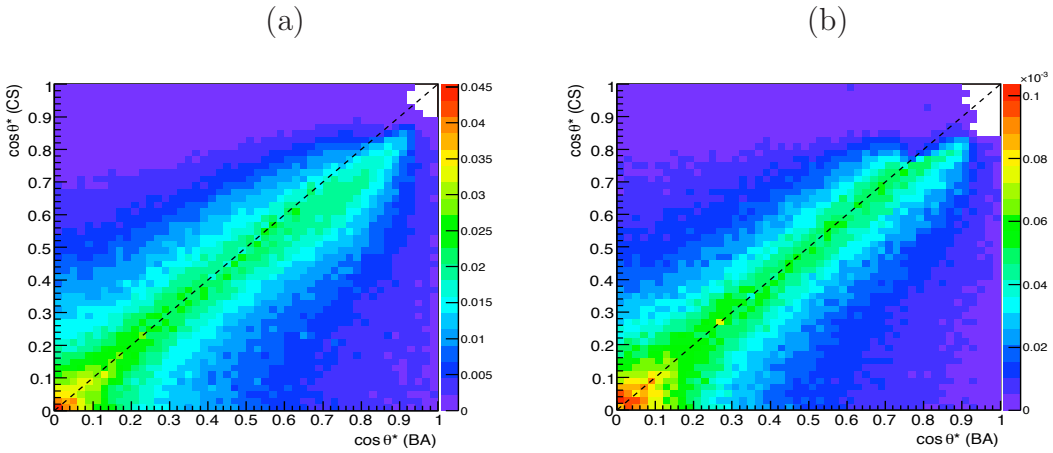

Figure 8.31: $cos\theta_{BA}*$ correlation with $cos\theta_{CS}*$ for the irreducible background (a) and the signal (b) using Resbos.

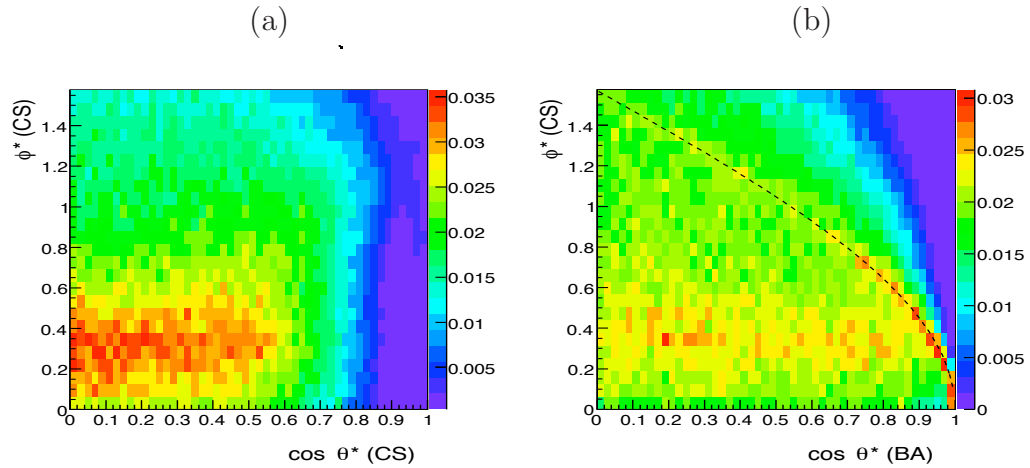

Figure 8.32: Correlations of the angle ϕ^* versus $cos\theta^*_{CS}$ (a) and $cos\theta^*_{BA}$ (b) for the background using Resbos. The dashed line corresponds to the function: $f(cos\theta^*) = acos(cos\theta^*) = \theta^*$.

compute soft QCD corrections [85], and when considering the correlation of the $cos\theta^*$ variable with the invariant mass (Figure 8.28) the correlation seems simpler in the case of the Collins Soper frame. This translates into a simpler discrimination when limiting the distributions in a small mass range as shown in Figure 8.27. For these reasons, the Collins Soper frame would tend to seem preferable, however it is best to keep the two possibilities until the first control samples are available.

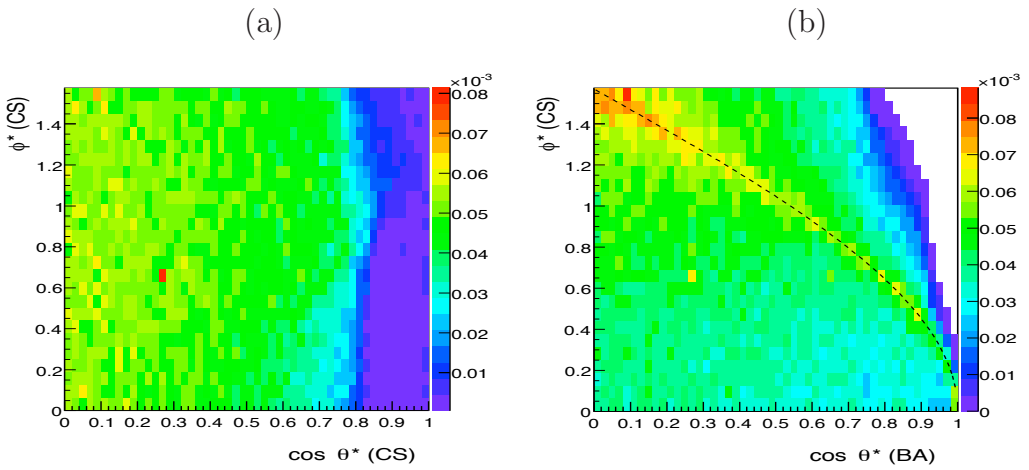

Figure 8.33: Correlations of the angle ϕ^* versus $cos\theta^*_{CS}$ (a) and $cos\theta^*_{BA}$ (b) for the signal using Resbos.

8.10.5 Other Variables

The di-photon Longitudinal Momentum ($P_{L\gamma\gamma}$)

Figure 8.34(a) shows the $P_{L\gamma\gamma}$ distributions. Their behaviors are expected to be rather sensitive to the choice of PDFs. The same PDFs are used for both the signal and the irreducible background in Resbos. Discriminating power does not seem to arise from this variable neither in its correlation with the invariant mass (Figure 8.34(b)).

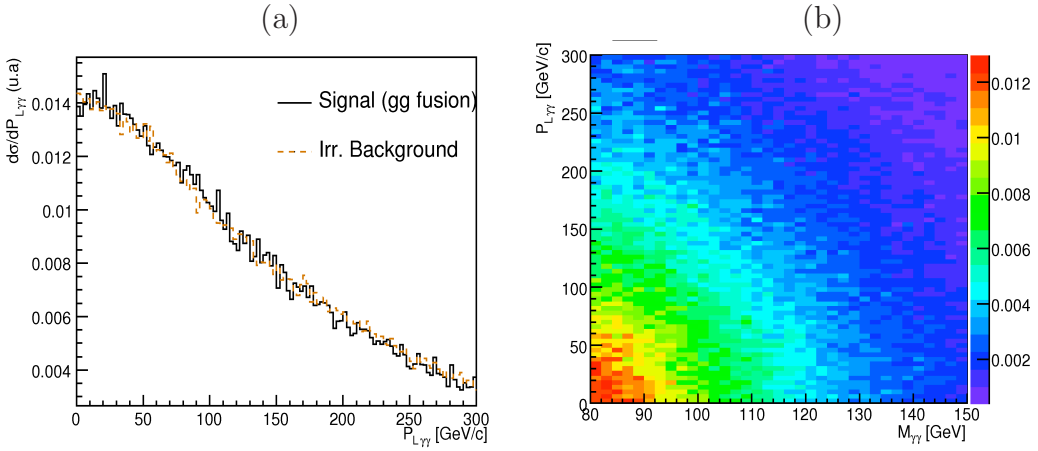

Figure 8.34: $P_{L\gamma\gamma}$ distribution (a) for the signal and the irreducible background with Resbos. $P_{L\gamma\gamma}$ correlation with $M_{\gamma\gamma}$ (b) for the irreducible background

The Transverse Momenta of the leading and sub-leading photons

Figures 8.35(a) and 8.35(b) display the distributions of the transverse momentum of the leading and sub leading photons P_{Tmax} and P_{Tmin}. At first sight these variables seem to be very discriminant. However, most of this discrimination is due to the correlation of these quantities with the invariant mass $M_{\gamma\gamma}$. As illustrated by the complete loss of discriminating power where a stringent cut on the invariant mass is applied. (Figure 8.37).

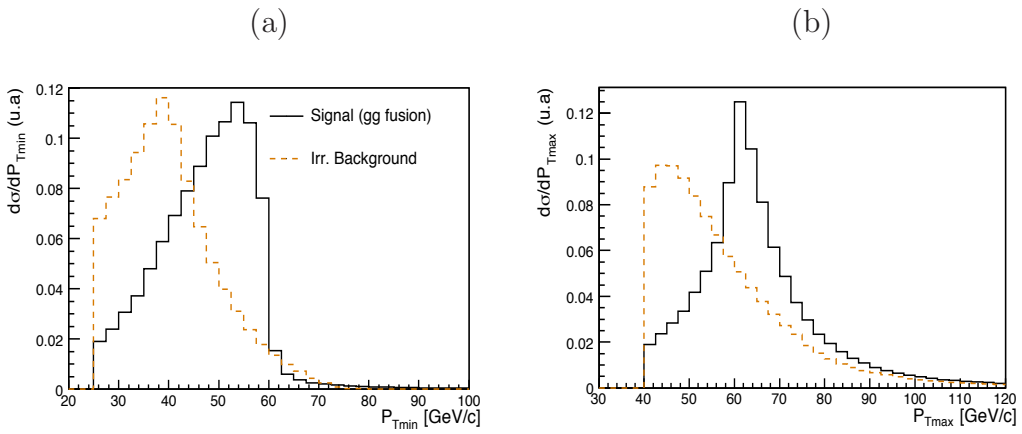

Figure 8.35: P_{Tmin} (a) P_{Tmax} (b) distribution for the irreducible background and the signal as generated with Resbos.

8.11 Systematic Uncertainties

8.11.1 Irreducible background

Various sources of systematic uncertainties associated to the irreducible background rate are estimated:

(i) To account for the incompleteness of the fixed order calculation, both the renormalization (μ_R) and the factorization (μ_F) scales are varied, from $0.5 \times c$ to $2 \times c$, with $c = M_{\gamma\gamma}$. When assuming $\mu_R = \mu_F$, an overall variation of $\pm 5\%$ to the cross section is observed, while when varying independently these scales the resulting variation enhances to $\pm 14\%$.

(ii) A comparison between cross sections given by Resbos and Diphox leads to an estimation of the systematic uncertainty related to the fragmentation contribution. Resbos and Diphox predictions agree within 16%.

(iii) To account for selection inaccuracy due to the fact that Diphox and Resbos perform a parton level calculation, the cuts (P_{Tmin}, P_{Tmax}) are varied by ± 1 GeV/c (roughly corresponding to the energy reconstructed resolution) around the central value (25,40). A relative variation of the total NLO cross section of $\pm 6\%$ is found.

(iv) To account for the isolation inaccuracy from the reconstruction point of view, in both Diphox and Resbos, the isolation criterion is varied around the central value ($[\Delta R = 0.4, E_T^{max} = 15\ GeV]$). A variation of $\pm 7\%$ on the total NLO cross section is observed.

(v) An additional systematic check of the Diphox calculation leads to an overall $\pm 1\%$ systematic uncertainty when varying the fragmentation scale μ_f from $0.5 \times M_{\gamma\gamma}$ to $2 \times M_{\gamma\gamma}$ (the relative contribution of the fragmentation and the direct processes change but not the total cross section).

(vi) The systematic uncertainty related to the PDFs is studied using Diphox with the set of PDF CTEQ61 (an update version of CTEQ6M). The largest difference with respect to

the central cross section when varying the 20 parameters of the parton densities is around ±7%.

(vii) To account for the different efficiencies for photons from the bremsstrahlung and fragmentation processes with respect to prompt photons of the box and born processes, an overall variation of the normalization of ±12% is taken as systematic uncertainty.

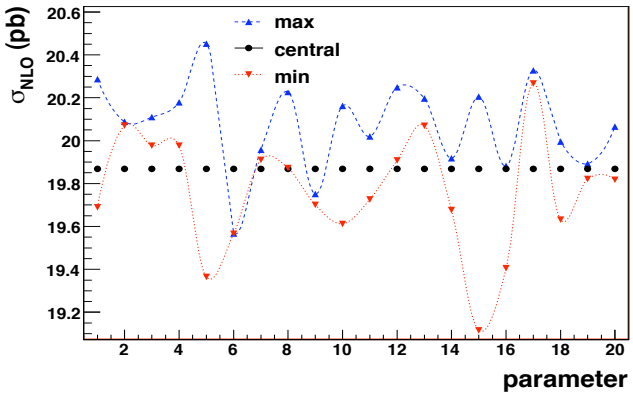

Figure 8.36: Variation of the NLO cross section when all 20 parameters of the parton distribution functions (CTEQ61) are varied independently. The upper and lower curves correspond to the variations of the cross section with respect to the central value.

Systematic uncertainties related to the irreducible background evaluation, summarized in Table 8.8, lead to an overall relative uncertainty of ±24%.

8.11.2 Signal

Similar sources of systematic uncertainties are also estimated for the signal:

(i) To account for the incompleteness of the fixed order calculation, both the renormalization (μ_R) and the factorization (μ_F) scales are varied, from $0.5 \times M_H$ to $2 \times M_H$. When assuming $\mu_R = \mu_F$, an overall variation of ±10% to the cross section is observed, while when varying independently these scales the resulting variation enhances to ±13%.

(ii) An additional systematic uncertainty is the difference between Resbos and HNNLO cross sections, due to the fixed order ME calculation in HNNLO with respect to a resummed NLO cross section in Resbos. This induces a relative difference between their NLO cross sections around 6% for the same set of PDF (CTEQ6M).

(iii) To account for selection inaccuracy due to the fact that HNNLO and Resbos perform a parton level calculation, the cuts (P_{Tmin}, P_{Tmax}) are varied by ±1 GeV/c leading to a relative variation of the total NLO cross section of ±1%.

(iv) To account for the different PDFs used in the calculation of the Resbos cross section and the NNLO k-factor with HNNLO, an additional systematic error is estimated by the relative difference between the NLO cross sections generated by HNNLO for the two PDF sets CTEQ6M and MRST2004, around 2%.

(vii) The systematic uncertainty related to the branching ratio of the Higgs boson into a pair of photon is studied using the HDecay program. The largest difference with respect to the central branching ratio when varying the SM parameters is around $(-8\%, +5\%)$.

The sources of systematic uncertainties are listed in Table 8.8, the global systematic uncertainty corresponding to $\pm 15\%$ of the total NLO cross section.

Potential sources	Relative uncertainty	
	Irr. Bck.	Signal
(i) Scale dependence	14%	13%
(ii) Phase space	6%	6%
(iii) Isolation	7%	1%
(iv) PDF	6%	2%
(v) Frag. scale	1%	-
(vi) Fragmentation	16%	-
(vi) brem. eff.	12%	-
(vii) B.R.	-	-8%,+5%
Total	$\sim 27\%$	$\sim 16\%$

Table 8.8: Summary of the relative systematic uncertainty on irreducible background and signal NLO normalizations.

Finally, to illustrate the impact of systematic uncertainties on the signal and background discriminating variables, the signal and background distributions with their associated theoretical systematic uncertainties are illustrated in Figures 8.37, 8.38 and 8.39. A small mass window around the Higgs boson mass ($M_{\gamma\gamma} \in [115, 125]\ GeV/c^2$) is selected.

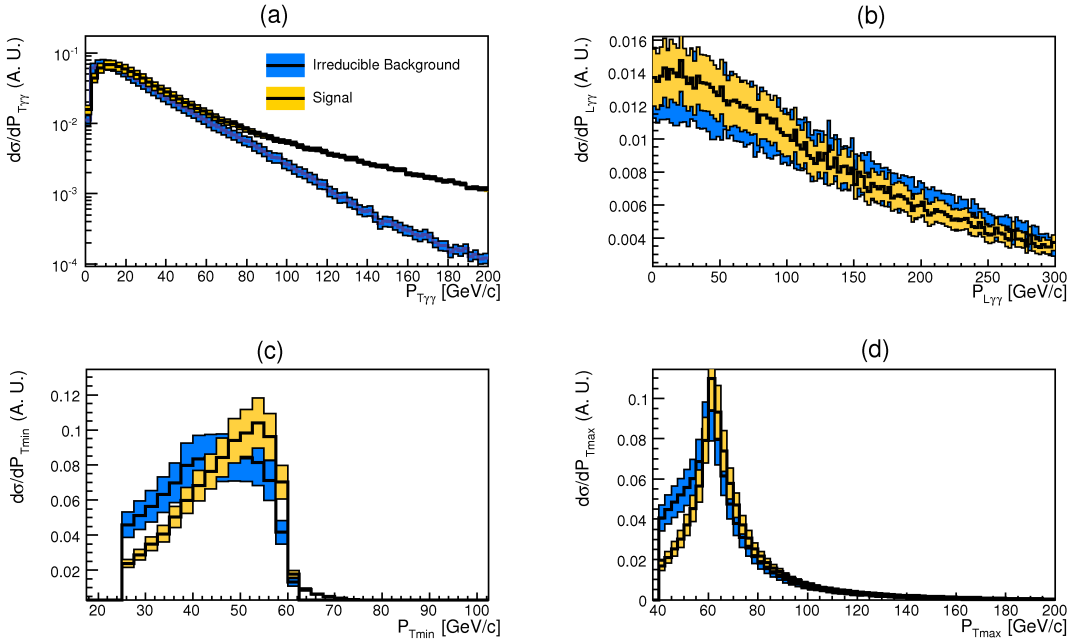

Figure 8.37: $P_{T\gamma\gamma}$ (a), $P_{L\gamma\gamma}$ (b), P_{Tmin} (c) and P_{Tmax} (d) distributions for the signal and the background, with their associated systematic uncertainties.

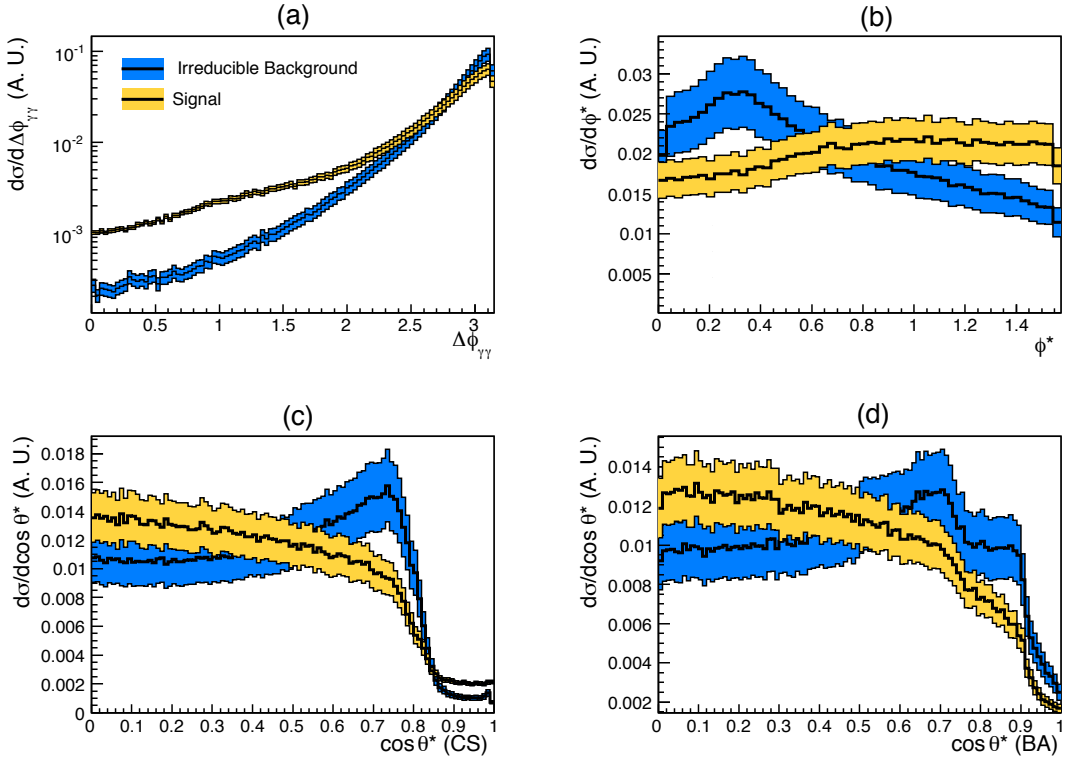

Figure 8.38: $\Delta\phi_{\gamma\gamma}$ (a), $\phi^*(CS)$ (b), $cos\theta^*_{CS}$ (c) and $cos\theta^*_{BA}$ (d) distributions for the signal and the background, with their associated systematic uncertainties.

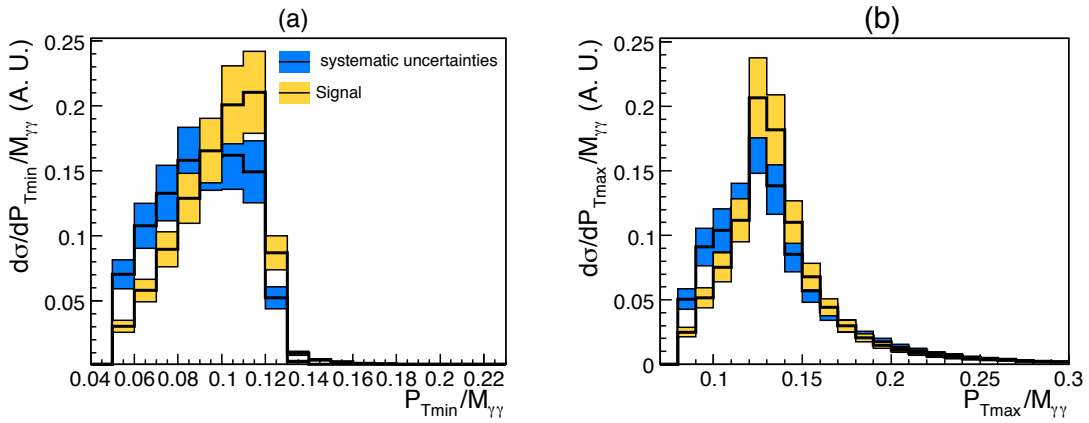

Figure 8.39: $P_{Tmin}/M_{\gamma\gamma}$ (a) and $P_{Tmax}/M_{\gamma\gamma}$ (b) distributions for the signal and the background, with their associated systematic uncertainties.

Conclusion

In this study different Monte-Carlo generators and programs are used to estimate the signal and irreducible background in the channel where the Higgs boson decays into two photons.

The gluon fusion signal rate is derived at NLO, a NNLO k-factor is also estimated of about 1.15 at $m_H = 120\ GeV/c^2$. An overall systematic uncertainty of about 16% is found.

The irreducible background rate is assessed from the comparison of the different predictions, accounting for the NLO QCD corrections and the NLO one photon fragmentation. A global systematic uncertainty of about 27% is estimated from the performances and limitations of the different simulation tools. A study of the influence of the photon isolation and identification efficiencies of the background normalization indicates that the method used in [64] slightly over-estimates the irreducible background rate. A refined normalization scheme to be used along with the reweighting method is proposed.

The discriminating power of all relevant variables is shown. A new variable potentially discriminant, the angle ϕ^* defined in the Collins-Soper frame, is also presented. However the discriminating power of this variable or the use of this variable in the analysis is debatable, large differences occurring in the background distributions generated by the different tools. The $cos\theta^*$ variable has been studied when defined in the boost axis frame and in the Collins-Soper frame. The discriminating power of this variable seems to be clearer in the Collins-Soper frame, as well as the correlation of the $cos\theta^*$ with the invariant mass $M_{\gamma\gamma}$ seems to be simpler. The strength of this correlation suggests to take into account for the mass dependence in the estimation of the sensitivity of this analysis. This correlation encourages an analysis from the sidebands of the $M_{\gamma\gamma}$ distribution.

Chapter 9

Normalization of the γ-jet background to the $H \to \gamma\gamma$ inclusive analysis

Introduction

The search for the Higgs boson in the inclusive two photons channel requires a good understanding and rejection of the large background associated to the signal, which presents a very small branching ratio. This analysis therefore crucially relies on the detector capacity to discriminate those backgrounds that can *a priori* be reduced. The largest of these reducible backgrounds is the production of one prompt photon and one or more jets when one of the jets fragments into a leading π^0 or η meson; it amounts almost to half of the total background.

The first sampling of the accordion structure of the ATLAS Liquid Argon electromagnetic calorimeter was in part designed for the purpose of separating π^0 mesons from photons. It is therefore very important that its contribution be properly normalized to optimize the search and assess its sensitivity.

Notwithstanding the total background will be normalized to the data, the analysis relies on a precise estimation of the background, limited by the Monte Carlo (MC) models, varying in term of QCD corrections order. The available MC simulations of γ-jet events in ATLAS all yield leading order (LO) predictions of the γ-jet cross section. A recent program, Jetphox [98], provides a next-to-leading (NLO) fixed-order prediction of the differential cross sections for the γ-jet processes, including the fragmentation of final-state partons into a leading photon.

This study aims to derive the normalization of this semi-reducible background to the inclusive Higgs boson search in the two photons final state based on a comparison between Jetphox and Pythia. A normalization of the Pythia LO prediction by the NLO prediction provided by Jetphox is proposed. The goal of this approach is to take advantage of the NLO with fragmentation fixed-order normalization of Jetphox, while keeping the benefits of Pythia as the primary event generator, as it incorporates full parton showering. The most important sources of systematic uncertainties on the overall cross section are also studied.

9.1 LO Estimation using Pythia

The Pythia code [77] implements the Matrix Element (ME) calculation of the γ-jet production only at the lowest order. The corresponding subprocesses simulated in Pythia are illustrated in

Figure 9.1(a-c). In terms of power counting in the strong interaction coupling α_s, the tree level processes $q\overline{q} \rightarrow g\gamma$ and $qg \rightarrow q\gamma$ are at LO ($O(\alpha\alpha_s)$) and the gluon fusion process $gg \rightarrow g\gamma$ (so-called *box* in reference to the quark loop) is at NLO ($O(\alpha\alpha_s^3)$). Given the quite large gluon luminosity at the LHC this contribution could be sizeable, but is almost negligible representing about 0.1% of the total cross section. At LO, the $q\overline{q}$ and qg processes contribute to approximately 95% and 5% respectively.

Contrary to a fixed-order NLO ME calculation, Pythia simulates a rather realistic description

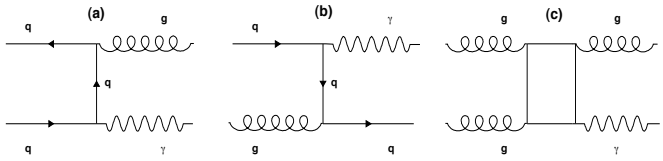

Figure 9.1: Feynman diagrams of the subprocesses of the γ-jet production at the lowest order in α_s.

of the γ-jet production events by implementing the parton shower (PS), although processes included in Pythia are at LO only. The showering process "dresses" an event by including initial- and final-state radiations from the hard process. Other features provide a non-null final-state transverse momentum, such as the underlying event and the primordial k_T. The underlying event in Pythia describes the fate of the remaining partons inside the two protons of the collision. The primordial k_T simulates the Fermi momentum, i.e the motion of the partons inside a proton. While a typical value of $< k_T > \sim 200 - 300\ MeV/c$ could realistically be expected, comparisons of Pythia to Tevatron data suggest that a larger value is required, about 4 GeV/c. The PS modifies the parton and photon phase space, but leaves the total cross section unchanged. The reach of Pythia events in the γ-jet phase space is illustrated in Figure 9.2. However, if further selection cuts in the aforementioned phase space are required, the cross section will unavoidably be altered.

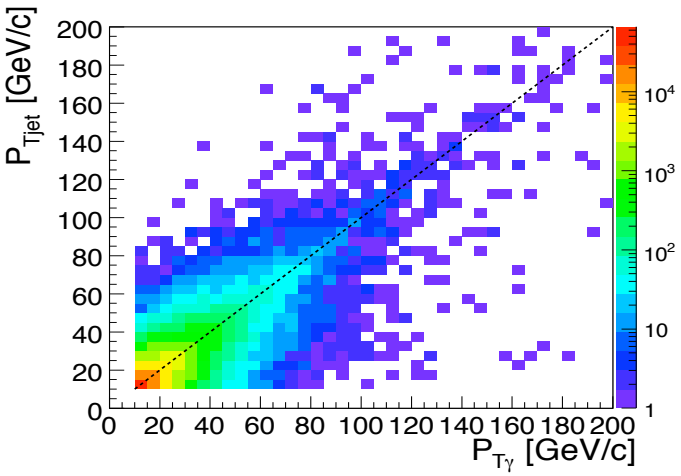

Figure 9.2: Pythia γ-jet phase space coverage for $P_{Tmin}^{jet} = P_{Tmin}^{\gamma} = 10\ GeV/c$.

9.2 NLO and Fragmentation estimation using Jetphox

Jetphox [98] is a fixed-order program of ME calculation almost fully at NLO[1)], including the one-photon fragmentation of a final-state parton. This code provides a sound treatment of the soft and collinear parts of the perturbative ME, leading to a meaningful physical total cross section, even if discontinuities may occur in the differential cross sections [99]. It treats the γ-jet production from a quasi-experimental standpoint by using isolation criteria usually required in collider experiments. The experimental selection criteria of prompt photons require isolation cuts to reject jets and efficiently select prompt photons. The isolation criteria typically use reconstructed charged particle tracks or energy deposition in a cone around the reconstructed photon. In Jetphox, a photon is considered as isolated if the hadronic transverse energy E_T^{had}, corresponding to the energy of the final-state partons deposited in a cone around the photon direction in the (η, ϕ) plane does not exceed a fixed value E_T^{max}. For the fragmentation processes, E_T^{had} will typically be the remaining energy of the parton fragmenting into a photon carrying almost all its transverse momentum. The typical isolation criterion is defined by $\Delta R = 0.4$ and $E_T^{max} = 15\ GeV$.

9.2.1 LO Comparison with Pythia

Jetphox is a fixed-order ME calculation. For a fair comparison between Jetphox and Pythia only the Jetphox LO direct (LO D) contribution should be taken into account and the PS and all features that provide a non-null transverse momentum to the hard interaction should be turned off in Pythia. The following kinematic cuts are used at the generation level:

$$P_{Tmin}^{\gamma} = 20\ GeV/c \quad P_{Tmin}^{jet} = 20\ GeV/c$$
$$|\eta_{\gamma,jet}| < 2.5$$

(a) (b)

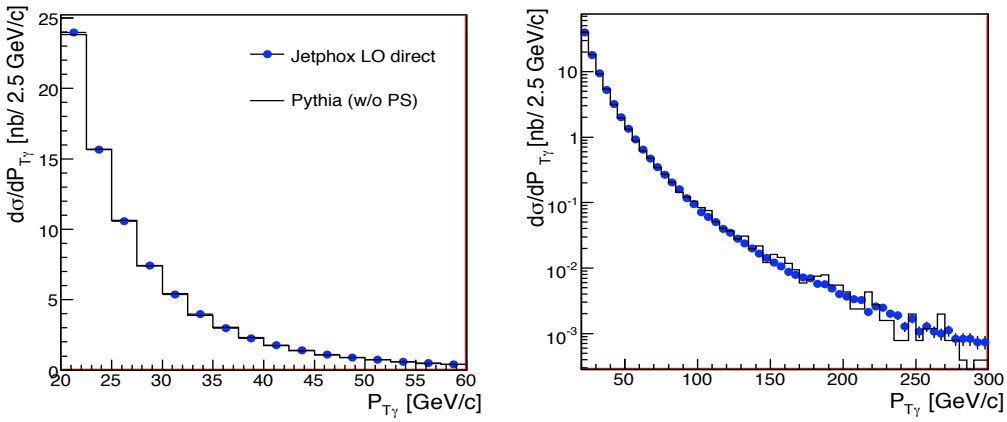

Figure 9.3: P_T^{γ} distributions as generated by Pythia without PS and Jetphox (LO Direct contribution) in linear scale (a) and logarithmic scale (b).

The standard photon isolation criterion is used and the parton distribution function (pdf) set used is CTEQ6L1 [100], with $\alpha_s(M_Z) = 0.129$[2)]. Figure 9.3 displays the distributions of the

[1)] The box subprocess is only implemented at LO.

[2)] for NLO cross sections, the PDFs CTEQ6M are used, corresponding to $\alpha_s(M_Z) = 0.1179$.

transverse momentum of the photon. As expected a good agreement is observed (the total cross sections agree to within 0.5%).

9.2.2 NLO Jetphox

The cross sections calculated with Jetphox are separated into specific processes according to their different initial- and final-states and mainly into two parts [99]:

(i) The direct part is represented at LO by the diagrams 9.1(a-b) and at NLO by the diagrams illustrated in Figure 9.4. The LO contribution coincides with the Pythia processes at LO without the box process. The Higher Order (HO) corrections correspond both to the emission of one initial or final-state parton from the LO process and to new initial-state processes with respect to the LO contribution such as diagrams (b), (c) and (e).

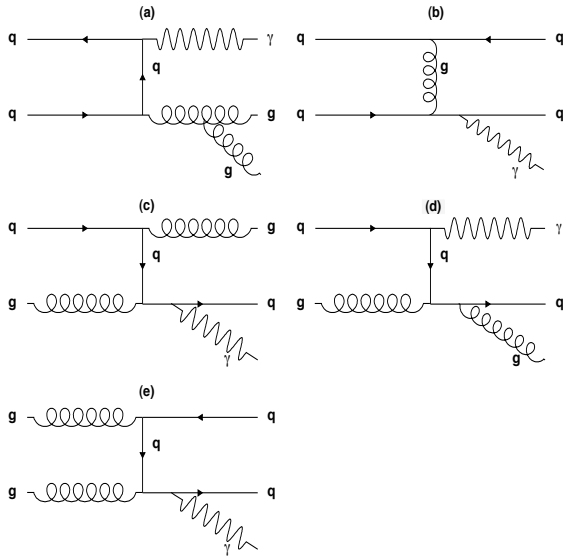

Figure 9.4: Feynman diagrams of the direct NLO contributions of the γ-jet Jetphox production.

(ii) The fragmentation part is represented at LO by the diagrams (a, b, d, f & g) and at NLO by the diagrams (c & e) illustrated in Figure 9.5.

The diagrams (b) of the direct and (b) of the fragmentation contributions illustrate essentially the same physical process. However, the direct case shows the complete diagram which requires a particular treatment of its collinear and infrared divergences. Whereas the second case illustrates the collinear approximation where a fragmentation function is used, and the final-state quark radiating the photon is neglected in the picture. In terms of power counting the fragmentation functions $D^{\gamma}_{q,g}(z,\mu_f)$ are of order $O\Big(\frac{\alpha}{\alpha_s}\Big)$. The z parameter represents the fraction of momentum carried by the photon with respect to the emitting parton and μ_f is the fragmentation scale.Varying μ_f strongly influences the direct and fragmentation cross sections separately but barely alters the total cross section.

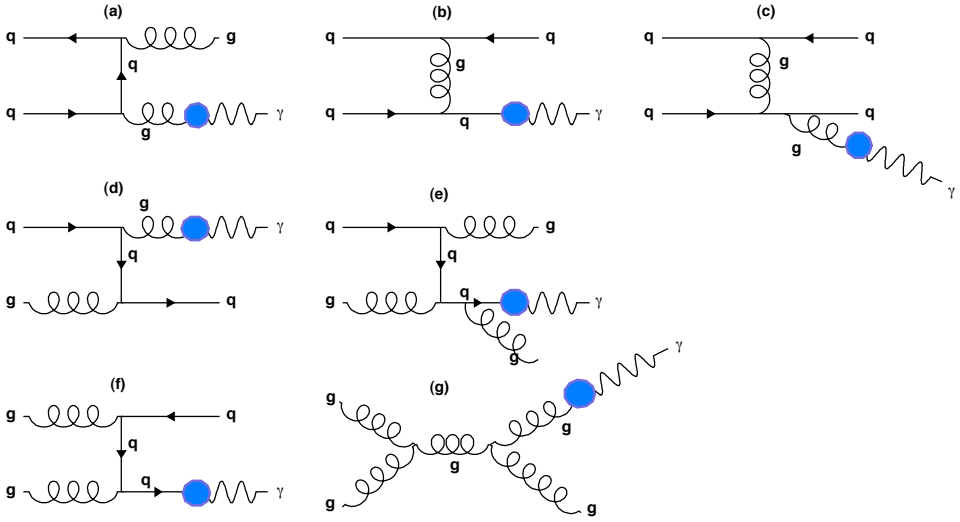

Figure 9.5: Feynman diagrams of the fragmentation LO and NLO contributions of the γ-jet Jetphox production.

9.2.3 NLO Results

Jetphox being a fixed-order program aimed at evaluating differential cross sections, it unavoidably presents various discontinuities in particular due to generator level cuts. At HO, Jetphox uses a merging function for a more realistic phase space definition of the leading jet. If a parton is in a cone around the jet direction in the (η, ϕ) plane smaller than a fixed value R_{kT} ($R_{kT} =$ 1.0 in this study), it is merged together with the jet.
The phase space covered by the Jetphox program in the $(P_T^{\gamma}, P_T^{jet})$ plane is shown in Figure 9.6. Any deviation from the diagonal in this Figure represents purely higher order corrections for the direct processes or the resulting allowed momentum within the isolation cone for the fragmentation. The events at low P_T^{γ} and high P_T^{jet} are largely due to the bremsstrahlung process (Figure 9.4(c)) which is absent in the Pythia sample. This illustrates how the relative event rate is strongly dependent on the kinematic cuts. Compared with the phase space generated with Pythia, the relative rates will thus also strongly depend on the basic kinematic cuts.

Results for the Direct Contribution

The kinematic cuts at the generation level are:

$$P_{Tmin}^{\gamma} = 10\ GeV/c \quad P_{Tmin}^{jet} = 20\ GeV/c$$
$$|\eta_{\gamma,jet}| < 2.5$$

Figure 9.7 dispalys the P_T^{γ} and P_T^{jet} distributions, for the direct contribution at LO and NLO as obtained with the Jetphox program. A singularity arises at $P_T^{\gamma} =$ 20 GeV/c in the P_T^{γ} distribution. In the LO case, this singularity is due to the necessary balance between the photon and the jet. At NLO, events with a photon $P_T^{\gamma} <$ 20 GeV/c are possible due to the

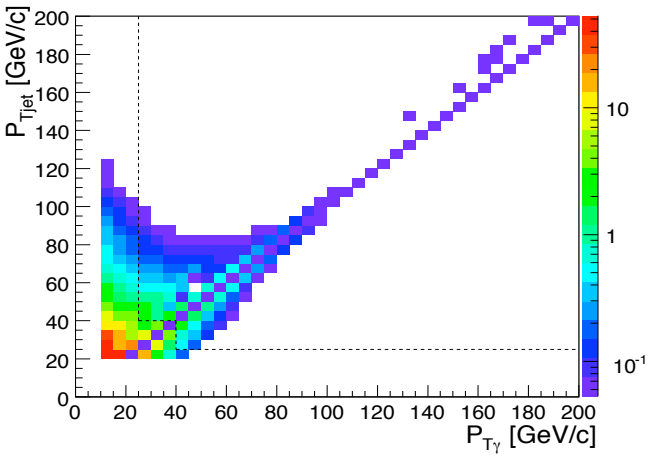

Figure 9.6: Jetphox γ-jet phase space coverage at NLO (direct and fragmentation), generated with $(P^{\gamma}_{Tmin}, P^{jet}_{Tmin}) = (10, 20)\ GeV/c$. The dashed lines delimit the region of interest after the analysis cuts are applied.

(a) (b)

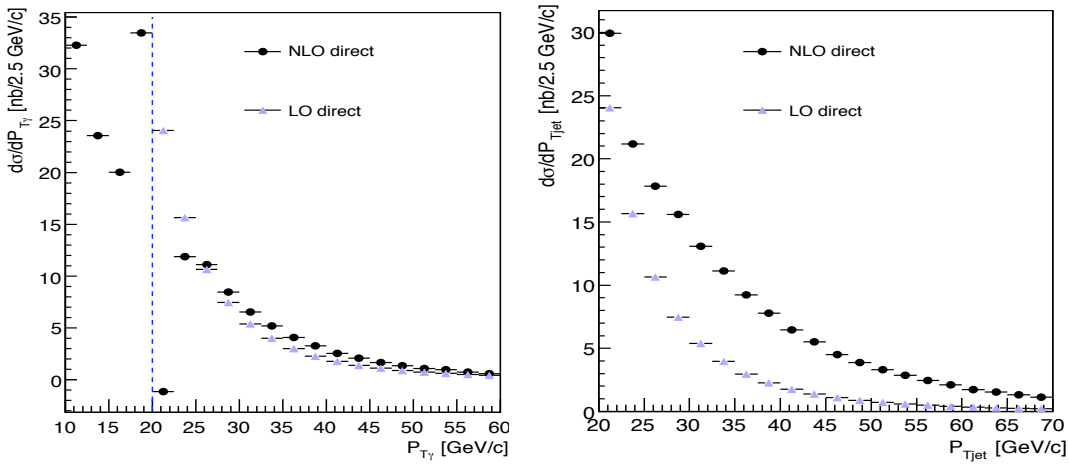

Figure 9.7: P^{γ}_{T} (a) and P^{jet}_{T} (b) distributions at LO and NLO for the direct contribution.

additional parton in the final state. However, a discontinuity still exists at the transition. It is a feature of the fixed-order calculation. Another discontinuity occurs in the P^{jet}_{T} distribution at $P^{\gamma}_{Tmin} + E_{Tmax}/c = 25\ GeV/c$. This effect corresponds to events with two final-state partons and one photon emitted from one of the two partons, as for instance in the subprocess $qq \to qq\gamma$ (Figure 9.4(b)). When the subleading jet's separation with the photon is smaller than the isolation cone (0.4), the isolation and kinematic conditions (the subleading jet transverse momentum must be smaller than E_{Tmax} and the photon transverse momentum must be greater than P^{γ}_{Tmin}) induce a discontinuity around $P^{\gamma}_{Tmin} + E_{Tmax}$.
The $P^{\gamma jet}_{T}$ spectrum is illustrated in Figure 9.8(a) at LO and NLO. The LO contribution is as expected gathered at 0 GeV/c. The NLO shape is characterized by a first negative bin and a discontinuity appearing around $P^{\gamma jet}_{T} = 15\ GeV/c$. This discontinuity occurs at E_{Tmax},

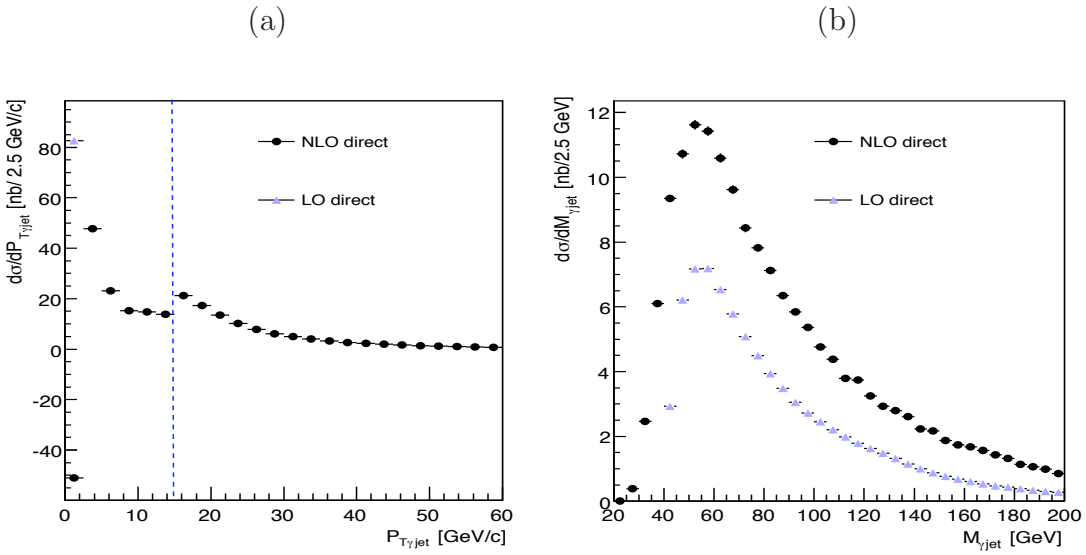

Figure 9.8: $P_T^{\gamma jet}$ (a) and $M_{\gamma jet}$ (b) distributions at LO and NLO for the direct contribution.

corresponding to the upper limit on the transverse momentum carried by the subleading jet when its separation with the photon is smaller than the isolation cone. Moreover, at NLO, when a subleading parton is clustered to the leading one, the total transverse momentum $P_T^{\gamma jet}$ vanishes.
The $M_{\gamma jet}$ spectrum is illustrated in Figure 9.8(b). At LO(NLO), a singularity arises at 40(20) GeV/c^2 due to the cut $P_{Tmin}^{jet} = 20\ GeV/c (P_{Tmin}^{\gamma} = 10\ GeV/c)$.

Results for the Fragmentation Contribution

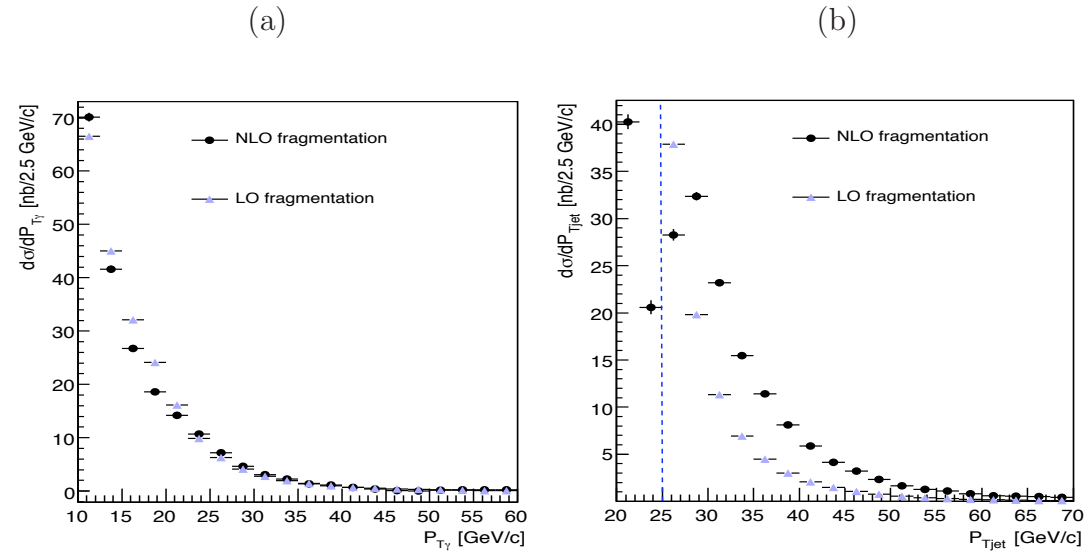

Figure 9.9: P_T^{γ} (a) and P_T^{jet} (b) distributions at LO and NLO for the fragmentation contribution.

The P_T^{γ} and P_T^{jet} distributions for the fragmentation processes are illustrated in Figure 9.9(a)

and 9.9(b respectively.
The discontinuity occurring in the P_T^{jet} distribution at $P_{Tmin}^{\gamma} + E_{Tmax}/c = 25\ GeV/c$. It appears for the same reasons discussed in the case of the direct contribution . Figure 9.10

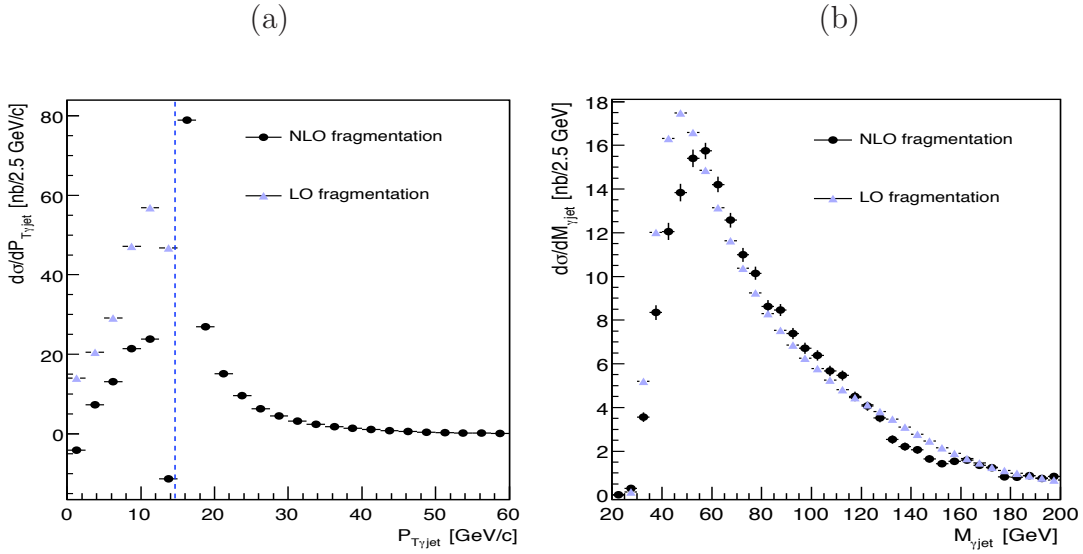

Figure 9.10: $P_T^{\gamma jet}$ (a) and $M^{\gamma jet}$ (b) distributions at LO and NLO for the fragmentation contribution.

displays the $P_T^{\gamma jet}$ distribution for the fragmentation contribution at LO and NLO. Contrary to the former case, fragmentation events at LO are present at $P_T^{\gamma jet}$ smaller than 15 GeV/c as the remnants of the parton fragmenting into a photon can carry a transverse momentum of up to E_{Tmax}. The discontinuity occurring at E_{Tmax} in the NLO differential cross section also results from the cone isolation requirement [101].
The $M_{\gamma jet}$ spectrum is displayed in Figure 9.10(b). Both LO and NLO differential cross sections are calculated with the NLO PDF CTEQ6M, inducing their surprisingly similar normalizations.

9.3 Global Normalization: Empirical k-factor

The ATLAS inclusive Higgs boson search in the two photons channel [102] uses NLO cross sections for the signal and most of the background processes. For the semi-reducible γ-jet background a k-factor of 1.7 is applied.

To better estimate the semi-reducible background normalization, accounting for the NLO corrections and the fragmentation contributions the Jetphox program is used [103]. The fragmentation process is not simulated by Pythia in the γ-jet samples but it is in the jet-jet samples. However the estimation of the semi-reducible and reducible backgrounds is done using rejection factors that do not take into account the photon fragmentation (it is removed by hand to estimate the jet rejection), the fragmentation part of the background is thus simply neglected. To properly normalize the semi-reducible background an empirical approach is used where the LO Pythia estimation is normalized to the NLO direct and fragmentation cross section of Jetphox. To further verify that a simply factor provides a sufficiently accurate description of the background at NLO, a detailed comparison is performed on the shapes of the discriminating

variables of the analysis.
The empirical definition of the k-factor is:

$$k = \frac{\sigma_D^{NLO} + \sigma_F^{NLO}}{\sigma_{Pythia}^{LO}}$$

where σ_D^{NLO} and σ_F^{NLO} are respectively the Jetphox predictions for the direct (D) and the fragmentation (F) contributions at NLO. The LO Pythia contribution is denoted σ_{Pythia}^{LO}.
Given the differences in phase space for the photon and the jet between Pythia and Jetphox large differences in the k-factor are expected to appear when varying the photon and jet selection criteria. The variations of the cross section with different kinematic cuts (P_{Tmin}, P_{Tmax}) are illustrated in Table 9.1. P_{Tmin} corresponds to the smallest of $P_{T\gamma}$ and P_{Tjet} while P_{Tmax} is the greatest.
The uncertainties quoted on the Jetphox cross sections at NLO are estimated from various sets of generation level cuts. It amounts to roughly few percent on the direct contribution but can be as large as 10% for the fragmentation alone. This error is likely due to the Jetphox internal precision in its NLO calculations, as illustrated by the large fluctuations in the distributions, in particular for the fragmentation at NLO. The uncertainty quoted on the Jetphox LO and Pythia cross sections is only statistical.
Given the singularities described in the previous section that are due to specific requirements when evaluating differential cross sections such as the isolation in the Jetphox program, the generation kinematic cuts are chosen in order to avoid discontinuities in the analysis acceptance. However, a thorough study of the impact of the generation requirements and in particular the isolation will be needed to evaluate the accuracy of the Jetphox prediction.

P_{Tmin}, P_{Tmax} (GeV/c,GeV/c)	NLO D (nb)	LO D (nb)	NLO F (nb)	Pythia (nb)
20, 30	55.5 ± 0.65	24.8 ± 0.1	27.8 ± 0.8	34.9 ± 0.4
20, 40	31.2 ± 0.25	10.2 ± 0.05	13.6 ± 1.0	16.6 ± 0.2
25, 40	25.2 ± 0.2	10.2 ± 0.05	9.6 ± 0.9	15.1 ± 0.2
30, 40	20.5 ± 0.15	10.2 ± 0.05	6.2 ± 0.9	13.05 ± 0.2

Table 9.1: Cross sections of the γ-jet production of the Jetphox direct and fragmentation contributions for different cuts. These cuts are applied *a posteriori* on the samples generated with the cuts ($P_{Tmin}^{\gamma} = 10\ GeV/c, P_{Tmin}^{jet} = 20\ GeV/c$).

9.3.1 Isolation requirements

The Jetphox program implements a pseudo-experimental isolation of the photon by requiring that no parton with transverse energy in excess of E_{Tmax} is found within ΔR of the photon. The typical requirement is $E_{Tmax} = 15\ GeV$ and $\Delta R = 0.4$. This requirement is of course unsatisfying from the reconstruction point of view, it is therefore varied in order to estimate a systematic uncertainty. Table 9.2 lists the cross sections for both the direct and the fragmentation contributions at NLO with various isolation criteria varying ΔR from 0.3 to 0.4 and E_{Tmax} from 10 GeV to 20 GeV. These cross sections are obtained by applying

the kinematic cuts ($P_{Tmin} = 25\ GeV/c, P_{Tmax} = 40\ GeV/c$) on the sample generated with ($P^{\gamma}_{Tmin} = 10\ GeV/c, P^{jet}_{Tmin} = 20\ GeV/c$).

$\Delta R, E_{Tmax}(GeV)$	NLO D (nb)	NLO F (nb)	NLO total (nb)
0.3,10	29.3 ± 0.2	8.5 ± 0.9	37.8 ± 0.9
0.3,15	26.4 ± 0.2	11.9 ± 1.0	38.3 ± 1.0
0.3,20	24.4 ± 0.2	14.1 ± 1.0	38.5 ± 1.0
0.4,10	27.3 ± 0.2	7.9 ± 0.9	35.2 ± 0.9
0.4,15	25.2 ± 0.2	9.6 ± 0.9	34.8 ± 0.9
0.4,20	23.4 ± 0.2	13.4 ± 1.0	36.8 ± 1.0

Table 9.2: Jetphox cross sections of the γ-jet production for the direct and fragmentation contributions, for different isolation cuts ($\Delta R, E_{Tmax}$).

At fixed ΔR, the NLO direct cross section surprisingly decreases with E_{Tmax} but it decreases with ΔR at fixed E_{Tmax}, which is a more intuitive behaviour. The fragmentation contribution follows a precisely opposite trend. The possibly counter intuitive behaviour of the individual processes result from the matching procedure between the brem component of the direct contribution and the collinear approximation of the fragmentation.
To cover potential errors arising from one particular choice of isolation criterion, the observed variations of the total cross section are used to estimate a systematic uncertainty.

9.3.2 Kinematic cuts

As was shown in Table 9.1, the cross sections are sensitive to variations of the kinematic cuts as they operate in critical phase space regions where some processes are accounted for in Jetphox but not in Pythia (for instance the bremsstrahlung process is simulated by Pythia but only in the jet-jet sample, it is therefore not taken into account here).
Furthermore, the cuts are applied on the true photon and parton momenta. A systematic uncertainty accounting for potential biases resulting from differences potentially occurring with respect to the event reconstruction are assigned.

9.3.3 Results

The $P_{T\gamma}$ and P_{Tjet} distributions for the differential cross sections at NLO and LO D (direct only) for Jetphox and Pythia are illustrated respectively in Figures 9.11(a) and 9.12(a). The ratio of the total NLO to LO D Jetphox estimations (k') as well as the k-factor are illustrated in Figures 9.11(b) and 9.12(b). Above 30 GeV/c in P^{γ}_{T} both k and k' are rather constant. Below this value, the k-factor increases by large amounts due to the additional processes which are present in NLO Jetphox prediction and are not in Pythia, while k' is bounded to its kinematically allowed region. k and k' are also rather stable above 30 GeV/c in P^{jet}_{T}, although at higher values of P^{jet}_{T}, an increase of k' and possibly k is visible. Such variation is not surprising given the numerous additional processes in the NLO total cross section estimate.
The values of k and k' for various selection cuts are listed in Table 9.3. As expected from the relative phase spaces of Jetphox and Pythia, k increases with P_{Tmin}. Therefore, the k-factor

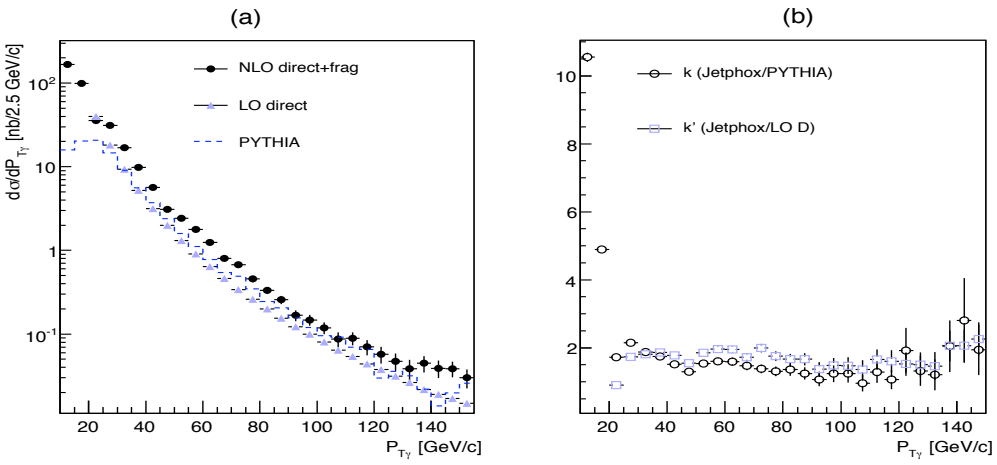

Figure 9.11: P_T^γ distributions (a) as generated by Jetphox (LO D and NLO contributions) and Pythia. The k-factors k and k' are illustrated in (b).

P_{Tmin}, P_{Tmax} (GeV/c, GeV/c)	$k' = \frac{\sigma_{D+F}^{NLO}}{\sigma_D^{LO}}$	$k = \frac{\sigma_{D+F}^{NLO}}{\sigma_{Pythia}^{LO}}$
$20, 30$	3.4 ± 0.1	2.38 ± 0.02
$20, 40$	4.5 ± 0.2	2.75 ± 0.08
$25, 40$	3.5 ± 0.1	2.35 ± 0.11
$30, 40$	2.8 ± 0.2	2.11 ± 0.12

Table 9.3: k and k' values for different kinematic cuts ($P_{Tmin}^\gamma, P_{Tmin}^{jet}$).

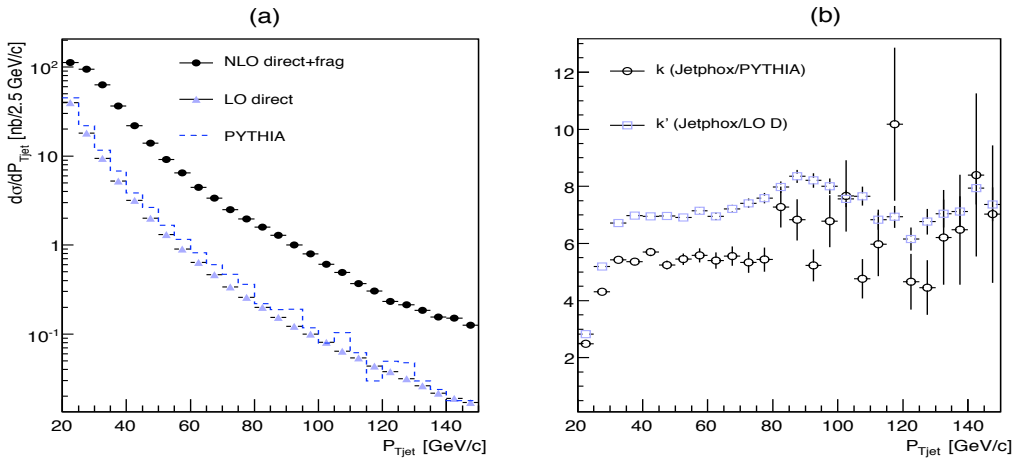

Figure 9.12: P_T^{jet} distributions (a) as generated by Jetphox (LO D and NLO contributions) and Pythia. The k-factors k and k' are illustrated in (b).

used to renormalize the semi-reducible background strongly depends on the kinematic cuts. Using the inclusive search for $H \to \gamma\gamma$ standard cuts [64]:

$$P_{Tmin} = 25\ GeV/c \quad P_{Tmax} = 40\ GeV/c$$
$$|\eta_{\gamma,jet}| < 2.5$$

the k-factor is $k = 2.35 \pm 0.11$

9.3.4 Analysis Acceptance and Preselection

The variables used in the preselection are: the pseudo-rapidity, the transverse momenta P_T^{γ} and P_T^{jet}.
Figure 9.13(a) displays the photon η (η_γ) distributions at LO and NLO predictions and 9.13(b) its associated ratios (or k-factors). The k-factor is rather stable in the region $|\eta_\gamma| < 1.5$ while it slightly increases beyond this region.
The ratio corresponding to the η_{jet} distributions, displayed in Figure 9.13(d) is rather stable.
The P_T^{γ} and P_T^{jet} distributions and their associated ratios are respectively illustrated in Figure 9.14(a-b) and 9.15(a-b). In the region neighboring the kinematic and acceptance cuts the ratios of the differential cross sections are not very stable. To cover this potential source of systematic error, the cuts will be varied and a systematic uncertainty will be assigned.

9.3.5 Local variations with relevant kinematic variables

In the inclusive Higgs boson search various kinematic variables are used to best discriminate the signal from the background to gain statistical discovery power. The variables used to derive the final result are the invariant mass $M_{\gamma jet}$, $P_T^{\gamma jet}$ and the $cos\theta^*$ defined in the boosted axis (BA) frame. Another definition of the axis in the γ-jet rest frame, the Collins-Soper (CS) frame, is studied, as for the irreducible background case.

This section devoted to verifying that the distribution of these variables at NLO including fragmentation are not too different from those generated by Pythia.

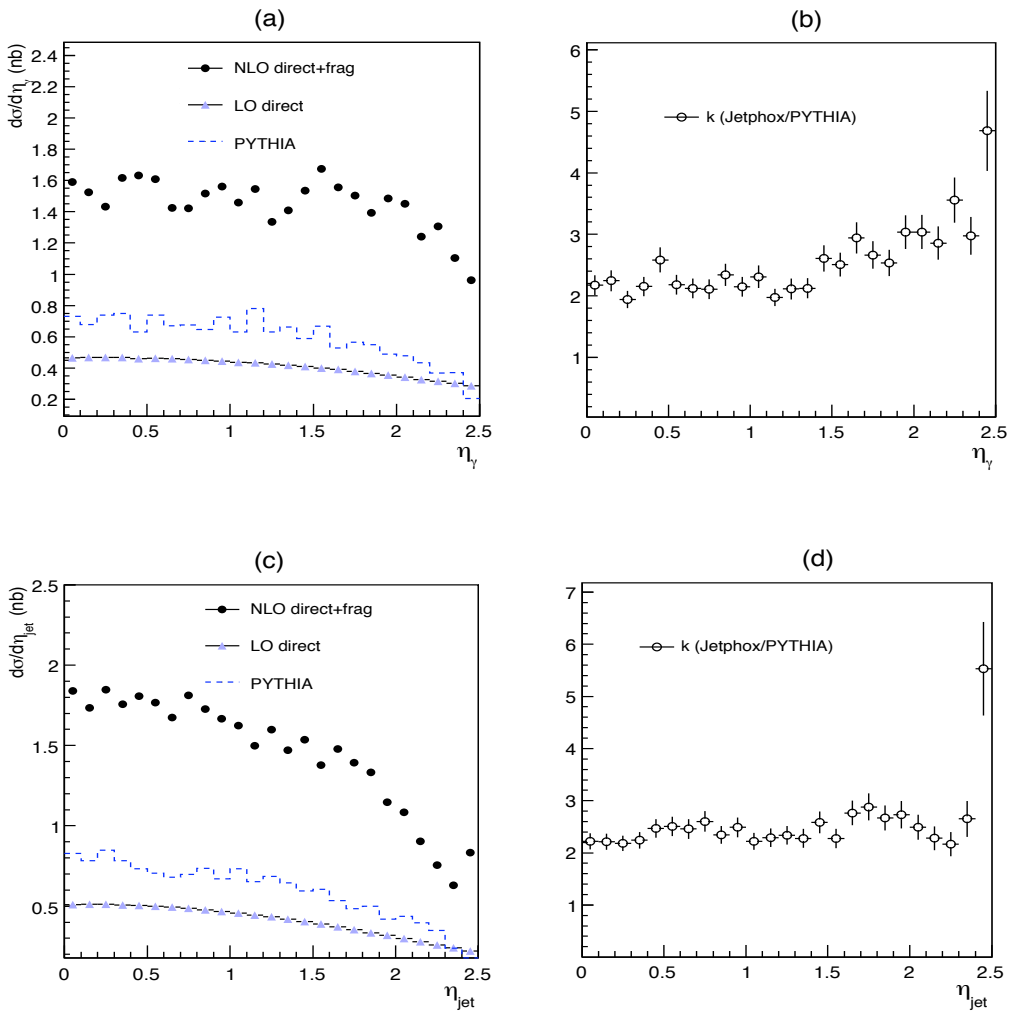

Figure 9.13: (a) η_γ and (b) η_{jet} distributions as generated by Jetphox at NLO (direct and fragmentation) and LO D and by Pythia. The k-factors k are shown in (b) and (d) respectively.

Figure 9.16(a) illustrates the $P_T^{\gamma jet}$ distributions and 9.16(b) its associated ratio. Instabilities occur in Jetphox when $P_T^{\gamma jet} \to 0$ and at $P_T^{\gamma jet} \sim E_{Tmax}$. Above this threshold, the k-factor increases with $P_T^{\gamma jet}$. This feature is not surprising, although it is not straightforward, given in particular the jet clustering algorithm of Jetphox that yields a harder $P_T^{\gamma jet}$ spectrum than Pythia.

The $M_{\gamma jet}$ NLO and LO predictions and the associated k-factor are respectively illustrated in Figure 9.17(a-b). The k-factor is rather stable around 2.5 in the mass range [100,150] GeV/c^2 although it increases slightly with $M_{\gamma jet}$ (from ~ 2 to ~ 3 in the mass range [60,200] GeV/c^2). In the low $M_{\gamma jet}$ region, there is a noticeable difference between the Pythia and Jetphox LO D contribution. The absence of soft radiation in the Jetphox program induces a sharper turn-on of the mass distribution due to the 40 GeV/c cut on both the photon and the jet.

Figure 9.18 displays the $cos\theta^*$ (CS and BA) distributions for Pythia and Jetphox NLO. The Jetphox distributions at NLO are rather flat for the two definitions. Because the Higgs boson

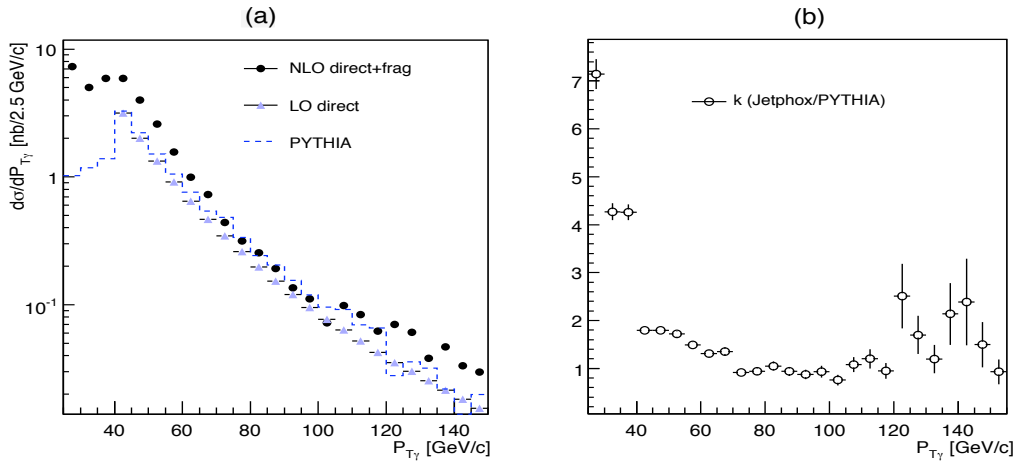

Figure 9.14: P_T^{γ} distributions (a) of the NLO and LO D contributions of Jetphox and Pythia. The k-factor k is shown in (b).

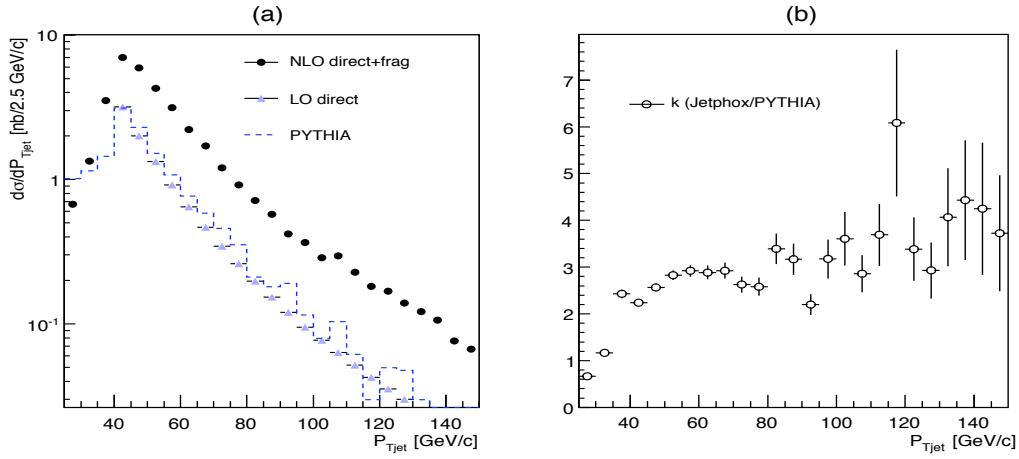

Figure 9.15: P_T^{jet} distributions (a) of the NLO and LO D contributions of Jetphox and Pythia. The k-factor k is displayed in (b).

is scalar these distributions for the signal are expected to be essentially flat as well. The $cos\theta^*$ (CS and BA) variables have therefore a marginal discriminating power. However, for the irreducible background a correlation between the invariant mass of the diphoton system and the $cos\theta^*$ is observed. Figure 9.19 shows the correlation of $M_{\gamma jet}$ versus $cos\theta^*$ (CS and BA) for the NLO direct and fragmentation contributions. As was the case in chapter 8 for the irreducible background, a non trivial correlation is observed between $M_{\gamma jet}$ and $cos\theta^*$. These distributions show that statistical discrimination is still present in the correlation, which can be illustrated by the fact that within a small mass window at a relative high mass, the background will no longer be flat. Figure 9.20 displays the $cos\theta^*$ distributions when selecting the mass range [105,150] GeV/c^2. These distributions illustrate the gain in discriminating potential of this variables when applying the lower cut limit $M_{\gamma jet} > 105\ GeV/c^2$.

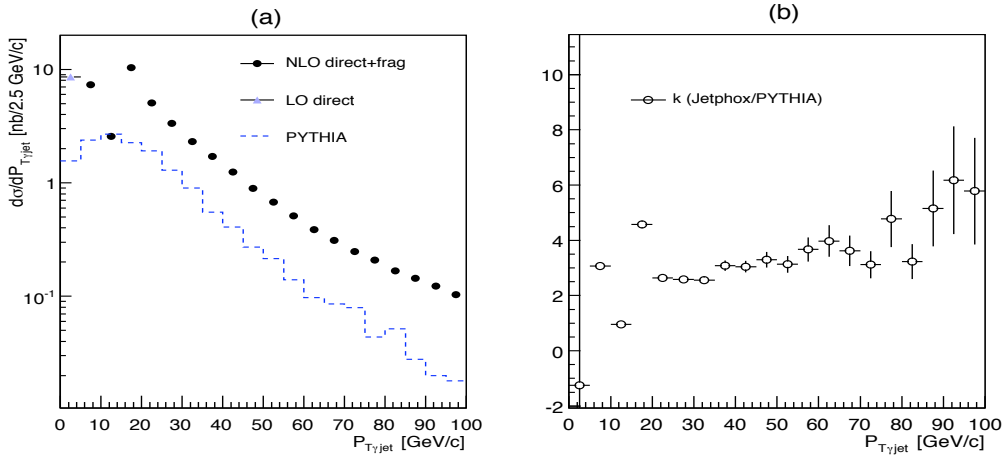

Figure 9.16: $P_T^{\gamma jet}$ distributions (a) of the NLO and LO D contributions of Jetphox and Pythia. The k-factor k is displayed in (b).

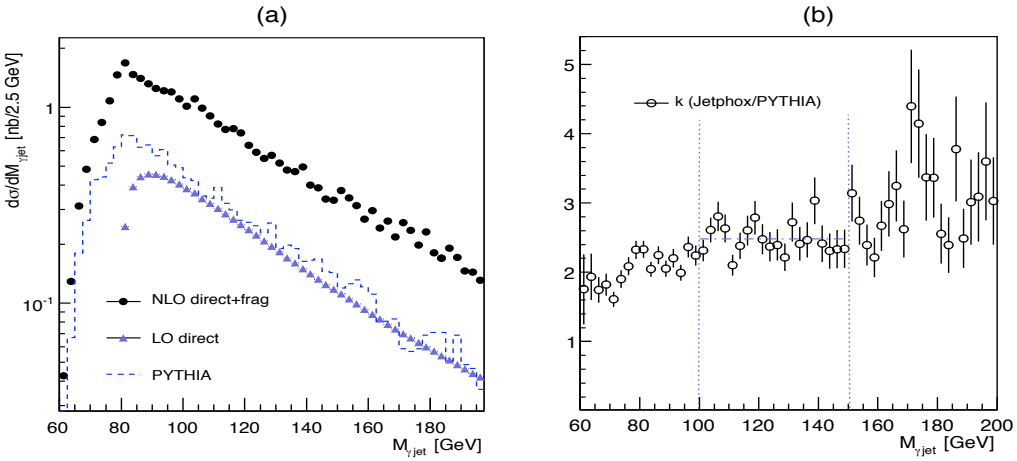

Figure 9.17: $M_{\gamma jet}$ distributions (a) of the NLO and LO D contributions of Jetphox and Pythia. The k-factor k is drawn in (b).

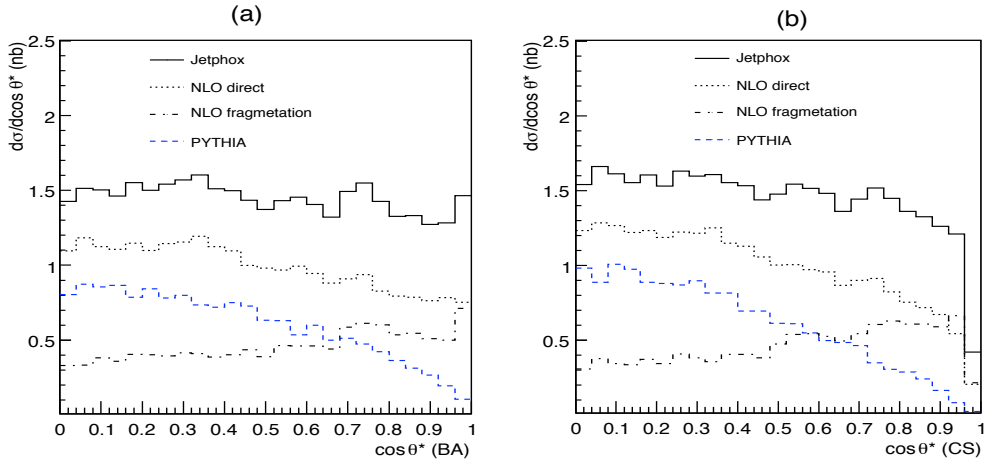

Figure 9.18: $cos\theta^*$ distributions for the Jetphox NLO and LO D contributions and for Pythia.

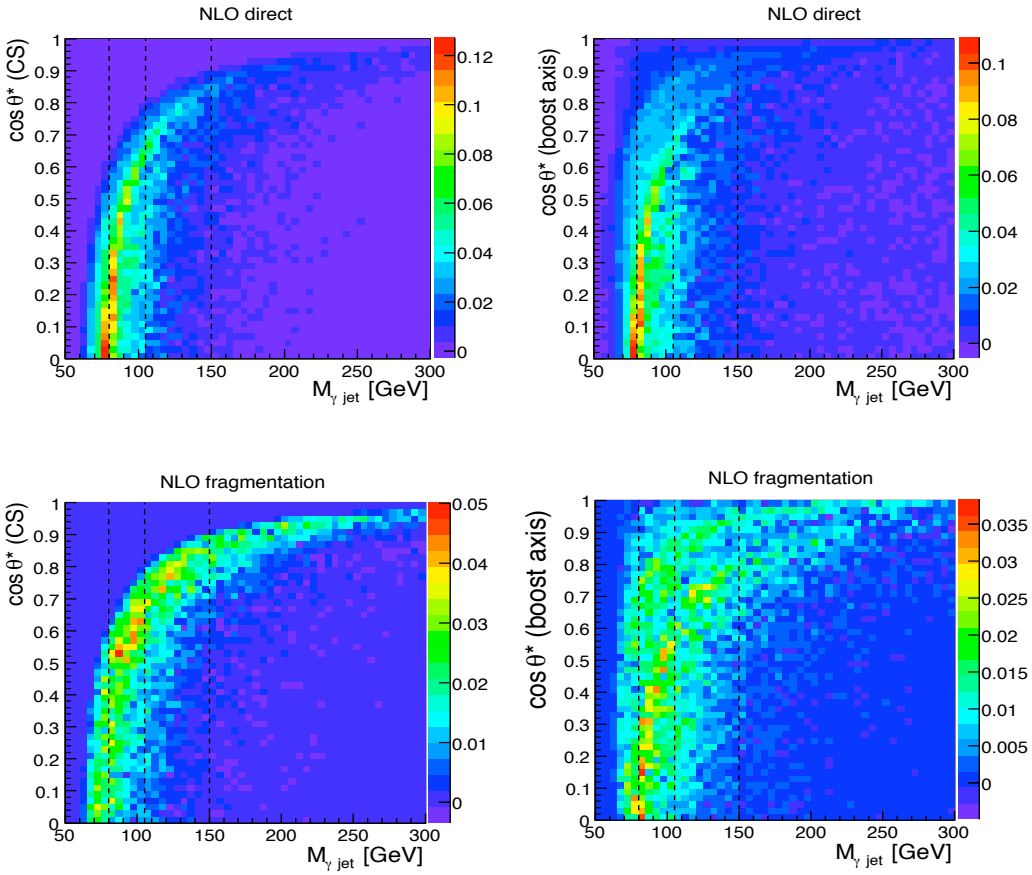

Figure 9.19: Jethox correlation between the invariant mass $M_{\gamma jet}$ and the $cos\theta^*$ (CS and BA). The dashed lines correspond to $M_{\gamma jet} = \{80, 105, 150\}\ GeV/c^2$.

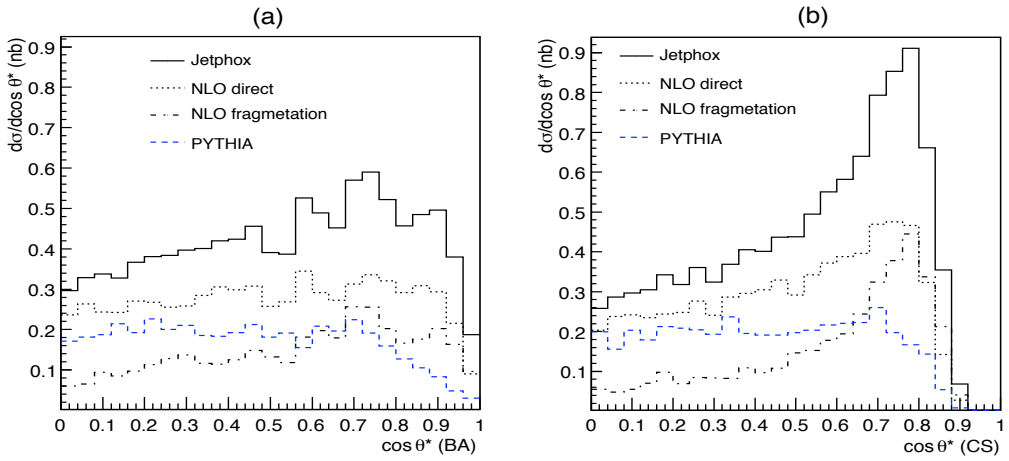

Figure 9.20: $cos\theta^*$ (BA and CS) distributions for Jetphox and Pythia when selecting the mass window: $105 < M_{\gamma jet} < 150\ GeV/c^2$.

Others potentially discriminating variables that are not used in the analysis are the longitudinal momentum of the γ-jet system $P_{T\gamma jet}$, P_{Tmin} the smallest of $P_{T\gamma}$ and P_{Tjet} and P_{Tmax} the greatest. The differential cross section corresponding to these variables and their corresponding k-factors are illustrated in Figure 9.21. In Jetphox, with two partons final state the jet is defined as the leading final-state parton if the two partons are well-separated in the (η, ϕ) plane or by the two partons clustered together if thus not isolated from each other. The final-state jet has generally a transverse momentum larger than that of the photon. This implies a similar behaviour of the $P_{Tmin}(P_{Tmax})$ and $P_{T\gamma}(P_{Tjet})$ distributions. The k-factor evaluated for a wide set of variables is rather stable. The instabilities occurring in the low transverse momenta region for $P_{T\gamma}$, P_{Tjet}, $P_{T\gamma jet}$ and P_{Tmin} result from discontinuities due the fixed-order ME calculation of Jetphox code. At first order the k-factor yields a fair normalization of the semi-reducible background prediction. It is however possible to take into account the differences in the shape of the discriminating variable either for a finer analysis or to assess a systematic uncertainty.

9.4 Refined normalization

The experimental signatures of light quark and gluon jets are quite different. In particular, their fragmentation functions into π^0 largely differ and gluon jets tend to be more massive and thus less isolated. As a consequence their rejection when applying photon identification (ID) cuts also differ. The gluon jet rejection is about 10 times larger [64] than that of a quark jet. The final distributions in the semi-reducible background are obtained using the Pythia γ-jet sample before applying stringent photon ID selections and applying a rejection factor instead. The gluon jet rejection factor should be applied to gluon-like jets and the quark rejection factor to quark-type jets. Similarly in order to correctly rescale the final distributions, the relative amounts of gluon and quark-like jets appearing at NLO and in the fragmentation processes should be taken into account.
In Jetphox processes are categorized based on their initial- and final-states. Using this infor-

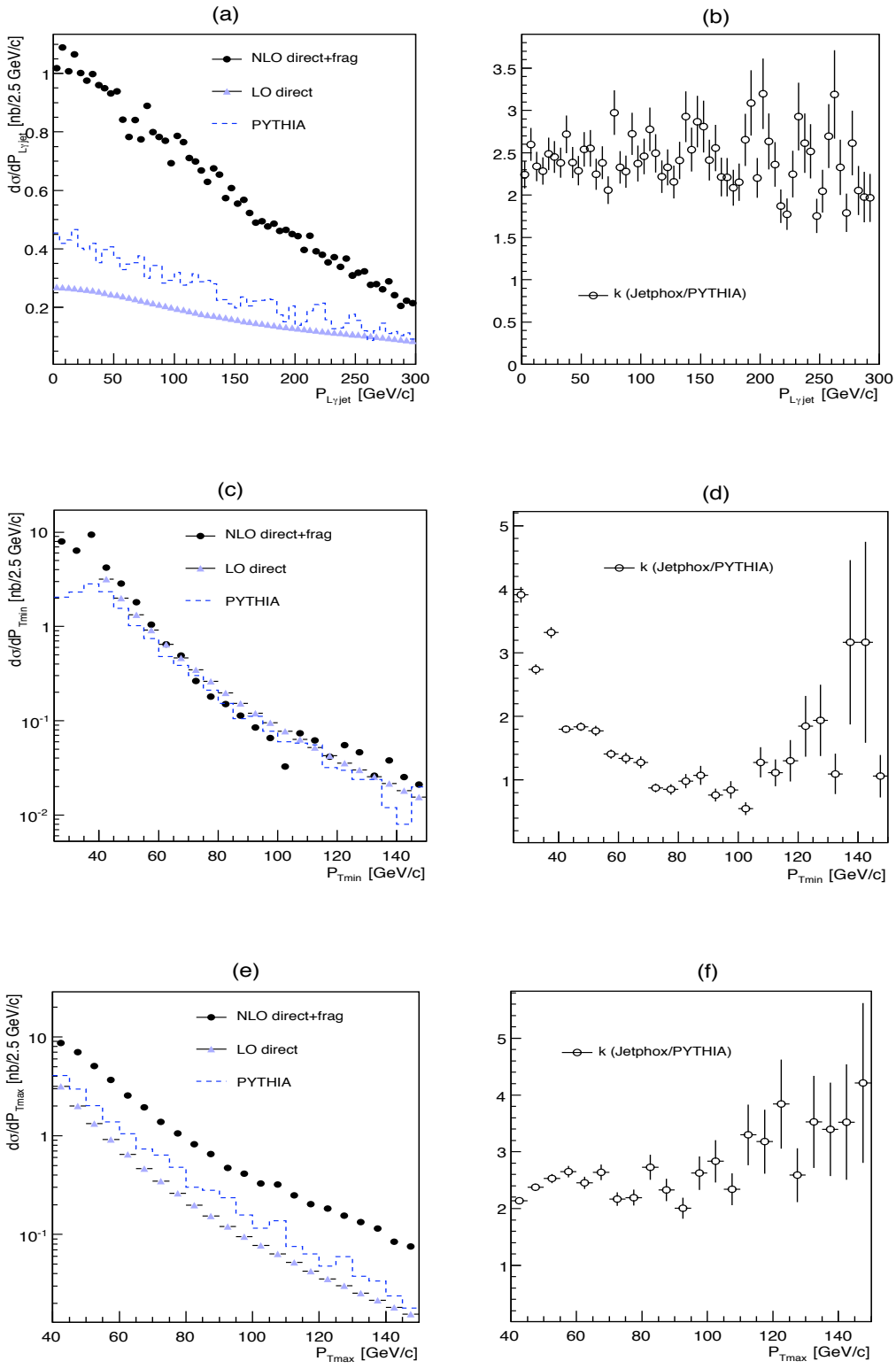

Figure 9.21: $P_L^{\gamma jet}$ (up), P_{Tmin} (middle) and P_{Tmax} (down) distributions (a) for Jetphox at NLO and LO D and for Pythia. The k are displayed in (b).

mation, processes can be divided into those dominated by gluon-like or quark-like jets:

(i) In the direct contribution, the processes with two different quarks in the initial-state only occur in the HO corrections (see for instance diagram 9.4(b)). As the two final-state partons are both quarks, this contribution is unambiguously quark-like.

(ii) When the two quarks correspond to a pair $(q_i, \overline{q_i})$ (diagrams 9.4(a-b), this contribution is at LO unambiguously gluon-like. HO corrections arise either with gluons emitted in the initial or final state, or in processes such as 9.4(a). In this case the final state is ambiguous (although it will be dominated by the jets of the gluon kind). The LO contribution amounts to more than than half the total cross section. Therefore this process is accounted for in the gluon category. Half of the HO contribution is taken as systematic uncertainty associated to the process classification.

(iii) For $q-g$ initial state (diagrams 9.4(c-d)), the HO corrections do not exceed 5% of the NLO cross section, this process is thus classified as quark-like and half of its HO contribution is accounted for as systematic uncertainty.

(iv) The two gluons initial-state processes (diagram 9.4(e)) is unambiguous gluon-like.

Similarly the fragmentation processes can be classified into quark and gluon kind. The diagrams 9.5(a,e & g) are gluon-like and the others are quark-like. Typically the direct processes are more of the quark kind and the fragmentation ones are more of the gluon kind.

9.4.1 Results

From the classification of subprocesses discussed above, two additive k-factors can be derived, each corresponding to the gluon and quark-like jets :

$$k_{quark} = \frac{\sigma^{NLO}_{D+F}(quark)}{\sigma^{LO}_{Pythia}} = 1.73 \pm 0.10$$
$$k_{gluon} = \frac{\sigma^{NLO}_{D+F}(gluon)}{\sigma^{LO}_{Pythia}} = 0.61 \pm 0.08$$

These k-factors are obtained when applying the $H \rightarrow \gamma\gamma$ standard cuts plus requiring the mass of the γ-jet system to be in the range $[80, 150]$ GeV/c^2. The uncertainties correspond to the possibility of mislabeling a jet as quark- or gluon-like[2)]. It is therefore fully correlated. The direct processes mostly contribute to k_{quark} ($\sim 90\%$), as it is itself dominated by the qg intial-state process, whereas the fragmentation is dominant in k_{gluon} ($\sim 80\%$). Among the processes contributing to k_{gluon}, the leading one is the qg intial-state (70%) and the process $gg \rightarrow g(g \rightarrow \gamma)$ represents 12%. The remaining 18% come from the $q\overline{q}$ initial-state processes in the direct contribution.

Using the aforementioned classification of processes it is also possible to study the different behaviours of the discriminating variables for both categories. Figure 9.22 displays the P_T^{γ}, P_T^{jet}, $P_T^{\gamma jet}$ and the $cos\theta^*$ (BA) distributions for the gluon-like and quark-like jet categories, separately and combined. The P_T^{γ}, P_T^{jet} and $P_T^{\gamma jet}$ distributions are all softer for the gluon-like

[2)] It also includes the statistical uncertainty associated to the Pythia sample.

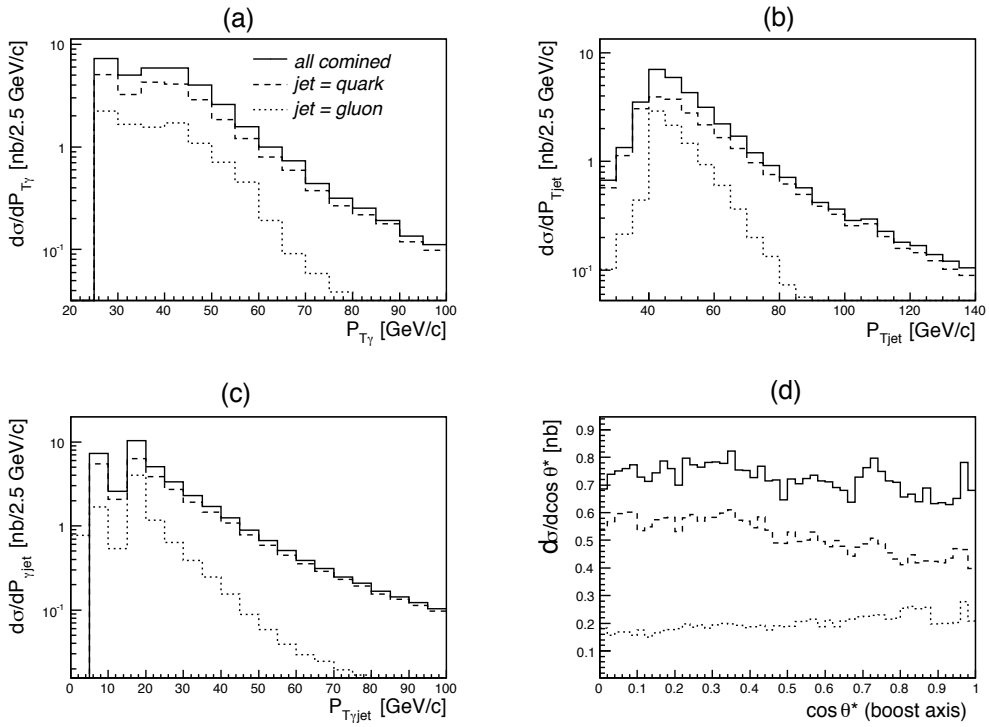

Figure 9.22: P_T^{γ} (a), P_T^{jet} (b), $P_T^{\gamma jet}$ (c) and $cos\theta^*$ (BA) (d) distributions at NLO for the quark-like and gluon-like jet categories.

jet category. In $cos\theta^*$, the two jet categories also display different behaviours. Since the gluons are more efficiently rejected, the shapes of the semi-reducible background will be closer to that of the quark-like category. For an accurate analysis of the discriminating power of the search, these differences should be taken into account.

9.4.2 Global k-factor

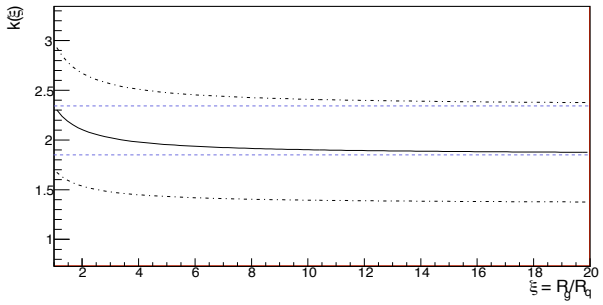

Figure 9.23: k-factor accounting for the quark and gluon rejection factors as a function of the ratio $\xi = \dfrac{R_g}{R_q}$. The dashed lines represent the upper and lower limit of k-factor values when ξ respectively tends toward low and high values.

The global k-factor formerly estimated of 2.35 ± 0.11 is a factor which is intended to normalize a sample of events generated by Pythia before the rejection factors on the stringent

photon identification cuts are applied (the relative amounts of quark-like and gluon-like jets in both the Pythia and the Jetphox estimates being those before photon identification). To properly apply a normalization factor to a Pythia sample when identification cuts on rejection factors are applied, the correct relative amounts of quark-like and gluon-like events should be taken into account. If $\sigma_{P,J}^{q,g}$ denotes the gluon and quark-like cross sections for Pythia (P) and Jetphox (J) and $R_{q,g}$ the rejection factors for gluon and quark jets, the k-factors to be applied can be written as follows:

$$k = \frac{R_q \sigma_J^q + R_g \sigma_J^g}{R_q \sigma_P^q + R_g \sigma_P^g} \tag{9.1}$$

Given that the Pythia sample (σ_P) is made of 93.55% of σ_P^q and 6.45% of σ_P^g, then

$$k = \frac{R_q \sigma_J^q + R_g \sigma_J^g}{(0.95 R_q + 0.05 R_g)\sigma_P} = \frac{R_q k_{quark} + R_g k_{gluon}}{0.9355 R_q + 0.0645 R_g} \tag{9.2}$$

The global k-factor then depends only on the gluon and quark-like k-factors and the ratio of the rejection $\xi = \frac{R_g}{R_q}$:

$$k = \frac{\xi k_{quark} + k_{gluon}}{0.9355\xi + 0.0645}$$

The k-factor is illustrated as a function of ξ in the range [1,20] in Figure 9.23.

When ξ tends toward 1, the k-factor tends approximatively to its initial value ignoring the gluon and quark-like jet categories. When $\xi \to \infty$, the k-factor tend toward $\frac{k_q}{0.9355} \sim 1.85$. The gluon and quark rejection factors calculated in [76] for jets with $E_T > 25\ GeV$, $R_g = 27500 \pm 2000$ and $R_q = 2760 \pm 100$ respectively, implies $\xi = 9.96 \pm 0.81$. The corresponding k-factor after photon identification cuts or rejection factors are applied is:

$$k = 1.90(1) \pm 0.19(7)$$

The systematic uncertainties associated to the quark-like and gluon-like k-factors are taken into account to evaluate the systematic uncertainties related to this global k-factor. The upper and lower dashed-dotted curves in Figure 9.23 correspond to the upward and downward variations of ξ due to the systematic errors detailed in the last section.

9.5 Systematic studies

Various sources of systematic uncertainties associated to the estimation of the k-factor are studied:

(i) To account for the incompleteness of the fixed-order calculation, both the renormalization (μ_R) and the factorization (μ_F) scales are varied, from $0.5 \times P_T^\gamma$ to $2 \times P_T^\gamma$. When assuming $\mu_R = \mu_F$, an overall variation of $\pm 5\%$ to the cross section is observed, while when varying independently these scales the resulting variation amounts to $\pm 20\%$.

(ii) To account for selection inaccuracy due to the fact that Jetphox is a parton level calculation. A relative variation of the total NLO cross section when varying the cuts (P_{Tmin}, P_{Tmax}) of $\pm 1\ GeV/c$ (roughly corresponding to the energy reconstructed resolution) around the central value (25,40) of $\pm 11\%$ is found.

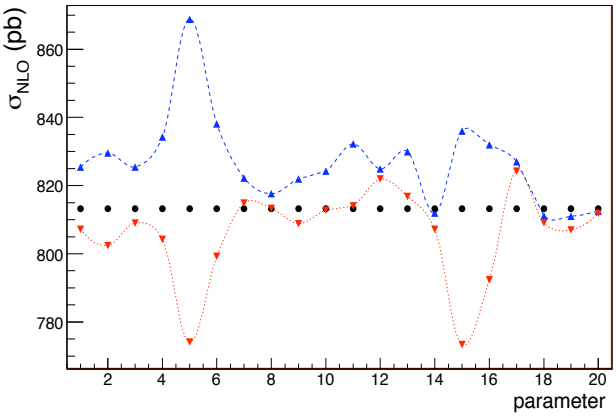

Figure 9.24: Variations of the NLO cross section when all 20 parameters of the parton distribution functions (CTEQ61) are varied independently. The upper and lower curves correspond to the upward and downward variations of parameters respectively.

(iii) Using the results of Table 9.2 obtained when varying the isolation criterion around the central value ($[\Delta R = 0.4, E_{Tmax} = 15\ GeV]$), a variation of $\pm 10\%$ on the total NLO cross section is observed.

(iv) The systematic uncertainty related to the PDFs is studied using Jetphox with the set of PDF CTEQ61 (an update version of CTEQ6M). The largest difference with respect to the central cross section value when varying the 20 parameters of the parton densities is around $\pm 7\%$.

(v) Two additional systematic checks of the Jetphox calculation lead to an overall $\pm 1\%$ systematic uncertainty: (a) when using different generation level cuts on the photon and the jet; (b) when the fragmentation scale μ_f is varied from $0.5 \times P_T^\gamma$ to $2 \times P_T^\gamma$ (the relative contribution of the fragmentation and the direct processes change but not the total cross section).

(vi) To account the difference between cross sections estimated from various sets of generation level cuts, a relative variation of the NLO cross section around $\pm 2.5\%$ is taken. It corresponds to a relative variation of the quark-like and gluon-like NLO cross sections respectively around 3.2% and 5.6%.

(vii) To evaluate the ambiguity when divided the Jetphox processes in quark-like and gluon-like categories, half of the HO contributions of ambiguous processes are accounted leading to an associated systematic uncertainty of around $\pm 5.5\%$ and $\pm 14\%$ respectively for the quark-like and gluon-like k-factors. The statistical uncertainty from the Pythia sample is also accounted for in this error.

The different sources of systematic uncertainties are listed in Table 9.4 for the global k-factor, the gluon-like and quark-like k-factors. The global k-factor for the semi-reducible background of the Higgs boson search in the di-photon channel is then:

$$\mathrm{k} = 2.34 \pm 0.61$$

Potential sources	relative uncertainty		
	k	k_{quark}	k_{gluon}
(i) Scale dependence	20%	20%	20%
(ii) Phase space	11%	11%	11%
(iii) Isolation	10%	10%	10%
(iv) pdf	7%	7%	7%
(v) Fragmentation scale	1%	1%	1%
(vi) MC generation	2.5%	3%	6%
(vii) process splitting	-	5.5%	14%
Total	$\sim 26\%$	$\sim 27\%$	$\sim 30\%$

Table 9.4: Summary of the relative systematic uncertainties on γ-jet production with Jetphox at NLO.

To illustrate the impact of systematic uncertainties on the semi-reducible background discriminating variables, the Pythia and Jetphox distributions are illustrated in Figures 9.25, 9.26 and 9.27(a). The associated ratios of the total NLO Jetphox differential cross section over the Pythia one are shown with their associated theoretical systematic in Figures 9.25, 9.26 and 9.27(b). A small mass window around the Higgs boson mass ($M_{\gamma\gamma} \in [115, 125]\ GeV/c^2$) is selected.

The gluon-like and quark-like k-factor are estimated as:

$$k_{quark} = \frac{\sigma^{NLO}_{D+F}(quark)}{\sigma^{LO}_{Pythia}} = 1.73 \pm 0.46$$
$$k_{gluon} = \frac{\sigma^{NLO}_{D+F}(gluon)}{\sigma^{LO}_{Pythia}} = 0.61 \pm 0.18$$

Assuming that the gluon jet rejection is about 10 times larger than that of a quark jet, the global k-factor is estimated as:

$$\mathrm{k} = 1.90 \pm 0.51$$

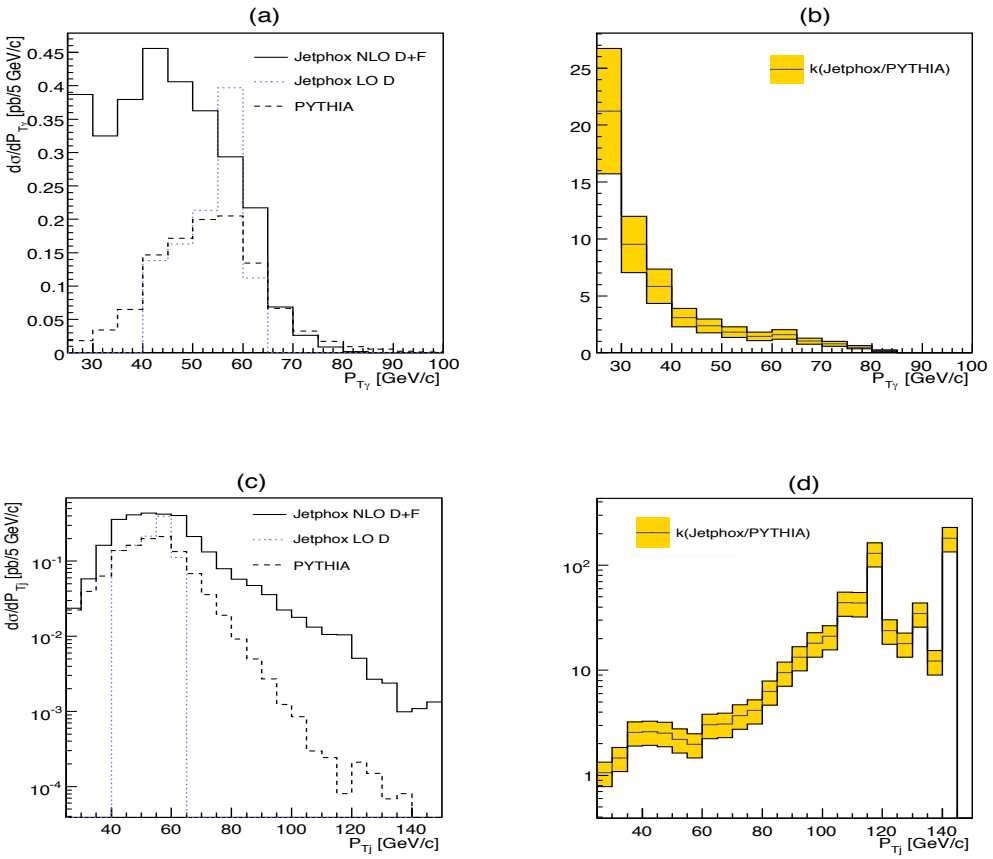

Figure 9.25: $P_{T\gamma}$ distributions (a) as generated with Jetphox, at NLO and LO (direct part only) and Pythia. (b): ratio of Jetphox NLO over Pythia differential cross sections with it associated systematic uncertainty. P_{Tjet} distributions (c) as generated with Jetphox and Pythia and the corresponding ratio (d) with it associated systematic uncertainty.

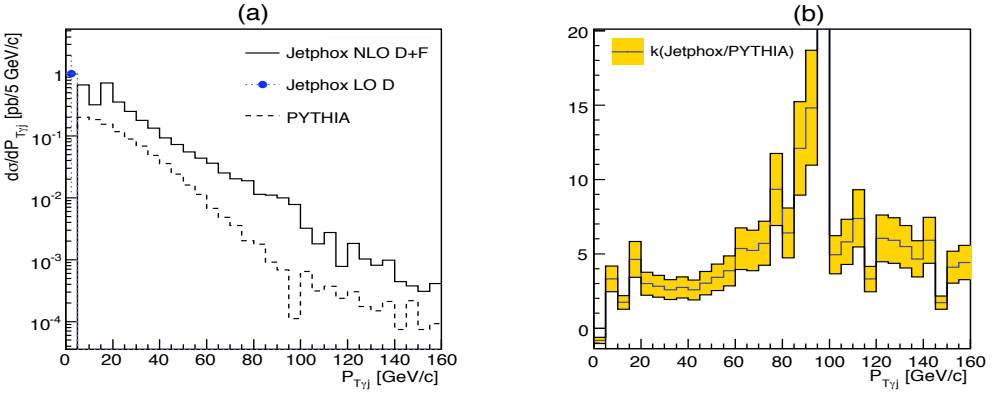

Figure 9.26: (a): $P_{T\gamma jet}$ distributions as generated with Jetphox, at NLO and LO (direct part only) and Pythia. (b): corresponding ratio with it associated systematic uncertainty.

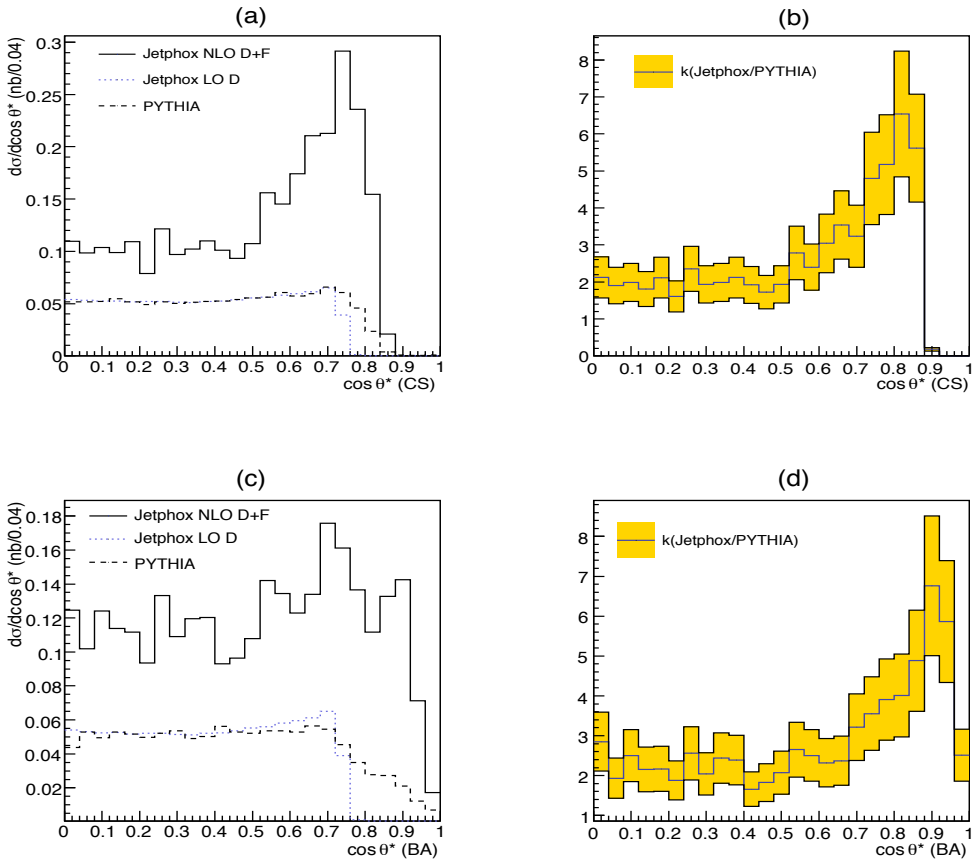

Figure 9.27: Top: $cos\theta^*_{CS}$ distributions (a) as generated with Jetphox, at NLO and LO (direct part only) and Pythia. (b): corresponding ratio with it associated systematic uncertainty. Bottom: $cos\theta^*_{BA}$ distributions (c) for Jetphox and Pythia and the corresponding ratio (d) with it associated systematic uncertainty.

Conclusion

This study presents a normalization scheme for the semi-reducible γ-jet background which accounts for both NLO corrections and the quarks and gluons fragmenting into photons is given. The NLO fixed-order Matrix Element calculation Jetphox was used to assess this correction. Its dependence on all relevant kinematic variables is studied to check that a simple normalization factor can be applied without altering the distributions of the discriminating variables. Some differences are observed, in particular between the direct and the fragmentation processes. However, these differences are not overwhelming and their impact on the sensitivity of the search can be easily assessed.

The normalization factor to be used to a sample of Pythia events before photon identification cuts are applied is 2.35.

A refined normalization scheme taking into account the quark and gluon nature of the final state jet ca, be used with a Pythia sample after photon identification cuts or rejection factors are applied. For a ratio of gluon to quark rejection factors of 10, the k-factor to be applied is

1.90.

Finally various sources of systematic uncertainties are identified leading to an estimate of this relative systematic error on the semi-reducible background of 26%.

Chapter 10

Prospect for Higgs Boson Exclusion in the $H \to \gamma\gamma$ channel

Introduction

This chapter presents the prospect for exclusion limit of the SM Higgs boson in the diphoton decay channel for the energy in the centre-of-mass of 10 TeV and a luminosity of 200 pb^{-1}. The simplest inclusive analysis is considered, only using the invariant mass as discriminating variable. The signal and background normalizations are derived at NLO. The statistical significance is computed for the Higgs boson mass hypotheses at 120, 130 and 140 GeV/c^2 with maximum likelihood method using Hfitter package. The results are extrapolated to 7 TeV energy and a luminosity of 1 fb^{-1} to estimate the sensitivity for a SM Higgs boson exclusion that can be achieved after the first LHC run phase (at the end of the year 2011).

10.1 Signal and Background Simulations

Different Monte-Carlo generators and programs are used to predict the the signal and background processes cross sections and differential cross-sections. In this study the signal and background normalizations are both computed at NLO. Although most of the tools used here were presented in the two previous chapters, some differences occur that lead to new normalizations.

10.1.1 Signal processes

Figure 10.1 displays the different Higgs boson production modes cross section as a function of the Higgs boson mass, computed at the best accuracy obtained for each mode.

The gluon fusion process, mainly produced through a top quark and W boson loop is the main Higgs boson production mode. It is simulated at LO by Pythia and Herwig MC generators and at NLO within the generator MC@NLO [88]. 3 samples generated with MC@NLO for the Higgs boson mass $m_H = \{120,\ 130 \text{ and } 140\}$ GeV/c^2 are used in this analysis.The NNLO(+NNLL) prediction for the gluon fusion process is achieved with programs such as hQt and HNNLO [104]. The second dominant mode of Higgs boson production is the vector boson fusion. This channel is essential in exclusive analysis, notably in the search of two photons

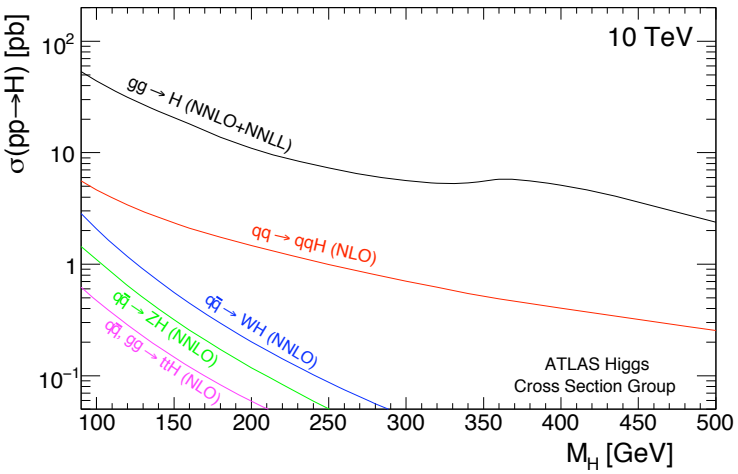

Figure 10.1: Cross section at different level of precision in QCD corrections for the different Higgs boson production modes at LHC with an energy in the centre-of-mass of 10 TeV, as a function the Higgs boson mass.

produced in association with two jets. The process is simulated at LO with Pythia and Herwig for a Higgs boson mass at 120 GeV/c^2. Different theoretical tools [105–107] are used to derive a normalization accounting for the NLO QCD corrections, the NLO EW corrections, the s-channel contribution (not included in Pythia and Herwig) and the Higgs boson decay branching ratio.

The other channels are the Higgs boson production in association with a weak boson and a top pair. There are simulated with Pythia for a Higgs boson mass at 120 GeV/c^2. The NLO QCD corrections to the associated production with a W or Z boson amounts to about 30% [108] . The NNLO QCD corrections have also been computed and amounts to 2 and 7% for the Higgs boson production respectively in association with a W and a Z boson [109]. The NLO EW corrections are also calculated and reduce the cross section of about 5% in both channels [110] . Finally the cross section of the associated production with a top pair is computed at NLO [111,112] and corresponds to an increase of about 30% the LO cross section.

Table 10.1 summarizes the NLO cross sections of the different Higgs boson production modes, at the three mass hypotheses considered in this analysis. The MC@NLO samples are used for the gluon fusion process, Herwig sample is used for the VBF process and Pythia samples are used for associated production modes. A weight is defined per event in these sample to normalize each data set at NLO and to an integrated luminosity of 200 pb^{-1}.

The branching ratio of the Higgs boson into two photons ($BR_{\gamma\gamma}$) is calculated with different programs. The HDecay program [90] computes the BR accounting for NLO QCD corrections (section 8.4.1). These results are corrected to account for EW corrections [104] that are small and of opposite sign of the QCD corrections, which therefore partially cancel these two effects. Table 10.2 lists the branching ratios used in this analysis.

process	$m_H = 120$ GeV/c^2	$m_H = 130$ GeV/c^2	$m_H = 140$ GeV/c^2
gg fusion	21.65 pb	18.61 pb	16.17 pb
VBF	2.40 pb	2.21 pb	2.03 pb
WH	1.15 pb	0.88 pb	0.69 pb
ZH	0.60 pb	0.47 pb	0.37 pb
$t\bar{t}H$	0.29 pb	0.23 pb	0.18 pb
TOTAL	26.09 pb	22.40 pb	19.44 pb

Table 10.1: Cross section of the different Higgs boson production modes, accounting for NLO QCD corrections, computed for the three Higgs boson mass hypotheses ($\sqrt{s} = 10\ TeV$).

	$m_H = 120$ GeV/c^2	$m_H = 130$ GeV/c^2	$m_H = 140$ GeV/c^2
$BR_{\gamma\gamma}$	2.18×10^{-3}	2.21×10^{-3}	1.91×10^{-3}

Table 10.2: Higgs$\rightarrow \gamma\gamma$ branching ratios at the Higgs boson mass hypotheses considered in this study.

10.1.2 Background processes

The Irreducible background

Different MC generators and programs are used to predict the three main processes of the irreducible background, that are the Born $q\overline{q} \rightarrow \gamma\gamma$, the bremsstrahlung $qg \rightarrow (q \rightarrow \gamma)\gamma$ and the Box $gg \rightarrow \gamma\gamma$ processes. As mentioned in Chapter 8, the Born and Box processes are relatively straightforward while the bremsstrahlung process requires a particular treatment of collinear and infrared divergences in the photon emission by the final-state quark.

The Born and bremsstrahlung processes are simulated with Alpgen, using the parton shower of Herwig. The LO matrix element of this process is implement in Alpgen with the possible emission of n=0..3 final state hard partons. The MLM prescription is used to avoid the double counting of events when switching on the showering process of Herwig. It is therefore used for its accurate treatment of jets and the benefit of the generator to produce reconstructed objets. The NLO normalization is derived with the use of Resbos and Diphox programs. Resbos notably provides a NLO prediction of the Born and bremsstrahlung cross section, including the one photon fragmentation contribution (at LO), and implements the resummation of soft gluons emission at initial-state, leading to a smooth and reliable shape of the transverse momentum of the diphoton pair, sensitive to such effect in the low region. Diphox is used for its accurate treatment of the fragmentation. It provides a NLO prediction of the Born and bremsstrahlung process with the account for the one and two photons fragmentation contributions at NLO.

The Box process is simulated with Pythia at LO. Resbos also calculates the NLO cross section of this process.

Two different technics are employed to normalize theses irreducible background processes: the Born and bremsstrahlung processes NLO cross section and differential cross section are obtained by an event-by-event reweighting of Alpgen fully simulated samples based on the transverse momentum of the diphoton pair, using Resbos spectrum. Resbos cross section is firstly rescaled to account for the fragmentation treatment performed in Diphox. The Box

process cross section and distributions are obtained with Pythia full simulated sample, rescaled by the Resbos NLO prediction.

The Reducible background

The reducible background is the production of a photon and a jet or multi-jet production with jet(s) reconstructed as photon(s). The prediction of the reducible background after it is "reduced" relies on the level of accuracy at which the initial cross section is predicted and on the abilities of the detector to reduce the amount of jets faking photons.

Pythia is used to generate fully simulated γ-jet and jet-jet samples. The Jetphox program provides a next-to-leading (NLO) fixed-order prediction of the differential cross-sections for the γ-jet processes, including the fragmentation of final-state partons into a leading photon. A normalization of the Pythia LO γ-jet prediction by the NLO prediction provided by Jetphox is used, accounting for the NLO with fragmentation fixed-order normalization of Jetphox, while keeping the benefits of Pythia as the primary event generator, as it incorporates full parton showering.

After photon identification and isolation, the remaining jets mis-reconstructed as photons are mainly jets that fragment into a leading π^0 or η meson. The jet rejection factors are calculated using the available fully simulated γ-jet and jet-jet MC samples. They are computed separately for jets originating from a quark or a gluon, to account for the differences in term of multiplicity and in the fragmentation shower shapes. After applying the rejection factors, the reducible background amounts to a third of the total background.

The jet-jet reducible background is simulated with Pythia at LO. There is no correction applied to the cross section.

***

The MC samples used for the signal and the irreducible and reducible background are listed in Tables 3 and 4 of [113]. The cross section, number of events and luminosity of these samples are also given in Table 5 of the same reference. They will be reminded when necessary.

10.2 Photon Selection

10.2.1 Photon Reconstruction

Photon candidates are reconstructed in the EM calorimeter of ATLAS in clusters drawn in the (η, ϕ) plane, of different size according to their η direction and their possible conversion in front of the calorimeter. In the barrel, the photon energy is the sum of the energy deposited in cells from a cluster of size 3×5 (per unit of Middle layer cell size, $\Delta\eta = 0.025$ and $\Delta\phi = 2\pi/256 \sim 0.025$) when the photon is unconverted and of size 3×7 when the photon converts. A larger cluster size in ϕ is chosen for converted photons to account for energy lost due to the spread of the electron and positron in ϕ induced by the magnetic field.

The photons are reconstructed in both the barrel and the end-cap parts although some fiducial cuts are applied to account for the EM calorimeter geometry. The barrel-endcap transition region, also called the crack region, arises at $\eta \sim 1.5$. This region is excluded, to prevent photons with less quality energy reconstruction. As well, the photons are required to have

a reconstructed pseudo-rapidity below the threshold of $\eta \sim 2.4$ given by the coverage of the Front end-cap layer. Finally, the photons are required to have a pseudo-rapidity in the range $|\eta| < 1.37 \cap 1.52 < |\eta| < 2.37$.

10.2.2 Photon Identification

The photon identification must provide an efficient reconstruction of the photons in the EM calorimeter and reject as much as possible jets. It is in particular crucial to reduce the jets faking photons in the γ-jet and jet-jet reducible backgrounds. The identification cuts use the hadronic leakage in the first layer of the hadronic calorimeter and the profile of the EM shower in the Middle layer. These variables are defined as:

- The normalized hadronic leakage:

$$R_{\text{had1}} = \frac{E_T^{\text{had1}}}{E_T} \tag{10.1}$$

  is the ratio of the transverse energy E_T^{had1} deposited in the first layer of the hadronic calorimeter to that of the electromagnetic cluster E_T. The transverse energy is defined by the relation $E_T = E/\cosh(\eta)$ where E and η are the reconstructed energy in the Middle and the η direction of the photon respectively. In the pseudo rapidity range $0.8 < |\eta| < 1.37$ (barrel part, electrode B) R_{had1} is replaced by R_{had}, the ratio of the transverse energy in the whole hadronic calorimeter to that of the EM cluster.

- The η energy ratio in the Middle compartment

$$R_\eta = \frac{E_{3\times7}^{S2}}{E_{7\times7}^{S2}} \tag{10.2}$$

  which corresponds to the ratio of the sum $E_{3\times7}^{S2}$ of the energies deposited in the Middle layer cluster of size 3×7 per cell unit to that of the sum $E_{7\times7}^{S2}$ of the energies deposited in a cluster containing 7×7 cells, both centered around the cluster seed.

- The ϕ energy ratio in the Middle layer

$$R_\phi = \frac{E_{3\times3}^{S2}}{E_{3\times7}^{S2}} \tag{10.3}$$

  is the ratio between the energy deposited in 3×3 cluster in the Middle and the sum $E_{3\times7}^{S2}$ of the energies of the Middle layer in a 3×7 tower, both centered around the cluster seed. The discriminating power of this variable is however reduced for converted photon due to the spread in ϕ.

- The width of the EM shower in the Middle layer

$$w_2 = \sqrt{\frac{\sum E_i \eta_i^2}{\sum E_i} - \left(\frac{\sum E_i \eta_i}{\sum E_i}\right)^2} \tag{10.4}$$

  measures the lateral shower width in the Middle layer, in a window $\eta \times \phi = 3 \times 5$, by weighting each cell by the energy deposited in it.

The jets are largely rejected using these photon identification criteria. The remaining jets faking photons contain mainly a leading π^0. The use of the thin longitudinal segmentation of the first compartment of the EM calorimeter, the Front, is needed to reject these jets. The variables are defined as:

- The side energy ratio in the Front layer

$$F_{\text{side}} = \frac{E(\pm 3) - E(\pm 1)}{E(\pm 1)} \tag{10.5}$$

  where $E(\pm n)$ is the energy deposited in the $\pm n$ neibhor cell of the Front (strips, $\Delta\eta = 0.025/8$ in the barrel part) around the cell with the largest energy, in the η direction. This ratio measures the shower profile in the first EM layer.

- The lateral width (3 strips) in the Front compartment

$$w_{s3} = \sqrt{\frac{\sum E_i (i - i_{\max})^2}{\sum E_i}} \tag{10.6}$$

  measures the shower width in the Front layer in a three strips region around the cell of maximum deposited energy. $i_{\max}$ corresponds to the cell of greatest deposited energy.

- The lateral width (total) in the first EMC layer, $w_{s,\text{tot}}$, is similar to the previous variable w_{s3} except that it measures the shower width in a window $\Delta\eta \times \Delta\phi = 0.0625 \times 0.2$, corresponding to approximately 20 strip cells in η and 2 in ϕ.

- The energy difference

$$\Delta E = E^{S1}_{2^{\text{nd}}\text{max}} - E^{S1}_{\text{min}} \tag{10.7}$$

  is the difference between the energy of the strips cell with the second greatest energy $E^{S1}_{2^{\text{nd}}\text{max}}$ and the energy E^{S1}_{min} in the strip cell with the smallest deposited energy located between the greatest and the second greatest energy.

- The rescaled second maximum energy

$$R_{max2} = \frac{E^{S1}_{2^{\text{nd}}\text{max}}/\text{MeV}}{1000 + 0.009 E_T/\text{MeV}} \tag{10.8}$$

  is the ratio between the second greatest energy $E^{S1}_{2^{\text{nd}}\text{max}}$ of the strip cells and a monotonic function of the total transverse energy E_T. It measures the relative difference between the maximum of energy deposited in a cell and the second maximum in the cluster.

These variable are particularly useful to distinguish the two energy maxima caused by photons from a meson decay and a single photon and therefore provide a powerful γ/π^0 discrimination.

The tight photon identification is based on a series of cuts using the EM shower shape properties in the different layers of the EM calorimeter and the hadronic leakage. These optimal cuts are computed separately for the unconverted and converted photon, to account for their different shower profile. The values of the different cut variables are derived, accounting for

possible correlation with each other, such that the optimal set of variables gives the lowest background (jet faking photon) efficiency for a given signal (photon) efficiency. The optimization is performed in seven η range[1)] and five bins in the photon transverse momentum P_T[2)].

Finally, the photon identification, commonly called *isEM*, has an efficiency of about 85% for photon with $P_T > 20$ GeV/c. Tables 10.3 and 10.4 illustrate the efficiency measured in signal and background samples for photons with a P_T greater than 25 GeV/c and 40 GeV/c respectively. Pythia fully simulated samples are used, including the gluon fusion and VBF processes for the signal and the Born and bremsstrahlung processes for the irreducible background. The efficiencies are defined by the ratio of the number of photons passing the identification criteria to that of reconstructed photons that match with a true photon (in the MC) from the Higgs boson decay and a prompt photon (or a radiated photon in case of bremsstrahlung) for the background. The photons are also required to have a pseudo-rapidity reconstructed in the acceptance region.

Sample	Efficiency (%)		
	all photons	unconverted	converted
$H \to \gamma\gamma$	90.55 ± 0.07	88.80 ± 0.09	94.22 ± 0.10
γ-jet	87.26 ± 0.04	85.20 ± 0.03	91.26 ± 0.03
$\gamma\gamma$	85.57 ± 0.15	83.60 ± 0.20	89.63 ± 0.23

Table 10.3: Tight photon identification efficiencies for photons with $P_T > 25$ GeV/c and reconstructed in the acceptance region, computed for signal, $\gamma\gamma$ and γ-jet background samples.

Sample	Efficiency (%)		
	all photons	unconverted	converted
$H \to \gamma\gamma$	91.87 ± 0.07	90.11 ± 0.10	95.62 ± 0.10
γ-jet	91.35 ± 0.03	89.20 ± 0.04	95.64 ± 0.03
$\gamma\gamma$	91.13 ± 0.25	88.82 ± 0.33	95.91 ± 0.30

Table 10.4: Photon identification efficiencies for photons with $P_T > 40$ GeV/c and reconstructed in the acceptance region, computed for signal, $\gamma\gamma$ and γ-jet background samples.

The different efficiencies for signal and background samples as observed in Table 10.3 but not in Table 10.4 are explained by the lower threshold on the photon transverse momentum. In signal events, the Higgs boson decays into two prompt photons while in the background, the photon is produced either directly or is radiated by a final-state parton. The angular separation between the photon and the parton is wider at small P_T inducing a more important activity around the photon. This justifies the better efficiency observed in the signal (and in the reducible background) with respect to $\gamma\gamma$ background, and the better efficiency found in Table 10.4 for larger P_T. A better efficiency is found for converted photons in each sample due to the reconstruction of the conversion vertex in the ID.

[1)] [0–0.6, 0.6–0.8, 0.8–1.15, 1.15–1.37, 1.52–1.81, 1.81–2.01, 2.01–2.37]

[2)] [20–30, 30–40, 40–60, 60–80, >80] GeV/c

10.2.3 Photon Isolation

After applying the photon identification selection, the remaining jets faking photon mainly contain one high energy π^0 and low P_T tracks around its direction.To further reduce the γ-jet and jet-jet background a track-based photon isolation is defined using the sum of the transverse momentum of tracks $\sum_{Trks} P_T$ located in a cone around the photon. Tracks with $P_T > 1GeV/c$ located in a ring $0.1 < \Delta R < 0.3$ around the photon direction are considered. The lower limit is made to avoid counting tracks from a converted photon in the sum. The tracks are required to have at least one hit in B-layer and seven hits in the Pixel+SCT device. A cut is also applied on their impact parameter, required to be smaller than 1 mm. The choice of the cut to applied on $\sum_{Trks} P_T$ is based on getting the better background rejection for an efficient signal selection. The rejection and efficiency are computed for truth and fake photons being in the acceptance region and with $P_T > 25\ GeV/c$. The $\sum_{Trks} P_T$ threshold is chosen optimal when the highest significance $S/\sqrt{B}$ is achieved, assuming the background B to be $\gamma\gamma$ and γ-jet events. In the CSC note, the cut $\sum_{Trks} P_T < 4\ GeV/c$ was chosen. The same cut is applied in this analysis, showing close performances. An efficiency of 99.2% is found for the signal and a background rejection factor of 1.6 is achieved. Figure 10.2(a) displays the rejection factor as a function of the signal efficiency obtained with Pythia samples. The red points correspond to the inclusive significance computed for different $\sum_{Trks} P_T$ thresholds, while the green and blue points correspond to the rejection of jets originating from gluons and quarks, respectively. A better rejection of the gluon-like jet than for a quark-like jet is found for a given signal efficiency. This is explained by the different fragmentation of quark and gluon. The gluon initiates a shower with a larger width and is therefore more rejected. After applying the photon identification selection, jets mainly contain a leading π^0. Figure 10.2(b) illustrates the distribution of the quark and gluon probability of fragmentation into a π^0 as a function of z, the fraction of momentum of the parton carried by the π^0. Less gluons fragment at large z which corresponds to the region of the remaining jets. The jet-jet background rejection has also been computed and shows equivalent result for the same cut $\sum_{Trks} P_T < 4\ GeV/c$.

10.2.4 Jet rejection

The identification and isolation cuts on photon have been optimized to reject a large fraction of jets, based on the profile, width and energy deposit of the photon shower. The rejection factor is defined as:

$$R = \frac{N_{jets}}{N_{fake\ \gamma}} \tag{10.9}$$

N_{jets} is the total number of jets produced in the acceptance region and $N_{fake\ \gamma}$ the fraction of jets that passe the photon identification and isolation criteria. The full simulated sample is produced with a filter at the generation level, based on cuts on the transverse energy of the jet and its pseudo-rapidity (see Table 4 of [113]). The total number of jets must be estimated from the initial number of jets produced in the background samples, before any selection cuts.

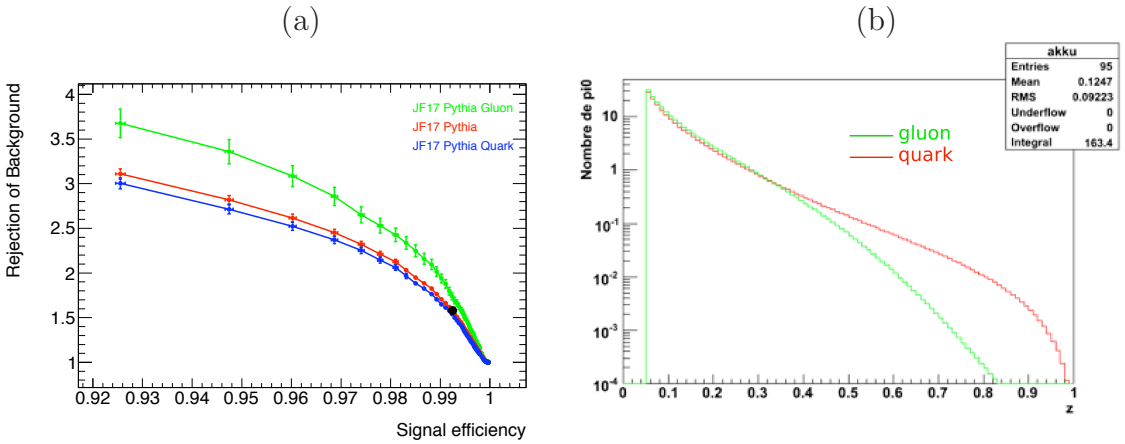

Figure 10.2: (a): Background rejection versus signal efficiency computed with Pythia γ-jet sample in red, for the jets originating from gluon or quark in green and blue respectively. The back point represents the selected threshold $\sum_{Trks} P_T < 4\ GeV/c$. (b): Quark and gluon probability of fragmenting into a π^0 as a function of $z = E_{\pi^0}/E_{q,g}$.

A high statistics sample is therefore required and must be obtained from a sample unfiltered at the generation level. The numbers of fake photons are obtained from fully simulated samples where the photon selection is applied. The jet rejection factor is re-expressed as:

$$R = \frac{N_{jets}^{unfilt}}{N_{fake\ \gamma}^{filt}} \frac{N_{event}^{filt}}{N_{event}^{unfilt}} \frac{1}{\epsilon_{filt}} \tag{10.10}$$

The total number of jets in the unfiltered sample N_{jets}^{unfilt} is normalized to the total number of events from the unfiltered sample N_{event}^{unfilt}. The number of jets faking photon in the filtered sample $N_{fake\ \gamma}^{filt}$ is normalized to the number of events from the filtered sampleN_{event}^{filt}, accounting for the filter efficiency ϵ^{filt}.

The rejection factors are computed in Pythia γ-jet and jet-jet samples and Herwig jet-jet sample. The rejections are given for all jets and separately for jets originating from quark or gluon in Tables 10.5 and 10.6, for jets with a transverse energy $E_T > 25\ GeV$ and $E_T > 40\ GeV$ respectively.

As mentioned above the jets of gluon are more rejected because of their larger shower profile (with respect to jets originating from a quark). The statistical uncertainties reflect that the gluons are dominant in the jet-jet sample while the quarks dominate in γ-jet events [114]. Differences arise in both quark and gluon rejection factors computed with Pythia and Herwig γ-jet samples. This is explained by the different fragmentation model implemented in the two generators. The showering process in Pythia relies on the tension connecting the proton remnants to the parton from the hard process while the process evolution in Herwig is performed by clustering the partons emitted from the hard process and then creating the hadrons and mesons from clusters decay.

	sample	generator	all	quark-jet	gluon-jet
Rejection	jj	Pythia	7777 ± 122	2517 ± 50	27218 ± 941
		Herwig	3398 ± 79	933 ± 25	16092 ± 940
	γj	Pythia	1929 ± 44	1657 ± 38	25846 ± 4361

Table 10.5: Jet rejections for all jets, jets originating from quark and gluon separately, from γ-jet and jet-jet samples, for $E_T > 25$ GeV. The errors are statistical only.

	sample	generator	all	quark-jet	gluon-jet
Rejection	jj	Pythia	8659 ± 362	2894 ± 141	40008 ± 3850
		Herwig	3323 ± 190	959 ± 61	24983 ± 4544
	γj	Pythia	2321 ± 106	2048 ± 96	38768 ± 17484

Table 10.6: Jet rejections for all jets, jets originating from quark and gluon separately, from $\gamma-$jet and jet-jet samples, for $E_T > 40$ GeV. The errors are statistical only.

10.3 Diphoton Pair Selection

10.3.1 Trigger Selection

The three step trigger selection chosen in this analysis is *2g20_loose*. The Level 1 trigger is *L1_2EM18*. A first selection of electromagnetic (photons and electrons) candidates is made by requiring the transverse energy deposited in $\Delta\eta \times \Delta\phi = 0.2 \times 0.2$ trigger towers to pass the threshold $E_T \gtrsim 18\ GeV$. Regions of Interest (RoI) are defined and treated at the second trigger level, *L2_2g20_loose*. The information contained in RoI is treated with the granularity of the detector. The photons selection is refined using a subset of photon identification variables described above, based on the hadronic leakage, the energy deposited and shower profile and width in the Middle and the Front compartment of the EM calorimeter. A large fraction of jets are rejected at that step. When the photons pass the level 2 trigger, the event filter *EF_2g20_loose* refines the selection. There is no isolation criteria required at the trigger level.

The trigger efficiency is compared to the offline selection (photon identification selection only) for signal and $\gamma\gamma$ and γ-jet background samples. The analysis cuts are applied on photon pair candidates (see next paragraph). Table 10.7 summarizes the trigger efficiency with respect to offline selection found and show results close to 100% as expected.

Sample	Efficiency (%)		
	L1_2EM18	L2_2g20_loose	EF_2g20_loose
$H \to \gamma\gamma$	99.98 ± 0.01	99.97 ± 0.01	99.86 ± 0.01
$\gamma\gamma$	99.96 ± 0.03	99.96 ± 0.03	99.83 ± 0.06
γj	99.84 ± 0.07	99.68 ± 0.09	99.19 ± 0.15

Table 10.7: Efficiency of the *2g20_loose* trigger items with respect to offline selection, measured on $H \to \gamma\gamma$, $\gamma\gamma$, γ-jet events.

10.3.2 Analysis Cuts

The photon pair candidates that pass the photon identification and isolation selections are kept in this analysis when passing the standard analysis cuts:

1. the reconstructed pseudo-rapidity of the two photons must be in the acceptance region $|\eta| < 1.37 \cap 1.52 < |\eta| < 2.37$.

2. the two highest transverse momentum photons are selected, the leading photon is required to have $P_T^{lead} > 40\ GeV/c$ and the sub-leading $P_T^{sub-lead} > 25\ GeV/c$.

10.3.3 Reconstruction of the Primary Vertex

When photon pair candidates pass the above selection, the invariant mass of the system is reconstructed using the photons kinematic information contained in the formula:

$$M_{\gamma\gamma} = \sqrt{2E_T^1 E_T^2[\cosh(\eta_1 - \eta_2) - \cos(\phi_1 - \phi_2)]} \tag{10.11}$$

where η_1, η_2 are the pseudo-rapidities, ϕ_1, ϕ_2 the azimuthal angles and E_T^1, E_T^2 the transverse energies of the photons. The η_1 and η_2 directions depend on the longitudinal position z of the primary vertex. For unconverted photons or converted photons with no hits in the SCT detector, the pseudo-rapidity of the photon is reconstructed with the so-called calorimeter pointing method, which draws a straight line in the (R,z) plane joining the energy barycentre of the EM shower in the Front and Middle layers. The primary vertex longitudinal position is given by z_{calo}. A more accurate estimation of z is achieved when the photons have converted and the tracks have at least one hits in the SCT. In that case the pseudo-rapidity is given by the straight line joining the conversion vertex to the energy barycentre of the Front layer. The longitudinal position is called $z_{calo+ID}$. This reduces the error on the primary vertex z position to approximatively 17 mm. The computation of the $z_{calo+ID}$ position is done using the likelihood given by the formula:

$$\mathcal{L}_{calo+ID}(z) = e^{-\frac{z^2}{2\sigma_{IR}^2}} \times e^{-\frac{(z-z_{calo+ID})^2}{2\sigma_{z_{calo+ID}}^2}} \times \frac{1}{e^{-\frac{z^2}{2\sigma_{IR}^2}}}\ . \tag{10.12}$$

The first term is the probability of having a hard process vertex z considering its mean value $z = 0$ and its uncertainty $\sigma_{IR} \approx 56\ mm$; the second factor is the probability of $z_{calo+ID}$ with its uncertainty $\sigma_{z_{calo+ID}}$; the third factor is the inverse of the probability of having a MB vertex z considering its mean value $z = 0$ and its uncertainty σ_{IR}.

At high luminosity scheme, the accurate estimation of z is more difficult because of the secondary vertices induced by minimum bias events. A detail study of the tracks information in minimum bias (MB) and signal (Higgs boson) events has been performed in [76]. It has been observed that the sum of the square of the tracks transverse momentum at MB and Higgs boson vertices shows the best discriminating power. This variable is used in a likelihood of the form:

$$\mathcal{L}_{P_T^2}(z) = \frac{Prob_H(z|P_T^2)}{Prob_{MB}(z|P_T^2)} \tag{10.13}$$

where $Prob_H(z|P_T^2)$ and $Prob_{MB}(z|P_T^2)$ are the probability of the vertex z, according to the sum of P_T^2 of the tracks in the MB event, for the Higgs boson hypothesis and for the MB hypothesis respectively.

The method employed to provide the best estimation of the common z position to the two photons is based on likelihood combining the EM calorimeter and Inner Detector information. The combined likelihood is given by the formula:

$$\mathcal{L}(z) = \mathcal{L}_{P_T^2}(z) \times \mathcal{L}_{calo+ID}(z) \tag{10.14}$$

The common z position for the two photons is obtained by using the likelihood output z value and error for each photon and the dispersion $\sigma_{IR} \approx 56\ mm$ on the longitudinal interaction point position:

$$Z_{common} = \frac{\frac{z_1}{(\sigma(z_1))^2} + \frac{z_2}{(\sigma(z_2))^2}}{\frac{1}{(\sigma(z_1))^2} + \frac{1}{(\sigma(z_2))^2} + \frac{1}{(\sigma_{IR})^2}} \tag{10.15}$$

The η_1 and η_2 directions of the photons are recomputed assuming this common vertex as the origin of the photons. The invariant mass of the diphoton pair is then calculated using these refined pseudo-rapidities.

10.4 Signal and Background Normalizations and diphoton invariant mass

10.4.1 Results for the Signal

Different Higgs boson mass hypotheses are considered in the study, m_H = 120, 130 and 140 GeV/c^2. The samples of signal events after selection of the diphoton pair candidates are normalized to an equivalent integrated luminosity $\mathcal{L} = 200\ pb^{-1}$. Table 10.8 summarizes the reconstruction efficiency found in the different signal samples, after the photons identification and isolation selection and analysis cut selection are performed. The expected numbers of events per Higgs boson production channel and per mass hypothesis are also given. As mentioned above, only gluon fusion samples have been produced for the mass hypotheses at 130 and 140 GeV/c^2. The numbers at these masses for the other channels are obtained by applying the efficiency ratio found in the gluon fusion for the case $m_H = 120\ GeV/c^2$ to that of 130 and 140 GeV/c^2 cases (assuming this ratio equivalent for other processes).

About five events are expected for a Higgs boson at 120 GeV/c^2 and a luminosity of 200 pb^{-1} at 10 TeV.

The reconstructed invariant mass is parametrized by a Crystal-Ball function, as described in the statistic analysis related section. This inclusive analysis only uses the invariant mass as kinematic variable, the transverse momentum of the diphoton pair is for instance not considered.

10.4.2 Irreducible background

The background is considered in a mass window large enough to contain the tails of the signal distribution for the different mass schemes: $100 < M_{\gamma\gamma} < 150\ GeV/c^2$. Different MC generators and programs are used to assess the NLO prediction and the distribution of the diphoton invariant mass of the irreducible background. The reweighting procedure (described in Chapter 8) is

production process	$m_H = 120\ GeV/c^2$		$m_H = 130\ GeV/c^2$		$m_H = 140\ GeV/c^2$	
	efficiency [%]	N_{evts}	efficiency [%]	N_{evts}	efficiency [%]	N_{evts}
ggH	44	4.15	46	3.78	48	2.96
VBF	57	0.48	60	0.47	62	0.39
$W(\to jj)H$	51	0.13	53	0.11	56	0.07
$W(\to l\nu)H$	55	0.07	58	0.05	60	0.04
$Z(\to jj)H$	52	0.07	54	0.06	57	0.04
$Z(\to \nu\bar{\nu})H$	56	0.02	59	0.02	61	0.01
$Z(\to ll)H$	55	0.01	58	0.01	60	0.01
ttH	46	0.05	48	0.04	50	0.03
Total		4.98		4.54		3.56

Table 10.8: Reconstruction efficiencies and expected number of signal events for an integrated luminosity $\mathcal{L} = 200\ pb^{-1}$. The latter are obtained accounting for the reconstruction efficiencies, the filter efficiencies of the different samples used, the NLO cross sections of the different processes and the branching ratios for different Higgs boson mass hypotheses.

employed for the Born and bremsstrahlung processes contribution while a usual normalization is applied to the Box process.

The Reweighting Procedure

Using Alpgen as a generator but accounting for the more accurate features of Resbos, a reweighting procedure based on the generated momentum of the diphoton pair $P_{T\gamma\gamma}$ is proposed, in the same spirit of what devised in Chapter 8. Given that the treatment of the photon-fragmentation is present in Diphox but not in Resbos, a preliminary correction of the Resbos sample is performed before the reweighting procedure. Figure 10.3(a) shows the NLO $P_{T\gamma\gamma}$ spectra obtained with Diphox (both direct and fragmentation contributions at NLO) and Resbos. The distribution corresponding to the NLO fragmentation contribution of Diphox is also illustrated (dashed histogram in Figure 10.3(a)). The Diphox and Resbos $P_{T\gamma\gamma}$ shapes agree reasonably well, and the relative difference between their cross-sections is 11%. The integrated singularity arising for $P_{T\gamma\gamma} \sim 15$ GeV/c in the Diphox spectrum is a feature of its fixed order calculation when $P_{T\gamma\gamma} = E_T^{max}/c$, where E_T^{max} is the maximal transverse energy allowed in a cone of 0.4 around the photon (see Section 8.5).

The fragmentation contributes to 40% of the total cross-section of Diphox. In Resbos, it consists in the LO one photon-fragmentation contribution while Diphox also has the higher order corrections of the one photon-fragmentation contribution and the NLO two photon-fragmentation contribution. These last contributions can be used to reassess the Resbos cross-section. It contributes to 20% of the Diphox total cross-section. As shown in Figure 10.3(b), the fragmentation correction from Diphox is relatively independent of the $P_{T\gamma\gamma}$, except around the singularity at 15 GeV/c. Moreover, this correction does not depend on $M_{\gamma\gamma}$, although it is not shown here. This justifies the rescaling of the Resbos cross-section, before the reweighting

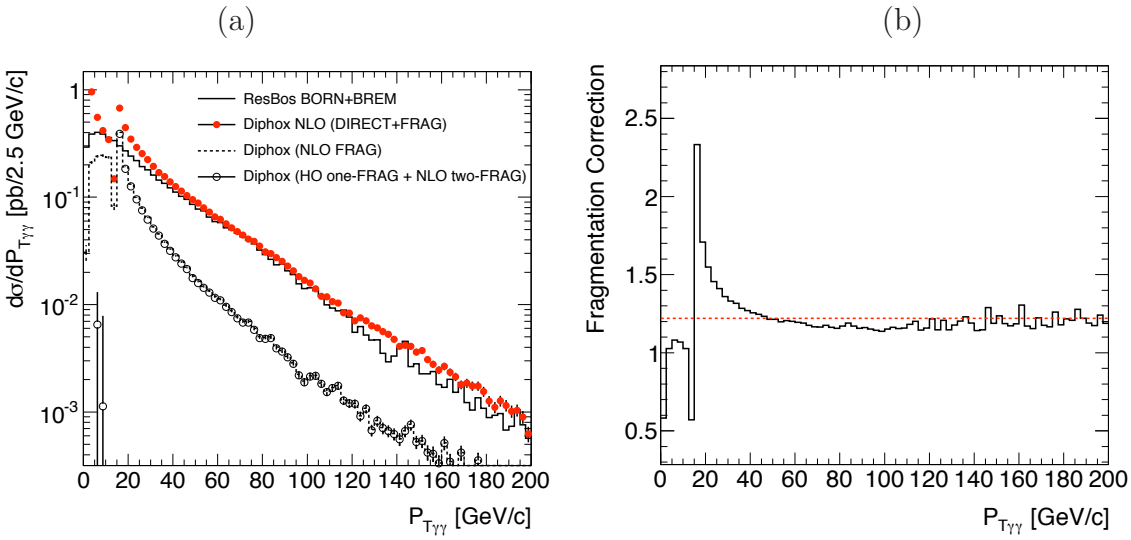

Figure 10.3: (a): Diphox and Resbos $P_{T\gamma\gamma}$ distributions for the Born and bremsstrahlung contributions. The NLO fragmentation contribution of Diphox is represented by the dashed histogram while the part from this contribution that is not included in Resbos is represented with open circles: it corresponds to the higher correction (HO = NLO - LO) of the one photon-fragmentation contribution and the NLO two photon-fragmentation contribution. (b): Distribution of the Diphox fragmentation correction to Resbos (Equation 10.16), as a function of $P_{T\gamma\gamma}$.

procedure, as follows:

$$\sigma_{ResBos} \rightarrow \sigma_{Resbos} \times \left(1 + \frac{\sigma^{NLO-LO}_{Diphox}(one\ \gamma - frag.) + \sigma^{NLO}_{Diphox}(two\ \gamma - frag.)}{\sigma_{ResBos}}\right) \qquad (10.16)$$

which corresponds to an increase of the Resbos cross-section of about 22%.

The reweighting of the Alpgen sample is performed using the rescaled Resbos sample. The true diphoton transverse momentum $P_{T\gamma\gamma}$ distributions of Alpgen and Resbos are illustrated in Figure 10.4(a).

The colored regions, denoted n *parton*(s) in the legend, correspond to the contribution of the Alpgen samples simulating the production of the tree-level processes $\gamma\gamma + n$ *partons*, with $n = 0, 1, 2, \geq 3$. A large difference is observed between the Alpgen and Resbos predictions in the low $P_{T\gamma\gamma}$ region, notably due to the resummed part present in Resbos while Alpgen enjoys an approximative resummation through the parton shower of Herwig. In the large $P_{T\gamma\gamma}$ region, the Resbos shape is very similar to that of the Alpgen inclusive $\gamma\gamma+1$ *parton* sample, indicating a good matching between the NLO perturbative part of Resbos and the LO tree-level process + one hard emitted parton in Alpgen.

This weight per bin of $P_{T\gamma\gamma}$, defined by the ratio of true diphoton transverse momentum $P_{T\gamma\gamma}$ distributions of Resbos to that of Alpgen is shown in Figure 10.4(b). Above ~ 40 GeV/c, the result of a fit with the sum of an exponential and a two degree polynomial function is used to avoid statistical fluctuations.

The event-by-event weight defined through the reweighting procedure is used to correct the Alpgen shapes and corss section. The distribution of the reconstructed invariant mass for

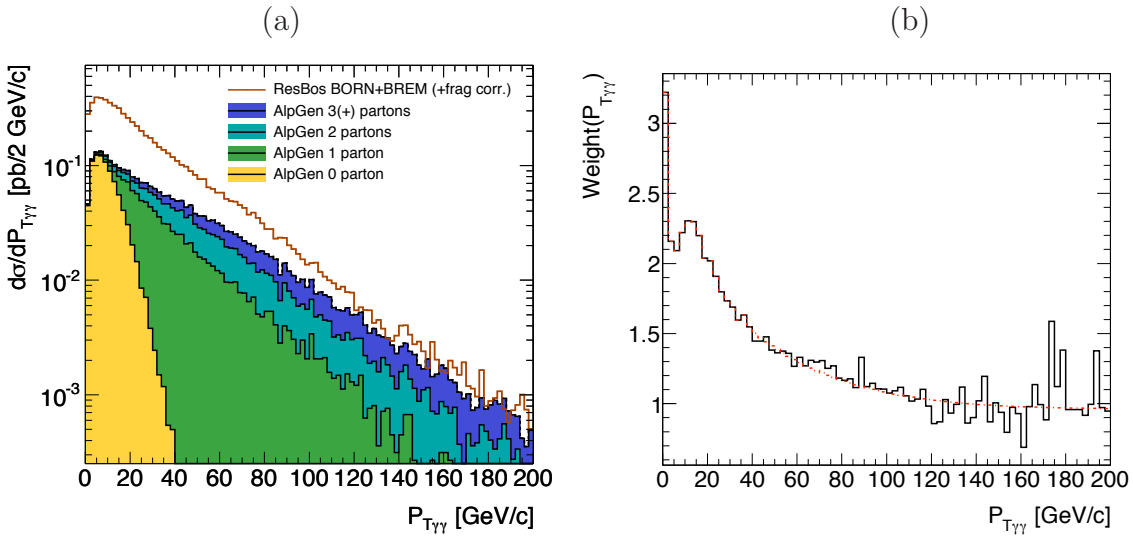

Figure 10.4: (a): $P_{T\gamma\gamma}$ distributions for Alpgen and Resbos corrected by Diphox fragmentation contribution. (b): Distribution of the weight used to reweight Alpgen as a function of $P_{T\gamma\gamma}$.

the Born and bremsstrahlung processes is obtained with this method. A final cross-section of $\sigma_{born+brem} = 5.64$ pb is found after reweighting which corresponds to an increase of about 2.2 times the initial cross-section given by Alpgen.

The Box process

In order to predict the spectrum shapes and the cross-section of the box process in the irreducible background, Pythia samples are used and a rescaling using the NLO prediction given by Resbos program is proposed. A good agreement between the shapes of the Resbos and Pythia $P_{T\gamma\gamma}$ distributions is shown in Figure 10.5(a). The $P_{T\gamma\gamma}$ in the box process simulated at LO in Pythia is due to initial-state radiations, while in Resbos, the emission of a hard parton contributes to the spectrum. This implies a relatively strong showering process in Pythia for this process.The good agreement between Pythia and Resbos shapes allows to account for the NLO computation of the box process in Resbos, by rescaling the Pythia cross-section by a normalization factor. This corresponds to an increase of the Pythia cross-section of about 22%. The Pythia cross-section found after rescaling is $\sigma_{box} = 1.12$ pb.

Summary of the Irreducible background contribution

The total NLO cross-section for the irreducible background in the mass range $100 < M_{\gamma\gamma} < 150\ GeV/c^2$ is $\sigma_{irreducible} = 6.77$ pb. The box contribution corresponds to about 20%. The global $M_{\gamma\gamma}$ distributions for the irreducible background are shown is Figure 10.5(b). For an integrated luminosity of 200 pb^{-1}, about 1353 events of irreducible background are expected.

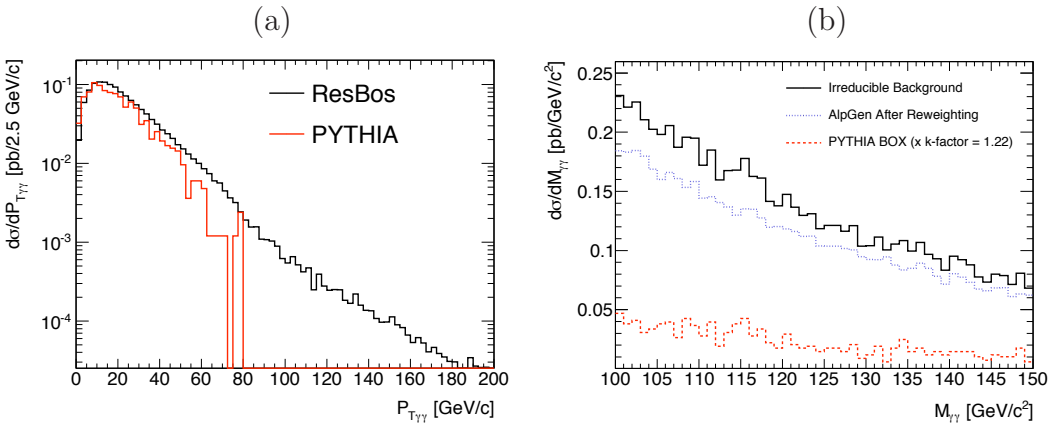

Figure 10.5: (a): Pythia and Resbos $P_{T\gamma\gamma}$ distributions for the Box process contribution. (b): Diphoton invariant mass distributions for the Born and bremsstrahlung processes as simulated by Alpgen (after reweighting) and for the Box process as simulated by Pythia (rescaled at NLO by Resbos).

10.4.3 γ-jet reducible background

LO prediction

The γ-jet reducible background shapes and cross section are predicted with Herwig and Pythia MC generators at LO. As already mentioned, the jets are largely rejected when performing the photon identification and isolation selection. In the considered mass widow, 334 ± 13 $\gamma\gamma$ events are found in the fully reconstructed sample. This small remaining statistics leads difficult the accurate estimation of the invariant mass spectrum and suggests the use of high statistics fast simulated samples in which photon efficiency and jet rejection factors are applied. As discussed in detail in [113], the distribution of the reconstructed diphoton invariant mass found in the fully simulated sample disagrees with the spectrum obtained with the fast simulated sample (after applying the rejection factors). An improved estimation of the γ-jet (and jet-jet) background invariant mass spectrum (and transverse momentum although not discussed here) is proposed, taking into account the difference between the transverse momentum of the initial jet (P_T^{jet}) and the jet faking photon ($P_T^{fake\ \gamma}$). The quark and gluon-like jet rejections dependence on P_T^{jet} illustrated in Figure 10.6(a) is used in the new parametrization. Figure 10.6(b) displays the diphoton invariant mass distribution as obtained with the fully simulated sample, reflecting the limited statistics of this sample and with the fast simulated sample, in blue squares after applying the photon efficiency and rejection factors computed in Tables 10.5 and 10.6 and in red triangles when accounting for the jet rejections distribution shown in Figure 10.6(a). A better agreement is observed between shapes from the full and fast simulation samples with the new parametrization. The expected numbers of events given in the legend also well agree.

NLO prediction

To properly normalize the LO Pythia estimation of the γ-jet reducible background cross-section σ_P^{LO} to the sum of the NLO direct (σ_D^{NLO}) and fragmentation (σ_F^{NLO}) cross-sections given by the program Jetphox, a refined normalization is used (9.4). The refined normalization factor

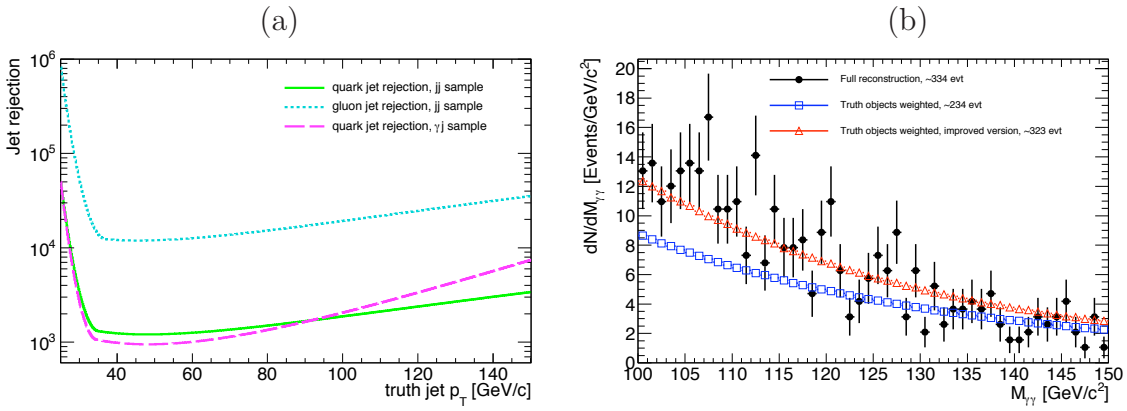

Figure 10.6: (a): Jet rejection as a function of the truth particle jet transverse momentum. (b): Distribution of the invariant mass obtained with the fully simulated sample after applying the photon identification and isolation requirement, with the fast simulated sample of Pythia, when using the standard rejection factors (blue squares) and the rejection distributions in (a) (red triangles).

uses the rejection factors estimated for jets originating from a quark or a gluon separately. The processes t NLO in Jetphox are split into two categories. The expression 9.2 is used although the contribution of quark- and gluon-like jet processes change. These respectively amount de 95.1% and 4.9%, leading to:

$$k = \frac{\rho k_{quark} + k_{gluon}}{0.951\xi + 0.049} \tag{10.17}$$

where $\xi = \dfrac{R_g}{R_q}$ is the ratio of the gluon over quark rejection. The quark and gluon k-factors are respectively:

$$k_{quark} = 1.77(6) \pm 0.47(9) \ , \quad k_{gluon} = 0.77(6) \pm 0.20(9) \tag{10.18}$$

The gluon and quark rejection factors calculated for jets with $E_T > 25$ GeV with the (Pythia) γ-jet sample and shown in Table 10.5, respectively $R_g = 25846 \pm 4361$ and $R_q = 1657 \pm 38$, are used. The rejection factors ratio is therefore $\xi = 15.59 \pm 0.36$. The corresponding k-factor used for renormalization after the kinematic and the photon identification cuts or rejection factors are applied is :

$$k = 1.90(3) \pm 0.52(3)$$

This leads to a cross-section for the γ-jet reducible background of about 3.22 pb after the isEM and isolation cuts and the kinematic selection.

10.4.4 jet-jet reducible background

The LO prediction of the jet-jet background invariant mass spectrum is obtained with the same method employed for the γ-jet background. Figure 10.7 displays the invariant mass distribution obtained with fast simulated sample in the cases the jet rejections are applied as an event-weight and when accounting for the jet rejection dependence on the jet transverse momentum. The distribution for the fully-simulated sample is not shown due to too large statistical fluctuations

(There $\sim$ 70 events) that see a reliable shape. With the new approach, the LO prediction of Pythia gives a cross-section for the jet-jet reducible background of about 0.35 pb.

There is no procedure developed to account for NLO corrections on the jet-jet cross section. Considering that after applying the rejection factors to the two final-state jets the jet-jet process contributes to $\sim 3\%$ of the total background, well below the contributions of the irreducible background ($\sim 66\%$) and the γ-jet reducible background ($\sim 31\%$), its under-estimation is not expected to have a large impact. Moreover, in the CSC note [64], a global k-factor of about 1.3 was used showing a small correction to the LO cross section.

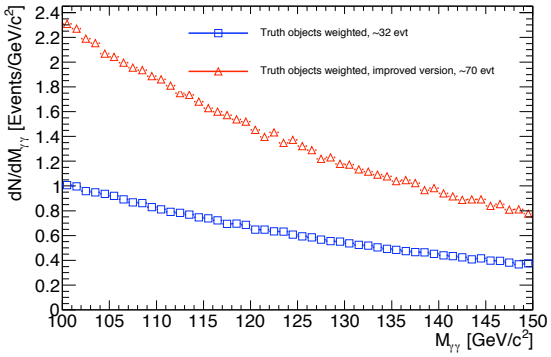

Figure 10.7: Distribution of the invariant mass obtained with the jet-jet fast simulated sample of Pythia, when using the standard rejection factors (blue squares) and the jet rejection dependence on P_T^{jet} (red triangles).

***

Table 10.9 summarizes the signal (all channels combined) and background cross sections and numbers of events expected for a luminosity scheme of 200 pb^{-1} at 10 TeV.

Sample	σ $[pb]$	N_{evts}
Signal	0.025	~ 5
Irreducible Back.	6.77	~ 1353
γ-jet Reducible Back.	3.22	~ 644
jet-jet Reducible Back.	0.35	~ 70

Table 10.9: Expected cross sections obtained for the signal (all channels, mass hypothesis at 120 GeV/c^2) and the different background categories in the range $100 < M_{\gamma\gamma} < 150$ GeV/c^2.The numbers of events corresponding to a luminosity of 200 pb^{-1} are also given.

10.5 Statistical Analysis

The computed cross sections and invariant mass distributions shown before for the signal and background events are used to set an exclusion limit on the cross section of the SM Higgs boson decaying into two photons at a given Higgs boson mass hypothesis, $\sigma_{SM}(m_H) \times BR_{SM}(H \rightarrow \gamma\gamma)$.

The results is derived using the profile likelihood technique as implemented in Hfitter package. The likelihood model allows the multiple dependent variables fits as well as the definition of events categories to separate the signal and background events into disjoint subsets. An unbinned multivariate maximum likelihood fit was performed in the CSC note [64]. The transverse momentum of the diphoton pair as well as the $\cos\theta^*$ (θ^* being the angle between a photon and Higgs boost axis in the diphoton rest frame) variable were used in addition to the diphoton invariant mass. Events were separated into categories based on the number of final state jet, the η direction of the photons (to account for the different mass resolution in calorimeter η regions), the cases with or without converted photon in the pair candidate (to account for a degraded resolution for the former case). Such likelihood model is defined as:

$$L = N_S f_{S,c} P_{S,c}(\mathbf{x}, \theta) + \sum_{i=1}^{n_{bkg}} N_{B_i,c} P_{B_i,c}(\mathbf{x}, \theta) \tag{10.19}$$

where $\mathbf{x}$ are the dependent variable values for the event, c a category index labeling which subset the event belongs to and θ the "nuisance parameters" that needs to be included in the fit to model the signal and background shapes (it corresponds to the variation of the parameters that describe the signal and background shapes); n_{bkg} is the number of background components, $N_{B_i,c}$ the number of events for background component i in category c, N_S the total number of signal events, and $f_{S,c}$ the fraction of those events in category c. $P_{S,c}$ and $P_{B_i,c}$ are PDFs respectively for signal and background component i in category c.

In this study, only the invariant mass of the diphoton pair is considered and there is no defined category. The likelihood model has therefore the simplified form:

$$L = N_S P_S(M_{\gamma\gamma}, \theta) + \sum_{i=1}^{n_{bkg}} N_{B_i} P_{B_i}(M_{\gamma\gamma}, \theta) \tag{10.20}$$

and uses two PDFs, one for the signal combining all Higgs boson production channels contribution and one for the sum of the irreducible and reducible backgrounds contribution. The PDFs are obtained by fitting the invariant mass distribution for the different samples, in the mass window $100 < m_H < 150\ GeV/c^2$.

10.5.1 Fit of the Invariant Mass distribution

The Signal

The invariant mass distribution of the two photons from the Higgs boson decays is rather well modeled by a Crystal-Ball PDF, which takes into account the tail on the left of the distribution due to bremsstrahlung effects:

$$P_S(M_{\gamma\gamma}) = N \cdot \begin{cases} \exp\left(-t^2/2\right) , & \text{for } t > -\alpha \\ (n/|\alpha|)^n \cdot \exp\left(-|\alpha|^2/2\right) \cdot (n/|\alpha| - |\alpha| - t)^{-n} , & \text{otherwise} \end{cases} \tag{10.21}$$

$t = (M_{\gamma\gamma} - m_H)/\sigma(M_{\gamma\gamma})$, N is a normalization parameter, m_H the Higgs boson mass, σ represents the diphoton invariant mass resolution; n and α parametrize the non-Gaussian tail. Figure 10.8 compares the fit of the invariant mass from gluon-gluon fusion only and for all the production processes together at the Higgs boson mass hypothesis $m_H = 120\ GeV/c^2$. The results

are very similar. This validates the assumption one needs for the spectrum shape for higher Higgs boson masses, for which only gluon fusion samples are available. These distributions also display in yellow the contribution from events with at least one converted photons which amounts to $\sim 60\%$ in gluon fusion process only. The results of the Crystal-Ball + Gaussian fit for the different Higgs boson mass scenarios are given in [113].

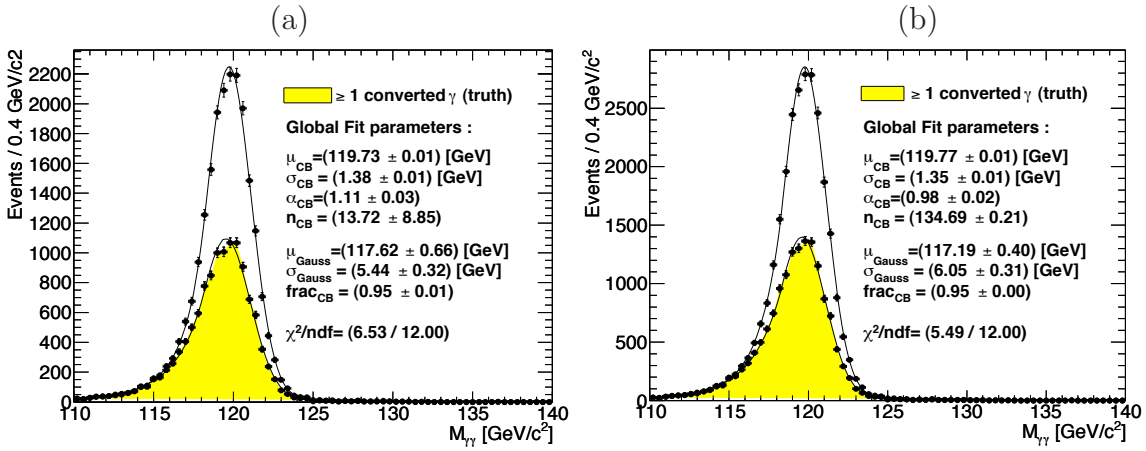

Figure 10.8: Distributions of the invariant mass of diphoton pair passing the selection criteria (a) for the gluon fusion process only and (b) when combining all Higgs boson production channels, with $m_H = 120\ GeV/c^2$. The parameters of the crystal-ball and gaussian functions extracted from the fit are quoted in the plots.

Backgrounds

The irreducible, γ-jet and jet-jet reducible background have a diphoton invariant mass that is rather well described by an exponential tail of slope ξ. The fitted numbers of events and slopes for each background contribution are summarized in Table 10.10.

	N_{evt}	ξ
$\gamma\gamma$ (Born+brem)	1129 ± 34	-0.0226 ± 0.0002
$\gamma\gamma$ (box)	223 ± 15	-0.0307 ± 0.0027
γj	643 ± 25	-0.0408 ± 0.0030
jj	70 ± 8	-0.0222 ± 0.0014
total	2066 ± 45	-0.0289 ± 0.0009

Table 10.10: Expected number of background events in the diphoton invariant mass region $100 < M_{\gamma\gamma} < 150$ GeV/c^2 after the analysis selection, for processes computed at NLO, with $\sqrt{s} = 10$ TeV, normalized to 200 pb^{-1}. Result of the unbinned fit of the signal invariant mass distribution with an exponential with slope ξ.

The background is then described by only one shape corresponding to the sum of all contributions.

10.5.2 Signal and Background uncertainty

Signal

A detailed overview of the systematic uncertainties associated to the signal cross section is proposed in section 8.11.2. Different systematic errors are derived in this study, based on detector abilities.

- The invariant mass fit model parameter α is varied by $\pm$ 50%. It indicates the slope of the tail towards low masses, relying on the number of converted photons. The number of conversions will however be measured in 7 TeV Data which will reduce the uncertainty associated to the slope.

- The σ parameter of the fit model reflects the energy resolution of the detector. To account for realistic schemes with photon energy calibration, the width of the mass distribution is varied with $\sigma = 1.37$ and $\sigma = 1.54$.

- Some simplest signal shapes have been tested, in particular using only the gaussian function in the fit model.

The systematic uncertainties associated to these different tests are listed in [113].

Background

The systematic uncertainties associated to the irreducible background have been studied in detail in section 8.11.1. Accounting for some differences in the normalization schemes used at 10 and 14 TeV the systematic error for the Born and bremsstrahlung processes amounts to 21% the total cross section while for the box process it is estimated of 17% the total cross section.

The systematic uncertainty associated to the refined NLO normalization of the γ-jet reducible background are studied in section 9.5 at 14 TeV. Some of the systematic error sources have been evaluated at 10 TeV and show similar contribution to the overall error.

No systematic error is associated to the jet-jet reducible background as it contribution to the background is very small.

At the end of the first phase of run of the LHC at 7 TeV, the background shape will be extracted in side-band analyses, providing an estimation of the total background cross section. Methods to discriminate the different background are being investigated [115]. As well, studies on jet rejection and photon cross section with the forthcoming data should provide a better normalization of the irreducible and reducible backgrounds separately.

For a more realistic impact on the significance accuracy the systematic uncertainties are obtained by varying the slope parameter of the background shape and the number of events by $\pm 1\ \sigma$.

10.5.3 Exclusion Limits

The exclusion limit is established in this study with the profile likelihood technique, used in the CSC note [64]. The likelihood expression 10.20 is re-expressed as a function of the signal (L_S) and background (L_B) likelihood:

$$L(\mu, \theta) = \mu N_S L_S + N_B L_B \tag{10.22}$$

where μ is the signal strength parameter, $\mu = 1$ in the SM case and $\mu = 0$ in the background only hypothesis. θ is the nuisance parameter, originating from the invariant mass fit models. It reflects the loss of information about μ due to systematic uncertainties.

The profile likelihood is written as:

$$\lambda(\mu) = \frac{L(\mu, \widehat{\widehat{\theta}})}{L(\widehat{\mu}, \widehat{\theta})} \tag{10.23}$$

where $\widehat{\widehat{\theta}}$ is the value of θ maximizing the likelihood when μ is fixed. It is called the maximum likelihood estimator (MLE). $\widehat{\theta}$ and $\widehat{\mu}$ are the values that maximize L when both θ and μ are left floating, $\widehat{\theta}$ and $\widehat{\mu}$ are the MLEs in that case. The definition of the profile likelihood [116] gives $0 \leq \lambda(\mu) \leq 1$ where $\lambda(\mu) = 1$ reflects a good agreement with data (or toy simulation in this study) and the hypothetic μ value. To evaluate the significance of the hypothesis, the test statistics defined by:

$$q_\mu = \{ \begin{matrix} -2ln\lambda(\mu) & if\ \widehat{\mu} \leq \mu \\ 0 & if\ \widehat{\mu} > \mu \end{matrix} \tag{10.24}$$

is commonly used. In opposite logic, the highest value of c indicates a poor agreement between the data and the hypothetic μ value.

Two distributions of q_μ are generated, one in the case of background only and one for background plus signal hypothesis. These distributions are obtained by generating a large number of pseudo-experiments, or toy Monte Carlo simulation. The expected numbers of signal and background events and the invariant mass distribution are given by the results presented above. Each sample is then fitted with a model where the number of signal events (as well as the number of background events and the slope of the exponential) is free and where it is given for a certain μ value hypothesis.

The distributions of q_μ for background and background plus signal hypotheses behave differently. In particular the latter distribution follows a $1/2\delta$ function at 0 plus a $1/2\chi^2$ function. It is therefore not necessary to simulate toy MC for that case. For the background only hypothesis, the distribution of the test statistics has a particular behavior that must be estimated with toy simulations.

This exercise is repeated for different μ value hypotheses. The confidence level at which a certain hypothesis is excluded (CL_{SB}) is given by: $CL_{SB} = 1$ - p_μ. The p-value p_μ, written as:

$$p_\mu = \int_{q_{\mu,obs}}^{\infty} f(q_\mu|\mu) dq_\mu \tag{10.25}$$

is given by the integral of the signal plus background distribution from the median of the distribution for background only hypothesis to the infinity. The $\pm 1\sigma(\pm 2\sigma)$ error on the excluded value are given by varying the integral range of the signal plus background distribution.

This procedure is repeated for different signal hypotheses in order to find the one corresponding to an exclusion at 95% confidence level (CL). Figure 10.9(a) shows the estimated CL obtained with the profile likelihood technique as a function of SM hypotheses (in black) for a Higgs boson mass at 120 GeV/c^2. This indicates that for a luminosity of 200 pb^{-1} and an energy in the centre-of-mass at 10 TeV, 5.96 times the SM ($\sigma_{SM}(H) \times BR_{SM}(H \rightarrow \gamma\gamma)$) is excluded with the inclusive search of the SM Higgs boson through its decay channel into two photons. Figure 10.9(b) displays the estimated number of SM signal cross sections excluded

for the three Higgs boson mass hypotheses considered in this study. The yellow(green) regions correspond to 1 σ(2 σ) deviation. The increasing numbers of SM cross section excluded with the Higgs boson mass hypothesis reflects the decreasing of $BR_{\gamma\gamma}$.

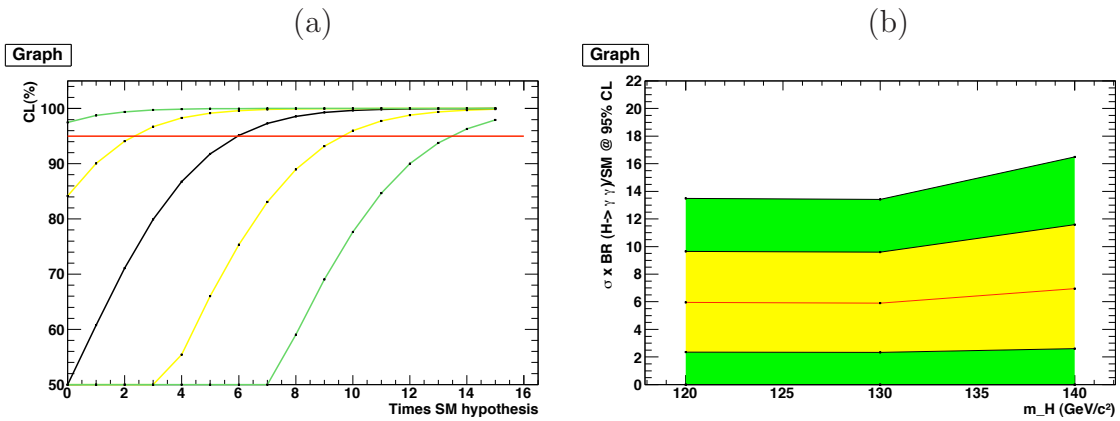

Figure 10.9: (a): Estimated Confidence Levels as a function of the hypothesis on the number of Standard Model signal cross section for $m_H = 120\ GeV/c^2$ using the CL_{SB} method. (b): Estimated number of Standard Model signal cross section excluded at 95% CL as a function of the Higgs boson mass.

Another definition for the confidence level is currently used:

$$1 - CL_S = 1 - \frac{(1 - CL_{SB})}{1 - CL_B} \tag{10.26}$$

where the p-value calculated on the background distribution $1 - CL_B$ is used as normalization factor of the p-value $1 - CL_{SB}$ calculated on the signal plus background distribution. This definition gives more conservative results, but has the advantage of not excluding 0 times the Standard Model (so the background itself) at 2σ. Moreover, as this is the approach used at Tevatron [117], it can be used for comparison purposes. This approach has been used already in ATLAS at several occasions since [118].

The results for $1 - CL_S$ are displayed in the Figure 10.10(a) and (b) and indicate that $7.16 \times \sigma_{SM}(H) \times BR_{SM}(H \to \gamma\gamma)$ is excluded for a Higgs boson mass at 120 GeV/c^2 , at 95% CL with an integrated luminosity of 200 pb^{-1}.

10.5.4 Extrapolation to 7 TeV

Considering the new LHC plane with a first phase of runs at 7 TeV the result of this analysis is extrapolated to give an expectation of the exclusion limit that will be set when ATLAS will have recorded integrated luminosities of 200 pb^{-1} and 1 fb^{-1} at a center-of-mass energy of 7 TeV.

1. This extrapolation relies on the hypothesis that the efficiencies and rejections are the same as in the cases of 7 and 10 TeV energy.

2. The cross-sections for $\sqrt(s) = 7\ TeV$ at NLO for the signal processes are taken into account [104]. The estimated numbers of events for each background component at 10 TeV

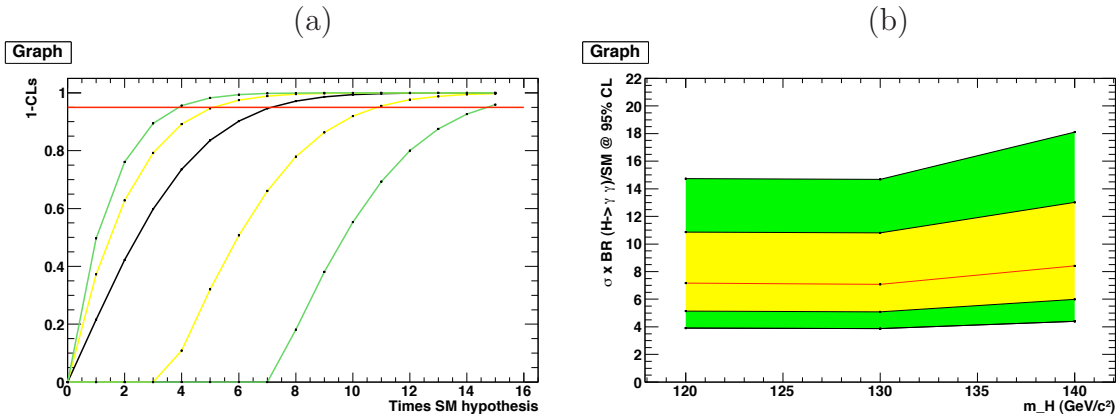

Figure 10.10: (a): Estimated Confidence Levels as a function of the hypothesis on the number of Standard Model signal cross section for $m_H = 120\ GeV/c^2$ using the CL_S method. (b): Estimated number of Standard Model signal cross section excluded at 95% CL as a function of the Higgs boson mass.

are rescaled by the factor corresponding to the ratio of the Pythia cross-section at 7 TeV to that at 10 TeV.

About 2.6 signal events are expected at 7 TeV for a luminosity of 200 pb^{-1} against approximatively 1663 background events in the mass window $100 < M_{\gamma\gamma} < 150\ GeV/c^2$.

The expected exclusion limits for 200 pb^{-1} and 1 fb^{-1} are shown in Figure 10.11 for the CL_{SB} method and in Figure 10.12 for the $1 - CL_S$ method. The numbers of signal Standard

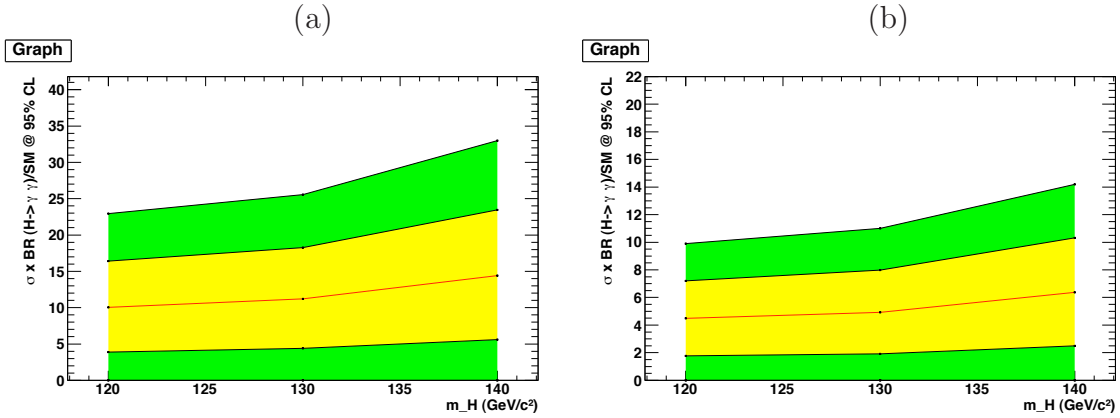

Figure 10.11: Expected exclusion limit of the SM at 95% CL using the CL_{SB} method, for $\sqrt{s} = 7\ TeV$ and a luminosity scheme of (a) 200 pb^{-1} and (b) 1 fb^{-1} .

Model cross-section that are expected to be excluded at 95% CL using the CL_{SB} method and the $1 - CL_S$ method are listed in Table 10.11 for both 200 pb^{-1} and 1 fb^{-1}.

The predictions obtained for 200 pb^{-1} are comparable than the current limits from each Tevatron experiment [15].

Figure 10.13 display the recent exclusion limits set by (a) the CDF [119] and (b) DØ [120] experiments at Fermilab for a luminosity of 5.4 and 4.2 fb^{-1} respectively. The CDF experiment

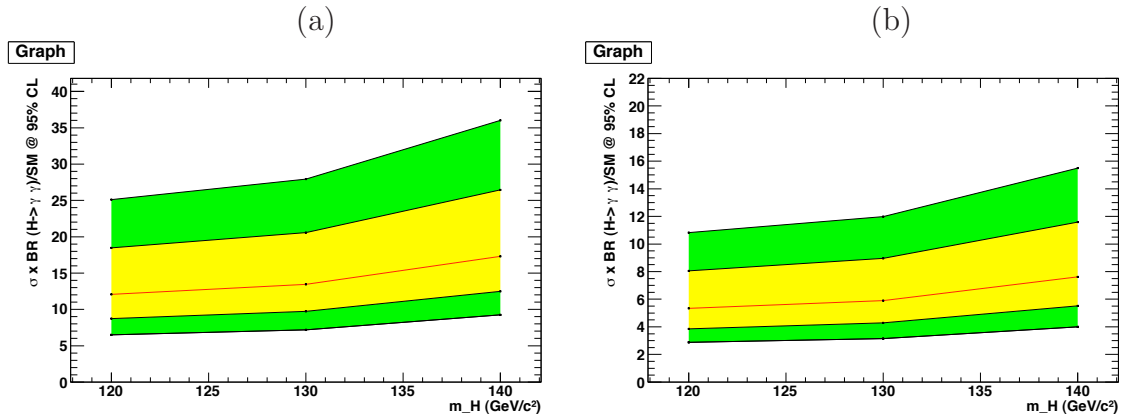

Figure 10.12: Expected exclusion limit of the SM at 95% CL using the $1 - CL_S$ method, for $\sqrt{s} = 7\ TeV$ and a luminosity scheme of (a) 200 pb^{-1} and (b) 1 fb^{-1}.

Luminosity	method	$m_H = 120$ GeV/c^2	$m_H = 130$ GeV/c^2	$m_H = 140$ GeV/c^2
200 pb^{-1}	CL_{SB}	10.04	11.21	14.42
	$1 - CL_S$	12.05	13.46	17.30
1 fb^{-1}	CL_{SB}	4.48	4.93	6.37
	$1 - CL_S$	5.35	5.90	7.62

Table 10.11: Signal cross-sections that are expected to be excluded at 95% CL with an integrated luminosity of 200 pb^{-1} and 1 fb^{-1}, at $\sqrt{s} = 7$ TeV, using the CL_{SB} and the $1 - CL_S$ methods.

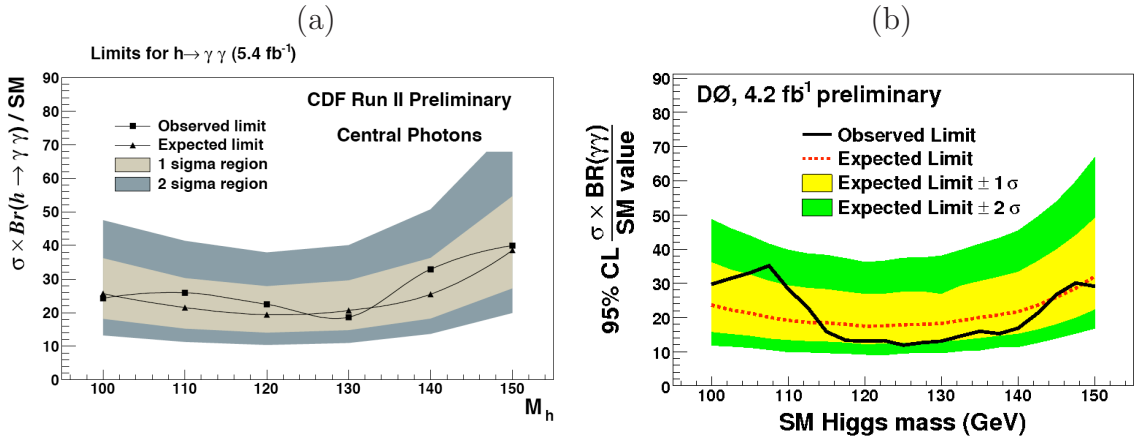

Figure 10.13: Exclusion limits on the Standard Model signal cross section set by (a) the CDF and (b) DØ experiments for a luminosity of 5.4 and 4.2 fb^{-1} respectively.

observes an exclusion of 22.5 times the SM cross section times the Higgs boson into $\gamma\gamma$ decay, for an expected exclusion of 19.4 the SM. In the DØ experiment the observed exclusion limit is at 13.1 times the SM and the expected one at 17.5. They should be competitive to what one could expect from the Tevatron experiments at the winter conferences of 2011, when ATLAS could have analyzed indeed 200 pb^{-1} at a center-of-mass energy of 7 TeV. For 1 fb^{-1}, the

predictions are better than what one would expect from Tevatron for the winter conferences of 2012.

10.6 Conclusion

This study presents a robust and relatively simple analysis for exclusion limits on the SM Higgs boson in the $\gamma\gamma$ decay channel at the centre-of-mass energy of 10 TeV and for a luminosity of 200 pb^{-1}.

A particular effort has been made to get a NLO normalization for all signal production channels and the irreducible and γ-jet reducible background. Moreover most of the signal and background samples used in this analysis are fully simulated samples. The quark and gluon jet rejection factors have been studied in detail and used to get a reliable prediction of the reducible background normalization and shapes.

Two methods are derived in the statistical analysis and provide slightly different results for exclusion prospects. For a proper comparison with Tevatron results the $1 - CL_S$ method is used and excludes about 7-8 times the SM cross section at 95% CL, in the low mass range ($120 < m_H < 140\ GeV/c^2$). The extrapolation to 7 TeV energy in the centre-of-mass is done in this exercise for two luminosity schemes (200 pb^{-1} and 1 fb^{-1}), and shows that about 5 times the SM cross section is expected to be excluded in the low mass region after the first phase of run at LHC.

I contributed mainly to the sections dedicated to the irreducible and reducible backgrounds normalization. This work gave me the possibility to further understand each steps leading to the exclusion limits that have been established.

Conclusion

My thesis work consisted essentially in three relatively independent parts, though each of them are related to the search for the Higgs boson in the $\gamma\gamma$ channel in the ATLAS experiment.

A.- A study of the intrinsic uniformity of the EM barrel calorimeter of ATLAS using the drift time measurement of ionization electrons is performed. About 500 000 cosmic muon pulses have been recorded and their shape predicted using the *First Principle Method*. The electrons drift time and electrode shift with respect to its centered position in a given cell are extracted from the signal pulse shape fit. The drift time dependence on the voltage applied on both sides of the electrode is studied and a comparison with the drift time measurement at nominal voltage (2000 V on both sides of the electrode) is performed. The drift time uniformity in the Middle compartment of the barrel is derived per region of size 0.1×0.1 in the (η, ϕ) plane. Its impact on the calorimeter response uniformity is found to be of 0.29 % and 0.35%, respectively at nominal and all voltages. With the lead thickness variation expected to contribute by $\sim 0.18\%$, this leads to an intrinsic calorimeter uniformity in the barrel of:

$$\sqrt{(0.18\%)^2 + (0.29\%)^2} = 0.34\% \text{ at nominal voltage}$$
$$\sqrt{(0.18\%)^2 + (0.35\%)^2} = 0.39\% \text{ at all voltages}$$

The drift velocity of electrons is estimated from the drift time distribution in the different layers when rescaled to correspond to an electrical field of 1 kV/mm:

$$V(E = 1kV/mm) = 4.58 \pm 0.07 mm.\mu s^{-1}$$

which is in good agreement with previous measurements of the drift velocity for free electrons in the LAr at an operating temperature of 88.5 K. Good agreement is found with measurements done with another signal prediction model (RTM).

B.- The accurate knowledge of the upstream material is essential to calibrate the photons energy, knowing that a large fraction of photons are converted before reaching the calorimeter. One method to estimate the inner most distribution of the material upstream of the calorimeter is to measure the conversion rates as a function of the conversion location. This material mapping method however requires either a knowledge of the initial flux of photon in minimum bias events or the mapping will be relative to a well known reference piece of a material. In ATLAS this is achieved using the Beam Pipe (BP). However another possibility to normalize the overall flux of photons and verify the BP conversion

rate, given that a vast majority of the photons in MB events originates from π^0 decays, is to use the π^0 Dalitz decays, thus estimating the initial number of π^0.

The connection between the BP material and the actual rate of BP conversions per event cannot be trivially derived. It relies on the underlying hard scattering process and its accurate simulation. However a large number of systematic uncertainties cancel in the ratio of the BP conversions rate to that of Dalitz decays. The meaningful observable comparing the data to the Monte-Carlo (MC) is the ratio of reconstructed BP conversions to Dalitz decays. It has been estimated with recent 7 TeV data and agrees well with the MC prediction:

$$\left(\frac{N_{BP}^{reco}}{N_{Dz}^{reco}}\right)^{data} = \frac{8463}{4519} = 1.87 \pm 0.03 \; \left(\frac{N_{BP}^{reco}}{N_{Dz}^{reco}}\right)^{MC} = \frac{3256}{1727} = 1.88 \pm 0.06$$

The errors quoted are purely statistical. Systematic errors on the BP conversion probability are estimated and amount to (-4%,+2%) when using the ratio of the number of reconstructed BP conversions to that of Dalitz decays measured in data. A detailed study of the systematic error related to the Minimum Bias event model simulated in the MC using for instance the various Pythia tunings is ongoing.

The BP conversion rate estimated in the data well agrees with prediction from the MC simulation:

$$P_{acc}(\text{data 7 TeV}) \longrightarrow 17.87 \pm 0.92 \text{ (stat)} \; ^{+0.36}_{-0.72} \text{ (syst)} \; {}^{0}\!/_{00}$$
$$P_{acc}(\text{MC 7 TeV}) \longrightarrow 17.99 \pm 0.01 \text{ (stat)} \; {}^{0}\!/_{00}$$

The amount of material in the BP that represents about 0.7% of X_0 is estimated with (-6.5%,+5.5%) accuracy.

C.- Finally a study of the signal and background normalizations and discrimination potential in the $H \rightarrow \gamma\gamma$ channel is performed. I have first derived a NLO normalization of the signal and irreducible background in this channel and studied the discrimination potential of various variables. I have compared the predictions from different Monte-Carlo generators and Matrix Element calculation programs, with different features: initial-state soft gluons resummation, photon fragmentation of final-state parton, MC parton showering process. A NLO normalization of the irreducible background accounting for the one and two photon fragmentation of the final parton in the bremsstrahlung process is obtained. Its related systematic uncertainty is also estimated and amounts to about 26%. The signal produced by gluon fusion is also normalized at NLO, with 16% of systematic error. A NNLO k-factor is estimated of 1.15.

The $\cos\theta^*$ variable defined in the Collins-Soper (CS) and boost axis frames presents a strong correlation with the invariant mass of the diphoton system. It has a good discriminating power at high masses. The ϕ variable in the CS frame also presents a potentially interesting discriminating power in the prediction made by Resbos but the background shapes estimated by other generators do not confirm it.

I have studied the normalization of the semi-reducible background that comprises of the production of a photon and a jet reconstructed as a photon. A NLO normalization

accounting for the photon fragmentation is derived with 27% of systematic error. A refined normalization that should be applied after the photon identification is developed. It accounts for the different rejections of jets originating from a quark and a gluon by distinguishing events with quark- or gluon-like final-state jets. The refined normalization is then reduced since the gluon-initiated jet rejection is much greater that that of the quark-initiated jets. It amounts to 1.9 ± 0.6.

Finally I have participated to the study of prospects for the exclusion of a Higgs boson at 10 and 7 TeV centre-of-mass energy and a luminosity of 200 pb^{-1}.

To conclude I would like to apologize to the reader for the length of the manuscript, I did not find the time to make it shorter. I will nevertheless try to emphasize in a few sentences which aspects of my work have actually contributed to new developments in the collaboration. The drift time measurements allowed to assess the intrinsic uniformity of the LAr calorimeter *in situ* for the first time and check that this contribution to the constant term is under control. A future development of this analysis would be to actually correct for the variations in drift time. The measurement of the absolute Beam Pipe conversion rate using Dalitz decays of π^0 mesons is also a completely new analysis. The detailed study of the normalization and discrimination potential of the background and signal in the $H \to \gamma\gamma$ channel is not new but its reappraisal is important to assess accurately the sensitivity of the search. The most important aspects of this topic are the study of the shape of the transverse momentum of the diphoton system, the correlation between the $\cos\theta^*_{CS}$ and the invariant mass $M_{\gamma\gamma}$, and the matching of a parton level isolation criteria with the experimental isolation. Finally, the refined NLO normalization of the γ-jet reducible background which takes into account the underlying nature of the jet is also new approach. Of course, al of these topics were treated in close collaboration and guidance of a number of researchers whom I acknowledge in the dedicated section of this manuscript.

Remerciements, Acknowledgments

Je voudrais remercier Guy Wormser pour m'avoir accueilli au Laboratoire de l'Accélérateur Linéaire pendant ces trois années de thèse. Je remercie aussi toutes les personnes du service du personnel et les "dames des missions". Merci Annick pour ton sourire et ta bonne humeur permanente. Geneviève, merci d'être au petit soin avec nous, merci pour ta bonne humeur et ton soutien.

Je remercie également les membres du Jury : Guy, Michel Fontannaz, Aleandro Nisati, Philippe Bloch, Aurelio Juste Rozas et Marumi Kado. Philippe et Aurelio, merci d'avoir accepté d'être rapporteurs de ma thèse et Michel, merci pour ta grande disponibilité au cours de ma thèse et ton aide précieuse dans l'étude de la production diphoton.

J'aimerai exprimer ma gratitude à toute l'équipe ATLAS du LAL. En commençant par Marumi Kado, mon directeur de thèse.

Marumi, je suis très contente d'avoir fait ma thèse avec toi. Merci pour ton incroyable pédagogie, ta grande curiosité, ta patience et ton formidable sens critique. Merci pour ton encouragement, ton écoute et tes conseils sur chaque aspect d'un travail de recherche. Merci d'avoir composé avec mon stress parfois excessif et de m'avoir toujours recentrée. Enfin, merci d'avoir cherché à développer en moi la réflexion et le sens critique.

Je remercie aussi Daniel et Caroline, j'ai particulièrement apprécié notre travail pendant ma deuxième année de thèse. Daniel, merci d'avoir eu l'idée du calorimètre, merci pour ta pédagogie et tes bonnes idées pour l'étude que nous avons réalisé, merci pour ta curiosité et ton dynamisme. Caroline, merci pour ta grande disponibilité et tes explications toujours très claires. Merci pour ta bonne humeur, ton écoute et ton amitié.

Jean-Ba, tu as tant contribué à mon travail, toujours avec humilité et gentillesse. Merci pour ton aide et ta grande disponibilité. Merci Ilija, cher collègue de bureau et ami. Merci pour toutes nos discussions, ton aide, merci d'avoir apprécié le café et nettoyé nos bureaux de gâteaux et sucreries en tout genre ☺. Marthe, tu es une super collègue, vivante et toujours de bonne humeur, même au petit matin... ☺ Merci pour ta disponibilité, les morceaux de classique que je ne connaissais pas et ta formidable culture G.

Merci aux thésards du LAL : Mathieu 1 (ou P. ☺, merci pour ton super manuscrit de thèse), Emmanuel, Dimitris (merci pour ta pédagogie et ta bonne humeur festive), Iro (merci pour ton dynamisme, ta gaieté et aussi pour ton travail sur le Higgs en gamma gamma), Nanci, Adrien (merci pour ton soutien et ton esprit festif), Henso (Señor Henso, maître dans la réjection des jets, merci pour tes explications. Et ton jeu de ping-pong ☺), François (ton niveau de geekitude et ta connaissance des séries imposent le respect ☺), Jean-Baptiste (t'es drôlement

grand!), Fany (merci pour nos discussions dans les moments de doute, merci pour tes bons gâteaux), Clément, Yasmine, João et Viola. Djimbo, you are a really good ping-pong player, thank you for the games.

Marc, merci pour ta spontanéité et ton exactitude. Merci d'avoir relu et corrigé (en 24h!) mon manuscrit. Dirk, merci pour ta disponibilité, tes blagues, et tes cours d'école doctorale sur le LHC. Merci Louis pour tes bonnes idées et ton dynamisme. Merci à Laurent Serin et Sophie pour votre aide. Merci Lydia, ton dynamisme est exemplaire et tes plats d'aubergines sont divins! Dudu, merci pour tout, ton écoute et ton aide en tous points. Nikola, merci pour tes conseils et ton boulot sur les jets. Merci Luc pour ton humeur joviale et taquine. Abdenour, merci pour ta bonne humeur et nos échanges sur nos étudiants. Claire merci de ta bonne et franche humeur. Merci Sébastien, David et Jean-Ba pour votre aide avec cette boîte noire qu'est Athena. Francesco, merci pour ta gentillesse et bonne humeur italienne. Merci pour ta grande disponibilité et ton incroyable travail sur l'analyse à 10 TeV. Merci également à Lydia Roos, j'ai beaucoup appris à vos côtés. Patrick, merci pour ton franc-parlé, ta fabuleuse disponibilité, tes conseils pour le monitorat, tes histoires et situations de folies qui nous font tous tant relativiser. J'admire ton investissement, ton dynamisme et ta vivacité! Merci Reisaburo pour tes questions sur le Higgs, et merci de travailler le dimanche et d'avoir été là pour là pour transmettre à Marumi mon manuscrit de thèse. Merci Jean-François pour tes questions pertinentes et ta franchise.

Les Mat(t)hieux : merci d'avoir été là chaque jour, chaque matin pour nos cafés-clopes, merci pour toutes ces soirées et bons moments partagés. Vous êtes des compagnons de route incroyables. Matthieu, mon cher ami, merci pour ton encouragement, ton aide à tout moment, nos discussions du matin, merci pour ton aide avec la luminosité, merci de m'avoir expliqué avec tant de patience et de talent ALFA. Et merci de m'avoir présenté ta soeur, Flo garde moi une petite place à la Villa Vanilla ☺. Annalisa, merci Bella pour ces bons repas, merci de m'avoir appris à faire le *risotto* aux asperges et merci pour les échanges hispanico-italien ☺. Mathieu, merci pour ton soutient et ton amitié, merci de m'avoir expliqué les pixels, la différence sensor/detector, les jonctions np, nn.... et ré-expliqué ☺. Merci pour tout ce que tu m'as transmit de la culture québécoise (merci pour *les invincibles* et *les bougeons*). Yves, merci pour les pauses cafés et les bonnes soirées.

Nicoletta, je te remercie pour ta bonne humeur, ton incroyable soutien et tes bons conseils. Xavier, merci pour ton écoute et ton incroyable audace, je n'avais jamais entendu dire que la vitesse de la lumière pourrait ne pas être constante! Mes excuses tardives aux étudiants qui m'ont eu en TD pour avoir clamé que c'était une constante de la nature sans préciser qu'il s'agissait d'un postulat ☺. Sophie, merci pour ces bons moments partagés et ton humeur taquine.

This thesis work was realized in close collaboration and guidance of researchers whom I would like to acknowledge: Aleandro Nisati, Leonardo Carminati, Bruce Mellado, Michel Fontannaz, Jean-Philippe Guillet, Pavel Nadolsky, Csaba Balazs, Yaquan Fang, Carolina Gabaldon, Isabelle Wingerter-Seez, Pavol Strizenec, Mauro Donega, Thomas Koffas, Kerstin Tachmann and many others.

Je voudrais aussi remercier Philippe Schwemling et léquipe ATLAS du LPNHE. Vous m'avez chaleureusement accueilli pendant mon stage de maîtrise et à chaque visite depuis.

Merci Gavin pour ta gentillesse et ton amitié. Merci pour les cours que tu as donné à l'école d'été du CERN, j'admire la sérénité et la clarté dont tu fais preuve dans la transmission de ton savoir.

Merci aux GO des JJC : Pierre et Stéfanie, merci pour votre dynamisme et bonne humeur, merci pour la poire ☺ et merci pour ce petit bout d'ange que vous avez créé, tant de beauté chez un si petit être, ça vous transforme ☺), J.S (merci d'être le poète gluonique et alambiqué de ces dames!), Caroline et Auguste (merci à vous deux pour les repas au CERN et les mots d'encouragement).

Merci à mes compagnons de route pendant ces années d'études : Julie, Adrien, Amandine, Loic, Andreas, Alex, Romain, Antoine et Sarah. Merci Alex pour ce merveilleux bout de chemin que nous avons fait ensemble, ton amour, ton amitié et ton écoute ont été des ingrédients indispensables à la concrétisation de cette thèse. J'ai beaucoup appris à tes côtés et t'en remercie humblement. Sarah, je te remercie infiniment, tu es une amie formidable, la meilleure. Tu m'as tant soutenu pendant ces années, pour les bons moments et les plus difficiles aussi. Merci pour ton calme, ton incroyable disponibilité et ta merveilleuse écoute. Merci d'être là ma chérie!

Marie, merci pour tout, cette thèse n'aurait pu se faire sans votre aide. Merci Ariane et Claudine pour votre présence et soutien ces dernières années.

Un grand merci à toute ma famille. Je remercie mes parents pour leur soutien et leur encouragement durant toutes ces années. (Ces quelques mots ne pourraient traduire le millième de mes émotions). Merci d'avoir tout fait pour me permettre d'être là aujourd'hui. Moon, merci pour tes bons petits plats, les week-end à la campagne et ton incroyable écoute. Papa, merci pour tes conseils, nos longues discussions, la culture rock et hippies 70's, et ton soutien. Isabelle, merci d'être là et merci pour tout ce que tu es. Merci Julien, Céline, Pierre, et Lucie pour les bons moments partagés. Hélène, petite soeur, merci pour ton soutien et ton amour et ces moments de complicité incomparables. Merci aussi de m'avoir écouté tant de fois prononcer la phrase critique "j'ai des jobs à lancer", merci d'avoir prêté l'oreille à mes problèmes de physique, merci pour le coup de main avec les notes d'examen de mes étudiants.

Enfin, je souhaiterai exprimer ma reconnaissance à toutes celles et ceux mentionnés, ou que j'aurai pu oublier. Plus qu'un travail c'est la thèse de ma vie. Merci à tous qui avaient tant contribué à la réalisation de ce projet.

Bibliography

[1] S. Weinberg. The Making of the Standard Model. hep-ph/0401010. Jan 2004.

[2] A. Djouadi. The Anatomy of Electro-Weak Symmetry Breaking. I: The Higgs boson in the Standard Model. hep-ph/0503172. May 2005.

[3] S. Weinberg. A model of leptons. *Phys. Rev. Lett.*, 19(21):1264–1266, Nov 1967.

[4] A. Salam and J. C. Ward. Electromagnetic and Weak Interactions. *Phys. Lett. 13 (1964), 168.*

[5] S. Weinberg. A Model of Leptons. *Phys. Rev. Lett.*, 19(21):1264–1266, Nov 1967.

[6] R. Godement. *Introduction à la théorie des groupes de Lie*, volume IX. 2004.

[7] P. W. Higgs. Broken Symmetries and the Masses of Gauge Bosons. *Physical Review Letters*, 13(16):508–509, Oct 1964.

[8] F. Englert and R. Brout. Broken Symmetry and the Mass of Gauge Vector Mesons. *Physical Review Letters*, 13(9):321–323, Aug 1964.

[9] G. S. Guralnik. The History of the Guralnik, Hagen and Kibble development of the Theory of Spontaneous Symmetry Breaking and Gauge Particles. Jul 2009.

[10] G. Arnison. Experimental observation of lepton pairs of invariant mass around 95 GeV/c^2 at the CERN SPS collider. *Physics Letters B*, 126(5):398–410, July 1983.

[11] P. Bagnaia et al. Evidence for Z0 → e+ e- at the CERN anti-p p collider. *Phys. Lett.*, B129:130–140, 1983.

[12] M. E. Peskin and D. V. Schroeder. *An Introduction To Quantum Field Theory (Frontiers in Physics)*. Westview Press, October 1995.

[13] G. Abbiendi. Search for the Standard Model Higgs Boson at LEP. hep-ex/0306033. Jun 2003.

[14] P. Teixeira-Dias. Observation of an excess in the ALEPH search for the Standard Model Higgs boson. hep-ex/0108001. Aug 2001.

[15] Tevatron New Phenomena, Higgs working group, C. D. F. Collaboration, and DZero Collaboration. Combined CDF and DZero Upper Limits on Standard Model Higgs Boson Production with up to 4.2 fb-1 of Data. Mar 2009.

[16] M. Lancaster, R. W. L. Jones, and E. Thomson. W mass measurements at LEP and the Tevatron. *Journal of Physics G: Nuclear and Particle Physics*, 26(5):616–626, 2000.

[17] S. Heinemeyer. Electroweak Precision Physics from Low to High Energies. Oct 2007.

[18] H. Flaecher et al. Revisiting the Global Electroweak Fit of the Standard Model and Beyond with Gfitter. Feb 2009.

[19] S. P. Martin. A Supersymmetry Primer. hep-ph/9709356. Dec 2008.

[20] A. Djouadi. The Anatomy of Electroweak Symmetry Breaking Tome II: The Higgs bosons in the Minimal Supersymmetric Model. *Physics Reports*, 459(1-6):1–241, April 2008.

[21] A. A. Glazkov et al. Duoplasmatron-type Ion Source with Improved Technical and Operational Performance for Linear Accelerator. 1992.

[22] P. Cortese et al. *ALICE physics performance: Technical Design Report*. Technical Design Report ALICE. CERN, Geneva, 2005.

[23] *LHCb : Technical Proposal*. Tech. Proposal. CERN, Geneva, 1998.

[24] N. V. Krasnikov and V. A. Matveev. Physics at the large hadron collider. *Physics of Particles and Nuclei*, 28(5):441–470, 1997.

[25] A. de Roeck et al. *CMS physics: Technical Design Report*. Technical Design Report CMS. CERN, Geneva, 2006.

[26] The T. O. T. E. M. Collaboration et al. The TOTEM Experiment at the Cern Large Hadron Collider. *Journal of Instrumentation*, 3(08):S08007, 2008.

[27] The L. H. C. Collaboration et al. The LHCf detector at the CERN Large Hadron Collider. *Journal of Instrumentation*, 3(08):S08006, 2008.

[28] C. Schmidt. Beam loss scenarios and strategies for machine protection at the lhc. LHC Project Report 665.

[29] M. Lamont. Summary of the LHC beam commissioning workshop held at Evian (19-20 january 2010).

[30] L. Fabbri. ATLAS and forward physics. Technical Report ATL-COM-LUM-2009-024, CERN, Geneva, Dec 2009.

[31] W. Bonivento. Online luminosity monitoring with liquid Argon calorimeters at ATLAS and D0. Technical Report ATL-LARG-2001-001, CERN, Geneva, Nov 2000. revised version number 1 submitted on 2000-12-22 10:49:45.

[32] S. Arfaoui. Etude et optimisation du systéme haute tension du calorimètre lectromagnétique du détecteur ATLAS. application à une mesure de luminosité du LHC. Master's thesis, 2008.

[33] M. Villa. The Luminosity Monitor of the ATLAS Experiment. Technical Report ATL-LUM-PROC-2009-004. ATL-COM-LUM-2009-017, CERN, Geneva, Nov 2009.

[34] S Ask et al. Luminosity measurement at ATLAS - development, construction and test of scintillating fibre prototype detectors. May 2006.

[35] M. Heller. Mesure de la luminosité absolues et de la section efficace totale proton-proton dans l'expérience ATLAS au LHC. March 2010.

[36] The ATLAS experiment at the CERN Large Hadron Collider. Technical Report ATL-COM-PHYS-2007-102. ATL-COM-PHYS-2007-098, CERN, Geneva, Dec 2007.

[37] G. Darbo. The ATLAS IBL Project. Technical Report ATL-COM-INDET-2010-031, CERN, Geneva, Feb 2010.

[38] C. Amsler. Particle data group. *Physics Letters B667, 1 (2008) and 2009 partial update for the 2010 edition.*

[39] M. Aharrouche et al. Response uniformity of the ATLAS liquid argon electromagnetic calorimeter. *Nuclear Instruments and Methods in Physics Research Section A: Accelerators, Spectrometers, Detectors and Associated Equipment*, 582(2):429–455, November 2007.

[40] B Aubert et al. R&D proposal : liquid argon calorimetry with LHC-performance specifications. Technical report, 1990.

[41] S. Amoruso et al. Study of electron recombination in liquid argon with the ICARUS TPC. *Nuclear Instruments and Methods in Physics Research Section A: Accelerators, Spectrometers, Detectors and Associated Equipment*, 523(3):275–286, May 2004.

[42] A. Bazan et al. The ATLAS liquid argon calorimeter read-out system. *IEEE Transactions on Nuclear Science*, 53(3):735–740, June 2006.

[43] W. Cleland. Signal processing considerations for liquid ionization calorimeters in a high rate environment. *Nuclear Instruments and Methods in Physics Research Section A: Accelerators, Spectrometers, Detectors and Associated Equipment*, 338(2-3):467–497, January 1994.

[44] D. Banfi, M. Delmastro, and M. Fanti. Cell response equalisation of the ATLAS electromagnetic calorimeter without the direct knowledge of the ionization signals. *J. Instrum.*, 1(SN-ATLAS-2005-054), 2004.

[45] C. Collard, D. Fournier, S. Henrot-Versillé, and L. Serin. Prediction of signal amplitude and shape for the ATLAS electromagnetic calorimeter. Technical Report ATL-LARG-PUB-2007-010. ATL-COM-LARG-2007-009, CERN, Geneva, Sep 2007.

[46] S. Baffioni et al. Electrical Measurements on the ATLAS Electromagnetic Barrel Calorimeter. Technical Report ATL-LARG-PUB-2007-005. ATL-COM-LARG-2006-009, CERN, Geneva, Oct 2006.

[47] B. Aubert et al. Construction, assembly and tests of the ATLAS electromagnetic barrel calorimeter. *Nuclear Instruments and Methods in Physics Research Section A: Accelerators, Spectrometers, Detectors and Associated Equipment*, 558(2):388–418, March 2006.

[48] F. James. The minuit package webpage, http://root.cern.ch/root/html/tminuit.html.

[49] C. Gabaldon, M. Kuna, F. Hubaut, and P. Pralavorio. Check of the signal reconstruction in the EM calorimeter with beam splash data. Technical Report ATL-LARG-INT-2009-005. ATL-COM-LARG-2009-009, CERN, Geneva, Apr 2009.

[50] P. Bernat, C. Collard, D. Fournier, and M. Kado. Measurement of the drift time in the ATLAS barrel electromagnetic calorimeter using cosmic muon data. Application to the Calorimeter uniformity of response. Technical Report ATL-COM-LARG-2009-024, CERN, Geneva, Jul 2009.

[51] J. B. Blanchard et al. Performance of the cryogenic regulation and the monitoring system of the liquid argon calorimeter temperature. Technical Report ATL-COM-LARG-2010-003, CERN, Geneva, Jan 2010.

[52] B. Dowler. Performance of the ATLAS hadronic end-cap calorimeter in beam tests. *Nuclear Instruments and Methods in Physics Research Section A: Accelerators, Spectrometers, Detectors and Associated Equipment*, 482(1-2):94–124, April 2002.

[53] W. Walkowiak. Drift velocity of free electrons in liquid argon. *Nuclear Instruments and Methods in Physics Research Section A: Accelerators, Spectrometers, Detectors and Associated Equipment*, 449(1-2):288–294, July 2000.

[54] C. Gabaldon et al. Measurement of the drift time in the ATLAS electromagnetic calorimeter using cosmic pulses. Technical Report ATL-COM-LARG-2009-051, CERN, Geneva, Oct 2009.

[55] C. Collard and C. Gabaldon. Drift Time Measurement in the ATLAS Liquid Argon Electromagnetic Calorimeter using Cosmic Muons Data. Technical Report ATL-COM-LARG-2009-056, CERN, Geneva, Nov 2009.

[56] http://atlas.web.cern.ch/atlas/groups/operations/ databases/dddb/materials.php.

[57] http://atlas.web.cern.ch/atlas/groups/operations/ databases/dddb/tag_hierarchy_browser.php.

[58] G. et al. Aad. The ATLAS Experiment at the CERN Large Hadron Collider. *Journal of Instrumentation*, 3(08):S08003, August 2008.

[59] R. Veness. ATLAS BEAM VACUUM SYSTEM INTERFACES. Technical Report ATL-TECH-PUB-2008-003. ATL-COM-TECH-2008-001, CERN, Geneva, Apr 2008.

[60] G. Gorfine. Beam Pipe and Pixel, Feb 2th 2010. $http : //indico.cern.ch/materialdisplay.py?contribid = 1\&materialid = slides\&confid = 83874$. ($http : //indico.cern.ch/materialDisplay.py?contribId = 1\&materialId = slides\&confId = 83874$), Feb 2010.

[61] M. Donega, L. Serin, and K. Tackmann. Photon Conversions at $\sqrt{s} = 900$ GeV with the ATLAS Detector. Technical Report ATL-COM-PHYS-2010-083, CERN, Geneva, Feb 2010.

[62] G. Aad et al. Charged-particle multiplicities in pp interactions at $\sqrt{s} = 900$ GeV measured with the ATLAS detector at the LHC. Technical Report arXiv:1003.3124. CERN-PH-EP-2010-004, Mar 2010.

[63] ATLAS detector and physics performance. Technical Design Report. Vol. 2.

[64] G. Aad et al. Prospects for the Discovery of the Standard Model Higgs Boson Using the H to gamma gamma Decay. Technical Report ATL-PHYS-PUB-2009-053. ATL-COM-PHYS-2009-204, CERN, Geneva, Mar 2009.

[65] W. Chi-Min. QCD predictions for the distribution functions of the photon using Altarelli-Parisi type equations. *Nuclear Physics B*, 167(3):349–363, May 1980.

[66] S. Albino, B. A. Kniehl, G. Kramer, and W. Ochs. Generalizing the dokshitzer-gribov-lipatov-altarelli-parisi evolution of fragmentation functions to the smallest x values. *Phys. Rev. Lett.*, 95(23):232002, Dec 2005.

[67] S. Albino, B. A. Kniehl, G. Kramer, and W. Ochs. Generalizing the Dokshitzer-Gribov-Lipatov-Altarelli-Parisi Evolution of Fragmentation Functions to the Smallest x Values. *Physical Review Letters*, 95(23):232002+, Dec 2005.

[68] F. P. Schilling. Inclusive Diffraction at HERA. Technical Report hep-ex/0210027, DESY, Hamburg, Oct 2002.

[69] Alan D. Martin. Proton structure, Partons, QCD, DGLAP and beyond. Feb 2008.

[70] CTEQ Group webpage: http://www.phys.psu.edu/cteq/.

[71] MRST Group webpage: http://durpdg.dur.ac.uk/hepdata/mrs.html.

[72] J. Pumplin et al. New Generation of Parton Distributions with Uncertainties from Global QCD Analysis. *Journal of High Energy Physics*, 2002(07):012, July 2002.

[73] A. Djouadi and S. Ferrag. PDF uncertainties in Higgs production at hadron colliders. hep-ph/0310209. Oct 2003.

[74] G. Sterman. *An introduction to quantum field theory*. Cambridge University Press, 1993.

[75] C. Balazs. Soft gluon effects on electroweak boson production in hadron collisions. hep-ph/9906422. 1999.

[76] I. Koletsou and L. Fayard. *Recherche du boson de Higgs dans le canal diphoton au LHC avec le détecteur ATLAS*. PhD thesis, Orsay, Paris 11, Orsay, 2008.

[77] T. Sjostrand, S. Mrenna, and P. Skands. PYTHIA 6.4 Physics and Manual. May 2006.

[78] G. Corcella et al. HERWIG 6.5: an event generator for Hadron Emission Reactions With Interfering Gluons (including supersymmetric processes). Oct 2002.

[79] D. Rainwater and D. Zeppenfeld. Searching for H $\rightarrow$ gamma gamma in Weak Boson Fusion at the LHC. Dec 1997.

[80] L. Dixon and M. S. Siu. Resonance-continuum interference in the di-photon Higgs signal at the LHC. Feb 2003.

[81] J. C. Collins and D. E. Soper. Angular distribution of dileptons in high-energy hadron collisions. *Physical Review D*, 16(7):2219–2225, Oct 1977.

[82] M. L. Mangano, M. Moretti, F. Piccinini, R. Pittau, and A. D. Polosa. ALPGEN, a generator for hard multiparton processes in hadronic collisions. May 2003.

[83] S. Hoeche et al. Matching Parton Showers and Matrix Elements. Feb 2006.

[84] C. Balázs. Resbos Webpage: http://www.pa.msu.edu/balazs/RESBOS.

[85] C. Balázs, E. L. Berger, P. M. Nadolsky, and C. P. Yuan. Calculation of prompt diphoton production cross sections at Tevatron and LHC energies. Jul 2007.

[86] J. P. Guillet. Diphox Webpage: http://www.lapp.in2p3.fr/lapth/PHOX_FAMILY/DIPHOX.html.

[87] T. Binoth, Ph, E. Pilon, and M. Werlen. A full Next to Leading Order study of direct photon pair production in hadronic collisions. Apr 2000.

[88] S. Frixione and B. R. Webber. Matching NLO QCD computations and parton shower simulations. *Journal of High Energy Physics*, 2002(06):029+, June 2002.

[89] S. Catani and M. Grazzini. An NNLO subtraction formalism in hadron collisions and its application to Higgs boson production at the LHC. Jun 2007.

[90] A. Djouadi, J. Kalinowski, and M. Spira. HDECAY: a Program for Higgs Boson Decays in the Standard Model and its Supersymmetric Extension. Apr 1997.

[91] Michael Spira. QCD CORRECTIONS TO HIGGS BOSON DECAYS. Apr 1995.

[92] S. Actis. NLO Electroweak Corrections to Higgs Decay to Two Photons. Jan 2009.

[93] G. Degrassi and F. Maltoni. Two-loop electroweak corrections to the Higgs-boson decay H $\rightarrow$ gamma gamma. Apr 2005.

[94] A. D. Martin, R. G. Roberts, W. J. Stirling, and R. S. Thorne. Physical Gluons and High e_T Jets. Oct 2004.

[95] Z. Bern, L. Dixon, and C. Schmidt. Isolating a light Higgs boson from the di-photon background at the LHC. Aug 2002.

[96] D. Froidevaux and D. Zerwas. Electron/Photon CSC Chapter. Technical Report ATL-COM-PHYS-2008-110, CERN, Geneva, Aug 2008.

[97] E. Barberio. The Geant4-Based ATLAS Fast Electromagnetic Shower Simulation. Technical Report ATL-SOFT-CONF-2007-002. ATL-COM-SOFT-2007-014, CERN, Geneva, Oct 2007.

[98] J. P. Guillet. Jetphox Webpage: http://lappweb.in2p3.fr/lapth/PHOX_FAMILY/jetphox_soon.html.

[99] S. Catani, M. Fontannaz, Ph, and E. Pilon. Cross section of isolated prompt photons in hadron-hadron collisions. hep-ph/0204023. Jun 2002.

[100] J. M. Campbell, J. W. Huston, and W. J. Stirling. Hard interactions of quarks and gluons: a primer for LHC physics. Nov 2006.

[101] S. Catani, M. Fontannaz, and E. Pilon. Factorization and soft-gluon divergences in isolated-photon cross sections. Apr 1998.

[102] M. Bettinelli and L. Carminati. Search for a SM Higgs decaying to two photons with the ATLAS detector. Technical Report ATL-PHYS-PUB-2007-013. ATL-COM-PHYS-2007-011, CERN, Geneva, Mar 2007.

[103] P. Aurenche, M. Fontannaz, J.-P. Guillet, E. Pilon, and M. Werlen. A new critical study of photon production in hadronic collisions. hep-ph/0602133. Feb 2006.

[104] N. Andari et al. Higgs Production Cross Sections and Decay Branching Ratios. Technical Report ATL-COM-PHYS-2010-046, CERN, Geneva, Jan 2010.

[105] M. Spira. http://people.web.psi.ch/spira/vv2h/.

[106] K. Arnold et al. VBFNLO: A parton level Monte Carlo for processes with electroweak bosons. Mar 2009.

[107] M. Ciccolini, A. Denner, and S. Dittmaier. Electroweak and QCD corrections to Higgs production via vector-boson fusion at the LHC. Oct 2007.

[108] M. Spira. http://people.web.psi.ch/spira/v2hv/.

[109] O. Brein, A. Djouadi, and R. Harlander. NNLO QCD corrections to the Higgs-strahlung processes at hadron colliders. Jul 2003.

[110] M. L. Ciccolini, S. Dittmaier, and M. Krämer. Electroweak Radiative Corrections to Associated WH and ZH Production at Hadron Colliders. Jun 2003.

[111] W. Beenakker, S. Dittmaier, M. Krämer, B. Plümper, M. Spira, and P. M. Zerwas. NLO QCD corrections to t anti-t H production in hadron collisions. Nov 2002.

[112] S. Dawson, C. Jackson, L. H. Orr, L. Reina, and D. Wackeroth. Associated Higgs production with top quarks at the Large Hadron Collider: NLO QCD corrections. hep-ph/0305087. Jul 2003.

[113] H. Abreu et al. Prospects for the Exclusion of a SM Higgs Decaying into Two Photons. Technical Report ATL-COM-PHYS-2010-170, CERN, Geneva, Jan 2010.

[114] J. Tanaka. Study of Systematic Uncertainty of Fake Photon Estimation: Difference Coming from MC Event Generators. Technical Report ATL-COM-PHYS-2009-420, CERN, Geneva, Aug 2009.

[115] J. Ocariz. Data-driven extraction of background spectra using photon/jet discrimination (http://indico.cern.ch/materialdisplay.py?contribid=2&materialid=slides&confid=74579).

[116] G. Cowan and E. Gross. Statistical combination of several important Standard Model Higgs boson search channels. Technical Report ATL-COM-PHYS-2008-203, CERN, Geneva, Nov 2008.

[117] CDF, D0 Collaborations, and T. Aaltonen. Combination of Tevatron searches for the standard model Higgs boson in the W+W- decay mode. Feb 2010.

[118] H. Wang. Presentation at the HSG1 meeting of 20-05-2009.

[119] The CDF Collaboration. Search for a SM Higgs Boson with the Diphoton Final State at CDF. CDF/PUB/EXOTIC/PUBLIC/10065, February 2010.

[120] The DO Collaboration. Search for the Standard Model Higgs Boson in $\gamma\gamma$ final states at D0 with L=4.2 fb-1. DO Note 5858-CONF, February 2009.